UC San Diego

UC San Diego Electronic Theses and Dissertations

Title

Identification and Multi-scale Analysis of Successive Atmospheric Rivers in California

Permalink

https://escholarship.org/uc/item/8c43730c

Author

Fish, Meredith

Publication Date

2020

Peer reviewed|Thesis/dissertation

eScholarship.org Powered by the California Digital Library
University of California

UNIVERSITY OF CALIFORNIA SAN DIEGO

Identification and Multi-Scale Analysis of Successive Atmospheric Rivers in California

A dissertation submitted in partial satisfaction
of the requirements of the degree
Doctor of Philosophy

in

Oceanography

by

Meredith A. Fish

Committee in charge:

Arthur J. Miller, Co-Chair
F. Martin Ralph, Co-Chair
Ian Eisenman
Sarah T. Gille
Joshua Graff Zivin
Shang-Ping Xie

2020

Copyright

Meredith A. Fish, 2020

All rights reserved.

The Dissertation of Meredith A. Fish is approved, and it is acceptable in quality and form for publication on microfilm and electronically:

_____

_____

_____

_____

_____
Co-Chair

_____
Co-Chair

University of California San Diego

2020

DEDICATION

To all the girls that aren't sure how big to dream; keep dreaming.

And to my parents, who encouraged my pursuits and fostered my independence from a young age.

EPIGRAPH

Nevertheless, she persisted.

Senate Majority Leader Mitch McConnell in reference to Senator Elizabeth Warren not silencing her objection to the confirmation of Senator Jeff Session as U.S. Attorney General

TABLE OF CONTENTS

LIST OF ABBREVIATIONS

AR……...Atmospheric River
ARO……Atmospheric River Observatory
ASMR……..Advanced Microwave Scanning Radiometer
ASTD……Air-sea temperature difference
AVHRR…….Advanced Very High Resolution Radiometer
BBY……Bodega Bay, CA
CCS……..California Current System
DJF……..December, January, February
EC……..Extra-tropical Cyclone
ELI……...ENSO Longitude Index
ENSO……..El Niño/Southern Oscillation
GHRSST……Group for High Resolution Sea Surface Temperature
IVT…….Integrated Vapor Transport
IWV…….Integrated Water Vapor
JPL……Jet Propulsion Laboratory
MAM……...March, April, May
MERRA-2…… Modern-Era Retrospective Analysis for Research and Applications, Version 2
MFW……..Mesoscale Frontal Wave
MODIS……...Moderate Resolution Imagining Spectroradiometers
MUR……Multi-scale Ultra-high Resolution
NASA……National Aeronautics and Space Administration
NCAR……National Center for Atmospheric Research
NOAA……..National Oceanic and Atmospheric Administration
OI……...Optimally Interpolated
PA…….....Persistent Anomaly
PR……Point Reyes, CA
PRISM……..Parameter-elevation Regressions on Independent Slopes Model
SF…….San Francisco, CA
SLP……..Sea-Level Pressure
SON…….September, October, November
SST……Sea Surface Temperature
SSTa……...Sea Surface Temperature Anomaly
WY……..Water Year
z500……...500-hPa Geopotential Heights

LIST OF SYMBOLS

W……....Weight
ϕ……...Latitude
π…….....Pi
σ……..Standard Deviation

LIST OF FIGURES

LIST OF TABLES

ACKNOWLEDGEMENTS

Thank you to my academic advisors, Art Miller and Marty Ralph, for providing me this opportunity to complete a PhD. Art, thank you for your constant guidance and support, your focus on student well-being and for being a prime example of an exemplary role model. Marty, thank you for the freedom to pursue my own scientific interests, the endless professional development opportunities and the financial support. Thank you to my committee members, Ian Eisenman, Sarah Gille, Shang-Ping Xie and Josh Graff Zavin for the feedback and support.

My graduate school experience and research has been shaped by many more than just my academic advisors. Anna Wilson: You have had a profound impact on my approach to science and development towards becoming a scientist, you selfishly gave me ample hours of your time throughout my PhD and I wish I could give you more credit than this. Thank you for every piece of writing you have reviewed, every figure you've critiqued, every pep talk you've given and more. James Done and Daniel Swain: thank you for being interested in my scientific questions and helping me pursue them further than I could have imagined. Through supporting my visits to NCAR, weekly science discussions and more, you both have been pushed me to ask better questions and stand on my own two feet. Allison Michaelis: Thank you for the feedback, encouragement and friendship over these past few years. You have played an integral role in my scientific advancement and experience at SIO.

To the many members of CW3E, including Rachel Weihs, Luca Delle Monache, Maryam Lamjiri, Carly Ellis, Mike DeFlorio, Forest Cannon, Jay Cordeira, and the many others, who have helped me in some way through this process, thank you. The early mornings and field work memories, friendship, scientific and technical support, and shared experiences across the years have left long lasting positive memories of my time here.

To the amazing Team Miller, the shared comradery of being advised by Art, in both science and life, is a bond that I believe, will last forever. The interactions and support from you all always left me feeling uplifted and fulfilled. Cheers to the many shared glasses of wine over discussions about climate, ocean and atmospheric variability.

I will always have fond memories of my time in San Diego as it has been shaped by many experiences and memories with friends. To Kara Voss, Maya Becker, Charlotte and Jesse DeWald, Liz Oliver, Lindsey Jasperse, Nicole Yen, Caroline Lowcher, Will Cyr, Elizabeth Suto, Emily Sawyer, and many more: your friendship and support has meant the world to me, I would not be at this point if it weren't for you all, thank you.

While I am a first-generation graduate student, the unwavering support from my family has been crucial to my success. Mom and Dad: thank you for supporting my move across the country, spending the holidays on the West Coast, and sacrificing your own desires so your daughters could succeed. To Sarah: Thank you for always being there when I needed it; your continuous support and love is remarkable and I'm grateful to have you as a sister. To Amanda: Following you out to California was one of the best decisions I have ever made, and I would have never had the confidence to go through with it, if it weren't for you. Your home in LA became home to me, and for the first few years, I often could relieve my homesickness by driving up to see you. You will always be my best friend and big sister, thank you for your unwavering support. It means the world to me.

Lastly, Patrick, you have been an incredible partner during this, at times stressful, endeavor. You celebrate my highs and wallow in the lows, just as if they were your own. I have relied on your steadiness and support throughout this process and your ability to lift my spirits is unmatched. I am so thankful for everything you have done for me over these past five years.

Chapter 2, in full, is a reprint of the material as it appears in the Journal of Hydrometeorology 2019. Fish, M. A., A. M. Wilson, F. M. Ralph (2019): "Atmospheric river families: Definition and associated synoptic conditions", *Journal of Hydrometeorology*, 20, 2091-2108, doi: 10.1175/JHM-D-18-0217.1. The dissertation author was the primary investigator and author of this paper.

Chapter 3, in full, is the material submitted to the as Journal of Climate. Fish, M. A., J. M. Done, A. M. Wilson, D. L. Swain, F. M. Ralph (2020): "Large-scale drivers of successive atmospheric river events in California", *Journal of Climate*, submitted 5/11/2020. The dissertation author was the primary investigator and author of this paper.

Chapter 4, in part is currently being prepared for submission for publication of the material. Fish, M. A., Michaelis, A., D. L. Swain, J. M. Done, and F. M. Ralph. The dissertation author was the primary investigator and author of this paper.

Chapter 5, in part is currently being prepared for submission for publication of the material. Fish, M. A., R. Weihs, A. Michaelis, A. J. Miller, L. D. Monache, and F. M. Ralph. The dissertation author was the primary investigator and author of this paper.

VITA

2015	Bachelor of Science in Meteorology, Pennsylvania State University
2015-2020	Graduate Student Researcher, Scripps Institution of Oceanography, UCSD
2020	Master of Science in Oceanography, Scripps Institution of Oceanography, UCSD
2020	Doctor of Philosophy in Oceanography, Scripps Institution of Oceanography, UCSD

PUBLICATIONS

Fish, M. A., J. M. Done, A. M. Wilson, D. L. Swain, and F. M. Ralph, 2020: Large-scale drivers of successive atmospheric river events in California, *J. Climate (in review)*

Cannon, F., N. Oakley, C. Hecht, R. Demirdjian, A. Michaelis, **M. A. Fish**, B. Kawzenuk, and A. M. Wilson, 2020: Observations and predictability of narrow cold frontal rainbands in Southern California. *Wea. Forecasting (in review)*

Adusumili, S., A. Borsa, **M. A. Fish**, H. McMillan, and F. Silverii, 2019: A decade of terrestrial water storage changes across the contiguous United States from GPS and GRACE. *Geophys. Res. Lett.*, doi: 10.1029/2019GL085370.

Fish, M. A., A. M. Wilson, and F. M. Ralph, 2019: Atmospheric river families: Definition and associated synoptic conditions. *J. Hydrometeorol.*, **20**, 2091–2108, https://doi.org/10.1175/JHM-D-18-0217.1.

ABSTRACT OF THE DISSERTATION

Identification and Multi-Scale Analysis of Successive Atmospheric Rivers in California

by

Meredith A. Fish

Doctor of Philosophy in Oceanography

University of California San Diego, 2020

Arthur J. Miller, Co-Chair
F. Martin Ralph, Co-Chair

California has extremely high interannual variability in precipitation, and this is projected to increase with climate change. During northern California's wettest year on record (2017), successive atmospheric river (AR) events associated with extreme precipitation served both to alleviate drought conditions and contribute to the Oroville Dam crisis. This dissertation investigates the characteristics, synoptic patterns, and drivers of these successive ARs.

First, this dissertation introduces the concept of "AR families" using an objective method to identify successive AR events at a single location (Bodega Bay, CA). Compared to single AR events, AR families exhibit unique, identifiable and semi-stationary patterns across the North Pacific. The algorithm was then applied to all AR events impacting California over 39 years, 1981-2019. K-means clustering identified six distinct clusters of large-scale patterns associated with AR families. These clusters represent two types of predominant patterns: meridional and zonal, and two show strong relationships with the El Niño/Southern Oscillation.

Persistent anomalies (PAs) across the North Pacific are evaluated for their association with AR families and drought conditions. This analysis is sensitive to methodology including detrending and determining the appropriate magnitude for the PA, ultimately impacting the identification of PAs associated with drought conditions or AR families in California. Traditional methodologies lack a strong correlation between PA frequency and precipitation in California, therefore new methods are explored to meaningfully relate the frequency and location of PAs to anomalous precipitation statewide.

Two satellite sea surface temperature (SST) datasets are used to assess the relationship between wintertime SST variability and AR activity, showing low levels of spatial SST variability co-occur with low AR frequency. Within AR events, near shore buoy data shows that the air-sea temperature difference prior, during, and post AR passage is consistent with an approaching warm front, AR conditions and cold air advection, respectively. Case studies of AR families further investigate the variability between AR activity, SST, and precipitation.

These findings identify the importance of successive AR events to California's climate and characterize their synoptic precursors and meteorological drivers that provide the foundation for increased situational awareness and predictability of their occurrence and impacts.

Chapter 1

Introduction

1.1 Motivation

Western North America and other Mediterranean climates around the world are known for their variability in interannual and intra-annual precipitation. The combination of ever-increasing demand, inconsistent supply, and additional stressors, such as extended drought periods and early season snowmelt, has led to the development of extensive water infrastructure. Throughout the western US and other Mediterranean climates, this infrastructure was built to slow the release of winter precipitation and spring snowmelt (Grantham et al. 2012). In recent years, natural variability amplified by climate change induced variability have increased the occurrences of extreme daily precipitation events (Kharin et al. 2013, Polade et al. 2014) and drought (Diffenbaugh et al. 2015), straining the capacity of water resources throughout the western US.

In the last decade alone, California has endured successive periods of extreme precipitation contributing to the Oroville Dam failure (White et al. 2018) and multi-year droughts costing the state approximately $3.8 billion just in agricultural economic losses (Lund et al. 2018 and references therein). These examples highlight the importance of studying weather and climate extremes to fully understand the physical drivers and impacts of these extreme events, which can be applied to better predict and be more resilient to these impacts.

Compound events have been defined by the Intergovernmental Panel on Climate Change Special Report on Climate Extremes, as 1) extreme events occurring successively, 2) the

combination of extreme events or 3) the combination of regular events having extreme impact (Seneviratne et al. 2012). Previous studies on compound events have focused on the co-occurrence of extreme drought and heat waves (e.g. AghaKouchak et al. 2014), storm surge and precipitation (e.g. van den Hurk et al. 2015) and other concurrent extremes, with less focus on successive-type compound events. While this compound event framework has not been extensively used in the atmospheric sciences, identifying and studying serial or successive events is certainly not new to the meteorological community. Cyclone families, defined as a temporally clustered series of extra-tropical cyclones were first identified by Bjerknes and Solberg (1922) in the North Atlantic. These successive cyclones favor certain atmospheric conditions and dynamical mechanisms, such as, an intensified eddy driven jet or Rossby wave breaking, and are known to produce greater impacts than individual cyclones (Mailier et al. 2006, Vitolo et al. 2009, Pinto et al. 2014). In addition to the increased risk associated with these compound events, it is important to quantify their occurrence in the current climate to help understand other precipitation related risks in vulnerable regions (Zscheischler and Seneviratne, 2017, Zscheischler et al. 2018), such as the variable climate of the western US.

Studies project increased precipitation volatility in California through the 21st century (Swain et al. 2018), which has the potential to wreak havoc on the water infrastructure throughout the western US (Dettinger et al. 2015). Thus, water managers, especially in California, are increasingly seeking scientific advancements to help optimize water management and improve interannual resilience (Jasperse et al. 2015, FIRO Steering Committee 2017). Precipitation volatility in California is largely tied to the presence or lack of atmospheric rivers (ARs; Dettinger et al. 2011). ARs are long, narrow and transient corridors of water vapor often found in the cold sector of an extra-tropical cyclone (Zhu and Newell 1998; Ralph et al. 2004,

2005, Guan and Waliser 2017, Ralph et al. 2017). Hydrologic impacts of ARs are modulated by duration (Ralph et al. 2013, Payne and Magnusdottir 2016, Lamjiri et al. 2017) and environmental pre-conditions, such as soil moisture (Ralph et al. 2013). Dynamical mechanisms, such as Rossby wave breaking and North Pacific jet dynamics, which act on longer temporal and spatial scales than ARs, foster AR and cyclone development; therefore, understanding the relationship between them aids in our ability to forecast such events (Hu et al. 2017, Mundhenk et al. 2016, Griffin and Martin 2017).

Due to the shared atmosphere-ocean boundary and the ocean's higher heat content, additional predictability can often be found from studying the connection between ocean conditions and downstream weather. For North America, the teleconnection between the equatorial Pacific sea surface temperature (SST) and western US precipitation has long been studied (Ropelewski and Halpert 1986, Cayan et al. 1998, McCabe and Dettinger 1999, Gershunov and Barrett 1998). The oscillation of warm and cool SST across the equatorial Pacific initiates the poleward propagation of a Rossby wave train into the mid-latitudes, strengthening the Gulf of Alaska low pressure system, leading to an increase in extra-tropical cyclone and AR activity. Multiple studies have demonstrated that AR frequency throughout the North Pacific basin is strongly modulated by the El Niño/Southern Oscillation (ENSO) (Bao et al. 2006, Ryoo et al. 2013, Mundhenk et al. 2016). Increased predictability is not confined to the equatorial Pacific; the development and installation of SST and surface wind satellites was influential in the understanding of mid-latitude air-sea interactions, particularly at the mesoscale (Chelton and Xie 2010). These advances led to the discovery of positive correlations between SST and surface wind speed at 10-1000 km, thus having a positive impact on the response of the atmospheric boundary layer through various coupling mechanisms (Small et al. 2008, Gemmrich and

Monahan 2018). While the eastern Pacific is not known for its large SST variability, the California Current System is dominated by mesoscale eddy activity and summertime upwelling. Unique ship-based observations of SST, air temperature, sensible and latent heat fluxes during the CalWater-2015 campaign (Ralph et al. 2016) on the NOAA *Ronald H. Brown* showed the increased air and sea temperature variability co-occurring with the presence of ARs, changing the surface fluxes and stability of the boundary layer (Neiman et al. 2017).

Combining a variety of observational and reanalysis data, the following dissertation is motivated by large-scale ocean and atmosphere variability impacting characteristics of AR families and ocean mesoscale features modulating boundary layer processes in successive ARs.

1.2 Dissertation Overview

The objective of this dissertation is to apply the compound event framework to ARs impacting California to define and identify successive AR events, termed AR families, using a combination of atmospheric reanalysis and observational data across a multitude of scales in the atmosphere and ocean. This dissertation is motivated by the hypothesis that compound events, such as successive ARs, exhibit distinct and identifiable patterns that are more predictable and contribute to more severe impacts across California.

The dissertation is organized as follows. In Chapter 2, the term "AR families" is introduced and defined using a unique hourly observational dataset in Northern California. This chapter identifies the synoptic conditions associated with AR families, distinguishes different types of AR families and highlights why water year (WY; October 1-September 30) 2017 was a particularly wet year for California. Chapter 3 draws motivation from the earlier chapter to create a 39-year dataset of AR families that impact all of California using reanalysis data. K-means

clustering is applied to the longer dataset to evaluate the different large-scale drivers that can lead to AR family variability. This chapter also starts to address the impacts of AR families through analysis of precipitation impacts associated with the resulting clusters, representing the main modes of variability. Additionally, with the longer dataset, Chapter 3 explores the relationship between ENSO and AR families. Chapter 4 takes a broader view to address how characteristics of persistent anomalies and AR families are related to interannual precipitation variability throughout the western US. Lastly, Chapter 5, focuses on near-shore ocean and boundary layer processes to investigate the air-sea temperature relationship before, during and after AR passage and determine how successive AR events can change surface processes.

References

AghaKouchak, A., Cheng, L., Mazdiyasni, O. & Farahmand, A., 2014: Global warming and changes in risk of concurrent climate extremes: insights from the 2014 California drought. *Geophys. Res. Lett.* **41**, 8847–8852.

Bao., J.W., S.A. Michelson, P.J. Neiman, F.M. Ralph, and J.M. Wilczak, 2006: Interpretation of Enhanced Integrated Water Vapor Bands Associated with Extratropical Cyclones: Their Formation and Connection to Tropical Moisture. *Mon. Wea. Rev.,* **134**, 1063-1080, doi: 10.1175/MWR3123.1.

Bjerknes, J., and H. Solberg, 1922: Life cycle of cyclones and the polar front theory of atmospheric circulation. *Geophys. Publ.,* **3**, 1-18.

Cayan, D. R., K. T. Redmond, and L. G. Riddle, 1999: ENSO and Hydrologic Extremes in the Western United States. *J. Clim.*, **12**, 2881–2893.

Chelton, D., and S.-P. Xie, 2010: Coupled Ocean-Atmosphere Interaction at Oceanic Mesoscales. *Oceanography*, https://doi.org/10.5670/oceanog.2010.05.

Dettinger, M. D., F. M. Ralph, T. Das, P. J. Neiman, and D. R. Cayan, 2011: Atmospheric Rivers, Floods and the Water Resources of California. *Water*, **3(2)**, 445-478, doi:10.3390/w3020445.

Dettinger, M. D. Udall, and A. Georgakakos, 2015: Western water and climate change. *Ecological Applications*, doi: 10.1890/15-0938.1.

Diffenbaugh, N. S., D. L. Swain, and D. Touma, 2015: Anthropogenic warming has increased drought risk in California. *Proc. Natl. Acad. Sci., **112**(13), 3931-3936, doi: 10.1073/pnas.1422385112.*

Gemmrich, J., and A. Monahan, 2018: Covariability of Near-Surface Wind Speed Statistics and Mesoscale Sea Surface Temperature Fluctuations. *J. Phys. Oceanogr.*, **48**, 465–478, https://doi.org/10.1175/JPO-D-17-0177.1.

Gershunov, A., and T. P. Barnett, 1998: Interdecadal Modulation of ENSO Teleconnections. *Bull. Am. Meteorol. Soc.*, **79**, 2715–2726.

Griffin, K. S., and J. E. Martin, 2017: Synoptic features associated with temporally coherent modes of variability of the North Pacific jet stream. *J. Climate,* **30**, 39-54, doi:10.1174/JCLI-D-15-0833.1.

Grantham, T. E., R. Figueroa, and N. Prat, 2012: Water management in Mediterranean river basins: a comparison of management frameworks, physical impacts, and ecological responses. *Hydrobiologia*, doi: 10.1007/s10750-012-1289-4.

Guan, B., and D. E. Waliser, 2017: Atmospheric rivers in 20 year weather and climate simulations: A multimodel, global evaluation. *J. Geophys. Res.*, **122**, 5556-5581, doi:10.1002/2016JD026174.

Hu, H., F. Dominguez, Z. Wang, D. A. Lavers, G. Zhang, and F. M. Ralph, 2017: Linking atmospheric river hydrological impacts on the U.S. West Coast to Rossby wave breaking. *J. Climate,* **30**, 3381-3399, doi: 10.1175/JCLI-D-16-0386.1.

van den Hurk, B., van Meijgaard, E., de Valk, P., van Heeringen, K.-J. & Gooijer, J., 2015: Analysis of a compounding surge and precipitation event in the Netherlands. *Environ. Res. Lett.* **10**, 035001.

Jasperse, J., F. M. Ralph, M. Anderson, L. Brekke, M. Dillabough, M. Dettinger, R. Hartman, C. Jones, P. Rutten, C. Talbot, R. Webb, D. Ford, A. O'Donnell, and A. DuBay, 2015: A comprehensive plan to evaluate the viability of forecast informed reservoir operation for Lake Mendocino. *Sonoma County Water Agency report,* 1-374.

Kharin, V. V., F. W. Zwiers, X. Zhang, and M. Wehner, 2013: Changes in temperature and precipitation extremes in the CMIP5 ensemble. *Clim. Change*, **119**(2), 345-357, doi: 10.1007/s10584-013-0705-8.

Lamjiri, M. A., M. D. Dettinger, F. M. Ralph and B. Guan, 2017: Hourly storm characteristics along the U.S. West Coast: Role of atmospheric rivers in extreme precipitation. *Geophys. Res. Lett.*, **44**, 7020-7028, doi:10.1002/2017GL074193.

Lund, J., J. Medellin-Azuara, J. Durand, and K. Stone, 2018: Lessons from California's 2012-2016 drought. *J. Water Res. Planning Man.*, **144**(10), doi: 10.1061/(ASCE)WR.1943-5452.0000984.

Mailier, P. J., D. B. Stephenson, C. A. T. Ferro, and K. I. Hodges, 2006: Serial Clustering of extratropical cyclones. *Mon. Wea. Rev.,* **134**, 2224-2240, doi:10.1175/MWR3160.1.

Mccabe, G. J., and M. D. Dettinger, 1999: DECADAL VARIATIONS IN THE STRENGTH OF ENSO TELECONNECTIONS WITH PRECIPITATION IN THE WESTERN UNITED STATES. *Int. J. Clim.*, **19**, 1399–1410.

Mundhenk, B. D., E. A. Banks, and E. D. Maloney, 2016: All-season climatology and variability of atmospheric river frequencies over the North Pacific. *J. Climate,* **29**, 4885-4903, doi: 10.1175/JCLI-D-15-0655.1.

Neiman, P. J., N. Gaggini, C. W. Fairall, J. Aikins, J. R. Spackman, L. R. Leung, J. Fan, J. Hardin, N. R. Nalli, and A. B. White, 2017: An Analysis of Coordinated Observations from NOAA's *Ronald H. Brown* Ship and G-IV Aircraft in a Landfalling Atmospheric River over the North Pacific during CalWater-2015. *Mon. Weather Rev.*, https://doi.org/10.1175/MWR-D-17-0055.1.

Payne, A. E., and G. Magnusdottir, 2016: Persistent landfalling atmospheric rivers over the west coast of North America. *J. Geophys. Res.*, **121**, 13287-13300, doi: 10.1002/2016JD025549.

Pinto, J. G., I. Gomara, G. Masato, H. F. Dacre, T. Woollings, and R. Caballero, 2014: Large-scale dynamics associated with clustering of extratropical cyclones affecting Western Europe. *J. Geophys. Res. Atmos.,* **119**, 13704-13719, doi: 10.1002/2014JD022305.

Polade, S. D., D. W. Pierce, D. R. Cayan, A. Gershunov, and M. D. Dettinger, 2014: The key role of dry days in changing regional climate and precipitation regimes. *Nat. Sci. Rep.*, **4**, 4364, doi: 10.1038/srep04364.

Ralph, F. M., P. J. Neiman, and G. A. Wick, 2004: Satellite and CALJET Aircraft Observations of Atmospheric Rivers over the Eastern North Pacific during the Winter of 1997/1998. *Mon. Wea. Rev.*, **132**, 1721-1745, doi:10.1175/1520-0493(2004)132<1721:SACAOO>2.0.CO;2.

Ralph, F. M., P. J. Neiman, and R. Rotunno, 2005: Dropsonde observations in low-level jets over the northeastern Pacific Ocean from CALJET-1998 and PACJET-2001: Mean vertical-profile and atmospheric-river characteristics. *Mon. Wea. Rev.,* **133**, 889–910

Ralph, F. M., S. F. Iarcobellis, P. J. Neiman, J. M. Cordeira, J. R. Spackman, D. E. Waliser, G. A. Wick, A. B. White, and C. Fairall, 2017: Dropsonde Observations of Total Integrated Water Vapor Transport within North Pacific Atmospheric Rivers. *J. Hydrometeor.*, **18**, 2577-2596, doi:10.1175/JHM-D-17-0036.1.

Ralph, F. M., T. Coleman, P. J. Neiman, R. J. Zamora, and M. D. Dettinger, 2013: Observed Impacts of Duration and Seasonality of Atmospheric-River Landfalls on Soil Moisture and Runoff in Coastal Northern California. *J. Hydrometeor.*, **14**, 443-459, doi:10.1175/JHM-D-12-076.1.

Ralph, F. M., K. A. Prather, D. Cayan, J. R. Spackman, P. DeMott, M. Dettinger, C. Fairall, R. Leung, D. Rosenfeld, S. Rutledge, D. Waliser, A. B. White, J. Cordeira, A. Martin, J. Helly, and J. Intrieri, 2016: Calwater field studies designed to quantify the roles of atmospheric rivers and aerosols in modulating U.S. West Coast Precipitation in a changing climate. *Bull. Am. Meteorol. Soc.*, **97**, 1209–1228, https://doi.org/10.1175/BAMS-D-14-00043.1.

Ropelewski, Chester, F., Halpert, M. S., 1986: North American Precipitation and Temperature Patterns Associated with the El Nino/Southern Oscillation (ENSO). *Mon. Weather Rev.*, **114**, 2352–2362.

Ryoo, J.M., Y. Kaspi, D.W. Waugh, G.N. Kiladis, D.E. Waliser, E.J., Fetzer, and J. Kim, 2013: Impact of Rossby Wave Breaking on U.S. West Coast Winter Precipitation during ENSO Events. *J. Climate*, **26**, 6360-6382, doi:10.1175/JCLI-D-12-00297.1.

Small, R. J., S.P. deSzoeke, S.P. Xie, L. O'Neil, H. Seo, Q. Song, P. Cornillon, M. Spall and S. Minobe, 2008: Air-sea interaction over ocean fronts and eddies. *Dyn. Atmos. Ocean.*, https://doi.org/10.1016/j.dynatmoce.2008.01.001.

Swain, D. L., B. Langenbrunner, J. D. Neelin, and A. Hall, 2018: Increasing precipitation volaitility in twenty-first century California. *Nat. Clim. Change,* doi: 10.1038/s41558-018-0140-y.

Vitolo, R., D. B. Stepenson, L. M. Cook, K. Mitchell-Wallace, 2009: Serial clustering of intense European storms. *Meteorologische Zeitschrift,* **18**, 411-424, doi: 10.1127/0941-2948/2009/0393.

White, A. B., B. J. Moore, D. J. Gottas, and P. J. Neiman, 2019: Winter storm conditions leading to excessive runoff above California's Oroville Dam during January and February 2017. *Bull. Amer. Meteor. Soc.*, doi: 10.1175/BAMS-D-18-0091.1.

Zhu, Y., and R. E. Newell, 1998: A Proposed Algorithm for Moisture Fluxes from Atmospheric Rivers. *Mon. Wea. Rev.*, **126**, 725-735, doi:10.1175/1520-0493(1998)126<0725:APAFMF>2.0.CO;2.

Zscheischler, J., and S. I. Seneviratne, 2017: Dependence of drivers affects risks associated with compound events. *Sci. Adv.* **3**, e1700263.

Zscheischler, J., S. Westra, B.J.J.M. Hurk, *et al.,* 2018: Future climate risk from compound events. *Nature Clim Change* **8,** 469–477, doi:10.1038/s41558-018-0156-3.

Chapter 2

Atmospheric River Families: Definition and Associated Synoptic Conditions

Abstract

Atmospheric rivers (AR) can cause flooding when they are strong and stall over an already wet watershed. While earlier studies emphasized the role of individual, long-duration ARs in triggering floods, it is not uncommon for floods to be associated with a series of ARs that strike in close succession. This study uses measurements from an atmospheric river observatory at Bodega Bay (BBY), in Northern California, to identify periods when multiple AR events occurred in rapid succession. Here, an AR "event" is the period when AR conditions are present continuously at BBY. An objective method is developed to identify such periods, and the concept of "AR families" is introduced. During the period studied there were 228 AR events. Using the AR family identification method, a range of aggregation periods (the length of time allowed for ARs to be considered part of a family) were tested. For example, for an aggregation period of 5 days, there were 109 AR families, with an average of 2.7 ARs per family. Over a range of possible aggregation periods, typically there were 2-6 ARs per family. Compared to single AR events, the synoptic environment of AR families is characterized by lower geopotential heights throughout the mid-latitude North Pacific, an enhanced subtropical high, and a stronger zonal North Pacific jet. Analysis of water year 2017 demonstrated a persistent geopotential height dipole throughout the North Pacific and a positive anomaly of integrated water vapor extending toward California. AR families were favored when synoptic features were semi-stationary.

2.1 Introduction

An atmospheric river (AR) is defined as a long, narrow and transient corridor of strong horizontal water vapor transport typically associated with an extratropical cyclone (Zhu and Newell 1998; Ralph et al. 2004, 2005, Guan and Waliser 2017, Ralph et al. 2017). ARs are the primary mechanism for water vapor transport into the mid-latitudes although they cover 10% or less of the globe (Zhu and Newell 1998). ARs are characterized by abundant moisture in the lower troposphere and the presence of a low-level jet, and they can contribute to extreme precipitation (Dettinger et al. 2011, Lamjiri et al. 2017). Globally, ARs most frequently impact the windward side of continents (Guan and Waliser 2017), though ARs have supported extreme precipitation in other locations too, such as the eastern or central United States (Moore et al. 2012, Lavers and Villarini 2013, Mahoney et al. 2016). Through mechanisms such as lifting associated with fronts and orographic lift upon interaction with terrain, ARs can produce heavy rain (Ralph et al. 2011, 2013, Rutz et al. 2014, Lamijri et al. 2017) and flooding (Ralph et al. 2006, Neiman et al. 2008, 2011, Ralph et al. 2013).

While the entire U.S. West Coast is impacted by ARs, Northern California's Russian River watershed in particular receives 60-70% of its total annual precipitation from ARs (Gershunov et al. 2017), and ARs were associated with all seven floods that occurred in the watershed between 1997-2006 (Ralph et al. 2006). Between the two ingredients necessary for high precipitation, rainfall rate and duration (Doswell et al. 1996), within California, storm duration is a strong indicator for higher precipitation and streamflow totals (Ralph et al. 2013, Lamjiri et al. 2017); orientation and water vapor transport intensity have also been shown to impact precipitation distributions from ARs in the Russian River watershed (Hecht and Cordeira 2017).

Ensemble forecasts (from 1-16 day lead times) of western United States landfalling ARs, in terms of the integrated water vapor transport, exhibit higher skill than ensemble forecasts of precipitation distributions at the same spatial scale (Lavers et al., 2016), and this can improve situational awareness. However, the intensity and duration of ARs are difficult to accurately forecast at the temporal and spatial resolution necessary to provide information critical for water management decisions and emergency preparedness (Ralph et al. 2019). AR forecast skill degrades with increasing lead time and exhibits significant errors in landfall location, up to 800-km over a 10-day lead time (Wick et al. 2013; Nardi et al. 2018). While AR forecasts do improve within a 4-day lead time as ARs approach the coast, there are still inaccuracies in AR amplitude, position and duration which can lead to impactful forecast errors in precipitation distribution both in coastal and inland regions (Ralph et al. 2011).

While ARs are synoptic-scale features that can span entire ocean basins, smaller-scale features can not only influence forecast skill but also alter hydrologic impacts. Mesoscale frontal waves (MFWs) associated with an AR can modify the spatial distribution of the AR and increase the total event precipitation (Ralph et al. 2011). For one case in Southern California, an AR affected by a MFW caused an increase in the convergence and ascent along frontal boundaries within the AR, accounting for 35-36% of the storm total precipitation, 3 times larger in the region influenced by the MFW (Neiman et al. 2004). Persistent ARs with durations longer than 63 hours (the 85th percentile) have a much greater moisture content than non-persistent ARs, enhancing the hydrologic impact of these events (Payne and Magnusdottir 2016). This aligns with observations of higher precipitation accumulations and streamflow impacts from longer duration storms (Ralph et al. 2013, Lamjiri et al. 2017). Dynamical mechanisms, such as Rossby wave breaking and North Pacific jet dynamics, which act on longer temporal and spatial scales

than AR events, foster AR and cyclone development (Hu et al. 2017, Mundhenk et al. 2016, Griffin and Martin 2017) and can modulate AR duration as well.

Water year (WY, October 1 – September 30) 2017 was a record wet year in Northern California. Many ARs were observed to be more impactful simply by virtue of arriving shortly after a previous AR, where the watershed had yet to recover its storage space in streams and soils to accommodate additional rainfall. This led to additional flooding. These ARs were not necessarily long duration ARs or persistent ARs, but rather a series occurring in close temporal proximity. In order to explore the dynamical forcings and synoptic regimes through this lens to gain greater insight into the relevant scales, mechanisms, and potential predictability of these phenomena, we introduce the term "AR families", which will be defined in detail in Section 2. While assessing the direct impacts of AR families is out of the scope of this study, case study analyses of AR families compared to single AR events show increased precipitation totals and elevated stream discharge rates for AR families (not shown).

While ARs have not previously been classified in precisely this way, cyclone families were first identified in the literature by Bjerknes and Solberg (1922), and have been shown to produce greater impacts than individual cyclones (Vitolo et al. 2009). Cyclone families exhibit periodicity, enabling the division of cyclones into groups. Families develop along the same polar front with the first cyclone traveling along a track north of the family and the last cyclone so far south it reaches the trade winds. As a cyclone family passes a fixed point, usually four cyclones can be observed, although that number can vary considerably from one family to another (Bjerknes and Solberg 1922). Extratropical cyclones (ECs) frequently occur all over the globe independent of ARs; however, 82 percent of ARs are associated with ECs in the North Pacific

(Zhang et al. 2018). Therefore, we will begin our assessment of AR families by reviewing the methodologies used to investigate cyclone families.

Mailier et al. (2006) investigated cyclone families in western Europe, and noted that the complexity and variety of mechanisms that govern fronts and cyclones may generally indicate that cyclone clusters can be produced by a wide variety of synoptic regimes and multiscale processes. Methods including serial randomness, clustering, and regularity for identification of cyclone families were also described therein. Pinto et al. (2014) further found that, in the same region, the serial clustering of cyclones occurs more frequently than expected by chance, suggesting dynamical mechanisms may favor their occurrence. Numerical simulations of general atmospheric circulation led to the conclusion that parent cyclones, through the production of fronts, can create smaller, at times multiple, secondary cyclones (Eliassen 1966). Multiple cyclones in Norway throughout December 2006 combined with the meridional transport of moisture through associated ARs led to above average temperature and precipitation during that month (Sodemann and Stohl 2013). In the North Pacific storm track, downstream energy dispersion from baroclinic waves extending eddy activity eastward toward areas of less baroclinicity can play a role in the initiation of cyclone families (Chang and Orlanski 1993, 1994). Upstream development has also been attributed to the genesis of cyclone families (Wernli et al. 1999).

In this work, we will use a combination of in situ observations and reanalysis to first create a catalog of AR families, where our identification methodology is informed by the literature on cyclone families and long duration, persistent ARs, and then conduct a thorough evaluation of the synoptic environment in which they occur. Our hypothesis is that if the large-scale environment conducive to the continuous production and evolution of ARs to form an AR

family is identifiable, then perhaps these impactful periods can be predicted with better skill than for individual ARs.

This study is organized as follows. In section 2, a description of the algorithm created to identify AR families, including the observational data used to determine the presence of an AR, is presented, along with the method used to calculate anomalous and climatological values of large scale atmospheric conditions from reanalysis. Section 3 provides statistics related to the occurrence of AR families and describes their synoptic-scale characteristics in the Russian River watershed. Section 4 continues this synoptic evaluation of AR families and includes a discussion of the synoptic-scale differences between all AR families, single AR events, AR families with multiple AR events and AR families with few AR events. Section 5 provides a case study of WY 2017. Section 6 includes the conclusion and discussion.

2.2 Methods

a. Observational Data

As part of the California Department of Water Resources Enhanced Flood Response and Emergency Preparedness Program, networks of observing stations have been established to monitor and study ARs along the U.S. West Coast (White et al. 2013). This includes stations known as Atmospheric River Observatories (AROs), which are at a minimum equipped with vertically profiling wind radars, global positioning system (GPS) receivers, and surface meteorology sensors including temperature, relative humidity, precipitation, and pressure.

This study uses the Ralph et al. (2013) methodology to create a catalog of AR events based on AR conditions observed at the Bodega Bay (BBY) ARO in the Russian River watershed (38N, 123W) from 13 November 2004 through 31 April 2017. These start and end

dates encompass all months and days between them, and were chosen based on the start of available data (see Ralph et al. 2013), and the last full month of available data at the time that this study began. AR events were identified via three criteria: integrated water vapor (IWV) equal to or exceeding 2 cm, upslope IWV flux perpendicular (230°) to the local mountains equal to or exceeding 15 cm ($m\ s^{-1}$) and both variables continuously meeting or exceeding these conditions for a minimum of 8 hours. These criteria were determined to be optimal constraints on Northern California ARs through the evaluation of AR precipitation over almost ten winter seasons by Neiman et al. (2009) and Ralph et al. (2004, 2006). Based on results from Neiman et al. (2009) areas of orographic enhanced precipitation can be identified by determining the position of the controlling layer, which is defined as the layer of maximum correlation between the horizontal component of the upslope wind and the rainfall downwind in the mountains. In Northern California, the controlling layer is roughly 1-km above sea level, which makes physical sense given that the water vapor is primarily located in the lowest few kilometers along the coastal region. The upslope IWV flux can then be computed by combining the upslope winds of a vertically pointing wind profiler and the GPS-derived IWV to identify AR conditions at BBY (Ralph et al. 2006). In total, 228 AR events were identified year-round beginning in November 2004 and ending in April 2017.

Due to various factors, most importantly mechanical outages, periods of data are missing from this observational dataset. Ralph et al. (2018) maximized the amount of data available by compiling data from the ARO IWV flux table data output, raw observations from the profiler and GPS sensors, and the AR catalog in Ralph et al. (2013), in that order. However, that still left over 36,000 hours of missing data over the entire period of record, which results in an undercounting of overall AR events. In WY 2013 alone, 77% of October – March hourly data records are

missing. The ARO reported observations of five ARs during WY 2013, which is about one quarter of the average yearly AR count at this location. Using this observational dataset, the average number of AR events per year, excluding WY 2013, is 19.

Despite the periods of missing data, this observational dataset was chosen to identify AR events and AR families due to its unique hourly resolution for AR event onset and cessation. The accuracy in duration of AR events was important for correctly identifying AR families.

This study, like Ralph et al. (2013), uses AR conditions at a point to identify AR events. This is distinct from other AR identification algorithms that identify AR objects in reanalysis datasets. Ralph et al. (2018) assesses the difference between these types of algorithms at BBY and found that while the observational based AR catalog may underestimate the number of AR events it otherwise agrees well with reanalysis based AR catalogs. The updated AR catalog was compared against the Rutz et al. (2014) AR catalog which defines AR objects based on a continuous region ≥ 2000km in length and integrated water vapor transport ≥ 250kg m^{-1} s^{-1} to confirm identification of AR events through this methodology. Despite the large periods of missing data from the updated Ralph et al. (2013) AR catalog, there was general agreement in both catalogs to observe the same AR events (not shown).

b. Reanalysis Data

The Modern-Era Retrospective analysis for Research and Applications, Version 2 (MERRA-2) dataset (Gelaro et al. 2017) was used to create a daily climatology of several relevant atmospheric variables. The MERRA-2 dataset was used due to its high spatial resolution, 0.625°x0.5° (longitude-latitude), improved representation of extreme precipitation events and length of analysis period. MERRA-2 assimilates a high volume of meteorological

data, including space-based estimates of aerosols, GPS-radio occultation measurements, and ozone profile observations. MERRA-2 also assimilates observations from numerous satellites that observe atmospheric motion and surface wind vectors influential for U.S. West Coast phenomena, such as ARs.

The daily climatology was created using a 30-year (1987-2016), 21-day running mean technique (Hart and Grumm 2001) of the following relevant atmospheric variables: 500-hPa and 850-hPa geopotential heights, 850-hPa air temperature, 250-hPa wind speed and IWV. A climatology and composite analysis of integrated water vapor transport, often an important identifier of AR activity, was not shown for this study. This analysis would be important to address potential intensity differences between the climatological background, AR events and AR families, which are relatively small (on the order of 20 kg/m/s) at landfall in the composites. A detailed investigation of AR intensity is out of the scope of this paper. This climatology was used to create a background seasonal climatology for December – February (DJF) to calculate anomalous characteristics of AR events and AR families. While the AR events and families can occur during any time of the year, we focus the background climatology on DJF because it has the highest climatological frequency of AR occurrence (Gershunov et al., 2017, Lamjiri et al., 2017).

These reanalysis data were sampled to create mean and anomaly composites of different subsets of identified AR families (e.g., number of distinct ARs in a family; length of aggregation period). The composites are calculated throughout the duration of the AR family. Using these composites, the difference between the population means was calculated. The Welch's t-test determined whether the differences were statistically significant at the 99% confidence level.

The Welch's t-test is ideal for this application as it is designed for different sample sizes, and allows for the calculation of the degrees of freedom for individual grid boxes.

c. AR Families Algorithm

AR families are two or more distinct AR events that occur within a given aggregation period. During development of this algorithm, we explored how different aggregation periods change the distribution of AR families. Aggregation periods, calculated from the end time of the first AR, were binned using 12- and 24-hour time intervals, with the overall periods considered ranging from 12 hours to 216 hours. The shortest aggregation period used was determined by the distribution of time between all AR events within the AR catalog from 0-600 hours; the maximum number of AR events occur within 12 hours of one another (Fig. 2-1). The longest aggregation period was based on cyclone family literature which categorized the persistence of the atmosphere and cyclone clustering to occur between 6-9 days (144-216 hours) (Nakamura 1992, Nakamura and Sampre 2002, Pinto et al. 2014).

Identifying a suitable maximum aggregation period for AR families impacting Northern California is one fundamental contribution of this study. Mailier et al. (2006) discussed the idea of serial regularity, where there is a natural cause for regular patterns such that there is a minimum permissible distance and time between any two events. ECs in particular have associated spatial scales in which successive cyclone centers cannot be closer than the combined radii of the cyclones, leading to the expectation of a regular pattern especially during instances of high cyclone rates. In this study, maximum aggregation periods between 120-600 hours were evaluated. The leveling off in the increase in additional AR families after the 120-hour aggregation period led to the decision to evaluate the synoptic regimes of AR families at the 120-

hour aggregation period (Fig. 2-1). While the extended analysis out to 600 hours shows there are multiple scales at which AR families impact Northern California, with secondary increases in AR families from 144 – 240 hours and a third increase from 360 – 480 hours, this 120-hour threshold will allow a focus on AR families that occur within a subweekly period that could be associated with baroclinic waves or migratory eddies (Nakamura 1992, Nakamura and Sampre 2002).

Using the updated ARO catalog, the time between the end of the first AR event and the start of the second AR event was calculated. The count of AR events within an AR family continues until the time between the end of the first event and the start of subsequent AR events is greater than the longest aggregation period. AR families can become enhanced, with a higher count of AR events in the family, when the aggregation period increases (e.g., if there are 2 ARs in a 72-hour aggregation period, and another one or more is added when the aggregation period increases to the 120-hour aggregation period) (Fig. 2-2). Due to the 12-hour separation in aggregation periods and the minimum duration required for an AR, any AR family that has more than two AR events is considered an enhanced AR family. Each AR event is counted once per aggregation period for a distinct count of the total number of AR events in each AR family for the associated aggregation period. As the aggregation period lengthens, the chance of another AR event occurring increases. The increase in aggregation period length could therefore allow two AR events categorized as single ARs to constitute an AR family in a longer aggregation period. Consider two ARs, where the second AR starts 78 hours after the end of the first AR. In a 72-hour aggregation period, these would be considered two single AR events. However, in a 120-hour aggregation period, these two events would be an AR family. Therefore, lengthening the aggregation period can increase the number of AR families initiated.

A summary of terms used throughout the study are as follows:

- **AR Event** – AR conditions observed at the BBY ARO for at least 8 continuous hours.
- **AR Family** – two or more AR events occurring within one aggregation period.
- **Enhanced AR Family** – an AR family that is composed of subsets of at least one other AR family identified within shorter aggregation periods.
- **Aggregation Period** – the length of time, in hours, allowed between the end of the first AR event and the start of serial AR events. All AR events within the aggregation period are counted as one AR family.
- **Total Family Duration** – the number of hours from the start hour of the first AR event in the AR family to the end hour of the last AR event within the AR family.

We hypothesize that AR families can originate from multiple dynamic regimes. To stratify AR families into subsets, we completed subjective visual comparison of case studies, looking primarily at different aggregation period lengths and different numbers of AR events within families. The visual inspection of various case studies allowed us to identify patterns within subsets that when viewed as a whole contain large variability. Two distinct subsets of AR families arose and were then selected for further analysis to compare their synoptic environments and investigate our hypothesis. The first subset is composed of AR families consisting of two AR events separated by 12 hours or less, which could be associated with a mesoscale frontal wave. The second subset is composed of AR families consisting of 3+ AR events within the 120-hour aggregation period, which could be associated with a large parent cyclone with multiple short wave propagations. Thus the following terms are introduced (Fig. 2-2):

Dual AR Event AR Family – a two AR event family within the 12-hour aggregation period.

Multi-AR Event AR Family – a three or more AR event family within the 120-hour aggregation period.

During the period from November 2004 through April 2017, the BBY ARO catalog reports 228 AR events. The AR family algorithm shows that 109 of those events (47.8% of the total) occur within 120 hours of one another. In the next section, MERRA-2 reanalysis is used to investigate characteristics of AR families identified within the BBY ARO catalog, which will hereafter be referred to as the AR families catalog.

2.3 Characteristics of Atmospheric River Families

We used the AR families catalog to investigate and quantify general characteristics of AR families such as frequency, seasonality and interannual variability. In order to pick the most suitable maximum aggregation period for AR families in Northern California, the distribution of AR families across a range of aggregation periods was evaluated and this is described in section 2. This evaluation also included an assessment of the effect of maximum aggregation period on AR characteristics of interest. As mentioned in section 2, maximum aggregation periods of 120-216 hours were evaluated based on previous cyclone family literature. The 216-hour aggregation period results are presented in this section to assess the upper bound of the maximum aggregation period.

While the number of new AR families increases with aggregation period (Fig. 2-3a), the longer aggregation periods do not initiate as many new AR families. Instead, the longer aggregation periods generally lengthen pre-existing AR families and increase the number of AR events per AR family (enhanced AR families, Fig. 2-3b). Specifically, the number of new AR

families increases by >10 out to the 60-hour aggregation period, then increases more gradually out to 216 hours (Fig. 2-3a).

The number of AR families that have exactly two AR events is largest at the 72-hour aggregation period (Fig. 2-3b). The increase in the number of AR events per AR family as aggregation period lengthens is well depicted in the average number of AR events per AR family, which increases from 2.0 to 3.2, at the 12-hour and 216-hour aggregation period, respectively (Fig. 2-3b). Throughout all aggregation periods, the number of AR events per AR family ranges from 2-6 AR events. The distribution changes according to the aggregation period used with multi-AR event AR families occurring in the longer aggregation periods (Fig. 2-3b). For example, within the 216-hour aggregation period, there are 66 2-AR event families, 43 3-AR event families, 19 4-AR event families, 10 5-AR event families and one 6-AR event family (Fig. 2-3).

There is large variance in the total number of AR events and AR families between water years (Fig. 2-4b). WY 2017 contained the largest observed number of AR families, totaling 26 families using the 216-hour aggregation period. There were 34 AR events during WY 2017, and only 8 AR events were not considered part of an AR family. WY 2013 recorded one 5-AR event family, and no single AR events, but is misrepresented here due to the large periods of missing data previously mentioned in section 2. There is WY to WY variations between the total number of AR families; however, there is also variance within each WY dependent on the aggregation period (Fig. 2-4b). For some years, WY 2010 or 2012 for example, extending the aggregation period does not make a large difference. For these WYs, AR families occur far enough apart that extending the aggregation period does not increase the number of AR families. Comparatively, in WYs 2006 and 2015, the number of AR families greatly increases with aggregation period.

Seasonality also plays a role in the frequency of AR families. AR families, like AR events in general in this region, occur more frequently from December – February, with 70 families (50.36% of all AR families) occurring during these months for the 216-hour aggregation period (Fig. 2-4a). Two secondary maxima occur during March – May (MAM) and September – November (SON), with 29 and 34 AR families (20.86% and 24.46% of all AR families) respectively, observed (Fig. 2-4a).

After meeting the temporal criterion at the BBY ARO, AR families are assessed based on their composite spatial structure. AR families exhibit a zonal 250-hPa jet stream with two embedded jet streaks, one in the eastern and western Pacific, respectively (Fig. 2-5a). Zonally oriented geopotential heights at 500-hPa can also be found across the Pacific but curve cyclonically as they approach the US West Coast (Fig. 2-5a). The 850-hPa geopotential heights indicate a region of lower geopotential heights near the Alaska coastline but are otherwise zonal in nature (Fig. 2-5b). The IWV composite highlights the enhanced water vapor content extending from the tropics and impacting the US West Coast (Fig. 2-5b).

AR families are also assessed on their synoptic differences from the 30-year MERRA-2 DJF climatology described in section 2. On average, AR families show statistically significant (not shown) anomalous patterns from the DJF climatology (Fig. 2-6). Composites of all AR families, throughout the total family duration, have an anomalously low geopotential height center off the coast of British Columbia at 500-hPa and 850-hPa (Fig. 2-6a,c). These 109 AR families also have a cyclonically curved, enhanced jet at 250-hPa with the positive wind speed anomalies located above BBY, suggesting a zonal extension of the North Pacific jet stream (Fig. 2-6b). The location of the jet exit region with respect to BBY and enhancement for AR families is important for understanding the associated circulation pattern of rising (sinking) motion on the

cyclonic or cold (anticyclonic or warm) side of the jet (Naimas and Clapp 1949, Murray and Daniels 1953, Uccellini and Johnson 1979, Uccellini and Kocin 1987), helping to identify areas of storm development or suppression. The anomalous IWV observed in AR families is in a southwest to northeast orientation from 140W to inland California highlighting a common AR configuration, often termed the Pineapple Express (as described in Dettinger et al. 2011) (Fig. 2-6d). This result is consistent with findings from Payne and Magnusdottir (2016), who identified larger moisture content for persistent AR events compared to non-persistent ARs.

2.4 Synoptic Scale Patterns Associated with Atmospheric River Family Subsets

To investigate the hypothesis that AR families are associated with different synoptic regimes than single AR events a synoptic scale evaluation of AR families and single AR events was completed. The difference between average population subsets was computed to evaluate how the synoptic-scale conditions in AR families differ from single AR events and within subsets of AR families.

The composite of single AR events exhibits a zonal 250-hPa jet stream from Japan to 180W (Fig. 2-5c). Closer to the US West Coast, cyclonically curved wind speeds increase 4-8 m/s compared to the western Pacific (Fig. 2-5c). A discontinuous region of greater than 36 m/s wind speeds is co-located with a weaker 500-hPa geopotential height gradient between 180W and 150W (Fig. 2-5c). The composite of 850-hPa geopotential heights highlights the change in geopotential height gradient in the western Pacific compared to the eastern Pacific (Fig. 2-5d). The IWV composite of single AR events features enhanced water vapor poleward from Hawaii to California and between 150E and 180W (Fig. 2-5d).

a. AR Families Compared to Single AR Events

AR families (109 AR events) in comparison to single AR events (119 AR events) have a zonally extended area of lower geopotential heights across the North Pacific, seen in both the middle (500-hPa) and lower (850-hPa) atmosphere (Fig. 2-7a,c). The zonally elongated geopotential height differences could be a reflection of the occurrence of multiple successive ECs, favoring AR families, as opposed to single AR events. This result is also suggestive of the presence of a North Pacific wave guide associated with the development of successive ECs and accompanying ARs, which led to these successive AR events. AR families show significant higher subtropical geopotential heights with the leading edge of this region reaching up to 35 degrees north (Fig. 2-7a,c). The location and amplitude of this anticyclone can displace the landfalling location of AR events through the interaction of these opposite sign anomalies (Wallace et al. 1988). Analysis of the 250-hPa wind speed difference shows a significantly enhanced jet streak for AR families relative to single AR events (Fig. 2-7b). The jet streak, centered around 40N and 150W, is embedded within a stronger zonal jet stream that extends to the US West Coast compared to single AR events (Fig. 2-7b). A stronger and more zonally extensive jet stream across the North Pacific in the AR family composite suggests an enhanced waveguide for the propagation of successive baroclinic waves toward the U.S. West Coast, favoring the occurrence of AR families. The IWV difference between AR families and single AR events emphasizes regions where single AR events had higher moisture content (Fig. 2-7d). The difference between these two subsets shows significantly more moisture around Hawaii and in the North Pacific for single AR events, suggesting that single AR events have more meridional variability. AR families do exhibit significant positive IWV differences in the central/southern Central Valley in California. Although not directly relatable to inland IWV for the southern

Central Valley, the San Francisco Bay Area terrain gap is a well-defined corridor for vapor transport into the northern Central Valley (Lamjiri et al. 2018), alluding to the potential influence of terrain in this region as well. While not significant, differences are also seen in the northern Central Valley. The difference between AR families and single AR events show warmer tropical regions and cooler mid-latitude regions for AR families, suggesting enhanced baroclinicity favoring development and rapid eastward movement of ECs and ARs (Fig. 2-7e).

AR families, when compared to single AR events, indicate significant lower geopotential heights throughout the North Pacific, higher subtropical geopotential heights, a stronger zonally extended jet stream, higher IWV content close to the California coast and warmer tropical air temperature. Single AR events show significantly higher wind speeds, moisture content and air temperature along the Aleutian Islands, AK. These results lead to the prospective hypothesis that single AR events travel meridionally more than AR families, and that zonally travelling ARs may be more likely to be part of families through the zonally oriented baroclinic zone across the Pacific Ocean that previously has been shown to favor the repeated development of cyclones (Bjerknes and Solberg 1922).

b. Multi-AR Event AR Families versus Dual AR Event AR Families

From a hydrometeorological perspective, the longer lasting an AR event, the greater the potential for a high precipitation event, saturated soils and higher streamflow (Ralph et al. 2013, Lamjiri et al. 2017). Therefore, given the right pre-conditioning provided by the first event(s) in an AR family, there is a potential increased risk of hazardous impacts. To investigate whether longer lasting AR families are associated with different synoptic-scale circulations than shorter duration AR families, the 120-hour families were broken into two groups and analyzed as in

section 4a: Multi-AR Event AR families, greater than three AR events per AR family via the 120-hr aggregation period, and Dual AR Event AR families, two AR events per AR family via the 12-hr aggregation period (see section 2).

Composite analysis of Multi-AR Event AR families indicate a trans-Pacific zonally oriented, strong 250-hPa jet stream (Fig. 2-8a). Wind speeds are greater than 44 m/s across the entire Pacific Ocean (Fig. 2-8a). There is a wide, greater than 24 mm swath of IWV extending from the tropics to the US West Coast and a broad plume of IWV extending from 120E to 180W, up to 30N (Fig. 2-8b).

Dual AR Event AR families are associated with a ridge over the central North Pacific and a trough over the eastern North Pacific at 500-hPa (Fig. 2-8c). The 250-hPa wind speeds are strong, greater than 40 m/s, across the Pacific basin but are discontinuous in the fastest wind speeds, potentially due to a relatively weak geopotential gradient from the ridge (Fig. 2-8c). There could also be a smoothing effect here from the composite. IWV is above 20 mm, the minimum AR threshold, but not consistently greater than 24 mm between the tropics and subtropics (Fig. 2-8d). This composite also highlights 850-hPa geopotential heights below 1300 m off the coast of British Columbia, Canada, which are lower than the minimum geopotential heights for the Multi-AR Event AR families in the eastern Pacific (Fig. 2-8d).

Comparing these two subsets of AR families, the dominant feature of the geopotential height fields is the negative geopotential height differences for Multi-AR Event AR families over the central Pacific basin (Fig. 2-9a,c). At both 500-hPa and 850-hPa, the lower geopotential heights exhibit a large meridional extent for Multi-AR Event AR families compared to Dual AR Event AR families (Fig. 2-9a,c). At 850-hPa the negative geopotential height differences extends well into the tropics, below 20N (Fig. 2-9c). The negative geopotential height differences at 500-

hPa between the Multi-AR Event AR families and Dual AR Event AR families are consistent with positive differences in the 250-hPa wind speed extending across the North Pacific. Dual AR Event AR families have significantly higher 250-hPa wind speed around the Aleutian Islands, similar to what was discovered when comparing AR families and single AR events (Fig. 9b). Multi-AR Event AR families are associated with higher IWV values in tropical and subtropical moisture regions (south of 30N) while Dual AR Event AR families are associated with mid-latitude (30N-45N) higher IWV values (Fig. 2-9d). The multiple areas of positive IWV difference extending from the tropics into the subtropics, highlighted for Multi-AR Event AR families, overlaps with the negative geopotential height differences in the central Pacific (Fig. 2-9a,c,d). Evaluating the 850-hPa temperature differences between these two AR family subsets shows warmer temperatures for Dual AR Event AR families from 25-30N and extending from 160-140W (Fig. 2-9e). The AR families with more AR events instead have warmer temperatures around Hawaii and the Aleutian Islands. The co-occurrence of warmer temperatures and higher moisture content around Hawaii is suggestive of Pineapple Express type AR events (Fig. 2-7d,e).

Multi-AR Event AR families exhibit a region of lower geopotential heights extending farther into the central Pacific, a stronger jet stream from 25-40N, warmer tropical temperatures and higher moisture content in the subtropics and tropics than the Dual AR Event AR families. Compared to Multi-AR Event AR families, Dual AR Event AR families display a stronger jet north of 40N, a zonally extended region of higher moisture and warmer temperatures in the mid-latitudes. These conclusions could imply different processes acting to establish the regimes of Multi- versus Dual AR Event AR families, such as a large negative geopotential height region in the middle of the North Pacific basin embedded with multiple short-wave disturbances, which could produce independent ECs, or mesoscale frontal waves affecting landfalling AR events.

Documenting these robust signals in the average synoptic state for each subset may help to enhance situational awareness of these events. Future work may assess the potential increase in lead times for the predictability of the associated synoptic regimes leading to AR families. These synoptic regimes can also be applied to seasonal-to-subseasonal predictions to note their frequency in extended range forecast products and link their occurrence to precipitation anomalies on the US West Coast.

2.5 Water Year 2017 Case Study

WY 2017 was record breaking in many regards: there were 34 AR events to hit the Russian River watershed; the North Sierra Precipitation 8-Station Index, provided since 1922 by the California Department of Water Resources (cdec.water.gov), received record precipitation with a total of 94.7 inches (2405.38 mm); and Oroville Dam in Butte County, CA suffered significant damage to its main and emergency spillways prompting the evacuation of over 188,000 people (White et al. 2018). These conditions were preceded by AR events occurring in series, i.e., AR families, significantly impacting water resource management and the public.

As previously discussed, AR duration has been identified as the leading driver in precipitation totals (Lamjiri et al. 2017) and doubling AR duration produces six times the streamflow potential (Ralph et al. 2013). AR families last an average of 86 hours from the start of the first AR event to the end of the last AR event (total family duration), with AR conditions present, on average, during 40 of these hours. A 40-hour series of ARs is double the average duration of a single AR event (Ralph et al. 2013). AR families thus pose potentially higher risks from excessive precipitation, soil moisture and streamflow than single AR events, making WY 2017's numerous AR families even more impactful than other WYs. WY 2017 saw a total of 12

2-AR families, six 3-AR families, three 4-AR families, one 5-AR family and one 6-AR family determined via the 120-hour aggregation period (Table 2-1).

In order to investigate AR events as well as break periods throughout the family, we calculated the ratio of total AR hours to total family duration for all AR families (Fig. 2-10). If single AR events were included they would fall on the one-to-one line as their ratio of AR hours to total family duration is equal. Dual AR Event AR families are close to the one-to-one line with a range of total family durations (Fig. 2-10a). Multi-AR Event AR families have a higher ratio of AR hours to total family duration, which could be due to the higher number of AR events per AR family. Many WY 2017 AR families were long in duration with a higher ratio of AR hours to total family duration (Fig. 2-10b). Throughout the aggregation periods, the average number of AR hours is 40. However, as total family duration exceeds 100 hours the number of AR hours within the AR family increases to an average of 54.4 hours (Fig. 2-10).

The difference between the composite of the WY 2017 AR families from that of all AR families highlights the variation in synoptic conditions during WY 2017. The two significant and persistent high geopotential height regions at 500-hPa and 850-hPa outline the favored corridor for storm tracks into the Northern California area (Fig. 2-11a,c). An alternating pattern of high and low geopotential height regions as seen in Fig. 2-11 is suggestive of a potential Rossby wave train mechanism. The low geopotential height areas are elongated zones stretching from Hawaii to California instead of large circular areas seen in other composites. This is similar to results from previous studies evaluating Rossby wave propagation (Hsu and Lin 1992), however a full hemispheric analysis has not been completed in this study (Fig. 2-11a,c). The 250-hPa positive wind differences are positioned farther south, around Hawaii, approximately 25N, instead of 35-40N, as found in previous locations for this study, aligning with the lower geopotential height

region off the California coast (Fig. 2-11b). The wind speed is significantly stronger during WY 2017 AR families than in the composite of all AR families. A likely important contributor to the anomalous nature of this WY was the immense amount of water vapor available for transport. The location, positioned in the anomalously warm sector, and the amount, more than 8 mm higher than all AR families, of the moisture availability likely contributed to exceptionally wet conditions in Northern California (Fig. 2-11d). Air temperature at 850-hPa reflects the consistently warmer conditions in the tropics, south of 25N to west of 130W and south of 30N, extending to coastal Mexico, for WY 2017 AR families, which is even warmer and more widespread than all AR families (Fig. 2-11e). Collectively, the warm anomaly aligns with the anomalously high IWV and the negative geopotential height anomalies, all which extend from Hawaii to California (Fig. 2-11c,d,e). Many components, including the anomalously high IWV and negative geopotential height anomalies, helped contribute to the exceptional precipitation totals recorded in WY 2017.

One of the most impactful AR families during WY 2017 occurred over a 9-day period from February 2 – 10, 2017. The time evolution of the IVT field throughout this period clearly shows the multitude of AR events propagating across the Pacific (Fig. 2-12). Every day throughout this period, there is more than one AR associated with an independent EC or embedded mesoscale wave. This AR family led to the Oroville Dam crisis in Northern California after the Feather River Basin received as much as 690 mm of precipitation (White et al. 2018).

2.6 Conclusion and Discussion

This study has argued that AR families are a distinct class of long duration extreme events, that bring extended periods of AR conditions. As discussed by Lamjiri et al. (2017) and

Ralph et al. (2013), long duration AR events may contribute to the accumulation of large precipitation totals, elevate streamflow and therefore, can be difficult to predict and manage (Vano et al. 2018, White et al. 2018). AR families are important to understand as they may increase flood risk, threatening property and disrupting lives. An example of the consequences of this elevated risk is the damage sustained to emergency and main spillways at Oroville Dam in Northern California that was exacerbated after an AR family affected the region. This study provides a definition of "atmospheric river families," and evaluates relevant characteristics such as frequency of occurrence, seasonality, and intensity. The authors hope that by identifying and formally defining AR families, researchers, forecast meteorologists and water resource managers can use this concept to develop situational awareness of the potentially elevated impacts of these high impact extreme weather events.

This study concluded that 47.80% of all AR events are associated with AR families. AR families, like AR events, most often occur in DJF, but there is large interannual variability amongst water years. California is known to have a variable climate, with ARs often bringing the state out of drought conditions and/or causing excess precipitation and flooding (Dettinger, 2013). This study suggests that AR families might also play a large role in modulating which regime the state experiences. For example, WY 2017 experienced a record number of AR families, 26 total. The composite average of WY 2017 identified the presence of a persistent Rossby wave train-like pattern in the middle and lower atmosphere. One hypothesized driver for that record breaking WY was the unusually high amount of moisture available for transport extending from the tropics to the California coast.

AR families can be described by their average synoptic conditions. They exhibit an anomalous low central geopotential height region off the coast of British Columbia at 500-hPa

and 850-hPa, a zonal and enhanced 250-hPa jet stream with a positive wind speed anomaly above BBY and higher IWV off the coast of California extending towards Hawaii. Compared to single AR events, AR families are associated with lower geopotential heights across the North Pacific, higher geopotential heights over the subtropics, a stronger and more zonally elongated jet stream and warmer tropical air temperatures. Multi-AR event AR families, those with more than 3 AR events, exhibit a larger negative geopotential height anomaly throughout the Central Pacific. The positive 250-hPa wind speed anomaly, as in all AR families, is enhanced but for Multi-AR event AR families is located more centrally in the Pacific and is stronger than Dual AR event AR families. Distinctly, AR families have multiple plumes of enhanced IWV originating from the tropics across the Pacific Ocean.

Furthermore, this common synoptic regime shows that AR families may be predictable. Based on an assessment of this regime using MERRA-2 reanalysis data, it is hypothesized that AR families occur due to areas of negative geopotential height anomalies situated in the middle of the North Pacific basin often embedded with multiple short-wave disturbances, which produce independent ECs, or mesoscale frontal waves affecting landfalling AR events. The equatorward extent of the low geopotential height region brings the shortwaves and frontal structures closer to areas of tropical moisture to entrain higher values of IWV. This synoptic regime shows that on average AR families develop in highly zonal flows, which may support the development of multiple AR events.

Understanding AR families dynamically and further evaluating their predictability potential can help water resource managers and dam operators as they try to ensure a sustainable water supply and mitigate flood risk. Future studies on AR families will investigate the regional and interannual variability associated with these storms, further explore dynamical drivers of

these series of AR events and analyze the associated impacts including precipitation, soil moisture and streamflow. Investigating the identifiable synoptic patterns at different lead times, such as through the analysis of Rossby wave breaking or Rex blocking, could provide further insight into the predictability of AR families.

2.7 Acknowledgements

This research was supported by grant W912HZ-15-2-0019 from the US Army Corps of Engineers. We gratefully acknowledge the availability of the MERRA-2 reanalysis dataset available through the National Aeronautics and Space Administration (NASA) Global modeling and Assimilation Office. These data are available at MDISC, which is managed by the NASA Goddard Earth Sciences Data and Information Services Center. This work would also have not been possible without the Atmospheric River Observatory data provided by NOAA's Physical Sciences Division, Earth System Research Laboratory, from their website at http://www.esrl.noaa.gov/osd/. We would also like to acknowledge high-performance computing support from Cheyenne provided by NCAR's Computational and Information Systems Laboratory, sponsored by the National Science Foundation. The authors thank Drs. Art Miller, Jason Cordeira and Forest Cannon for thoughtful discussions and internal reviews of this manuscript. Thank you to the anonymous reviewers who provided valuable comments and discussion.

Chapter 2, in full, is a reprint of the material as it appears in the Journal of Hydrometeorology 2019. Fish, M. A., A. M. Wilson, F. M. Ralph (2019): "Atmospheric river families: Definition and associated synoptic conditions", *Journal of Hydrometeorology*, 20,

2091-2108, doi: 10.1175/JHM-D-18-0217.1. The dissertation author was the primary investigator and author of this paper.

Table 2-1. The number of AR events per AR family that made landfall in BBY during water year 2017 using the 120-hour aggregation period. Each row denotes an AR family and each column provides the start and end times of each AR event within the AR family.

	AR event (1) start: end (UTC)	AR event (2) start: end (UTC)	AR event (3) start: end (UTC)	AR event (4) start: end (UTC)	AR event (5) start: end (UTC)	AR event (6) start: end (UTC)
1.	1700 13 Oct 2016: 1800 14 Oct 2016	1000 15 Oct 2016: 0100 16 Oct 2016	1300 16 Oct 2016: 2000 16 Oct 2016			
2.	1000 15 Oct 2016: 0100 16 Oct 2016	1300 16 Oct 2016: 2000 16 Oct 2016				
3.	1200 24 Oct 2016: 0900 25 Oct 2016	1300 25 Oct 2016: 1300 26 Oct 2016	0600 27 Oct 2016: 0000 28 Oct 2016	0800 28 Oct 2016: 1500 28 Oct 2016	1800 28 Oct 2016: 1000 29 Oct 2016	2100 29 Oct 2016: 2000 30 Oct 2016
4.	1300 25 Oct 2016: 1300 26 Oct 2016	0600 27 Oct 2016: 0000 28 Oct 2016	0800 28 Oct 2016: 1500 28 Oct 2016	1800 28 Oct 2016: 1000 29 Oct 2016	2100 29 Oct 2016: 2000 30 Oct 2016	
5.	0600 27 Oct 2016: 0000 28 Oct 2016	0800 28 Oct 2016: 1500 28 Oct 2016	1800 28 Oct 2016: 1000 29 Oct 2016	2100 29 Oct 2016: 2000 30 Oct 2016		
6.	0800 28 Oct 2016: 1500 28 Oct 2016	1800 28 Oct 2016: 1000 29 Oct 2016	2100 29 Oct 2016: 2000 30 Oct 2016			
7.	1800 28 Oct 2016: 1000 29 Oct 2016	2100 29 Oct 2016: 2000 30 Oct 2016				
8.	1400 08 Dec 2016: 0000 09 Dec 2016	2100 09 Dec 2016: 0400 10 Dec 2016				
9.	2100 09 Dec 2016: 0400 10 Dec 2016	0100 14 Dec 2016: 0300 15 Dec 2016				
10.	0100 14 Dec 2016: 0300 15 Dec 2016	1700 15 Dec 2016: 0100 16 Dec 2016				
11.	1800 03 Jan 2017: 0900 04 Jan 2017	1500 07 Jan 2017: 0300 08 Jan 2017				
12.	0300 20 Jan 2017: 1200 20 Jan 2017	0100 22 Jan 2017: 1000 22 Jan 2017				
13.	0900 02 Feb 2017: 1900 02 Feb 2017	0100 03 Feb 2017: 1400 03 Feb 2017	1800 03 Feb 2017: 0900 04 Feb 2017	0000 06 Feb 2017: 0300 08 Feb 2017		
14.	0100 03 Feb 2017: 1400 03 Feb 2017	1800 03 Feb 2017: 0900 04 Feb 2017	0000 06 Feb 2017: 0300 08 Feb 2017	0500 08 Feb 2017: 1000 10 Feb 2017		
15.	1800 03 Feb 2017: 0900 04 Feb 2017	0000 06 Feb 2017: 0300 08 Feb 2017	0500 08 Feb 2017: 1000 10 Feb 2017			
16.	0000 06 Feb 2017: 0300 08 Feb 2017	0500 08 Feb 2017: 1000 10 Feb 2017				
17.	2000 15 Feb 2017: 1200 16 Feb 2017	1200 19 Feb 2017: 0300 20 Feb 2017	0600 20 Feb 2017: 0300 21 Feb 2017			
18.	1200 19 Feb 2017: 0300 20 Feb 2017	0600 20 Feb 2017: 0300 21 Feb 2017				
19.	0800 18 Mar 2017: 2000 18 Mar 2017	1400 20 Mar 2017: 0500 21 Mar 2017	0300 22 Mar 2017: 1000 22 Mar 2017			
20.	1400 20 Mar 2017: 0500 21 Mar 2017	0300 22 Mar 2017: 1000 22 Mar 2017	0500 24 Mar 2017: 1900 24 Mar 2017			
21.	0300 22 Mar 2017: 1000 22 Mar 2017	0500 24 Mar 2017: 1900 24 Mar 2017				
22.	1300 12 Apr 2017: 0400 13 Apr 2017	1500 16 Apr 2017: 0000 17 Apr 2017				
23.	1500 16 Apr 2017: 0000 17 Apr 2017	0100 18 Apr 2017: 0800 18 Apr 2017				

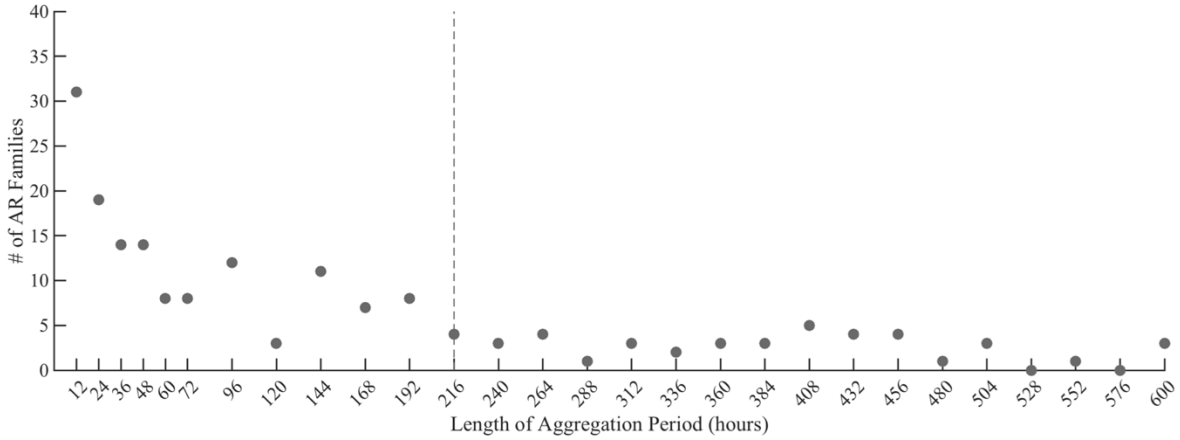

Figure 2-1. The number of AR families initiated as a function of aggregation period ranging from 12 to 600 hours. The vertical dashed line indicates the maximum aggregation period evaluated in this study.

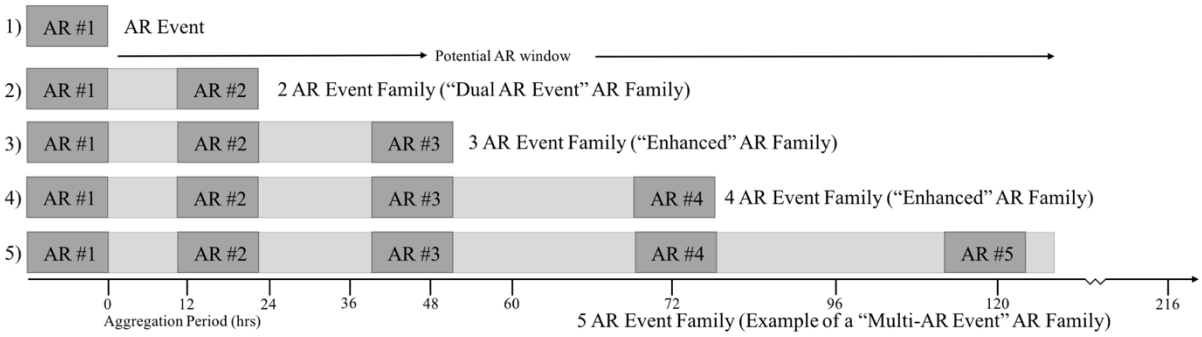

Figure 2-2. Schematic of the AR families algorithm. The dark gray boxes marked AR #n indicate an arbitrary length AR event. The potential window for a successive AR event to occur starts after the end of the first AR event. From the end of each AR event within the catalog, additional AR events are counted if they fall within the aggregation period duration (row 2). An AR event becomes an AR family if two or more AR events occur within the aggregation period. Families can become 'enhanced' if a longer aggregation period adds additional AR events to the existing family (row 3,4). Row 2 show the classification of a Dual AR Event AR family. Row 5 depicts an example of a Multi-AR Event AR family.

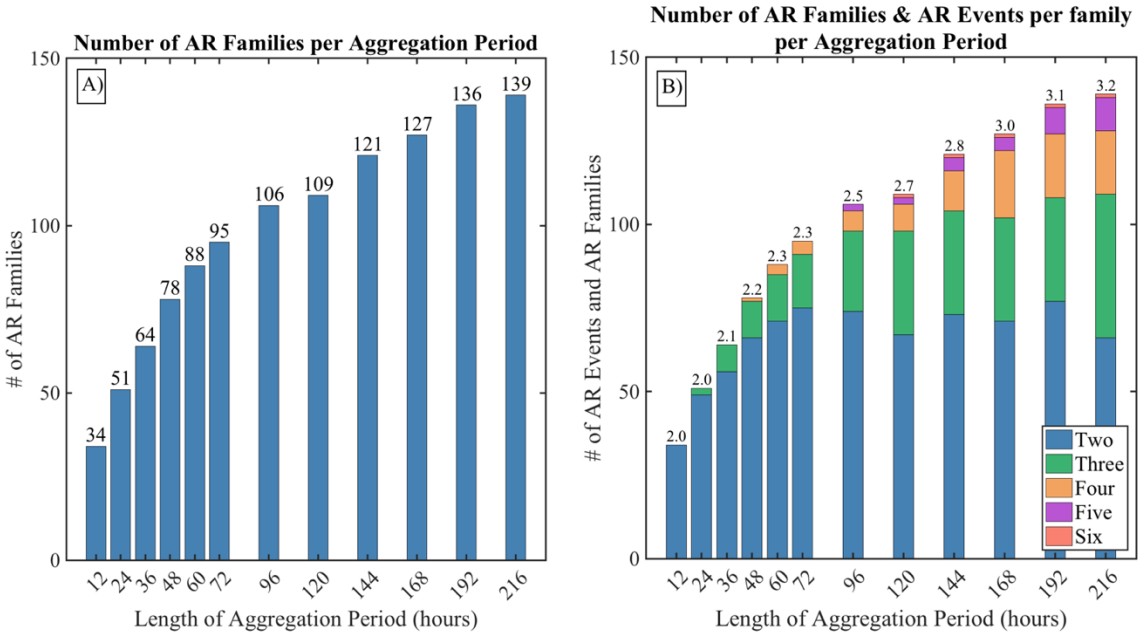

Figure 2-3. A) Total number of AR families within a range of aggregation periods. B) The total number of AR families per aggregation period, color coded by the number of AR events per aggregation period. The average number of AR events per family is depicted above each column for the associated aggregation period.

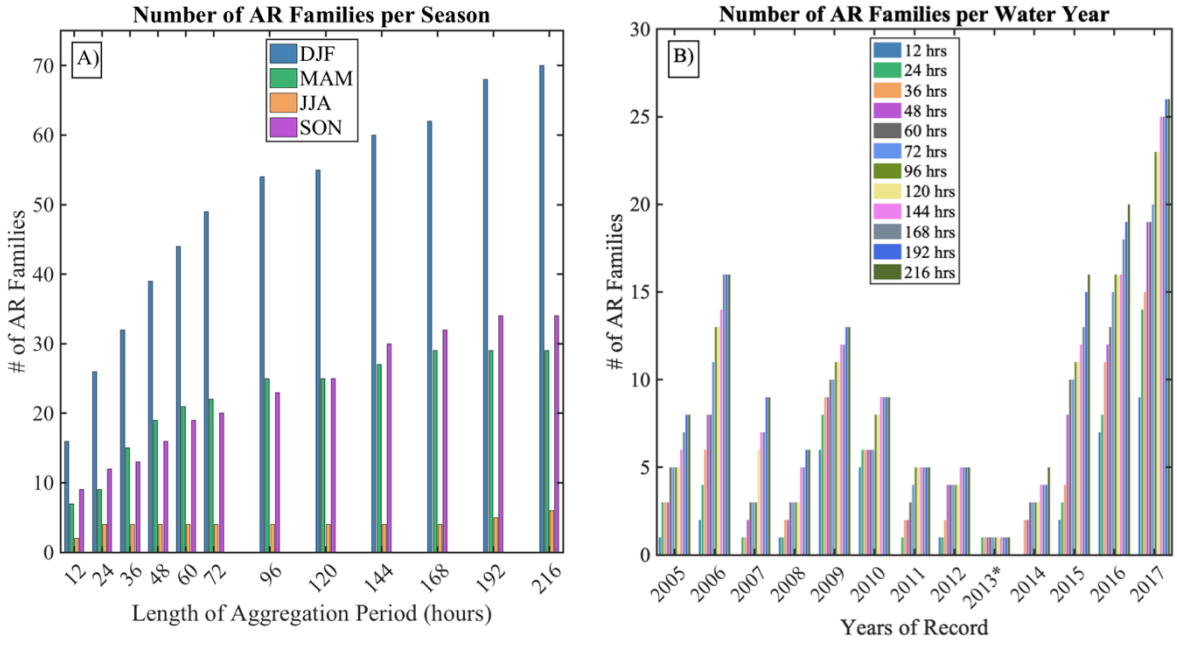

Figure 2-4. A) The number of AR families occurring for the different aggregation periods, stratified by season. B) The number of AR families occurring during water years 2005-2017 stratified by aggregation period. Starred WY depicts large portion of missing data.

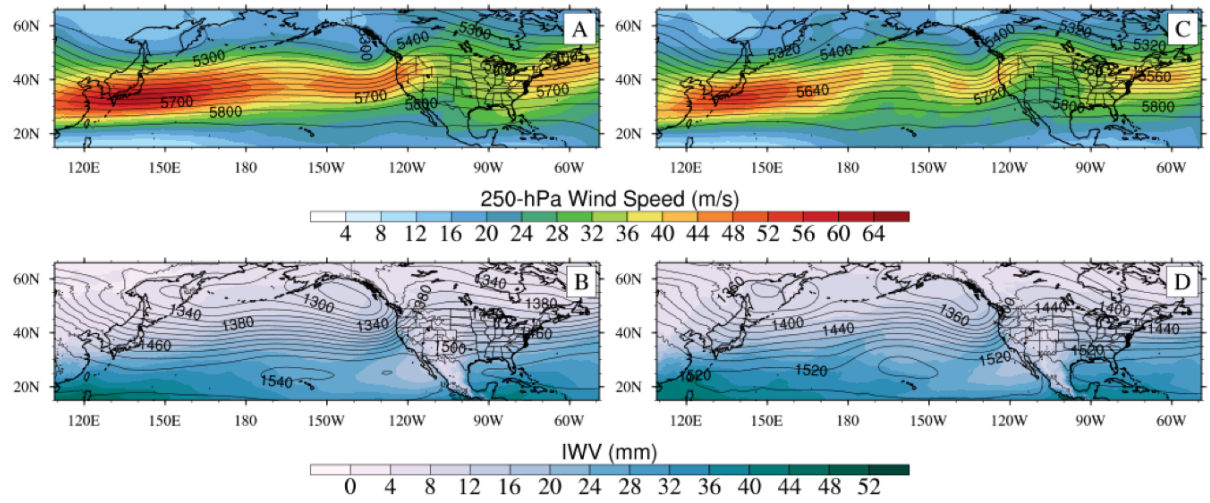

Figure 2-5. Mean composite fields of all 120-hour AR families (left, n = 944 time steps) and single AR events (right, n = 393 time steps) at BBY. Average 250-hPa wind speed (m/s) and 500-hPa geopotential heights (m), shaded and contoured, respectively for A) and C). Average IWV (mm) and 850-hPa geopotential heights (m), shaded and contoured, respectively for B) and D).

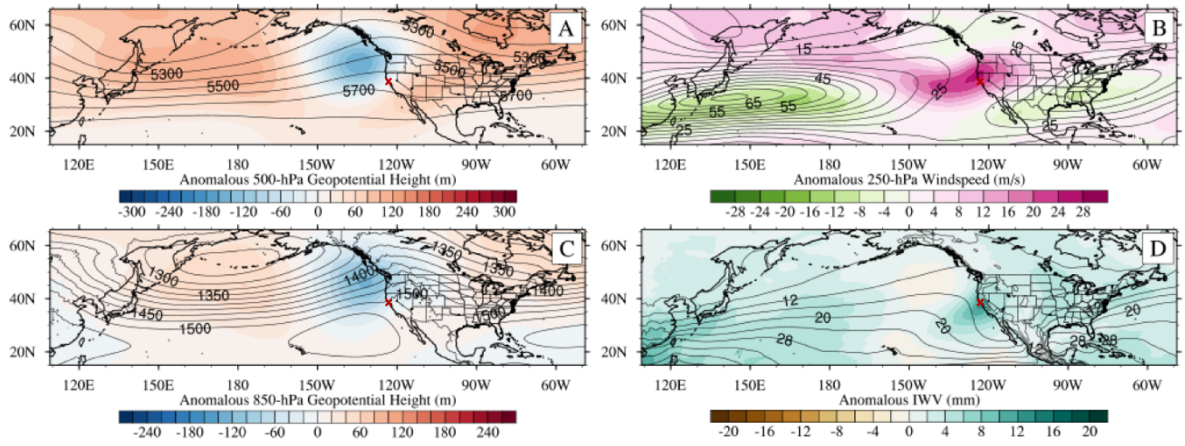

Figure 2-6. Composites of all 120-hour AR families at BBY, with anomalies shaded and DJF climatology in contour lines, of the following variables: A) 500-hPa geopotential heights (m), B) 250-hPa wind speed (m/s), C) 850-hPa geopotential heights (m), D) IWV (mm).

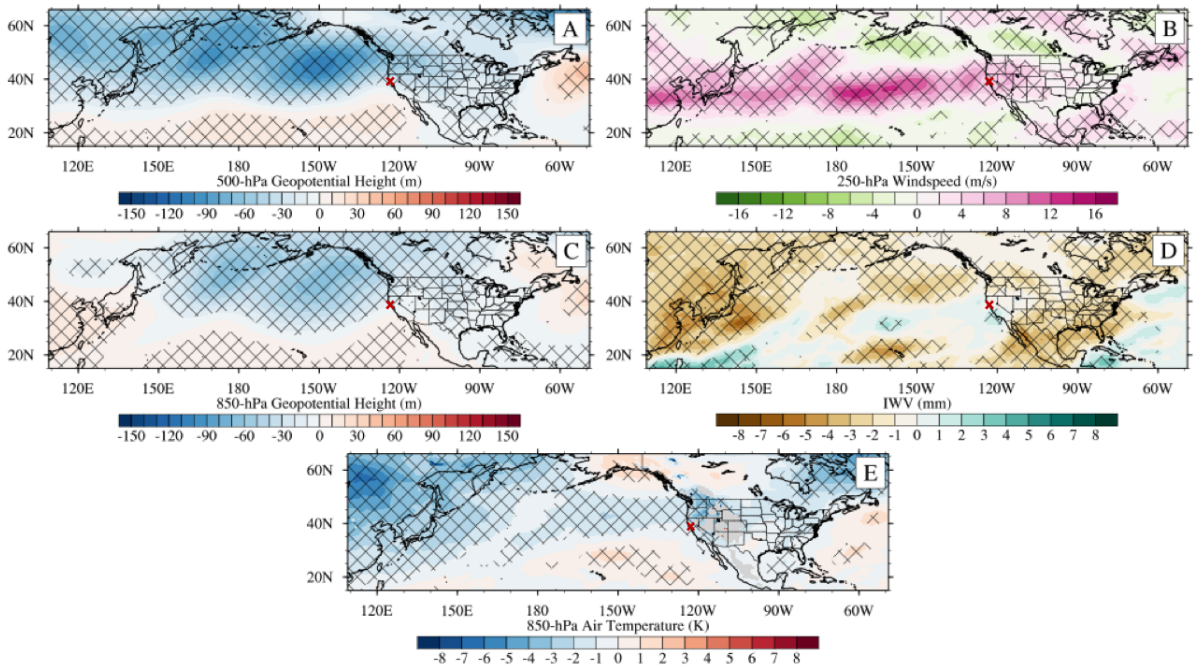

Figure 2-7. Composites of the difference between 120-hour AR families and all single AR events at BBY. Significance at 99% confidence marked by hatching. A) 500-hPa geopotential heights (m), B) 250-hPa wind speed (m/s), C) 850-hPa geopotential heights (m), D) IWV (mm), E) 850-hPa temperature (K).

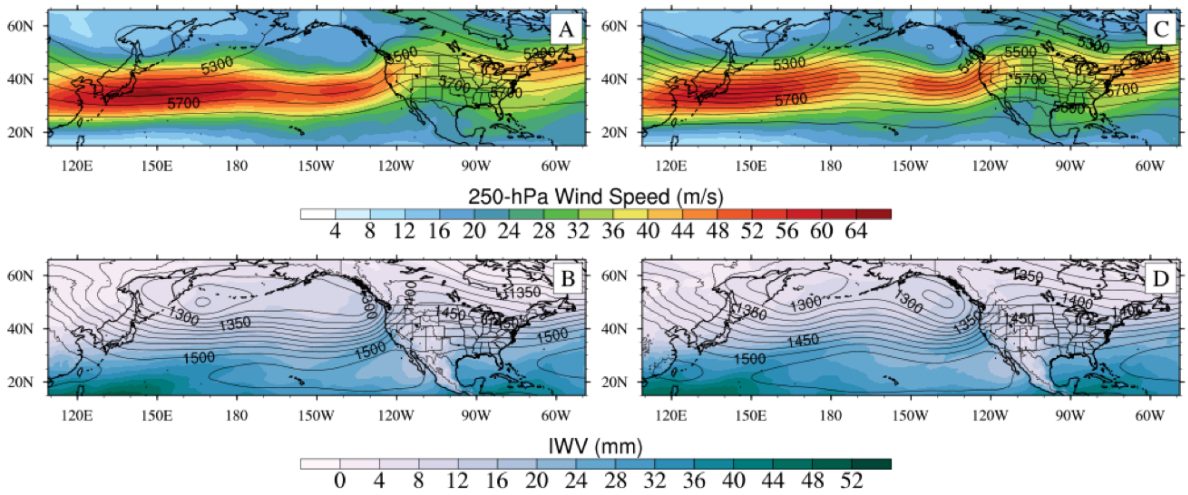

Figure 2-8. Mean composite fields of all Multi-AR Event AR families (left, n = 240 time steps) and Dual AR Event AR families (right, n = 367 time steps) at BBY. Average 250-hPa wind speed (m/s) and 500-hPa geopotential heights (m), shaded and contoured, respectively for A) and C). Average IWV (mm) and 850-hPa geopotential heights (m), shaded and contoured, respectively for B) and D).

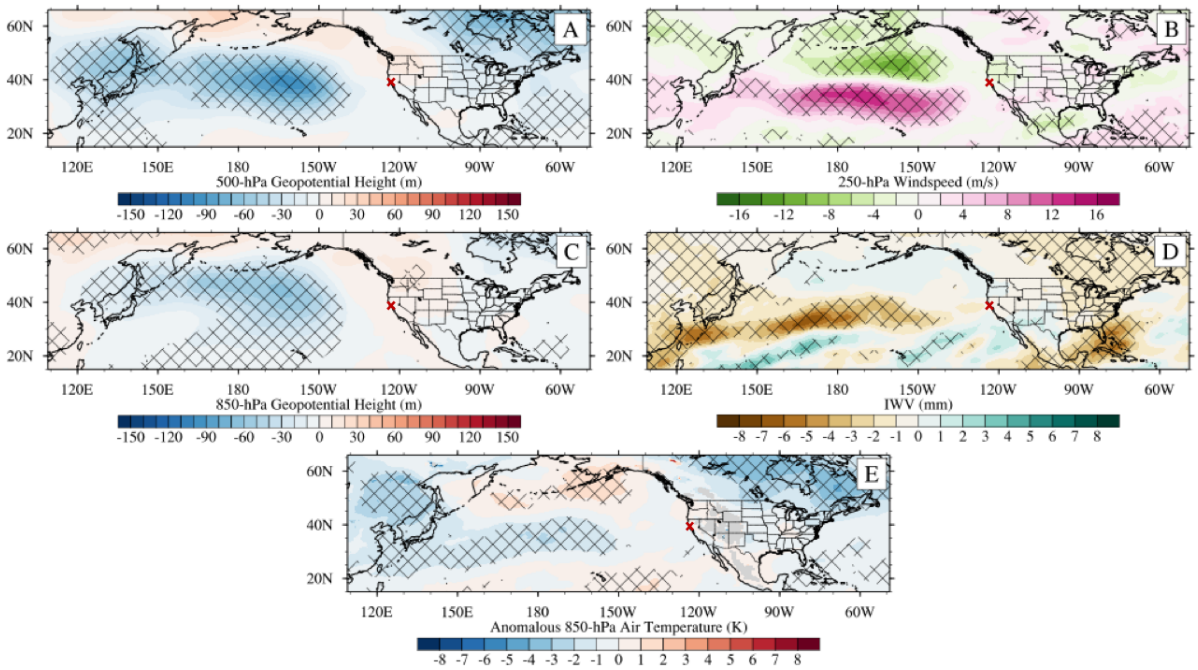

Figure 2-9. Composites of the difference between Multi-AR Event AR Families, 120-hour AR families with 3+ AR events, and Dual AR event AR Families, 12-hour AR families with 2 AR events. Significance at 99% confidence marked by hatching. A) 500-hPa geopotential heights (m), B) 250-hPa wind speed (m/s), C) 850-hPa geopotential heights (m), D) IWV (mm), E) 850-hPa temperature (K).

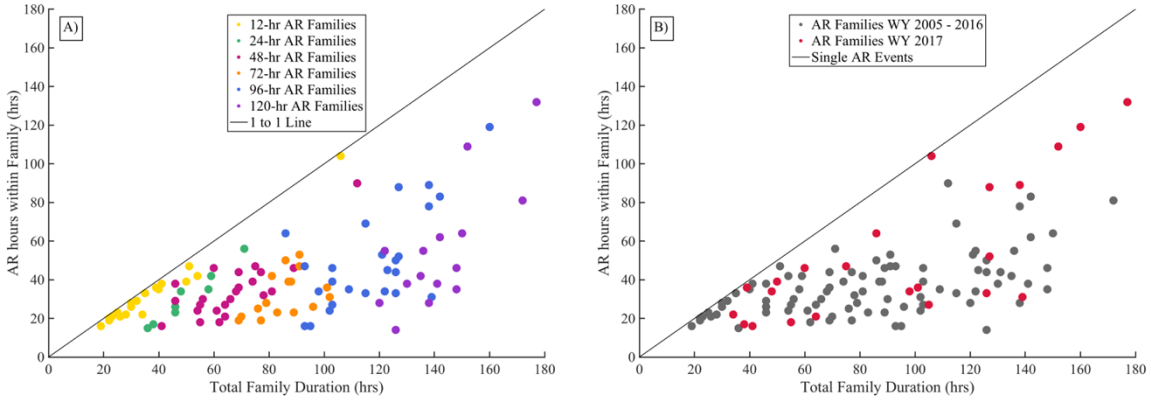

Figure 2-10. For each aggregation period, the total family duration, the duration from the start of the first AR event to the last AR event, is compared to the number of AR hours within the AR family for a ratio of AR hours to total family duration. The one-to-one line shows the maximum number of AR hours and indicate where single AR events would fall in this diagram. A) All AR families divided into six aggregation periods. B) Highlighting all WY 2017 AR families (red) compared to AR families during WY 2005-2016 (gray).

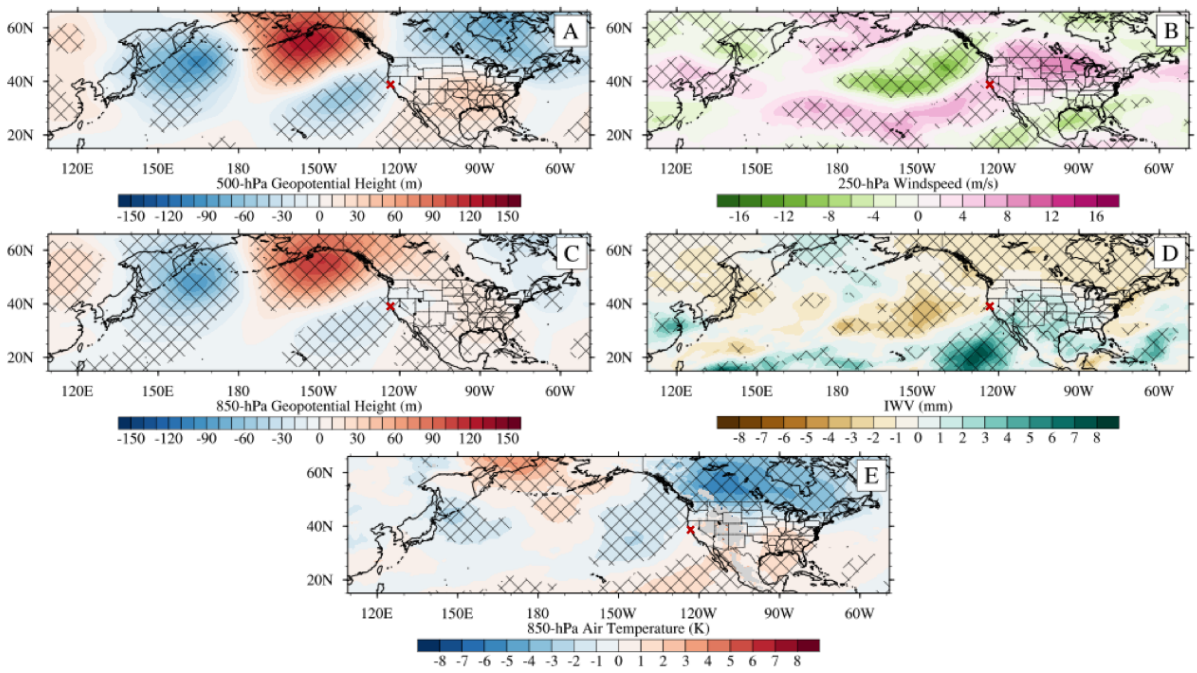

Figure 2-11. Composites of the difference between WY 2017 AR families (n = 208 time steps) and AR families. Significance at 99% confidence marked by hatching. A) 500-hPa geopotential heights (m), B) 250-hPa wind speed (m/s), C) 850-hPa geopotential heights (m), D) IWV (mm), E) 850-hPa temperature (K).

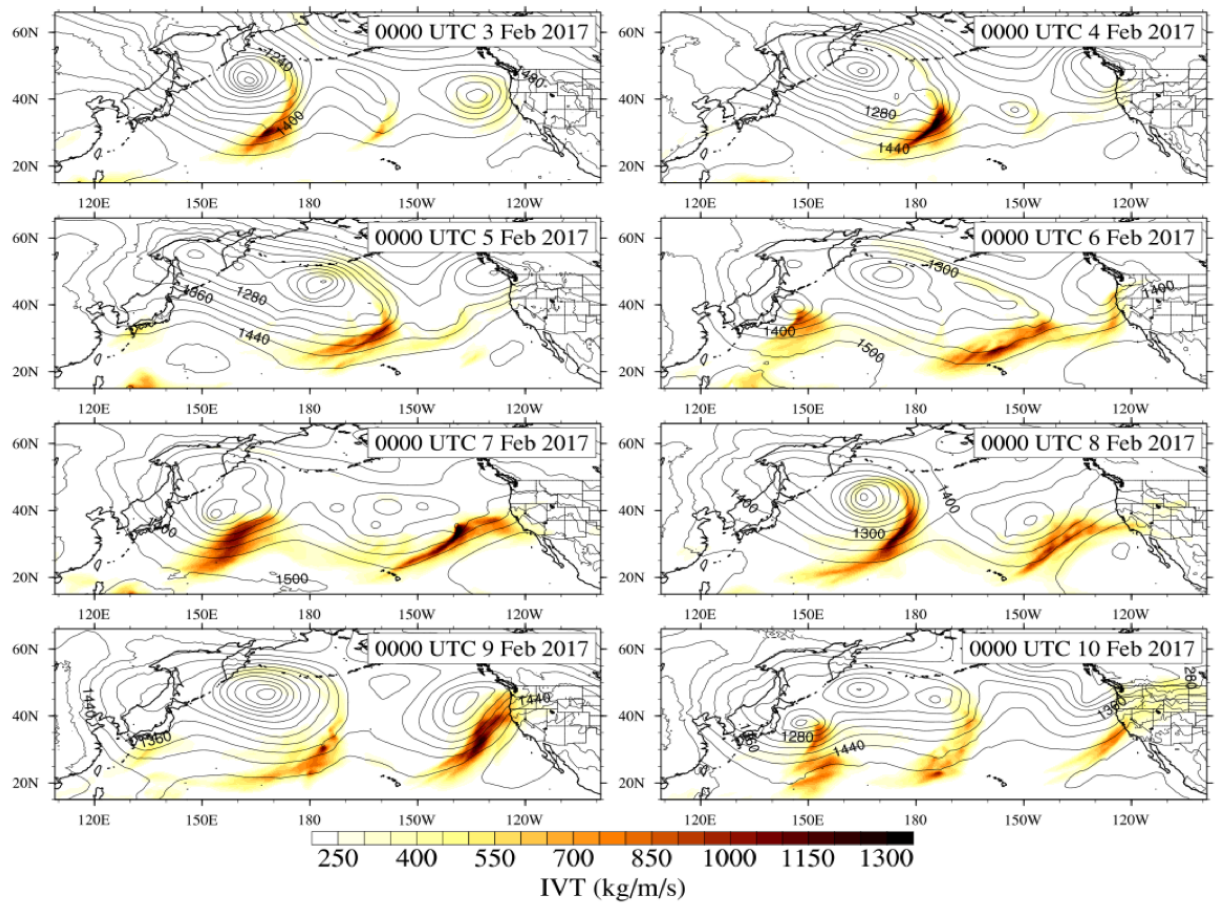

Figure 2-12. Time evolution of notable AR events in February 2017 showing the integrated water vapor transport, IVT (kg/m/s, colored contour) and 850-hPa geopotential heights (m, contour). Figures are every 24 hours starting on 03 February 2017 at 0000 UTC to 10 February 2017 0000 UTC from left to right, top to bottom.

2.8 References

Bjerknes, J., and H. Solberg, 1922: Life cycle of cyclones and the polar front theory of atmospheric circulation. *Geophys. Publ.,* **3**, 1-18.

Chang, E. K. M., and I. Orlanski, 1993: On the dynamics of a storm track. *J. Atmos. Sci.*, **50**, 999-1015.

Chang, E. K. M., and I. Orlanski, 1994: On energy flux and group velocity of waves in baroclinic flows. *J. Atmos. Sci.*, **51**, 3823-3828.

Dettinger, M. D., 2013: Atmospheric Rivers as Drought Busters on the U.S. West Coast. *J. Hydrometeor.*, **14**, 1721-1732, doi:10.1175/JHM-D-13-02.1.

Dettinger, M. D., F. M. Ralph, T. Das, P. J. Neiman, and D. R. Cayan, 2011: Atmospheric Rivers, Floods and the Water Resources of California. *Water*, **3(2)**, 445-478, doi:10.3390/w3020445.

Doswell, C. A., H. E. Brooks, and R. A. Maddox, 1996: Flash flood forecasting: An ingredients-based methodology. *Wea. Forecasting*, **11**, 560–581, doi:https://doi.org/10.1175/1520-0434(1996)011<0560:FFFAIB>2.0.CO;2.

Eliassen, A., 1966: Motions on intermediate scales: Fronts and cyclones. *Advances in Earth Science*, E.D. Hurley, Ed., MIT Press, 111-138.

Gelaro, R., W. McCarty, M. J. Suarez, R. Todling, A. Molod, L. Takacs, C. A. Randles, A. Darmenov, M. G. Bosilovich, R. Reichle, K. Wargan, L. Coy, R. Cullather, C. Draper, S. Akella, V. Buchard, A. Conaty, A. M. da Silva, W. Gu, G.-K. Kim, R. Koster, R. Lucchesi, D. Merkova, J. E. Nielsen, G. Partyka, S. Pawson, W. Putman, M. Reinecker, S. D. Schubert, M. Sienkiewicz and B. Zhao, 2017: The Modern-Era Retrospective Analysis for Research and Applications, Version 2 (MERRA-2). *J. Climate*, **30**, 5419-5454, doi:10.1175/JCLI-D-16-0758.1.

Gershunov, A., T. Shulgina, F. M. Ralph, D. A. Lavers, and J. J. Rutz (2017), Assessing the climate-scale variability of atmospheric rivers affecting western North America, *Geophys. Res. Lett.*, 44, doi:10.1002/2017GL074175.

Griffin, K. S., and J. E. Martin, 2017: Synoptic features associated with temporally coherent modes of variability of the North Pacific jet stream. *J. Climate,* **30**, 39-54, doi:10.1174/JCLI-D-15-0833.1.

Guan, B., N. P. Molotch, D. E. Waliser, E. J. Fetzer and P. J. Neiman, 2010: Extreme snowfall events linked to atmospheric rivers and surface air temperature via satellite measurements. *Geophys. Res. Lett.*, **37**, L20401, doi:10.1029/2010GL044696.

Guan, B., and D. E. Waliser, 2015: Detection of atmospheric rivers: Evaluation and application of an algorithm for global studies. *Geophys. Res. Lett.*, **120**, 12514-12535, doi:10.1002/2015JD024257.

Guan, B., and D. E. Waliser, 2017: Atmospheric rivers in 20 year weather and climate simulations: A multimodel, global evaluation. *J. Geophys. Res.*, **122**, 5556-5581, doi:10.1002/2016JD026174.

Hart, R. and R. Grumm, 2001: Using normalized climatological anomalies to rank synoptic-scale events objectively. *Mon. Wea. Rev.,* **129**, 2426-2442, doi: 10.1175/1520-0493(2001)129<2426:UNCATR>2.0.CO;2.

Hecht, C. W., and J. M. Corderia, 2017: Characterizing the influence of atmospheric river orientation and intensity on precipitation distributions over North Coastal California. *Geophys. Res. Lett.*, **44**, doi:10.1002/2017GL74179.

Hsu, H. and S. Lin, 1992: Global teleconnections in the 250-mb streamfunction field during northern hemisphere winter. *Mon. Wea. Rev.*, **120**, 1169-1190, doi: 10.1175/1520-0493(1992)120<1169:GTITMS>2.0.CO;2.

Hu, H., F. Dominguez, Z. Wang, D. A. Lavers, G. Zhang, and F. M. Ralph, 2017: Linking atmospheric river hydrological impacts on the U.S. West Coast to Rossby wave breaking. *J. Climate,* **30**, 3381-3399, doi: 10.1175/JCLI-D-16-0386.1.

Lamjiri, M. A., M. D. Dettinger, F. M. Ralph and B. Guan, 2017: Hourly storm characteristics along the U.S. West Coast: Role of atmospheric rivers in extreme precipitation. *Geophys. Res. Lett.*, **44**, 7020-7028, doi:10.1002/2017GL074193.

Lamjiri, M.A., M. D. Dettinger, F. M. Ralph, N. S. Oakley, and J. J. Rutz, 2018: Hourly analyses of the large storms and atmospheric rivers that provide most of California's precipitation in only 10 to 100 hours per year. *San Francisco Estuary and Watershed Science.*, **16(4)**, doi: 10.15447/sfews.2018v16iss4art1.

Lavers, D. A., and G. Villarini, 2013: Atmospheric rivers and flooding over the central United States. *J. Climate*, **26**, 7829-7836, doi:10.1175/JCLI-D-13-00212.1.

Lavers, D. A., D. E. Waliser, F. M. Ralph, M. D. Dettinger, 2016: Predictabiliy of horizontal water vapor transport relative to precipitation: Enhancing situational awareness for forecasting western U.S. extreme precipitation and flooding. *Geophys. Res. Lett.*, **43**, 2275-2282, doi: 10.1002/2016GL067765.

Mahoney, K., D. L. Jackson, P. Neiman, M. Hughes, L. Darby, G. Wick, A. White, E. Sukovich, and R. Cifelli, 2016: Understanding the role of atmospheric rivers in heavy precipitation in the southeast United States. *Mon. Wea. Rev.,* **144**, 1617-1632, doi: 10.1175/MWR-D-15-0279.1.

Mailier, P. J., D. B. Stephenson, C. A. T. Ferro, and K. I. Hodges, 2006: Serial Clustering of extratropical cyclones. *Mon. Wea. Rev.,* **134**, 2224-2240, doi:10.1175/MWR3160.1.

Moore, B. J., P. J. Neiman, F. M. Ralph, and F. E. Barthold, 2012: Physical processes associated with heavy flooding rainfall in Nashville, Tennessee, and Vicinity during 1-2 May 2010: The role of an atmospheric river and mesoscale convective systems. *Mon. Wea. Rev.,* **140**, 358-378, doi:10.1175/MWR-D-11-00126.1.

Mundhenk, B. D., E. A. Banks, and E. D. Maloney, 2016: All-season climatology and variability of atmospheric river frequencies over the North Pacific. *J. Climate,* **29**, 4885-4903, doi: 10.1175/JCLI-D-15-0655.1.

Murray, R., and S. M. Daniels, 1953: Transverse flow at entrance and exit to jet streams. *Q. J. R. Meteorol. Soc.,* **79**, 236-241, doi: 10.1002/qj.49707934005.

Naimas, J., and P. F. Clapp, 1949: Confluence theory of the high tropospheric jet stream. *J. Meteorol.,* **6**, 330-336, doi: 10.1175/1520-0469(1949)006<0330:CTOTHT>2.0.CO;2.

Nakamura, H., 1992: Midwinter suppression of baroclinic wave activity in the Pacific. *J. Atmos. Sci.,* **49**, 1629-1642, doi: 10.1175/1520-0469(1992)049<1629:MSOBWA>2.0.CO;2.

Nakamura, H., and T. Sampre, 2002: Trapping of synoptic-scale disturbances into the North-Pacific subtropical jet core in midwinter. *Geophys. Res. Lett.,* **29**, 8-1-8-4, doi: 10.1029/2002GL015535.

Nardi, K. M., E. A. Barnes, and F. M. Ralph, 2018: Assessment of numerical weather prediction model re-forecasts of the occurrence, intensity and location of atmospheric rivers along the West Coast of North America. *Mon. Wea. Rev.,* **146**, 3343-3362, doi: 10.1175/MWR-D-18-0060.1.

Neiman, P. J., P. O. G. Persson, F. M. Ralph, D. P. Jorgensen, A. B. White, and D. E. Kingsmill, 2004: Modification of fronts and precipitation by coastal blocking during an intense landfalling winter storm in Southern California: Observations during CALJET. *Mon. Wea. Rev.,* **132**, 242-273, doi: 10.1175/MWR-D-18-0060.1.

Neiman, P. J., F. M. Ralph, G. A. Wick, Y. H. Kuo, T. K. Wee, Z. Ma, G. H. Taylor, and M. D. Dettinger, 2008: Diagnosis of an Intense Atmospheric River Impacting the Pacific Northwest: Storm Summary and Offshore Vertical Structure Observed with COSMIC Satellite Retrievals. *Mon. Wea. Rev.*, **136**, 4398-4420, doi:10.1175/2008MWR2550.1.

Neiman, P. J., A. B White, F. M. Ralph, D. J. Gottas, and S. I. Gutman, 2009: A water vapor flux tool for precipitation forecasting. *Pro. Inst. Civ. Eng. Water Manage.*, **WM2**, 83-94, doi:10.1680/wama.2009.162.2.83.

Neiman, P. J., L. J. Schick, F. M. Ralph, M. Hughes, and G. A. Wick, 2011: Flooding in Western Washington: The Connection to Atmospheric Rivers. *J. Hydrometeor.*, **12**, 1337-1358, doi:10.1175/2011JHM1358.1.

Payne, A. E., and G. Magnusdottir, 2016: Persistent landfalling atmospheric rivers over the west coast of North America. *J. Geophys. Res.*, **121**, 13287-13300, doi: 10.1002/2016JD025549.

Pinto, J. G., I. Gomara, G. Masato, H. F. Dacre, T. Woollings, and R. Caballero, 2014: Large-scale dynamics associated with clustering of extratropical cyclones affecting Western Europe. *J. Geophys. Res. Atmos.,* **119**, 13704-13719, doi: 10.1002/2014JD022305.

Ralph, F. M., P. J. Neiman, and G. A. Wick, 2004: Satellite and CALJET Aircraft Observations of Atmospheric Rivers over the Eastern North Pacific during the Winter of 1997/1998. *Mon. Wea. Rev.*, **132**, 1721-1745, doi:10.1175/1520-0493(2004)132<1721:SACAOO>2.0.CO;2.

Ralph, F. M., P. J. Neiman, and R. Rotunno, 2005: Dropsonde observations in low-level jets over the northeastern Pacific Ocean from CALJET-1998 and PACJET-2001: Mean vertical-profile and atmospheric-river characteristics. *Mon. Wea. Rev.,* **133**, 889–910

Ralph, F. M., P. J. Neiman, G. A. Wick, S. I. Gutman, M. D. Dettinger, D. R. Cayan, and A. B. White, 2006: Flooding on California's Russian River: Role of atmospheric rivers. *Geophys. Res. Lett.*, **33**, L13801, doi:10.1029/2006GL026689.

Ralph, F. M., P. J. Neiman, G. N. Kiladis, K. Weickmann and D. W. Reynolds, 2011: A Multiscale Observational Case Study of a Pacific Atmospheric River Exhibiting Tropical-Extratropical Connections and a Mesoscale Frontal Wave. *Mon. Wea. Rev.*, **139**, 1169-1189, doi:10.1175/2010MWR3596.1.

Ralph, F. M., T. Coleman, P. J. Neiman, R. J. Zamora, and M. D. Dettinger, 2013: Observed Impacts of Duration and Seasonality of Atmospheric-River Landfalls on Soil Moisture and Runoff in Coastal Northern California. *J. Hydrometeor.*, **14**, 443-459, doi:10.1175/JHM-D-12-076.1.

Ralph, F. M., S. F. Iarcobellis, P. J. Neiman, J. M. Cordeira, J. R. Spackman, D. E. Waliser, G. A. Wick, A. B. White, and C. Fairall, 2017: Dropsonde Observations of Total Integrated Water Vapor Transport within North Pacific Atmospheric Rivers. *J. Hydrometeor.*, **18**, 2577-2596, doi:10.1175/JHM-D-17-0036.1.

Ralph, F. M., A. M. Wilson, T. Shulgina, B. Kawzenuk, S. Sellers, J. J. Rutz, M. A. Lamjiri, E. A. Barnes, A. Gershunov, B. Guan, K. M. Nardi, T. Osborne and G. A. Wick, 2018: ARTMIP-early start comparison of atmospheric river detection tools: how many atmospheric rivers hit northern California's Russian River watershed? *Cli. Dyn.,* doi: 10.1007/s00382-018-4427-5.

Ralph, F. M., M. D. Dettinger, M. M. Cairns, T. J. Galarneau, and J. Eylander, 2018: Defining "Atmospheric River": How the *Glossary of Meteorology* Helped Resolve a Debate. *Bull. Amer. Meteor. Soc.*, doi: 10.1175/BAMS-D-17-0517.1.

Ralph, F. M., J. J. Rutz, J. M. Cordeira, M. Dettinger, M. Anderson, D. Reynolds, L. J. Schick, and C. Smallcomb, 2019: A Scale to Characterize the strength and impacts of atmospheric rivers. *Bull. Amer. Meteor. Soc.*, doi: 10.1175/BAMS-D-18-0023.1.

Ramos, A. M., R. Nieto, R. Tome, L. Gimeno, R. M. Trigo, M. L. R. Liberto, and D. A. Lavers, 2016: Atmospheric rivers moisture sources from a Lagrangian perspective. *Earth Syst. Dynami.*, **7**, 371-384, doi:10.5194/esd-7-371-2016.

Rutz, J. J., W. J. Steenburgh, and F. M. Ralph, 2013: Climatological Characteristics of Atmospheric Rivers and Their Inland Penetration over the Western United States. *Mon. Wea. Rev.*, **142**, 905-921, doi:10.1175/MWR-D-13-00168.1.

Sodemann, H., and A. Stohl, 2013: Moisture origin and meridional transport in atmospheric rivers and their association with multiple cyclones. *Mon. Wea. Rev.,* **141**, 2850-1868, doi: 10.1175/MWR-D-12-00256.1.

Uccellini, L. W., and D. R. Johnson, 1979: The coupling of upper and lower tropospheric jet streaks and implications for the development of severe convective storms. *Mon. Wea. Rev.,* **107**, doi: 10.1175/1520-0493(1979)107<0682:TCOUAL>2.0.CO;2.

Uccellini, L. W., and P. J. Kocin, 1987: The interaction of jet streak circulations during heavy snow events along the East Coast of the United States. *Wea. Forecasting,* **2**, 289-308, doi: 10.1175/1520-0434(1987)002<0289:TIOJSC>2.0.CO;2.

Vano, J. A., M. Dettinger, R. Cifelli, D. Curtis, A. Dufour, K. Miller, J. A. Olsen, A. M. Wilson, 2018: Hydroclimatic extremes as challenges for the water management community: Lessons from Oroville Dam and Hurricane Harvey. *Bull. Amer. Meteor. Soc.*, doi:10.1175/BAMS-D-18-0219.1.

Vitolo, R., D. B. Stepenson, L. M. Cook, K. Mitchell-Wallace, 2009: Serial clustering of intense European storms. *Meteorologische Zeitschrift,* **18**, 411-424, doi: 10.1127/0941-2948/2009/0393.

Wallace, J. M., G. H. Lim, and M. L. Blackmon, 1988: Relationship between cyclone tracks, anticyclone tracks and baroclinic waveguides. *J. Atmos. Sci.,* **45(3)**, 439-462, doi: 10.1175/1520-0469%281988%29045<0439%3ARBCTAT>2.0.CO%3B2.

Wick, G. A., P. J. Neiman, F. M. Ralph, and T. M. Hamill, 2013: Evaluation of forecasts of the water vapor signature of atmospheric rivers in operational numerical weather prediction models. *Wea. Forecasting,* **28**, 1337-1352, doi: 10.1175/WAF-D-13-00025.1.

Wernli, H., M. A. Shapiro, and J. Schmidli, 1999: Upstream development in idealized baroclinic wave experiments. *Tellus*, **51A,** 574–587, doi:10.3402/tellusa.v51i5.14476.

White, A. B., M. L. Anderson, M. D. Dettinger, F. M. Ralph, A. Hinojosa, D. R. Cayan, R. K. Hartman, D. W. Reynolds, L. E. Johnson, T. L. Schneider, R. Cifelli, Z. Toth, S. I. Gutman, C. W. King, F. Gehrke, P. E. Johnson, C. Walls, D. Mann, D. J. Gottas, and T. Coleman, 2013: A Twenty-first-century California observing network for monitoring extreme weather events. *J. Atmos. Oceanic Technol.*, **30**, 1585–1603, doi:10.1175/JTECH-D-12-00217.1.

White, A., B. Moore, D. Gottas, and P. Neiman, 2018: Winter storm conditions leading to excessive runoff above California's Oroville Dam during January and February 2017. *Bull. Amer. Meteor. Soc.,* doi:10.1175/BAMS-D-18-0091.1, **in press**.

Zhang, Z. F. M. Ralph, and M. Zheng, 2018: The relationship between extratropical cyclone strength and atmospheric river intensity and position. *Geophys. Res. Lett.,* doi:10.1029/2018GL079071.

Zhu, Y., and R. E. Newell, 1998: A Proposed Algorithm for Moisture Fluxes from Atmospheric Rivers. *Mon. Wea. Rev.*, **126**, 725-735, doi:10.1175/1520-0493(1998)126<0725:APAFMF>2.0.CO;2.

Chapter 3

Large-scale drivers of successive atmospheric river events in California

Abstract

Successive atmospheric river (AR) events—known as AR families—can result in elevated hydrological impacts relative to single ARs due to the lack of recovery time between periods of precipitation. Despite the outsized societal impacts that often stem from AR families, the large-scale meteorological drivers associated with these compound events remain poorly understood. A new 39-year catalog of 248 AR family events impacting California between 1981 and 2019 is introduced based on atmospheric reanalysis data. Using K-means clustering on the 500-hPa geopotential height field, six distinct clusters of large-scale patterns associated with AR families are identified. These clusters broadly represent two types of predominant patterns: those characterized by meridional flow and persistent ridging upstream of California, and those characterized by strongly zonal flow across the North Pacific. Two clusters are of particular interest due to their strong relationship with phases of the El Niño/Southern Oscillation (ENSO). Cluster 3, characterized by a strong ridge in the Bering Sea, most frequently occurs during La Niña and Neutral ENSO years and is associated with the highest cluster-average precipitation across California. Cluster 4, characterized by a zonal elongation of lower geopotential heights across the Pacific basin and an extended North Pacific Jet, most frequently occurs during El Niño years and is associated with lower cluster-average precipitation across California but a longer AR family duration. This study advances the understanding of the large-scale environments and

underlying physical drivers associated with AR families—with the ultimate aim of supporting near-real time predictability applications.

3.1 Introduction

Compound climate events—defined as multivariate extremes, combinations of two or more events occurring simultaneously or successively, or the combination of non-extreme events that lead to an extreme impact (Seneviratne et al. 2012)—often bring greatly elevated societal impacts relative to single extreme climate events. Early studies of compound events focused on a broad range of physical event types, including the co-occurrence of storm surge and precipitation (Wahl et al. 2015, van der Hurk et al. 2015), precipitation and wind extremes (Martius et al. 2016), and heat and precipitation extremes (Zscheishler and Seneviratne 2012, AghaKouchak et al. 2014, Kirono et al. 2017, Sedlmeier et al. 2018). These studies collectively highlight the importance of a formal frameworks for characterizing compound events, especially in the context of risk assessments (Palmer and Raisanen 2002, Leonard et al. 2014, Zscheishler et al. 2018). However, few studies to date have directly addressed the causes and impacts of successive compound events of the same type.

Serial or successive events are certainly not new to the meteorological community. Cyclone families—defined as a temporally clustered series of extra-tropical storms and first identified by Bjerknes and Solberg (1922)—arise via the development of multiple successive cyclones along the polar front in a particular region. Identification and analysis of cyclone families affecting western Europe has shown that while these events occur under a wide variety of synoptic regimes, they occur more frequently than would be expected through random chance. This suggests that certain atmospheric conditions and dynamical mechanisms must favor

clustered cyclone development (Mailier et al. 2006, Pinto et al. 2014). Western European cyclone families are known to produce greater impacts than individual cyclones, and catastrophe models (such as those often used by the reinsurance industry (Vitolo et al. 2009) incorporate the characteristics and frequency of such events.

Recently, this meteorological "event family" framework has been applied to atmospheric rivers (ARs) affecting Northern California (Fish et al. 2019). ARs are long, narrow and transient corridors of horizontal water vapor transport typically associated with an extra-tropical cyclone (Zhu and Newell 1998; Ralph et al. 2004, 2005, Guan and Waliser 2017, Ralph et al. 2017). ARs are associated with very moist conditions in the lower troposphere and can sometimes produce extreme precipitation (Dettinger et al. 2011, Lamjiri et al. 2017, White et al. 2019, Moore et al. 2020). Hydrologic impacts of ARs are modulated by duration (Ralph et al. 2013, Payne and Magnusdottir 2016, Lamjiri et al. 2017)—which itself is often dictated by small-scale meteorological features, such as mesoscale frontal waves (Ralph et al. 2011, Neiman et al. 2016, Martin et al. 2019). In Water Year 2017, a record wet year in Northern California, many ARs occurred shortly after one another. Without time for watershed recovery between storms, these sequences led to very large cumulative rainfall accumulation for many locations in Northern California (White et al. 2019, Moore et al. 2020) and contributed to the crisis at Oroville Dam (Huang et al. 2018).

Using in-situ observations from the Bodega Bay Atmospheric River Observatory in Northern California, Fish et al. (2019) concluded that (similar to cyclone families) ARs that cluster within 120-hrs of another event exhibit large-scale characteristics distinct from those associated with single AR events. The use of a single point observational dataset constrained the identification and analysis to a 13-year dataset from 2005-2017, restricting the ability of a long-

term trend analysis or investigation of the relation to important teleconnections in the region, such as the El Niño/Southern Oscillation (ENSO).

The teleconnection between the equatorial Pacific sea surface temperature (SST) and western US precipitation has long been studied (Ropelewski and Halpert 1986, Cayan et al. 1998, McCabe and Dettinger 1999, Gershunov and Barrett 1998). The warm (El Niño) phase of ENSO is characterized by the shift in warm sea surface temperatures (SST) from the tropical western to tropical eastern Pacific (e.g., Philander 1983, Trenberth et al. 1998), often resulting in increased cool-season precipitation throughout the southwestern US—including portions of California. Conversely, the cooling of the eastern Pacific, which characterizes the La Niña phase of ENSO, is associated with below average precipitation in Southern California and above average precipitation in the Pacific Northwest. The dynamical mechanism for these ENSO-associated precipitation teleconnections is the poleward propagation of a Rossby wave train into the mid-latitudes, initially triggered by enhanced deep convective activity over the longitude-shifted region of warm tropical SST (Horel and Wallace, 1981, Trenberth et al. 1998, Alexander et al. 2002 and references therein, McPhaden et al. 2006). This teleconnection supports a seasonally strengthened Gulf of Alaska low pressure system, which in turn can lead to increased extratropical cyclone and AR activity. Indeed, multiple studies have demonstrated that AR frequency throughout the North Pacific basin is strongly modulated by ENSO (Bao et al. 2006, Ryoo et al. 2013, Mundhenk et al. 2016). Given that ENSO is a pronounced mode of global climate variability and exhibits seasonal/subseasonal predictability, understanding the physical linkages between ENSO and North Pacific ARs is crucial to improving AR predictability--which has major implications for water and flood risk management. In the present study, we use reanalysis data to create a 39-year dataset of AR families affecting California, and subsequently

evaluate the large-scale conditions linked to these events and their relationship to associated precipitation impacts. In the sections that follow, we first give a brief description of the AR detection and identification methods, as well as the clustering method chosen for analysis. We then describe results from our analysis using the new AR family catalogue, including a) interannual variability of AR families, b) large-scale atmospheric patterns associated with AR family clusters, c) thermodynamic and kinematic patterns linked to AR families, d) relationships between AR families and ENSO, and e) the precipitation characteristics of each cluster. Finally, we present results from two case studies drawn from notable AR clusters in 2016 and 2017.

3.2 Methods

a. Atmospheric Reanalysis Data

Following Fish et al. (2019), the Modern-Era Retrospective analysis for Research and Applications, Version 2 (MERRA-2) dataset (Gelaro et al. 2017) is used to create a daily climatology of several relevant atmospheric variables at 3-hr resolution. MERRA-2 is preferred due to its high spatial resolution and incorporation of numerous observations assimilated from a wide range of sources, including satellite-derived atmospheric motion and surface wind vectors important for the accurate detection of ARs.

The daily climatology computed in Fish et al. (2019) is expanded spatially to an area spanning all longitudes over the latitudes -20°S to 90°N. A smoothed daily climatology over the 30-year period, 1987-2016, is created using a 21-day running mean technique (Hart and Grumm 2001). This climatology is calculated for the following relevant atmospheric variables: 500-hPa and 850-hPa geopotential heights, 500-hPa and 850-hPa air temperature, 250-hPa wind speed, sea level pressure and integrated water vapor (IWV).

These reanalysis data are sampled to calculate anomalies over the duration of the MERRA-2 dataset (1980-2019). Anomalies associated with successive AR events were subsetted according to the AR detection algorithm defined in section II.b and the AR family algorithm defined in section II.c. These reanalysis data are also used to evaluate case study mean composites.

To objectively identify large-scale variability within successive AR events, k-means clustering is performed on anomalous 500-hPa geopotential heights in the North Pacific. Clustering on raw anomaly data instead of filtered empirical orthogonal function data is chosen because the raw anomaly data have a tendency to produce a higher number of optimal clusters. Applied to a region in the North Atlantic in previous work, use of raw anomaly data identified both phases of the Atlantic Ridge and Scandinavian Blocking, while the filtered data only identified the positive phases (Falkena et al. 2019)—highlighting the importance of using raw data to capture the full range of outcomes. K-means is an iterative clustering procedure that minimizes the sum of variance within each cluster (Diday and Simon 1976). This method was chosen for its success in previous studies aimed at identifying large-scale circulation patterns (Fereday et al. 2007, Moron et al. 2007, Jiang 2010, Roller et al. 2016), similar results to self-organizing maps (Gibson et al. 2017) and low computation time compared to other methods. Prior to clustering, data are weighted according to the following,

$$W = \sqrt{cos\left(\phi * \frac{\pi}{180}\right)},$$

where W is the weight and ϕ is latitude. The weight is applied to North Pacific latitudes, 20°N to 85°N, of the anomalous 500-hPa geopotential heights. Accuracy (within each cluster) and uniqueness (between the clusters) calculations are evaluated across a range of k values to determine the optimal k (Lee and Feldstein 2013, Gibson et al. 2016). K=6 is determined as the

most parsimonious and physically interpretable value, given the relatively flat uniqueness and accuracy curves and the qualitative discernibility of large-scale atmospheric patterns for k=6 (not shown). Clustering is calculated using data within a box in the Northern Pacific extending from 120°W to 270°E and 20°N to 85°N. Sensitivity calculations for box area showed little sensitivity to changes of 10° to 30° longitude and 10° to 20° latitude.

b. AR Detection Algorithm

AR objects are identified using the global AR detection algorithm, tARget version 2.0 (Guan et al. 2018), applied to the 6-hr MERRA-2 reanalysis data, described above in section II.a. The AR detection algorithm uses integrated water vapor transport (IVT), direction, and geometry, described in detail in Guan and Waliser (2015) and refined in Guan et al. (2018). The key requirements are as follows: 1) IVT intensity greater than either the maximum 85th percentile or 100 kg m^{-1} s^{-1} at each grid cell, 2) mean IVT within 45 degrees of AR object shape and with large poleward component, and 3) object length greater than 2000 km and a length to width ratio greater than 2.

This study evaluates AR objects that made landfall anywhere along the California coast during a particular water year (henceforth, WY; defined as October 1-September 30 periods spanning two calendar years, beginning in October 1981 and ending in May 2019). The WY is referred to by the second calendar year, e.g. October 1, 1981-September 30, 1982 is WY 1982.

c. AR Families Algorithm

This study builds on the definition and identification of AR families presented in Fish et al. (2019). Previously, AR families were defined as successive AR events—AR conditions

identified via observational data—that made landfall at Bodega Bay, CA. Fish et al. (2019) determined that a 120-hr aggregation period was a suitable maximum aggregation period for Northern California AR events. Therefore, for this study, AR objects—AR conditions identified in reanalysis data—are classified as an AR family if two or more AR objects occurred within the 120-hr aggregation period. Once an AR object initiated a new AR family or followed a previously occurring AR object by less than 120-hrs (i.e., was included in an AR family), that AR object could no longer initiate a new AR family. Additionally, AR objects were counted at first landfall and their propagation was tracked.

AR family events are further filtered to retain only AR families with at least one 12-hr AR object, which removes instantaneous and short duration (6-hr, 1 timestep) AR objects. AR objects less than two grid points wide are also removed, since these objects are too narrow for the IVT computation. Therefore, AR families consisting of only narrow AR objects are removed. These additional requirements left ~900 AR objects, with almost 600 considered a part of an AR family and the remainder assumed to be single AR objects (Fig. 3-1). Single AR objects are formally defined as AR objects occurring without another AR object within 120-hrs before or after the event. Clustering is performed at single timestep resolution within the AR families; however, the AR family events are further partitioned according to their mode cluster throughout the event duration.

d. Precipitation Data

To investigate the impacts of AR families and whether large-scale atmospheric variability is related to precipitation outcomes, PRISM daily precipitation data from 1981-2019 is used. PRISM uses point data and a digital elevation model to generate gridded estimates of

precipitation and other climate variables (Daly et al. 1994, 2001, 2002). The PRISM daily precipitation dataset is chosen for its strength in representing precipitation in mountainous regions such as the western US and its high spatial resolution of 4km.

e. ENSO Data

The El Niño/Southern Oscillation (ENSO) Longitude Index (ELI) is a physically based metric dependent on the average Pacific longitude where equatorial sea surface temperature (SST) exceeds the threshold for deep convection (Williams and Patricola 2018). The ELI is used here to characterize ENSO variability and its relation to AR families over 1981-2019. While the traditional Niño3.4 index based on SST anomaly was also evaluated (not shown), the ELI was ultimately chosen due to its stronger relationship between tropical Pacific deep convection and geographically remote teleconnections—particularly those relevant to western US precipitation (Patricola et al. 2019).

The ELI dataset used here is provided by Patricola et al. (2020) and is calculated using the monthly 2.0° × 2.0° Extended Reconstructed SST v5 (Huang et al. 2017). ENSO events are defined as the December-February (DJF) average of the ELI (Patricola et al. 2019). El Niño events exhibit an ELI greater or equal to 162°E, La Niña events exhibit an ELI less than 158°E, and Neutral events, ELI are less than 162°E but greater than or equal to 158°E. Nine years were classified as El Niño (1983, 1987, 1992, 1993, 1995, 1998, 2003, 2010, 2016) and Neutral (1988, 1990, 1991, 1997, 2002, 2005, 2007, 2015, 2019) and the remaining 21 years were classified as La Niña (1981, 1982, 1984, 1985, 1986, 1989, 1994, 1996, 1999, 2000, 2001, 2004, 2006, 2008, 2009, 2011, 2012, 2013, 2014, 2017, 2018). Relationships between ELI and AR families are then based on the corresponding occurrences of AR families over the DJF months for each WY.

3.3 Results

a. Successive AR Variability

One key benefit of using reanalysis data instead of point-based observational data to detect AR families, as has been used in previous work (Fish et al. 2019), is that broader spatial and temporal variability that can be examined. The 39-year time series, from WY 1981-2019, allowed for the evaluation of interannual variability of a) the total number of AR events, b) the number of events in AR families, c) the resulting single AR events and d) the ratio of events in AR families to the total number of AR events (Fig. 3-2). We find that the total number of AR events ranges from a minimum of 11 AR events in WY 1991 to a maximum of 42 AR events in WY 1983. Events within AR families range from a low of four AR events in WY 1985 to a high of 34 AR events in WY 1983. Single AR events have a much smaller range—between four and 10 AR events per WY.

The number of AR events within AR families often follows the interannual variability of the total number of all AR events. This co-dependence is especially striking during both very active WYs, such as 1983 and 2017, and very inactive WYs, such as 1985, 1987 and 1991. The ratio of AR family events to total AR events highlights the co-dependence well, ratios greater than 0.5 during active WYs and less than 0.5 during inactive WYs. Out of the 39-year time series, only eight WYs had a ratio of AR family events to total AR events less than 0.5 (1985, 1987, 1991, 2001, 2003, 2007, 2008, 2009). In 31 of 39 years (79%), a majority of ARs occurred as part of an AR family, rather than as a single event.

b. Large-scale 500hPa height patterns associated with successive ARs

K-means cluster analysis on AR family events (k=6) on the anomalous 500-hPa geopotential height field reveals primary modes of large-scale variability during these events (Fig. 3-3). We find that there are two dominant types of large-scale pattern types associated with AR families: high-amplitude meridional flow and low-amplitude zonal flow. Clusters 1, 3, 5 and 6 all exhibit anomalously high geopotential heights upstream (west) of an anomalous low geopotential height region associated with AR activity, though magnitudes and precise locations vary. Clusters 2 and 4 exhibit a much more zonal pattern that distinctly lacks any upstream positive geopotential height anomalies.

Interestingly, when the same method is applied to isolated single AR events accuracy across k clusters comparing all events to the cluster average (using a range of k, from k=2 to k=20) was quite low (median less than 0.2). This result, which is robust to spatial shifts in the domain, suggests that atmospheric variability associated with isolated single AR events is much higher than for AR families. In other words: while there is clear evidence of preferred large-scale patterns conducive to AR family events, the range of patterns capable of producing a single landfalling AR in the study region is much wider. This also hints that AR families may potentially be physically linked to certain underlying modes of variability, whereas single events may be less so. These large-scale environments are described further below.

Clusters 1, 3, 5 and 6 all exhibit upstream positive z500 anomalies, classifying them as meridional patterns. Cluster 1 is similar to the anomalous pattern shown for WY 2017 AR families in Fish et al. (2019), with moderate positive geopotential height anomalies (i.e., ridging) in the central Pacific and two regions of negative geopotential height anomalies and associated minima just west of the Bering Sea and off the coast of Northern California, respectively. Cluster

3 exhibits a widespread region of anomalously high geopotential heights based in the Bering Sea, extending southward into the North Pacific, northward into the Arctic, eastward to Canada and westward into eastern Russia. This large region of positive geopotential height anomalies is suggestive of a large-scale steering pattern that would influence the propagation of cyclonic storms across the North Pacific (Shutts 1983, Carrera et al. 2004), perhaps by inducing an equatorward displacement and/or enhancement of the storm track downstream of the high-latitude ridge and yielding negative geopotential height anomalies across much of the subtropical and mid-latitude Pacific (20°N-45°N). East of Hawaii, the region of negative z500 anomalies follows the flow around the positive geopotential height anomaly region toward the Pacific Northwest, with a minimum located offshore of Washington state and British Columbia. Cluster 3 is similar to composite patterns shown by Moore et al. (2019) for extreme precipitation events affecting Northern California. Cluster 5 exhibits a region of positive z500 anomalies south of the Aleutian Islands around 30°N. Negative geopotential height anomalies are in a concentrated region along the US West Coast, extending in a more meridional alignment compared to other clusters. Cluster 6 has equal spatial extent of negative and positive regions of geopotential height anomalies. Similar to Cluster 3, Cluster 6 has an elongated region of negative z500 anomalies extending from the minimum, centered at 50°N 145°W, southeast into the subtropical region of the east central Pacific. The region of positive z500 anomalies is located in the eastern Bering Sea, off the coast of Russia, extending into the northern Eurasian continent. The location of this positive anomalous region and resultant counterclockwise flow around it allows the advection of the dominant flow regime and embedded short waves to propagate northward into British Columbia and the eastern maritime region of Alaska.

Cluster 2 and 4 lack enhanced meridional flow or upstream ridging and are thus classified as zonal patterns. Instead, Cluster 2 has a broad region of negative geopotential heights extending from the eastern edge of the Gulf of Alaska to eastern Russia through the Bering Sea. This cluster has the lowest average negative z500 anomaly of all clusters. While this cluster exhibits no upstream positive anomaly, anomalously high geopotential heights are still located throughout the domain, downstream over central eastern Canada and northeast of Hawaii. Cluster 4 describes a zonally elongated region of negative geopotential heights, with a minimum in the central Pacific extending toward the US West Coast. This pattern is similar to that which AR families with 3+ AR events exhibit in Fish et al. (2019). Reinforcing this pattern and its relation to multiple AR events, Cluster 4 is one of the clusters with the most (16) AR families with 3+ AR events, compared to all clusters (Table 3-1). This cluster notably lacks a ridging signal in either upstream or downstream regions. However, a positive z500 anomaly can be found throughout the Arctic region, particularly north Kamchatka.

c. Thermodynamic and kinematic composite patterns associated with successive AR clusters

K-means clustering on 500-hPa geopotential heights yielded insights regarding mid-tropospheric circulation patterns and steering flow associated with successive AR clusters. Next, we investigate other relevant atmospheric characteristics associated with the identified clusters. In addition to large-scale flow patterns, another important consideration is the amount of moisture present during the AR events. US West Coast AR events typically associated with high integrated water vapor (IWV) content near the coast (Zhu and Newell 1998, Ralph et al. 2019). To determine the variability of IWV, including its magnitude and spatial extent, we evaluate the composite IWV for each cluster (Fig. 3-4). Cluster 3 has the largest magnitude and spatial extent

of anomalous IWV. Along the California coast, the climatological average IWV ranges from 12-16 mm; however, Cluster 3 AR families are associated with average IWV 8mm above background levels, corresponding to a 50-66% increase. This region of anomalously positive IWV extends from Hawaii to the California coast and penetrates inland as far as Arizona and Utah. Cluster 6 AR families also exhibit a large magnitude of anomalous IWV similar to cluster 3 (also +8 mm). However, for Cluster 6 events, the region of anomalous IWV is more narrowly concentrated around coastal California, with a sharper gradient relaxing to climatological values on all sides of the anomalously positive region. Both of these clusters also exhibited negative geopotential height anomalies extending into the subtropics (Fig. 3-3). Cluster 2 AR families have the smallest spatial extent of anomalous IWV, as well as the lowest magnitude. Similar to their associated negative geopotential height anomalies, Clusters 1 and 5 show more meridionally-elongated positive IWV anomaly regions. Cluster 4 closely resembles previous results for ARs affecting California (Ralph et al. 2004), including those of long durations (Payne and Magnusdottir 2016, Fish et al. 2019, Moore et al. 2019).

Previous work has shown that jet stream position and strength modulates precipitation in downstream regions of the western US (Riehl et al. 1954, Reiter 1963, Hakim 2003, Barton and Ellis 2009, Griffin and Martin 2017). Here, our analysis of anomalous 250-hPa wind speeds supports the earlier finding that Clusters 1, 3, 5, and 6 are more meridional flows while Clusters 2 and 4 are zonal flows (Fig. 3-5). The strongest DJF climatological wind speeds (Fig. 3-10C) are concentrated in the eastern Pacific and extend to the central Pacific. For the meridional flow patterns (Clusters 1, 3, 5 and 6), the jet is shifted poleward, and a local maximum of anomalous jet-level wind exists in the vicinity of the Aleutian Islands, with a pronounced reduction in wind speed in the climatological (equatorward) region of the jet. These clusters also exhibit secondary

maxima anomaly regions in the western Pacific and over the continental US. The zonal patterns (Clusters 2 and 4), on the other hand, are distinguished by a narrowing and zonal (eastward) extension of the climatological jet that also extends to the continental US. Conditions in the Pacific are similar to average conditions, while the jet in the central and western Pacific shows a positive speed anomaly of greater than 20 m/s, as shown in Cluster 2.

Conditions in the lower troposphere, such as anomalous SLP and 850-hPa geopotential heights, show similar results to the initial 500-hPa geopotential height clustering (not shown). The average anomalous 850-hPa air temperature per cluster is consistent with previous literature on temperature extremes across regions of the US, as described below. Cluster 2 exhibits greater than 5 K warming over Canada and the upper Midwest, which is also seen during high-impact precipitation events over the Mackenzie River Basin in Canada (Lackmann and Gyakum 1996). Cluster 3 AR families, associated with positive geopotential heights over the Bering Sea, average greater than -8 K downstream cooling over western Canada and throughout the northwestern interior US states. Cooling is indeed a common consequence in the region of equatorward return flow on the downstream side of blocking patterns, as demonstrated in previous work (e.g., Winters et al. 2019). Air temperature during Cluster 6 shows a moderate (3-4 K) anomalous warming downstream along the Rocky Mountain Front Range and throughout the Midwest U.S., which is also consistent with a pattern previously associated with anomalous moisture transport into the Pacific Northwest (Lackmann and Gyakum 1999). These cluster-specific downstream temperature impacts suggest the potential implications for the mean freezing levels across the western U.S. and subsequent consequences for snow levels and rain/snow partitioning in mountainous regions, although a more comprehensive assessment is beyond the scope of the present analysis.

d. AR Metrics

Each cluster is associated with distinct large-scale features throughout the atmospheric column, both on the regional and continental scale. In addition to the clear structural differences between the large-scale spatial patterns driving these events, it is also evident that each AR family cluster type is associated with substantial differences in event temporal characteristics, such as storm duration and intensity (Table 3-1). Cluster 3 produces the longest duration AR families relative to the average across all AR families (114 total hrs per event). This result also holds when evaluating only AR hours within each AR family. Cluster 3 also yields the highest fraction of AR hours to total AR family duration (50%). Moreover, Cluster 3 is also associated with the highest average number of discrete AR events per AR family (3); all other clusters average 2 events per family. However, when specifically considering AR families with the maximum number of individual AR events (specifically, those with 3 or more), Clusters 2 and 4 rise to the top, with 16 AR families each. Accounting for the total occurrence of each cluster, Cluster 3 has the highest percentage (52%) of AR families with 3 or more AR events, while all other clusters are ~30%. Throughout the catalog, there are a total of 79 AR families with 3+ AR events, out of the total 249 AR families identified.

AR event duration has a strong positive association with the amount of total precipitation accumulation that occurs over the event (Ralph et al. 2013, Payne and Magnusdottir 2016, Lamjiri et al. 2017). Further, a large-scale pattern reminiscent of the Cluster 3 pattern has previously been linked to extreme precipitation events in Northern California (Moore et al. 2019). While more research is needed on the physical mechanisms operating within each cluster and possible linkages to AR family durations, identifying the relevant large-scale spatial patterns (as we do here) is a vital first step toward understanding these high-impact events.

We also evaluated various metrics of AR family event IVT to provide insight into differences in intensity between clusters. Event average IVT across all AR families is 361 kg m^{-1} s^{-1}. Cluster 2 has the highest event average IVT compared to all clusters (410 kg m^{-1} s^{-1}), and Cluster 1 has the lowest (319 kg m^{-1} s^{-1}). The average event maximum IVT across all events is 550 kg m^{-1} s^{-1}. Cluster 2 (594 kg m^{-1} s^{-1}) and Cluster 1 (499 kg m^{-1} s^{-1}) are again the clusters with the highest and lowest event maximum IVT, respectively (Table 3-1). Relating these metrics back to the large-scale features identified, Cluster 2 is classified as a zonal case, while Cluster 1 exhibits large positive upstream height anomalies and is classified as a meridional case.

Due to the importance of AR event duration for precipitation, we also calculate the average event total IVT (i.e., the time integrated IVT). Across all AR families, the average event total IVT is 2014 kg m^{-1} s^{-1}. Cluster 4 has the maximum event total IVT of all clusters (2402 kg m^{-1} s^{-1}), while Cluster 5 has the minimum average total IVT (1397 kg m^{-1} s^{-1}). As noted above, Cluster 4 includes the most 3+ AR event AR families, whereas Cluster 5 is one of the clusters with the fewest multi-AR event AR families. This suggests that the higher number of total AR hours per event in Cluster 4 (due to both the higher number of events per family and the longer duration of AR events within each family) are strongly associated with cumulative IVT fluxes—perhaps with significant implications for precipitation accumulation. Previous studies have explored the importance of large-scale flow on structure and evolution of cyclones (Shultz et al. 1998) and the relationship between cyclones and ARs (Zhang et al. 2018). The amplitude of the background flow pattern is also known to interact with the jet stream in a manner that tends to produce meridionally elongated (for high amplitude flow) or zonally elongated cyclones and fronts (for low amplitude flow) (Rossby and Willett 1948, Namias 1950). Such activity in the terminal zone of storm track regions (i.e., the jet exit region, such as occurs over the far eastern

Pacific near California) favors the formation of meridional cyclones, which have a greater fraction of precipitation along the cold front (Shultz et al. 1998). This prior work offers some clues regarding how to interpret our findings regarding the clustered large-scale patterns and their relationship to both topics, providing context for how these clusters might relate to AR family intensity. We find that an anomalously high amplitude jet stream occurs in clusters with positive geopotential heights upstream of the AR focus region, such as Cluster 1, suggesting that parent cyclones and associated ARs during these events may have a tendency to become more meridionally oriented. Conversely, a low amplitude jet is characteristic of the zonal clusters, such as Cluster 2. Previous work has shown that when strong cyclonic storms co-occur with ARs, IVT can be greatly enhanced due to the strong winds associated with strong surface pressure gradients (Zhang et al. 2018). Our findings suggest that anomalously low z500 co-located with regions of high-frequency cyclone activity (such as occurs in Clusters 2 and 3) are indeed associated with higher AR family event maximum IVT—which would be consistent with this prior work. Additionally, Cluster 3 includes a high amplitude, meridional flow pattern.

e. Cluster relationships to ENSO

Across the North Pacific and western US, ENSO strongly modulates cool-season storm activity and precipitation (Ropelewski and Halpert 1986, Schonher and Nicholson 1989, Cayan et al. 1999, McCabe and Dettinger 1999, Gershunov and Barrett 1998). As SSTs warm in the central and eastern equatorial Pacific during ENSO warm phase events, tropical convection moves eastward as well, following the warmer SSTs (Trenberth et al. 1998, Alexander et al. 2002). ENSO is often classified by the running 3-month mean SST anomaly (SSTa) in an equatorial box spanning -5°S to 5°N, 170°W to 120°W, termed the Niño3.4 region. Prior to the

much discussed 2015-2016 El Niño event, Niño3.4 SSTa were thought to be a reasonably strong indicator of ENSO's relationship to southwestern US precipitation (Mason and Goddard 2000). The failure of the strong 2015-2016 event to bring wet conditions to the Southwest, which has been explored in detail (Santoso et al. 2017, Siler et al. 2017, among others), motivated the search for more appropriate metrics that might better represent the multi-step teleconnection that occurs between tropical SSTs and western US precipitation. Williams and Patricola (2018) proposed one such new physically based metric, the El Niño Longitude Index (ELI), which characterizes the tropical regions available for deep convection based on SST. The ELI thus directly incorporates the threshold for initiation of the relevant tropical-extratropical teleconnection, leading to a more robust correlation between ELI and western US precipitation than traditional SSTa-based metrics (Patricola et al. 2019).

Using the ELI metric, the DJF AR family timesteps within each cluster were sorted by ENSO phases (La Niña, Neutral or El Niño) depending on the overall WY characterization (Table 3-2). Out of 3689 total DJF AR family timesteps, 2004 occurred in La Niña years, 619 in Neutral years and 1066 in El Niño years (although we note that there are twice as many La Niña years as Neutral or El Niño years in this dataset). Cluster 2 is the most frequently occurring cluster across all phases of ENSO, and Cluster 6 occurs least frequently. Cluster 3 occurrence is strongly associated with La Niña conditions, with 407 out of 604 (~67%) of total Cluster 3 timesteps occurring during the ENSO cool phase. Interestingly, Cluster 3 is largely absent during El Nino years (51 out of 611 total timesteps). Cluster 4 most frequently occurs in El Niño years (316 out of 602 (52%) of total cluster timesteps), with infrequent occurrences in Neutral years (Fig. 3-6).

f. Precipitation associated with clusters

AR family events are successive AR events and are typically characterized by multi-day (2-5) durations. Duration is an important factor for AR-associated precipitation, as long-duration events are typically associated with the highest accumulations (Ralph et al. 2013, Payne and Magnusdottir 2016, Lamjiri et al. 2017). Indeed, extreme precipitation events in Northern California are often multi-day events (Moore et al. 2019, White et al. 2018). For the events in this catalog, the average total precipitation accumulation across all AR family events varies substantially across California, with the highest values co-located with areas of enhanced orography (Fig. 3-7, A). Most AR family events impact the Northern Sierra Nevada mountains and the coastal mountains of Northern and Central California. The Transverse Ranges in Southern California can also receive heavy AR-related precipitation, but these are more often single events associated with a single, slow-moving closed low pressure system (Oakley et al. 2018). The AR family events, partitioned by their mode cluster per event, were sorted to evaluate how the different large-scale environments affected the average precipitation total per cluster (Fig. 3-7, B). While each cluster shows high precipitation totals across both the Coast Ranges and inland Sierra Nevada Mountains (Fig. 3-7, A), Clusters 2 and 6 show a preference for increased precipitation in coastal Northern California. Cluster 3 impacts the entirety of the Sierra Nevada mountains, northern California, and coastal central California. Cluster 5 AR family events not only affect northern California and the Sierra Nevada mountains but also the Transverse Ranges in Southern California.

We evaluate precipitation differences between clusters by comparing the anomaly of each cluster's average cumulative precipitation to the average precipitation accumulation across all

AR families (Fig. 3-7, C). We find that Cluster 3 generally brings much wetter conditions throughout California relative to the AR family mean, while Cluster 4 brings below average precipitation. From a spatial perspective, Clusters 5 and 6 are effectively inverted: Cluster 5 events bring enhanced precipitation to Southern California, while Cluster 6 events shift precipitation to Northern California and often are associated with dry conditions in Southern California. Cluster 1 and 2 events feature reduced precipitation in the Sierra Nevada mountains, but Cluster 2 events do produce above average precipitation along the coast of Northern California.

Event total precipitation is not the only important precipitation characteristic. Event average precipitation intensity, defined herein as total precipitation divided by event duration in days, is also critical to evaluate as this definition normalizes each event to equally weigh precipitation totals and efficiency across different durations. Additionally, the precipitation intensity of AR family events is likely related to the severity of its subsequent hydrologic impacts. The average event precipitation intensity across all AR family events (Fig. 3-8, A) follows a similar spatial pattern as the average total precipitation across all AR family events (Fig. 3-7, A). Maxima are located in the northern Sierra Nevada mountains and in the coastal mountains of Northern California. Clusters 1 and 5 have the weakest precipitation intensity, while Clusters 2, 3 and 6 have the highest precipitation intensity and average above 32 mm/day in some parts of Northern California and the Sierra Nevada mountains. The enhanced precipitation intensity in Cluster 3 (despite also having the longest cluster duration, Table 3-1) throughout the Sierra Nevada and Transverse Ranges, and in Cluster 6 events across Northern California (Fig. 3-8, C) is particularly noteworthy. Clusters 2 and 4 have precipitation intensities close to the average across all AR family events, except in coastal Northern California.

These substantial differences in the precipitation across clusters hints at potential linkages to associated large-scale patterns. In particular, AR family events associated with high-amplitude upstream blocking, as in Cluster 3, clearly favor enhanced precipitation across much of California. Conversely, AR family events associated with low-amplitude, largely zonal patterns, as in Cluster 4, tend to produce less intense precipitation in California. Collectively, this suggests that the type of large-scale pattern present over the North Pacific may be a useful predictive factor regarding the ultimate intensity of successive AR events in California.

g. Case studies for successive AR events in Jan 2016 and Jan 2017

Two case studies from recent history were selected to analyze the large-scale environment and precipitation response of various AR families. The strong association of Cluster 3 with La Niña years and Cluster 4 with El Niño years, in particular, motivate this further analysis.

We find that the high-impact AR family which occurred during January 4-11, 2017 is an exemplary case of a Cluster 3-type event (Fig. 3-9). This AR family was associated with persistently positive z500 anomalies (i.e., strong ridging) over the Bering Sea, an equatorward shift of the North Pacific Jet, a secondary jet maximum off the US West Coast and two separate plumes of enhanced IWV on either side of Hawaii (Fig. 3-9 A, C, E). Observed z500 anomalies are a strong match with the Cluster 3 composite (pattern correlation of 0.85). The anomalous 250-hPa windspeed and IWV from this case study (Fig. 3-9 D, F) are also similar to their respective cluster averages (Fig. 3-5 and 3-4) given the equatorward shift of the North Pacific Jet, the increased jet level winds in the Arctic, the large secondary maximum and enhanced region of IWV off the US West Coast. This event produced over 500 mm of precipitation in the

northern Sierra Nevada mountains and around 400 mm in the coastal regions (Fig. 3-10 B), and caused a number of adverse hydrologic impacts (Huang et al 2018). Compared to the average precipitation across all AR families, this case produced 300 mm of anomalous precipitation throughout the Sierra Nevada mountains and over 250 mm of anomalous precipitation over the coastal regions (Fig. 3-10 C). Based on the spatial average of the precipitation total in California of all events in Cluster 3, this event was a 72nd percentile case, and occurred during a moderate La Niña year (as classified by its ELI value of 155.73°E).

The Cluster 4 case study occurred during January 14-20, 2016 during a moderate El Niño year (ELI: 173.63°E). This AR family displayed low geopotential heights across a broad portion of the North Pacific, an extended North Pacific Jet, and enhanced IWV extending from the US West Coast to Hawaii (Fig. 3-11). To assess the representativeness of this event among Cluster 4 cases in El Niño years we computed a pattern correlation of 0.279. While this is a low pattern correlation, especially when compared to the previous case study, the generally low amplitude and gradients of height differences across the North Pacific for Cluster 4 and the variation of the central location of low geopotential heights across the cases within Cluster 4 (not shown) make it more difficult to produce strong pattern correlations. This case's pattern correlation is the highest among all cases within Cluster 4 El Niño years. The anomalous 250-hPa windspeed is similar to the cluster composite and is mainly characterized by an extended North Pacific Jet with a slight northeast tilt toward Northern California (Fig. 3-11 D). The anomalous maximum occurs further west in this case, compared to the average, around 150ºW. The anomalous IWV exhibits up to 12 mm of additional IWV between Hawaii and the US West Coast (Fig. 3-11 E), which is higher than the cluster average. This event primarily affected Northern California. Compared to the average AR family precipitation total, this event was relatively drier in Southern California and

produced more than 100 mm of anomalous precipitation in Northern California (Fig. 3-12 C). California precipitation spatial average for this case is in the 84th percentile of all Cluster 4 cases. While Cluster 4 cases generally produce precipitation throughout California, as shown in Fig. 3-7 and 3-8, the distribution of anomalous spatial averages of each case's total precipitation shows a more nuanced relationship (Fig. 3-7). This case in particular had a spatial average precipitation of 63.07 mm and anomaly of 24.68 mm, in comparison to the median precipitation across all Cluster 4 events of 28.51 mm and median anomaly of -9.87 mm.

3.4 Discussion and Conclusions

This study introduces a new catalog of AR families that affected California during 1981-2019. Using this 39-year dataset we conducted analysis of the background climatology and interannual variability of such events. In 79% of years half of all AR events occur as part of AR families (i.e., as successive AR events). Further, there is a strong positive relationship between the total number of AR families per year and the overall number of AR events. Clustering the anomalous 500-hPa geopotential heights associated with AR families reveals the optimal mode of large-scale variability for these events at k=6, suggesting that there are distinct large-scale patterns associated with different types of landfalling AR family events. In contrast, single AR events do not demonstrate obvious clustering of spatial patterns. The presence of such clustering for AR family events yet absence for single AR events suggests that the potential predictability of AR families may be enhanced relative to single AR events, especially on sub-seasonal to seasonal timescales.

The resultant clusters for AR families feature either meridional (Clusters 1, 3, 5 and 6) or zonal patterns (Clusters 2 and 4). The variability of the location and magnitude of persistent

ridging defines each meridional cluster, and the orientation and center location of low geopotential height regions define each zonal cluster. Additionally, the water vapor and jet stream variability also vary greatly across different types of AR families. Cluster 3, in particular, is associated with the highest water vapor. Meridional clusters are associated with a shift and split of the North Pacific jet, while zonal clusters occur during jet extension periods. Cluster 3 events (meridional) most often occur in La Niña or Neutral years, while Cluster 4 events (zonal) most often occur in El Niño years. Cluster 2 occurs equally across ENSO phases. Cluster 3 averages the longest duration AR families, with the highest ratio of AR hours to total AR family duration. However, Cluster 4 has the highest number of discrete AR events per AR family. On average, Cluster 3 AR families accumulate the most precipitation per event. Cluster 3 events are also associated with the most intense precipitation per event, particularly in the Sierra Nevada mountains and the Transverse Ranges. For all grid points in California, the most AR families make landfall between 36.5-37°N—suggesting that AR families are relatively rare in Southern California The evaluation of two case studies of Cluster 3 and 4 DJF AR families during La Niña and El Niño years, respectively, illustrated two clear cases of the large-scale environments matching composites from a specific cluster. However, the precipitation response within each cluster varied substantially. The Cluster 3 case study was associated with 72nd percentile precipitation among Cluster 3 events across California. Alternatively, the Cluster 4 case study was associated with 84th percentile precipitation across all Cluster 4 cases. Together, these cases highlight the distribution of precipitation within California for each cluster, while reinforcing the notion that Cluster 3 events are associated with especially high precipitation and elevated hydrologic impacts.

This study enhances our understanding of the large-scale variability relevant to successive AR events affecting California. Given that many of these events produce extreme precipitation, this study aims to further the meteorological situational awareness and understanding of potential precipitation impacts associated with successive AR events. The presence of persistent ridging in the North Pacific shown here to be associated with AR families, has also been shown to be associated with extreme precipitation events in Northern California (Moore et al. 2020) and increased frequency for ARs affecting the Pacific Northwest (Benedict et al. 2019). The agreement of these results emphasizes the strong potential for using ridging patterns to predict increased AR activity and extreme precipitation. Our findings in the present study suggest that the predictability of ARs occurring as part of a family may be more predictable than single AR events—which is potentially of considerable relevance in a water and flood management context given the outsized hydrologic impacts of such events. Future work will explore the potential enhanced predictability of AR families in more depth, as well as their relationship to the North Pacific jet, persistent atmospheric circulation events, and possible changes in a warming climate.

3.5 Acknowledgements

MAF and AMW were supported by grant W912HZ-15-2-0019 from the US Army Corps of Engineers and grant 4600013361 from California Department of Water Resources. DLS was supported by a joint collaboration between the Institute of the Environment and Sustainability at the University of California, Los Angeles; the Center for Climate and Weather Extremes at the National Center for Atmospheric Research; and the Nature Conservancy of California. This research was additionally supported by NSF awards 1854940 (to JD) and 1854761 (to DLS). We

gratefully acknowledge the availability of the MERRA-2 reanalysis dataset available through the National Aeronautics and Space Administration (NASA) Global modeling and Assimilation Office. These data are available at MDISC, which is managed by the NASA Goddard Earth Sciences Data and Information Services Center. We would also like to acknowledge high-performance computing support from Cheyenne provided by NCAR's Computational and Information Systems Laboratory, sponsored by the National Science Foundation. AR data were provided by Bin Guan, accessible via a public repository at URL: https://ucla.box.com/ARcatalog. Development of the AR detection algorithm and databases was supported by NASA. The authors thank Andreas Prein for the preprocessed PRISM data and Patricola et al. (2020) for the publicly available ELI data. MAF gratefully acknowledges the NCAR Visitor Program, specifically Cindy Bruyère for funding and support of this project. The NCAR is sponsored by the National Science Foundation.

Chapter 3, in full, is the material submitted to the as Journal of Climate. Fish, M. A., J. M. Done, A. M. Wilson, D. L. Swain, F. M. Ralph (2020): "Large-scale drivers of successive atmospheric river events in California", *Journal of Climate*, submitted 5/11/2020. The dissertation author was the primary investigator and author of this paper.

Table 3-1. AR family events classified by their mode cluster. Values along the bottom row represent totals or averages across all AR family events. 1) Number of events per cluster, 2) average duration of AR families (hrs), 3) average AR hours within AR family events (hrs), 4) number of AR family events with 3+ AR events, and 5) average AR family event maximum IVT (kg m^{-1} s^{-1}).

Cluster Number	1) # of AR Families	2) Duration of AR Families (hrs)	3) AR Hours per AR Family (hrs)	4) # of AR Families with 3+ AR events	5) Average AR Family Maximum IVT (kg m^{-1} s^{-1})
1	47	100	41	14	499
2	58	93	38	16	594
3	25	114	56	13	581
4	53	99	39	16	571
5	32	103	45	10	503
6	33	83	38	10	535
Total	248	98	41	79	550

Table 3-2. December-February (DJF) AR family timesteps partitioned according to DJF average ELI into La Niña, Neutral or El Niño years and according to corresponding cluster. Total timesteps per phase are provided in the bottom row. Total timesteps per cluster are provided in the rightmost column. Overall total number of timesteps are at bottom right.

Cluster Number	La Niña (21 years)	Neutral (9 years)	El Niño (9 years)	Total
1	291	154	116	561
2	583	171	333	1087
3	412	148	51	611
4	253	33	316	602
5	331	16	112	459
6	147	57	123	327
Total	2004	578	1043	3625

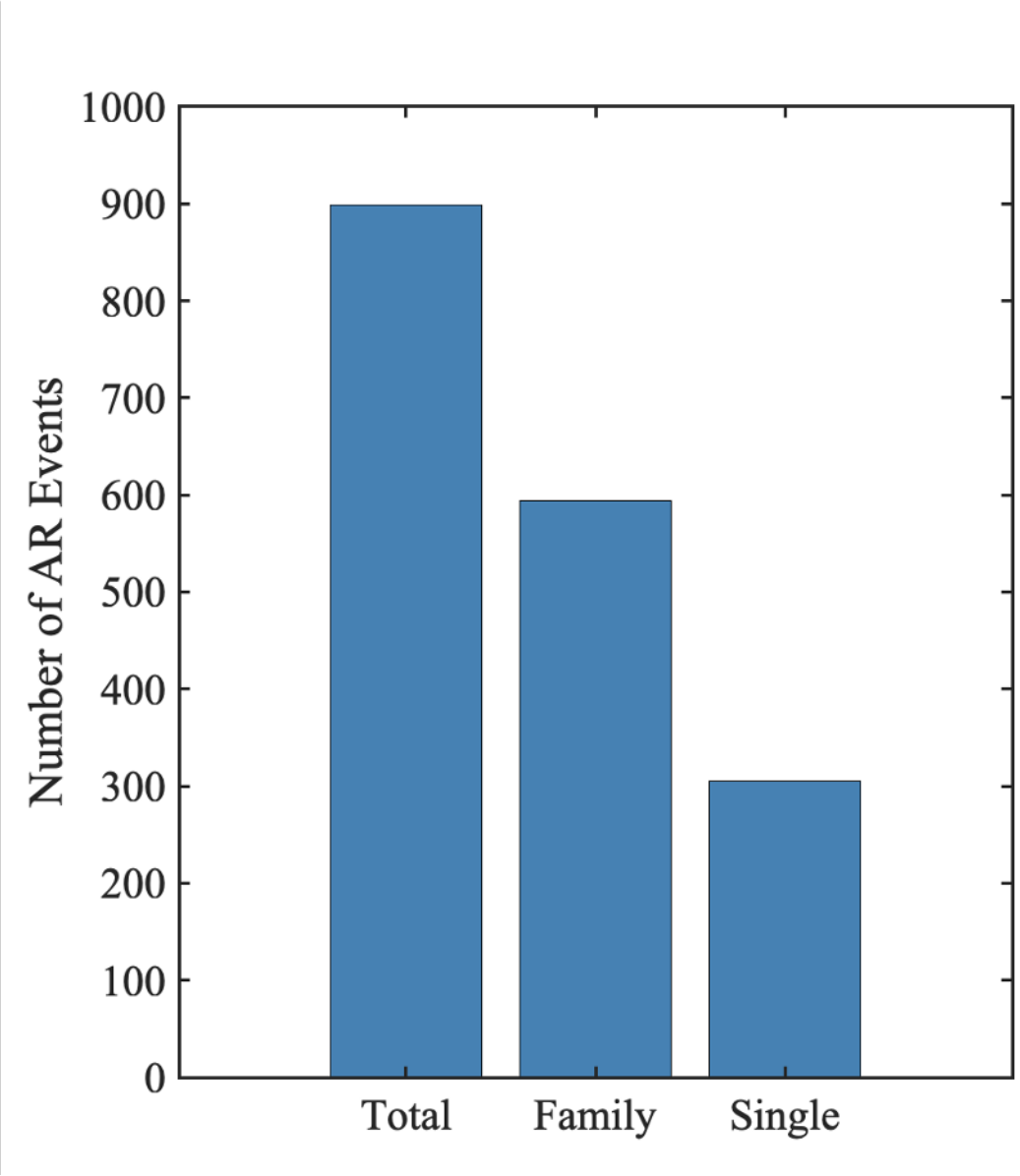

Figure 3-1. The total number of AR events across the 1980-2019 dataset and the classification of total events into those that occur within a family and those that occur as single events, according to whether the events occur within 120-hr of another.

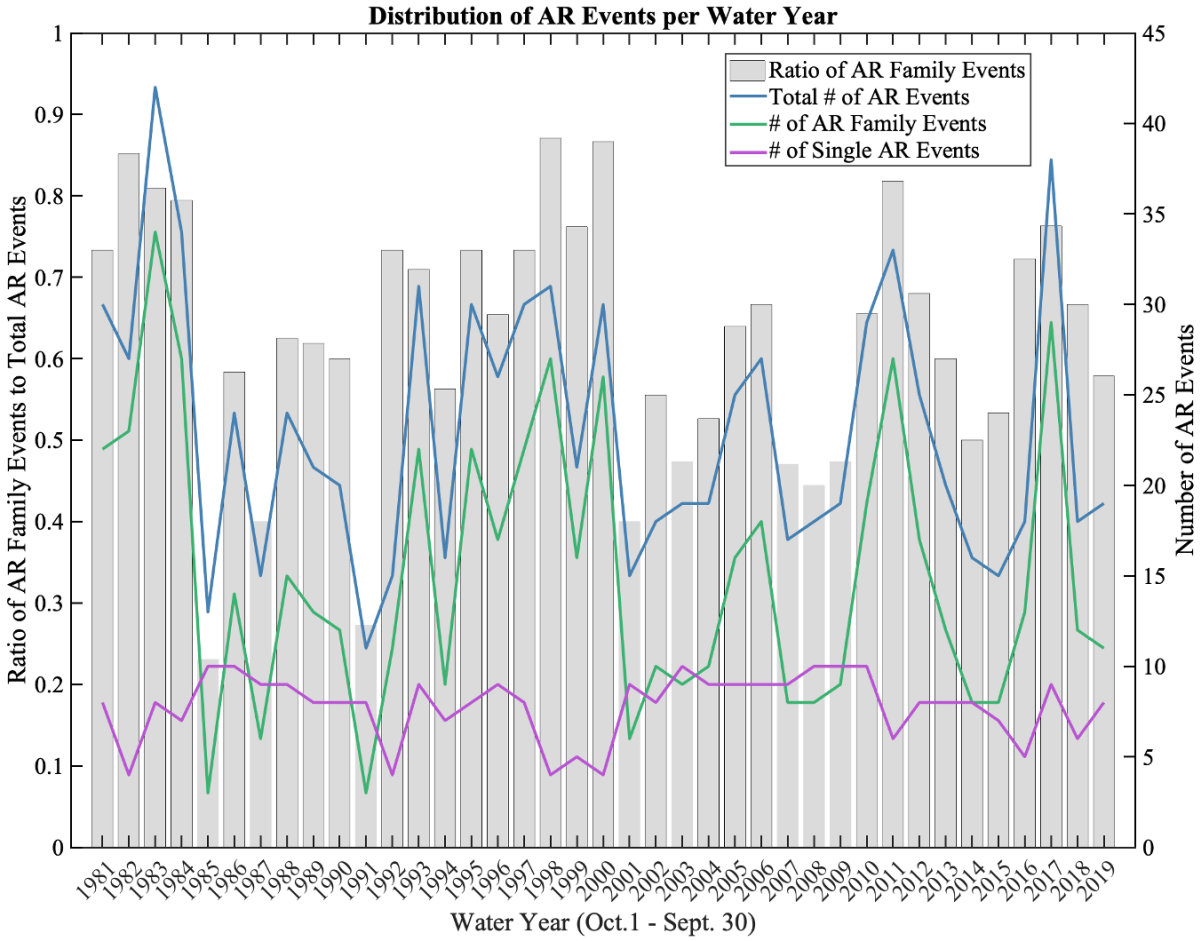

Figure 3-2. The distribution of AR events per water year by total AR events (blue), number of AR events within AR families (green) and number of single AR events (purple). The gray bars show the ratio of AR events within AR families to total AR events per water year. The bars (not) outlined in black have a (lower) higher than 0.5 ratio.

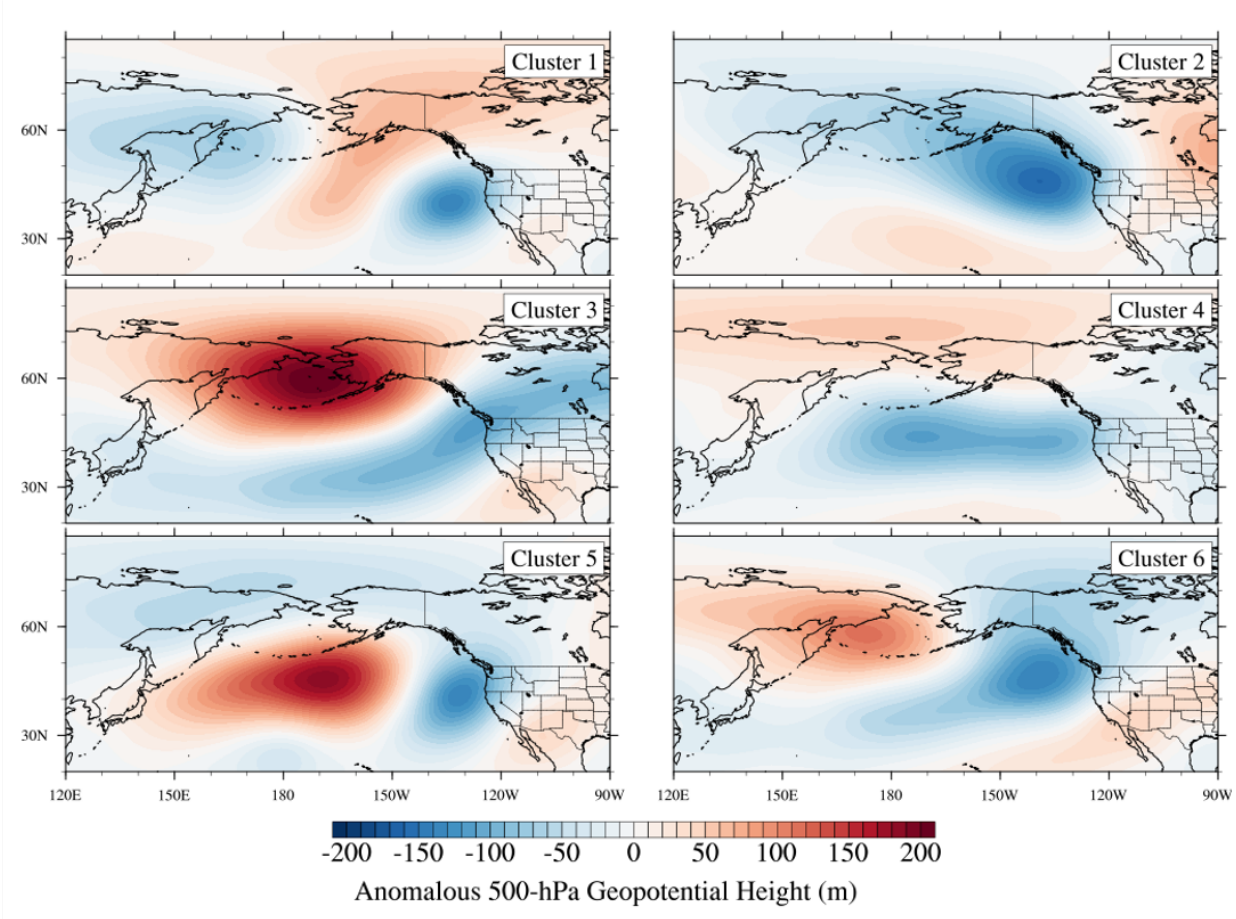

Figure 3-3. K-means clustering (k=6) on anomalous 500-hPa geopotential heights (shaded, m) for all timesteps within AR families. Cluster 1: n=1524, Cluster 2: n=2058, Cluster 3: n=911, Cluster 4: n=1681, Cluster 5: n=1160, Cluster 6: n=990.

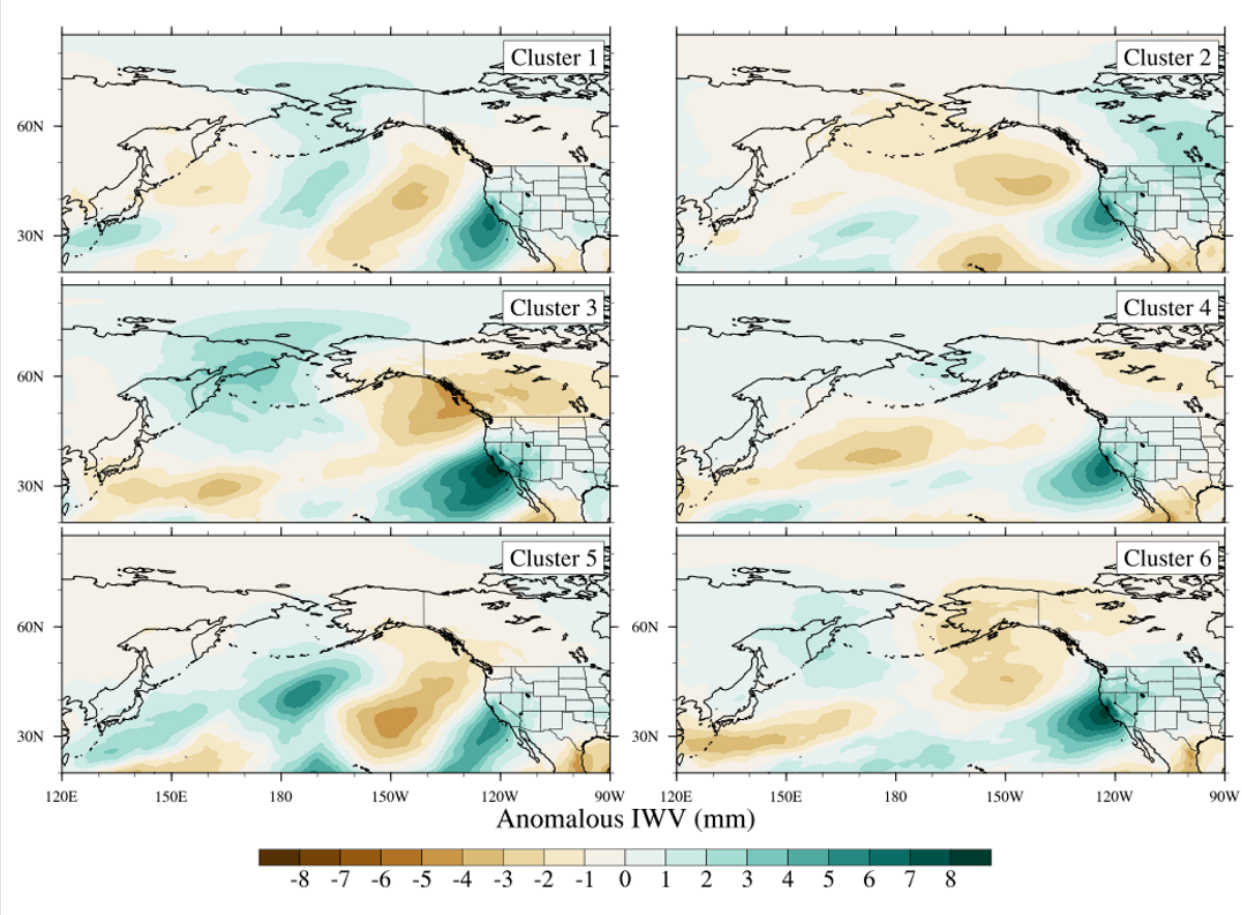

Figure 3-4. For the clusters identified in Figure 3, the associated anomalous IWV (shaded, mm) at the corresponding time.

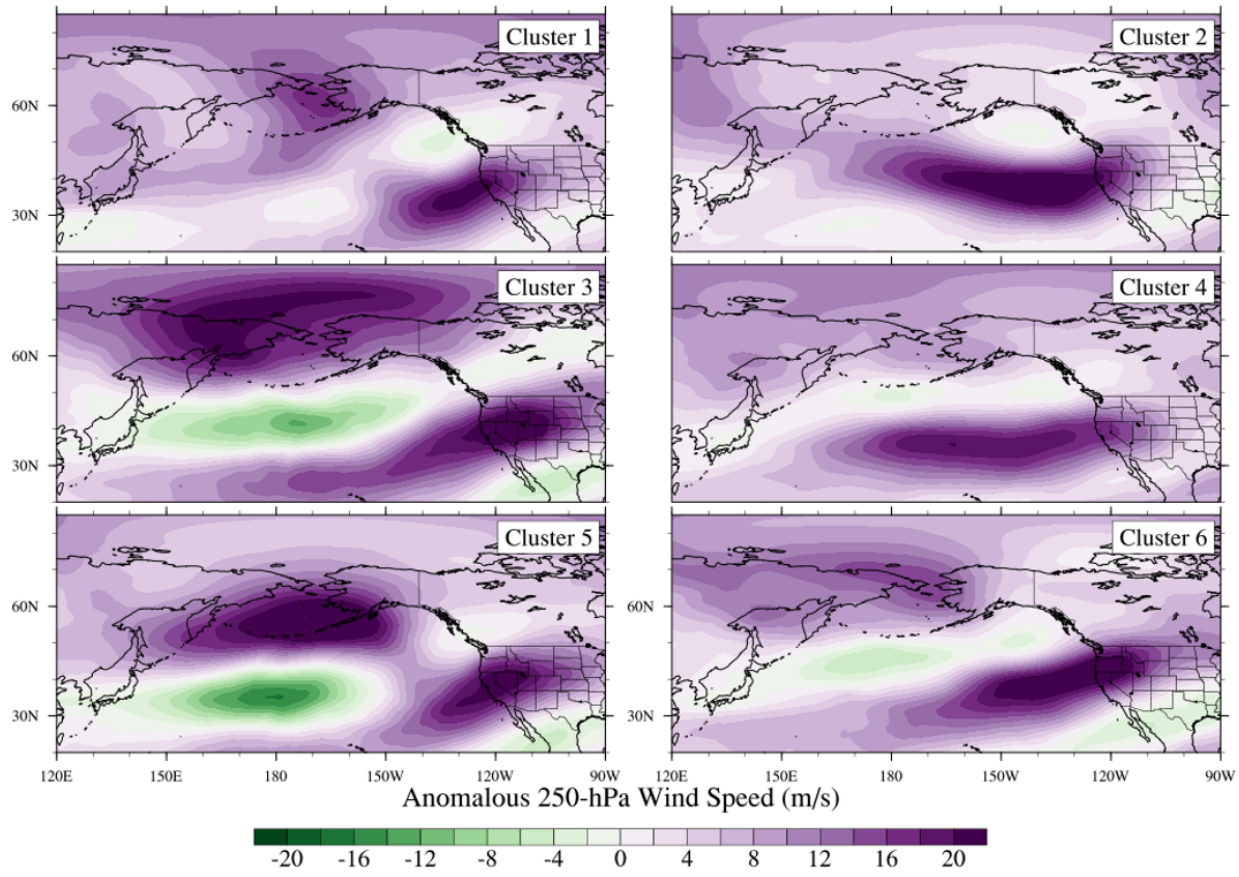

Figure 3-5. For the clusters identified in Figure 3, the associated anomalous 250-hPa wind speed (shaded, m/s) at the corresponding time.

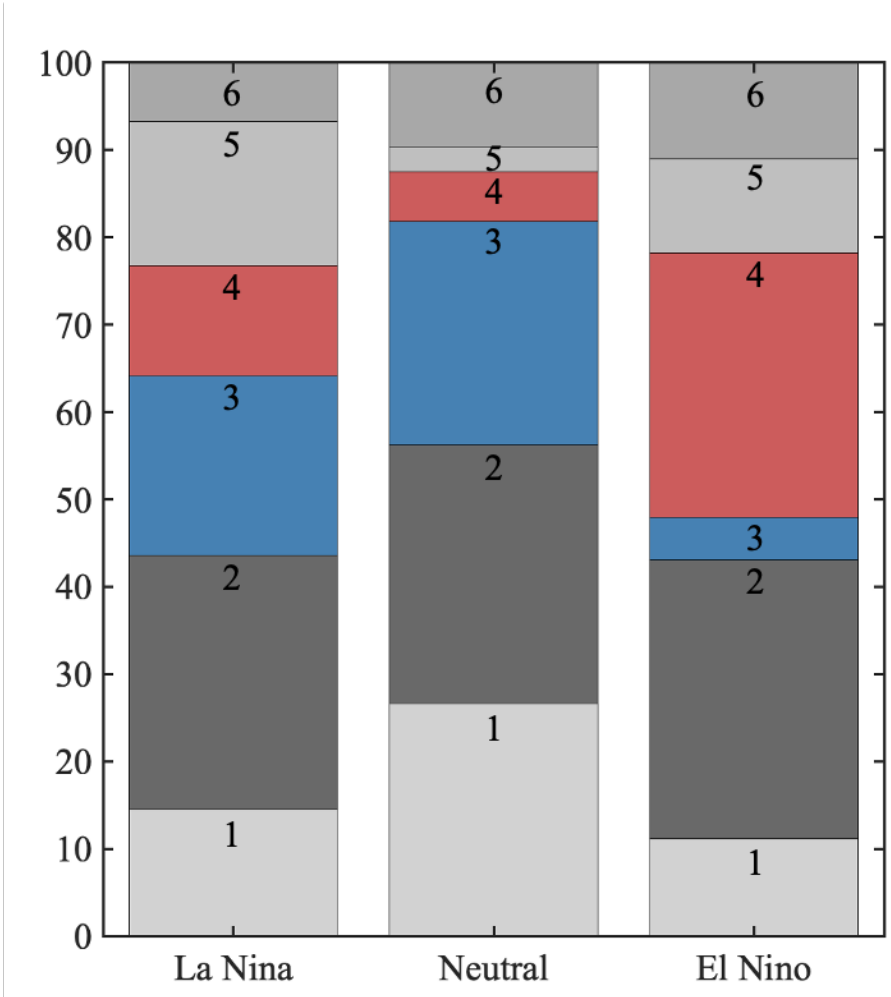

Figure 3-6. The fraction of DJF timestep occurrence per cluster compared to the total DJF timesteps within each ENSO phase (La Niña, Neutral, El Niño). Exact values in fraction are found in Table 3-2.

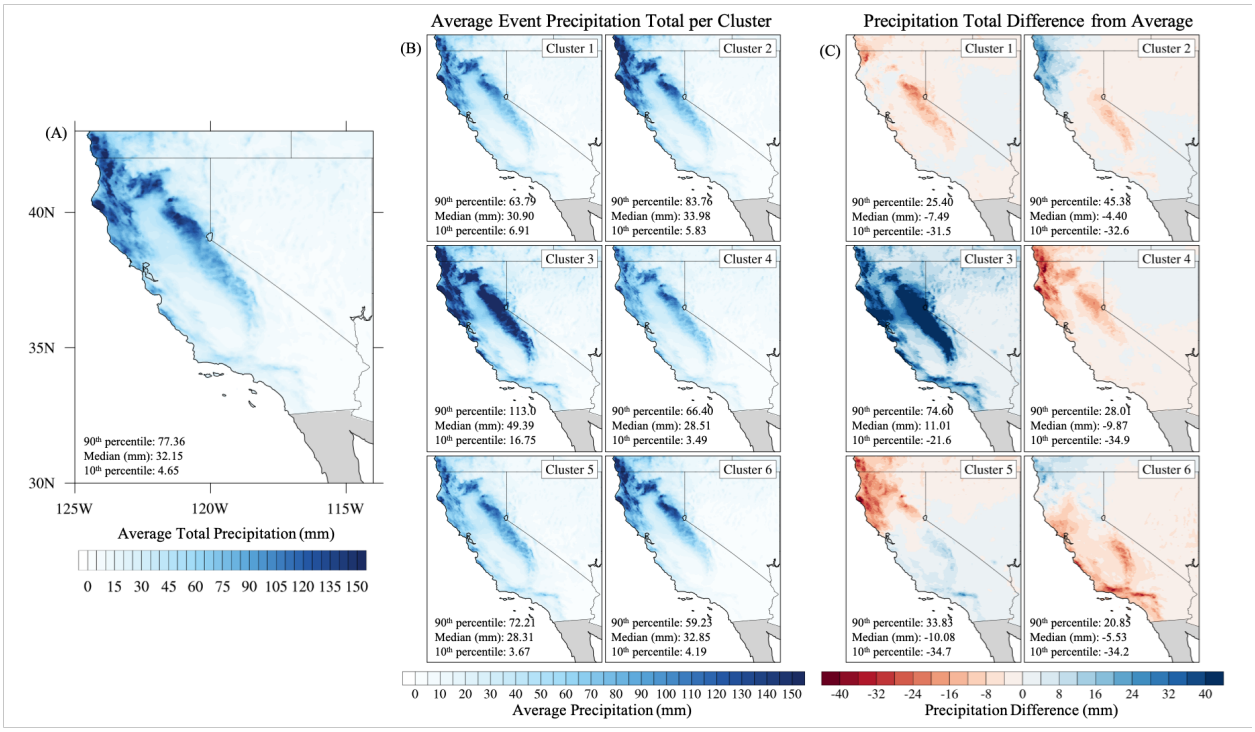

Figure 3-7. Average precipitation total (mm), for (A) all AR family events, (B) AR family events defined by mode cluster, (C) difference between each cluster average (B) and all AR family event average (A). For each cluster the 90th percentile, median and 10th percentile shown.

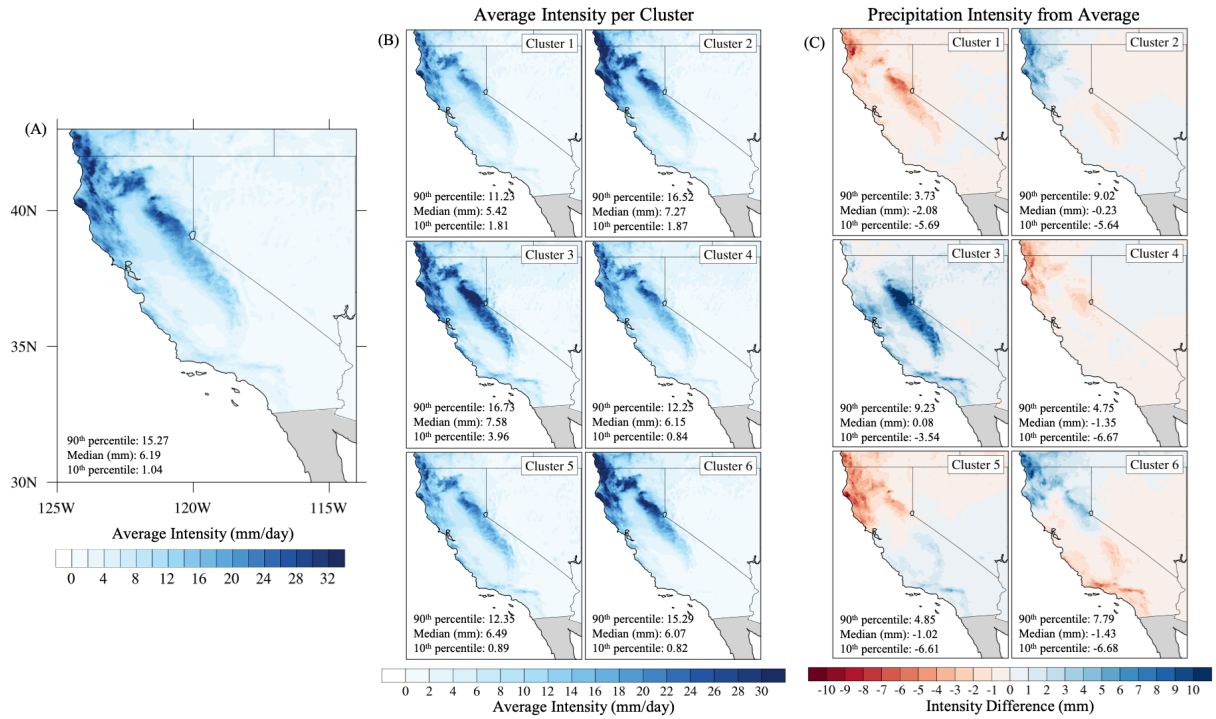

Figure 3-8. Average intensity, defined as the precipitation total divided by event duration, for (A) all AR family events, (B) AR family events defined by mode cluster, (C) difference between each cluster average (B) and all AR family event average (A). For each cluster the 90th percentile, median and 10th percentile shown.

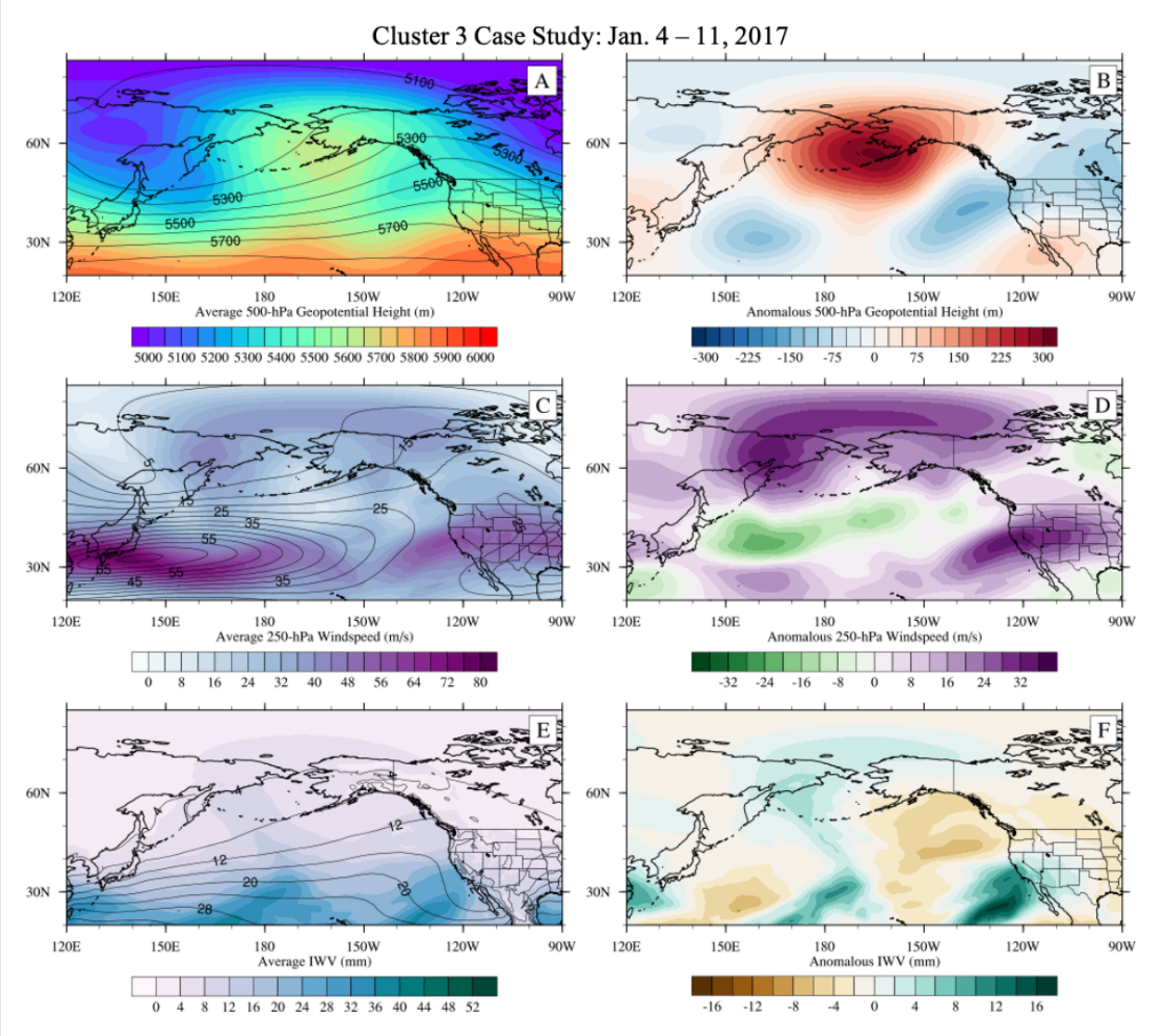

Figure 3-9. Average conditions for the Cluster 3 case study during January 4-11, 2017 (left panels, shaded) and DJF climatology (contours) of (A) 500-hPa geopotential height (m), (C) 250-hPa windspeed (m/s), and (E) IWV (mm). Anomalous conditions over the case study from a DJF climatology (right panels, shaded) of (B) 500-hPa geopotential heights, (D) 250-hPa windspeed (m/s) and (F) IWV (mm).

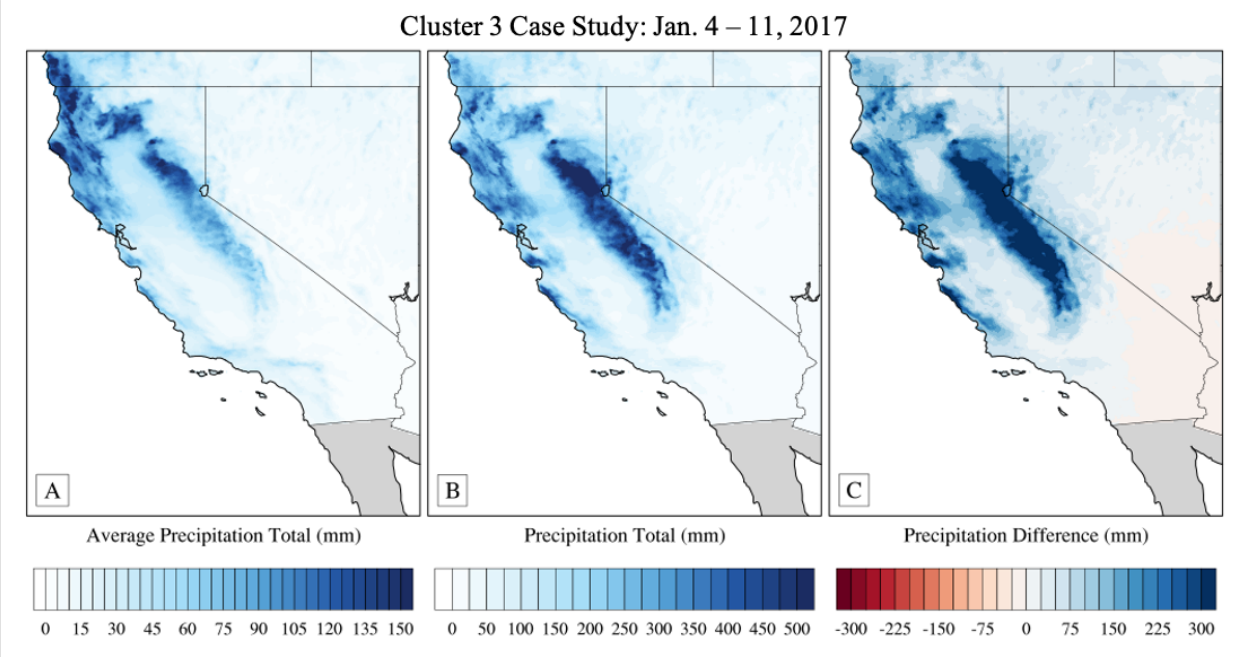

Figure 3-10. (A) Average total precipitation from all AR family events from WY 1981-2019. (B) Precipitation sum of Cluster 3 case study from January 4-11, 2017. (C) Precipitation difference between the case study (B) and the average of all AR families (A).

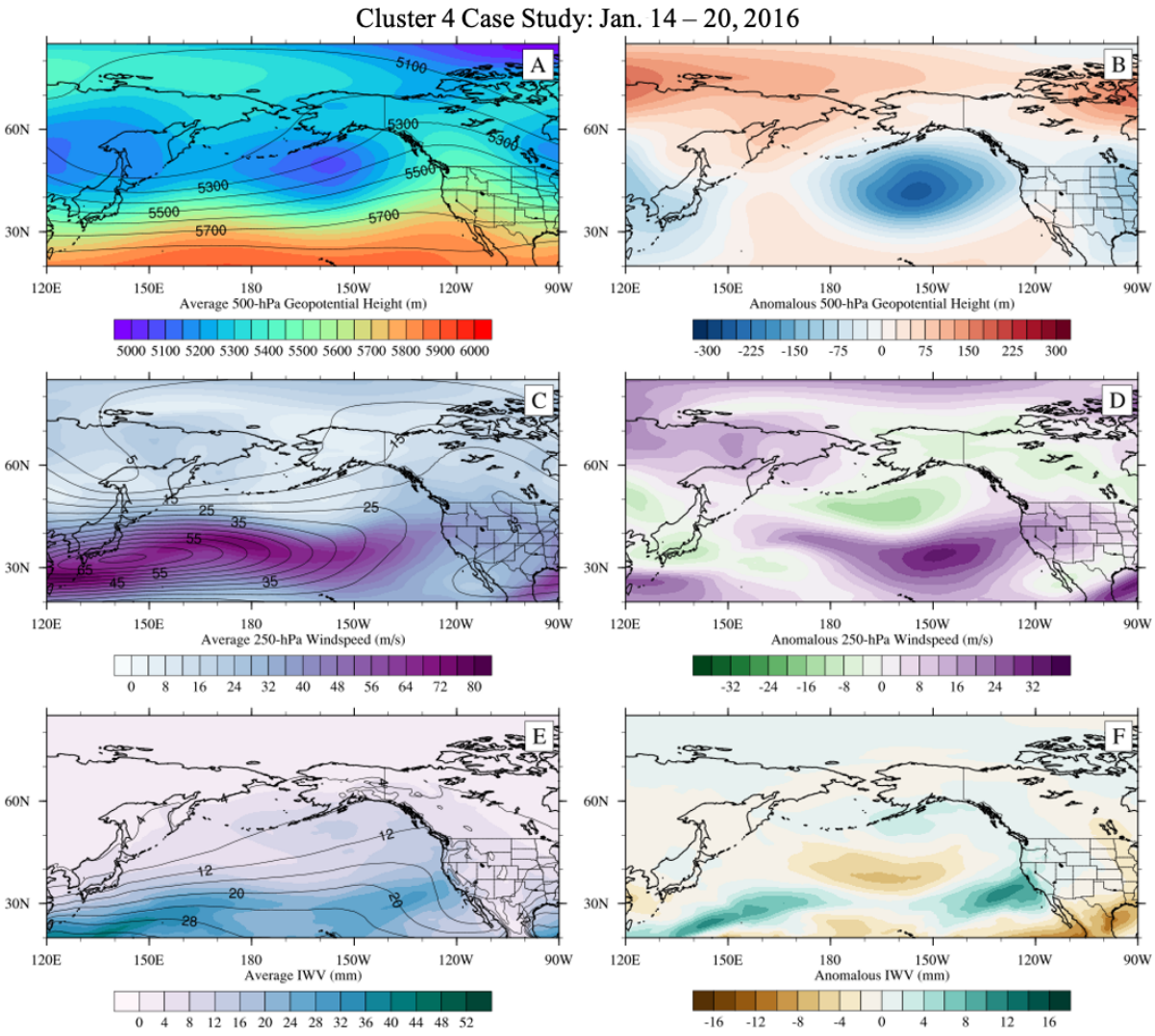

Figure 3-11. Average conditions for the Cluster 4 case study during January 14-20, 2016 (left panels, shaded) and DJF climatology (contours) of (A) 500-hPa geopotential height (m), (C) 250-hPa windspeed (m/s), and (E) IWV (mm). Anomalous conditions over the case study from a DJF climatology (right panels, shaded) of (B) 500-hPa geopotential heights, (D) 250-hPa windspeed (m/s) and (F) IWV (mm).

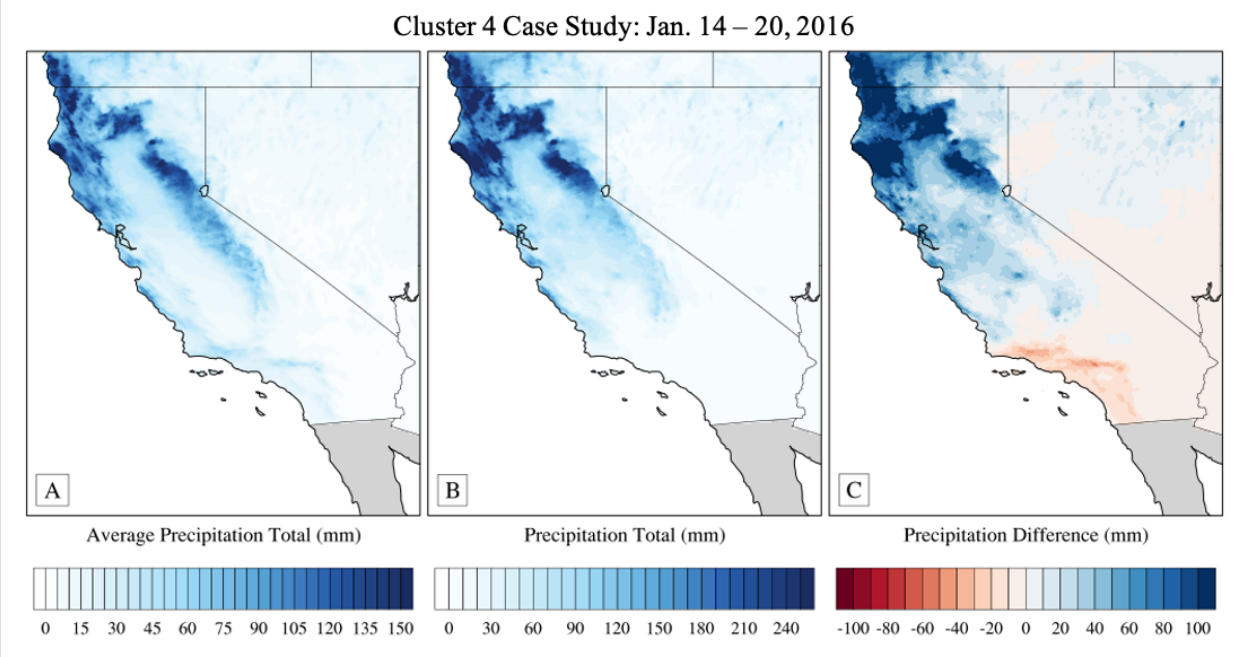

Figure 3-12. (A) Average total precipitation from all AR family events from WY 1981-2019. (B) Precipitation sum of Cluster 4 case study from January 14-20, 2016. (C) Precipitation difference between the case study (B) and the average of all AR families (A).

3.6 References

AghaKouchak, A., L. Cheng, O. Mazdiyasni, and A. Farahmand, 2014: Global warming and changes in risk of concurrent climate extremes: Insights from the 2014 California drought. *Geophys. Res. Lett.*, **41**, 8847–8852, https://doi.org/10.1002/2014GL062308.

Alexander, M. A., M. Newman, J. R. Lanzante And, N.-C. Lau, and J. D. Scott, 2002: The Atmospheric Bridge: The Influence of ENSO Teleconnections on Air-Sea Interaction over the Global Oceans. *J. Clim.*, **15**, 2205–2231.

Bao., J.W., S.A. Michelson, P.J. Neiman, F.M. Ralph, and J.M. Wilczak, 2006: Interpretation of Enhanced Integrated Water Vapor Bands Associated with Extratropical Cyclones: Their Formation and Connection to Tropical Moisture. *Mon. Wea. Rev.,* **134**, 1063-1080, doi: 10.1175/MWR3123.1.

Barton, N. P., and A. W. Ellis, 2009: Variability in wintertime position and strength of the North Pacific jet stream as represented by re-analysis data. *Int. J. Climatol.*, **29**, 851-862, doi: 10.1002/joc.1750.

Benedict, J. J., A. C. Clement, and B. Medeiros, 2019: Atmospheric Blocking and Other Large-Scale Precursor Patterns of Landfalling Atmospheric Rivers in the North Pacific: A CESM2 Study. *J. Geophys. Res. Atmos.*, **124**, 11330–11353, https://doi.org/10.1029/2019JD030790.

Bjerknes, J., Solberg, H., 1922: Life Cycle of Cyclones and the Polar Front Theory of Atmospheric Circulation. *Geof. Publ.*, **3**, 3–18.

Cayan, D. R., K. T. Redmond, and L. G. Riddle, 1999: ENSO and Hydrologic Extremes in the Western United States. *J. Clim.*, **12**, 2881–2893.

Daly, C., R. P. Neilson, and D. L. Phillips, 1994: A statistical-topographic model for mapping climatological precipitation over mountainous terrain. *J. Appl. Meteor.*, **33**, 140-158.

Daly, C., G. H. Taylor, W. P. Gibson, T. W. Parzybok, G. L. Johnson, and P. Pasteris, 2001: High-quality spatial climate data sets for the United States and beyond. *Trans. Amer. Soc. Agri. Eng.*, **43**, 1957-1962.

Daly, C., W. P. Gibson, G. H. Taylor, G. L. Johnson, and P. Pasteris, 2002: A knowledge-based approach to statistical mapping of climate. *Climate Res.*, 22, 99–113.

Dettinger, M. D., F. M. Ralph, T. Das, P. J. Neiman, and D. R. Cayan, 2011: Atmospheric Rivers, Floods and the Water Resources of California. *Water*, **3(2)**, 445-478, doi:10.3390/w3020445.

Diday, E., J. C. Simon, 1976: *Digital Pattern Recognition*. Springer, 208 pp.

Falkena, S. K. J., J. de Wiljes, A. Weisheimer, and T. G. Shepherd, 2019: *Revisiting the Identification of Wintertime Atmospheric Circulation Regimes in the Euro-Atlantic Sector*. http://arxiv.org/abs/1912.10838.

Fereday, D. R., J. R. Knight, A. A. Scaife, C. K. Folland, and A. Philipp, 2008: Cluster analysis of North Atlantic-European circulation types and links with tropical Pacific Sea surface temperatures. *J. Clim.*, **21**, 3687–3703, https://doi.org/10.1175/2007JCLI1875.1.

Fish, M. A., A. M. Wilson, and F. M. Ralph, 2019: Atmospheric river families: Definition and associated synoptic conditions. *J. Hydrometeorol.*, **20**, 2091–2108, https://doi.org/10.1175/JHM-D-18-0217.1.

Gershunov, A., and T. P. Barnett, 1998: Interdecadal Modulation of ENSO Teleconnections. *Bull. Am. Meteorol. Soc.*, **79**, 2715–2726.

Gelaro, R., W. McCarty, M. J. Suarez, R. Todling, A. Molod, L. Takacs, C. A. Randles, A. Darmenov, M. G. Bosilovich, R. Reichle, K. Wargan, L. Coy, R. Cullather, C. Draper, S. Akella, V. Buchard, A. Conaty, A. M. da Silva, W. Gu, G.-K. Kim, R. Koster, R. Lucchesi, D. Merkova, J. E. Nielsen, G. Partyka, S. Pawson, W. Putman, M. Reinecker, S. D. Schubert, M. Sienkiewicz and B. Zhao, 2017: The Modern-Era Retrospective Analysis for Research and Applications, Version 2 (MERRA-2). *J. Climate*, **30**, 5419-5454, doi:10.1175/JCLI-D-16-0758.1.

Gibson, P. B., P. Uotila, S. E. Perkins-Kirkpatrick, L. V. Alexander, and A. J. Pitman, 2016: Evaluating synoptic systems in the CMIP5 climate models over the Australian region. *Clim. Dyn.*, **47**, 2235–2251, https://doi.org/10.1007/s00382-015-2961-y.

——, S. E. Perkins-Kirkpatrick, P. Uotila, A. S. Pepler, and L. V. Alexander, 2017: On the use of self-organizing maps for studying climate extremes. *J. Geophys. Res.*, **122**, 3891–3903, https://doi.org/10.1002/2016JD026256.

Griffin, K. S., and J. E. Martin, 2017: Synoptic features associated with temporally coherent modes of variability of the North Pacific jet stream. *J. Clim.*, **30**, 39–54, https://doi.org/10.1175/JCLI-D-15-0833.1.

Guan, B., and D. E. Waliser, 2015: Detection of atmospheric rivers: Evaluation and application of an algorithm for global studies. *Geophys. Res. Lett.*, **120**, 12514-12535, doi:10.1002/2015JD024257.

Guan, B., and D. E. Waliser, 2017: Atmospheric rivers in 20 year weather and climate simulations: A multimodel, global evaluation. *J. Geophys. Res.*, **122**, 5556-5581, doi:10.1002/2016JD026174.

Guan, B., D. E. Waliser, and F. Martin Ralph, 2018: An intercomparison between reanalysis and dropsonde observations of the total water vapor transport in individual atmospheric rivers. *J. Hydrometeorol.*, **19**, 321–337, https://doi.org/10.1175/JHM-D-17-0114.1.

Hakim, G. J., 2003: Developing wave packets in the North Pacific storm track. *Mon. Weather Rev.*, **131**, 2824–2837, https://doi.org/10.1175/1520-0493(2003)131<2824:DWPITN>2.0.CO;2.

Hart, R. and R. Grumm, 2001: Using normalized climatological anomalies to rank synoptic-scale events objectively. *Mon. Wea. Rev.,* **129**, 2426-2442, doi: 10.1175/1520-0493(2001)129<2426:UNCATR>2.0.CO;2.

Horel, J.D., and J. M. Wallace, 1981: Planetary-scale atmospheric phenomena associated with the Southern Oscillation. *Mon. Wea. Rev.,* **109**, 813-829, https://doi.org/10.1175/1520-0493(1981)109<0813:PSAPAW>2.0.CO;2.

Huang, B., P. W. Thorne, V. F. Banzon, T. Boyer, G. Chepurin, J. H. Lawrimore, M. J. Menne, T. M. Smith, R. S. Vose and H-M. Zhang, 2017: Extended reconstructed Sea surface temperature, Version 5 (ERSSTv5): Upgrades, validations, and intercomparisons. *J. Clim.*, **30**, 8179–8205, https://doi.org/10.1175/JCLI-D-16-0836.1.

Huang, X., A. D. Hall, and N. Berg, 2018: Anthropogenic Warming Impacts on Today's Sierra Nevada Snowpack and Flood Risk. *Geo. Res. Lett.* **45**, 6215-6222, https://doi.org/10.1029/2018GL077432.

Van Den Hurk, B., E. Van Meijgaard, P. De Valk, K. J. Van Heeringen, and J. Gooijer, 2015: Analysis of a compounding surge and precipitation event in the Netherlands. *Environ. Res. Lett.*, **10**, https://doi.org/10.1088/1748-9326/10/3/035001.

Jiang, N., 2011: A new objective procedure for classifying New Zealand synoptic weather types during 1958-2008. *Int. J. Climatol.*, **31**, 863–879, https://doi.org/10.1002/joc.2126.

Kirono, D. G. C., K. J. Hennessy, and M. R. Grose, 2017: Increasing risk of months with low rainfall and high temperature in southeast Australia for the past 150 years. *Clim. Risk Manag.*, **16**, 10–21, https://doi.org/10.1016/j.crm.2017.04.001.

Lackmann, G. M., and J. R. Gyakum, 1996: The synoptic- and planetary-scale signatures of precipitating systems over the mackenzie river basin. *Atmos. - Ocean*, **34**, 647–674, https://doi.org/10.1080/07055900.1996.9649581.

Lackmann, G. M., and J. R. Gyakum, 1999: Heavy Cold-Season Precipitation in the Northwestern United States: Synoptic Climatology and an Analysis of the Flood of 17-18 January 1986. *Wea. Forecasting,* **14**, 687-700.

Lamjiri, M. A., M. D. Dettinger, F. M. Ralph and B. Guan, 2017: Hourly storm characteristics along the U.S. West Coast: Role of atmospheric rivers in extreme precipitation. *Geophys. Res. Lett.*, **44**, 7020-7028, doi:10.1002/2017GL074193.

Lee, S., S. B. Feldstein, 2013: Detecting ozone- and greenhouse gas-driven wind trends with observational data. *Sci.*, **339**, 563-567, doi: 10.1126/science.1225154.

Leonard, M., S. Westra, A. Phatak, M. Lambert, B. van den Hurk, K. McInnes, J. Risbey, S. Schuster, D. Jakob, and M. Stafford-Smith, 2014: A compound event framework for understanding extreme impacts. *Wiley Interdiscip. Rev. Clim. Chang.*, **5**, 113–128, https://doi.org/10.1002/wcc.252.

Mailier, P. J., D. B. Stephenson, C. A. T. Ferro, and K. I. Hodges, 2006: Serial Clustering of extratropical cyclones. *Mon. Wea. Rev.,* **134**, 2224-2240, doi:10.1175/MWR3160.1.

Martin, A. C., F. M. Ralph, A. Wilson, L. Dehaan, and B. Kawzenuk, 2019: Rapid cyclogenesis from a mesoscale frontal wave on an atmospheric river: Impacts on forecast skill and predictability during atmospheric river landfall. *J. Hydrometeorol.*, **20**, 1779–1794, https://doi.org/10.1175/JHM-D-18-0239.1.

Martius, O., S. Pfahl, and C. Chevalier, 2016: A global quantification of compound precipitation and wind extremes. *Geophys. Res. Lett.*, **43**, 7709–7717, https://doi.org/10.1002/2016GL070017.

Mason, S. J., and L. Goddard, 2001: *Probabilistic precipitation anomalies associated with ENSO*. *Bull. Amer. Meteor. Soc.*, 82, 619–638.

Mccabe, G. J., and M. D. Dettinger, 1999: DECADAL VARIATIONS IN THE STRENGTH OF ENSO TELECONNECTIONS WITH PRECIPITATION IN THE WESTERN UNITED STATES. *Int. J. Clim.*, **19**, 1399–1410.

McPhaden, M. J., S. E. Zebiak, and M. H. Glantz, 2006: ENSO as an Integrating Concept in Earth Science. *Sci.*, **314**, 1740-1745, doi: 10.1126/science.1132588.

Moore, B. J., A. B. White, D. J. Gottas, and P. J. Neiman, 2020: Extreme Precipitation Events in Northern California during Winter 2016–17: Multiscale Analysis and Climatological Perspective. *Mon. Weather Rev.*, **148**, 1049–1074, https://doi.org/10.1175/mwr-d-19-0242.1.

Moron, V., A. W. Robertson, M. N. Ward, and O. Ndiaye, 2008: Weather types and rainfall over Senegal. Part I: Observational analysis. *J. Clim.*, **21**, 266–287, https://doi.org/10.1175/2007JCLI1601.1.

Mundhenk, B.D., E.A. Barnes, and E.D. Maloney, 2016: All-Season Climatology and Variability of Atmospheric River Frequencies over the North Pacific. *J. Climate*, **29**, 4885-4903, doi: 10.1175/JCLI-D-15-0655.1.

Namias, J., 1950: The Index Cycle and Its Role in the General Circulation. *J. Meteorol.*, **7**, 130–139, https://doi.org/10.1175/1520-0469(1950)007<0130:ticair>2.0.co;2.

Neiman, P. J., B. J. Moore, A. B. White, G. A. Wick, J. Aikins, D. L. Jackson, J. Ryan Spackman, and F. Martin Ralph, 2016: An airborne and ground-based study of a long-lived and intense atmospheric river with mesoscale frontal waves impacting California during CalWater-2014. *Mon. Weather Rev.*, **144**, 1115–1144, https://doi.org/10.1175/MWR-D-15-0319.1.

Oakley, N. S., J. T. Lancaster, B. J. Hatchett, J. Stock, F. M. Ralph, S. Roj, and S. Lukashov, 2018: A 22-year climatology of cool season hourly precipitation thresholds conducive to shallow landslides in California. *Earth Interact.*, **22**, https://doi.org/10.1175/EI-D-17-0029.1.

Palmer, T. N., and J. Räisänen, 2002: Quantifying the risk of extreme seasonal precipitation events in a changing climate. *Nature*, **415**, 512–514, https://doi.org/10.1038/415512a.

Patricola, C. M., J. P. O'Brien, M. D. Risser, A. M. Rhoades, T. A. O'Brien, P. A. Ullrich, D. A. Stone, and W. D. Collins, 2020: Maximizing ENSO as a source of western US hydroclimate predictability. *Clim. Dyn.*, **54**, 351–372, https://doi.org/10.1007/s00382-019-05004-8.

Payne, A. E., and G. Magnusdottir, 2016: Persistent landfalling atmospheric rivers over the west coast of North America. *J. Geophys. Res.*, **121**, 13,287-13,300, https://doi.org/10.1002/2016JD025549.

Philander, S., 1983: El Nino Southern Oscillation phenomena. *Nature*, **302**, 295-301, doi: 10.1038/302295a0.

Pinto, J. G., I. Gomara, G. Masato, H. F. Dacre, T. Woollings, and R. Caballero, 2014: Large-scale dynamics associated with clustering of extratropical cyclones affecting Western Europe. *J. Geophys. Res. Atmos.,* **119**, 13704-13719, doi: 10.1002/2014JD022305.

Ralph, F. M., P. J. Neiman, and G. A. Wick, 2004: Satellite and CALJET Aircraft Observations of Atmospheric Rivers over the Eastern North Pacific during the Winter of 1997/1998. *Mon. Wea. Rev.*, **132**, 1721-1745, doi:10.1175/1520-0493(2004)132<1721:SACAOO>2.0.CO;2.

Ralph, F. M., P. J. Neiman, and R. Rotunno, 2005: Dropsonde observations in low-level jets over the northeastern Pacific Ocean from CALJET-1998 and PACJET-2001: Mean vertical-profile and atmospheric-river characteristics. *Mon. Wea. Rev.,* **133**, 889–910

Ralph, F. M., P. J. Neiman, G. N. Kiladis, K. Weickmann and D. W. Reynolds, 2011: A Multiscale Observational Case Study of a Pacific Atmospheric River Exhibiting Tropical-Extratropical Connections and a Mesoscale Frontal Wave. *Mon. Wea. Rev.*, **139**, 1169-1189, doi:10.1175/2010MWR3596.1.

Ralph, F. M., T. Coleman, P. J. Neiman, R. J. Zamora, and M. D. Dettinger, 2013: Observed Impacts of Duration and Seasonality of Atmospheric-River Landfalls on Soil Moisture and Runoff in Coastal Northern California. *J. Hydrometeor.*, **14**, 443-459, doi:10.1175/JHM-D-12-076.1.

Ralph, F. M., S. F. Iarcobellis, P. J. Neiman, J. M. Cordeira, J. R. Spackman, D. E. Waliser, G. A. Wick, A. B. White, and C. Fairall, 2017: Dropsonde Observations of Total Integrated Water Vapor Transport within North Pacific Atmospheric Rivers. *J. Hydrometeor.*, **18**, 2577-2596, doi:10.1175/JHM-D-17-0036.1.

Ralph, F. M., J. J. Rutz, J. M. Cordeira, M. Dettinger, M. Anderson, D. Reynolds, L. J. Schick, and C. Smallcomb, 2019: A Scale to Characterize the strength and impacts of atmospheric rivers. *Bull. Amer. Meteor. Soc.*, doi: 10.1175/BAMS-D-18-0023.1.

Reiter, E.R., 1963: Jet-stream Meteorology. The University of Chicago Press: Chicago; 515.

Riehl, H., M. A. Alaka, C. L. Jordan, R. J. Renard, 1954: The Jet Stream, Meteorological Monograph, 2. American Meteorological Society: Boston, MA; 1–100.

Roller, C. D., J. H. Qian, L. Agel, M. Barlow, and V. Moron, 2016: Winter weather regimes in the northeast United States. *J. Clim.*, **29**, 2963–2980, https://doi.org/10.1175/JCLI-D-15-0274.1.

Ropelewski, Chester, F., Halpert, M. S., 1986: North American Precipitation and Temperature Patterns Associated with the El Nino/Southern Oscillation (ENSO). *Mon. Weather Rev.*, **114**, 2352–2362.

Rossby, C. G., and H. C. Willett, 1948: The circulation of the upper troposphere and lower stratosphere. *Sci.*, **108**, 643-652, doi: 10.1126/science.108.2815.643

Ryoo, J.M., Y. Kaspi, D.W. Waugh, G.N. Kiladis, D.E. Waliser, E.J., Fetzer, and J. Kim, 2013: Impact of Rossby Wave Breaking on U.S. West Coast Winter Precipitation during ENSO Events. *J. Climate*, **26**, 6360-6382, doi:10.1175/JCLI-D-12-00297.1.

Santoso, A., M. J. Mcphaden, and W. Cai, 2017: The Defining Characteristics of ENSO Extremes and the Strong 2015/2016 El Niño. *Rev. Geophys.*, **55**, 1079–1129, https://doi.org/10.1002/2017RG000560.

Schultz, D. M., D. Keyser, and L. F. Bosart, 1998: The Effect of Large-Scale Flow on Low-Level Frontal Structure and Evolution in Midlatitude Cyclones. *Mon. Wea. Rev.*, **126**, 1767-1791.

Sedlmeier, K., H. Feldmann, and G. Schädler, 2018: Compound summer temperature and precipitation extremes over central Europe. *Theor. Appl. Climatol.*, **131**, 1493–1501, https://doi.org/10.1007/s00704-017-2061-5.

Seneviratne, S. I., N. Nicholls, D. Easterling, C. M. Goodess, S. Kanae, J. Kossin, Y. Luo, J. McInnes, M. Rahimi, M. Reichstein, A. Sorteberg, C. Vera, and X. Zhang, 2012: Changes in climate extremes and their impacts on the natural physical environment. In: Managing the Risks of Extreme Events and Disasters to Advance Climate Change Adaptation. A Special Report of Working Groups I and II of the IPCC. *A Spec. Rep. Work. Groups I II Intergov. Panel Climate Chang.*, 109–230.

Siler, N., Y. Kosaka, S. P. Xie, and X. Li, 2017: Tropical ocean contributions to California's surprisingly dry El Niño of 2015/16. *J. Climate*, **30**, 10067–10079, https://doi.org/10.1175/JCLI-D-17-0177.1.

Trenberth, K. E., G. W. Branstator, D. Karloy, A. Kumar, N.C. Lau, and C. Ropelewski, 1998: Progress during TOGA in understanding and modeling global teleconnections associated with tropical sea surface temperatures. *J. Geo. Res.*, **103**, 14291-14324, doi: 10.1029/97JC01444.

White, A. B., B. J. Moore, D. J. Gottas, and P. J. Neiman, 2019: Winter storm conditions leading to excessive runoff above California's Oroville dam during January and February 2017. *Bull. Amer. Meteor. Soc.*, **100**, 55–69, https://doi.org/10.1175/BAMS-D-18-0091.1.

Williams, I. N., and C. M. Patricola, 2018: Diversity of ENSO Events Unified by Convective Threshold Sea Surface Temperature: A Nonlinear ENSO Index. *Geophys. Res. Lett.*, **45**, 9236–9244, https://doi.org/10.1029/2018GL079203.

Winters, A. C., L. F. Bosart, and D. Keyser, 2019: Antecedent north pacific jet regimes conducive to the development of continental U.S. extreme temperature events during the cool season. *Wea. Forecasting*, **34**, 393–414, https://doi.org/10.1175/WAF-D-18-0168.1.

Vitolo, R., D. B. Stepenson, L. M. Cook, K. Mitchell-Wallace, 2009: Serial clustering of intense European storms. *Meteorologische Zeitschrift,* **18**, 411-424, doi: 10.1127/0941-2948/2009/0393.

Zhang, Z. F. M. Ralph, and M. Zheng, 2018: The relationship between extratropical cyclone strength and atmospheric river intensity and position. *Geophys. Res. Lett.,* doi:10.1029/2018GL079071.

Zhu, Y., and R. E. Newell, 1998: A Proposed Algorithm for Moisture Fluxes from Atmospheric Rivers. *Mon. Wea. Rev.*, **126**, 725-735, doi:10.1175/1520-0493(1998)126<0725:APAFMF>2.0.CO;2.

Zscheischler, J., and S. I. Seneviratne, 2017: Dependence of drivers affects risks associated with compound events. *Sci. Adv.,* **3**.

——, S. Westra, B. J. J. M. van den Hurk, S. I. Seneviratne, P. J. Ward, A. Pitman, A. AghaKouchak, D. N. Bresch, M. Leonard, T. Wahl and X. Zhang, 2018: Future climate risk from compound events. *Nat. Clim. Chang.*, **8**, 469–477, https://doi.org/10.1038/s41558-018-0156-3.

Chapter 4

Frequency of North Pacific Persistent Anomalies and their Relation to Western US Precipitation

Abstract

Persistent weather regimes can lead to droughts, heat waves, and increased precipitation and can often be identified by persistent 500-hPa geopotential height anomalies (PAs). PAs are defined as an anomalous feature that lasts for a given duration and magnitude. This study uses atmospheric reanalysis data to identify positive and negative PAs in the North Pacific from 1981-2019. To explore the sensitivity of PA identification to various methods, three detrending methods are applied and two threshold setting methods are used. Before computing the PAs, the geopotential height data is detrended three ways, 1) daily point-based trends, 2) monthly point-based trends and 3) monthly North Pacific averaged trends. Previous studies have used fixed and varying thresholds for PA magnitude; therefore, we explore the use of point-based percentiles compared to spatially averaged percentiles. The evaluation of anomalous precipitation accumulation during California's winters, highlights the strong interannual variability. One exceptionally dry year and one exceptionally wet year, water years (WY, October 1-September 30) 2014 and 2017, respectively, are chosen for a more in-depth analysis. In both cases, the methods, whether detrending or threshold setting, greatly change the identified PA frequency and location. However, these methods lack a strong correlation to anomalous conditions in California. For meaningful relationships between North Pacific PAs and California's climate, traditional PA methods need to be altered. Five-day smoothing and a lower percentile threshold

(75th) are explored. These results start to highlight the PA characteristics expected during the multi-year drought and wettest year on record for Northern California.

4.1 Introduction

Ordinary weather events become extreme and impactful due to strong intensities and long durations. Extreme weather events occur globally, in various forms, such as extreme heat, anomalous precipitation, increased storm surge, etc. and can be comprised of one single event or multiple. The cause of impactful weather is modulated by region but typically occurs due to atmospheric blocking mechanisms (Carrera et al. 2004, Marinro et al. 2015, Breeden et al. 2020), enhanced subtropical or polar jet conditions (e.g. Griffin and Martin 2017, Winters et al. 2019) and/or persistent geopotential height anomalies (PAs, Dole and Gordon 1983, Pinheiro et al. 2019).

PAs are defined as an anomaly that persists for a specified duration above a set threshold (Dole and Gordon 1983). PAs are often associated with extreme weather events such as anomalous precipitation leading to drought or floods and extended temperature anomalies, which can result in heat waves or long-term freezing conditions. Previous studies link PAs to economic impacts; an example of such being the summer of 2010 which saw the extreme heat wave over Russia and historic flooding in Pakistan (Galarneau et al. 2012). PA analyses can also help us understand circulation regimes for current day extreme events to gain insights into future climate extremes (Hoskins and Woollings 2015, Mann et al. 2018, Miller 2019).

Wintertime PAs in the North Pacific have been extensively studied to understand the characteristics and distribution of PAs as they relate to extra-tropical cyclones and their lifecycles (Dole and Gordon 1983, Dole 1989, Dole and Black 1990). In the North Pacific,

wintertime extra-tropical cyclones are often associated with atmospheric rivers (ARs; Zhang et al. 2018). ARs are long, filamentary features of enhanced water vapor transport in the lowest 3-km of the boundary layer (Ralph et al. 2004, 2005). ARs contribute to 50-80% of California's annual precipitation accumulation, making their annual occurrence important to reach normal precipitation levels (Gershunov et al. 2017). ARs are known to be drought busters and flood makers, yet they provide a crucial amount of precipitation for steady inflow to reservoirs statewide (Dettinger et al. 2011, Dettinger 2013, Lamjiri et al. 2020). The absence of ARs can push the state into drought conditions (Dettinger et al. 2011). This interplay between too many or too few AR events combined with the Mediterranean climate of California, leads to large swings in total water year (WY; October 1-September 30) accumulation. Rapid shifts from deficient to ample precipitation was recently experienced when the multi-year drought from 2012-2016, which costed the state billions of dollars in economic damages (Lund et al. 2018), directly preceded the extreme precipitation of winter 2017, which exacerbated conditions at Oroville Dam (White et al. 2019). The extreme precipitation accumulation over WY 2017 was due to periods of successive AR events, termed AR families (Fish et al. 2019). This interannual volatility in anomalous precipitation is expected to increase 25-100% by the end of the twenty-first century (Swain et al. 2018).

This study aims to apply PA methodologies to the North Pacific across known dry and wet years to investigate meaningful relationships between PA frequency, anomalous precipitation along the West Coast and the presence or lack of AR families. In the sections that follow, the different detrending methods, smoothing, anomaly calculation and methods for determining the PA magnitude threshold are presented, followed by a description of the PA identification methodology. We then describe the results of our PA analysis, including the

sensitivities to detrending and magnitude selection, relationships between PAs, precipitation and AR families and ideal method choices for investigating PAs impactful to California.

4.2 Methods

a. Detrending, Smoothing, and Anomaly Calculation

The Modern-Era Retrospective analysis for Research and Applications, Version 2 (MERRA-2) dataset (Gelaro et al. 2017) was used to detrend and identify persistent anomalies, defined in section 4.2.c, in the 500-hPa geopotential height field. The MERRA-2 dataset was used for its high spatial resolution, 0.625°x0.5° (longitude-latitude), improved representation of extreme precipitation and length of analysis period.

Three unique detrending methods were applied to understand how different methods impact residual trends. The methods are as follows: daily, monthly and North Pacific-averaged detrending. The daily detrending, calculates a daily trend, y=mx, based on the 39-year MERRA-2 reanalysis period, at each latitude and longitude point. This daily trend, which represents the increase in geopotential heights due to global warming (Fig. 4-1), is then removed from each day's average 500-hPa geopotential height resulting in a detrended dataset (i.e., a point-based trend calculated across all October 1 days is removed from all associated October 1 days and points). The monthly detrending, calculates a monthly trend, y=mx, at each latitude and longitude point. The monthly trend is then removed from each day's average 500-hPa geopotential height within the associated month (i.e., at each point the October trend is removed from the associated points for all days October 1-31). The North Pacific-average detrending, herein referred to as NP detrending, is based on the monthly detrending method above. For each month, the trend is calculated at each latitude and longitude point, then averaged across the

North Pacific, defined as 30-60°N, 120-240°W (Fig. 4-1). The monthly North Pacific-averaged trend is then removed from each day's average 500-hPa geopotential height field (i.e., the average NP October trend is removed from each point for all days in October).

Each of these methods creates a unique detrended dataset in which daily anomaly heights are calculated. Monthly averages calculated on each detrended 500-hPa geopotential height dataset are removed from each day's detrended value to create a detrended daily 500-hPa geopotential height anomaly.

For both the daily and monthly detrending methods, the raw 500-hPa geopotential heights are first latitude weighted according to the following,

$$W = \sqrt{cos\ (\phi * \frac{\pi}{180})}\ ,$$

where W is the weight and ϕ is latitude. For the NP detrending method, the trend calculation and detrending occurs before the latitude weighting is applied. Sensitivity tests for the daily and monthly detrending, show that latitude weighting prior or after detrending does not change the outcome, but it is required to be performed post-detrending for the NP detrending method.

A 5-day running average performed in time was additionally applied to each latitude and longitude point in the monthly detrended dataset for smoothed detrended data.

b. Persistent Anomaly Identification

Each detrending method creates three datasets of anomalous 500-hPa geopotential heights. To determine whether an anomaly is persistent or not, a magnitude and duration need to be specified. While some studies use fixed magnitude thresholds (e.g. Dole and Gordon 1983) others use monthly varying thresholds (Miller 2019). For this study, we applied a monthly percentile-based threshold calculated two ways, 1) averaged across the North Pacific basin,

region specified in section 4.2.a, and 2) at each latitude and longitude point. Three thresholds (75^{th}, 80^{th}, 90^{th}) were evaluated for each detrending method but only the 90^{th} percentile results are shown and discussed here. As defined by previous studies (e.g. Dole and Gordon 1983, Miller 2019), the duration of each anomaly must equal or exceed a five-day duration. The magnitude and duration thresholds are then applied to all points and calculated throughout a water year (WY; October 1 – September 30) for a catalog of persistent 500-hPa geopotential height anomalies (PAs) from 1981-2019.

c. Precipitation Data

To evaluate the relationship between PAs in the North Pacific and interannual precipitation variability, the PRISM daily precipitation data from 1981-2019 are used. PRISM data are generated via a digital elevation model and point-based observations to create a gridded estimate of precipitation (Daly et al. 1994, 2001, 2002). Besides the PRISM dataset's 4-km spatial resolution, this precipitation dataset is used for its increased precipitation accuracy in mountainous regions such as the western US.

4.3 Results

Having a Mediterranean climate, California receives the majority of its precipitation between October-March. However, California also experiences the largest of all states in year-to-year variability in the amount of precipitation it receives (Dettinger et al. 2011). From WY 1982-2019, the total amount of precipitation California receives each year varies (Fig. 4-2). This variability is more evident when we analyze anomalous precipitation totals from average October-March accumulation, which show many years experience either a 50% reduction in

normal precipitation accumulation or a 150% increase (Fig. 4.3). Two WYs in the recent record stand out for the strong reduction or amplification of accumulated precipitation, WY 2014 and WY 2017, respectively.

WY 2014, from October 2013-September 2014, occurred in the middle of the most damaging multi-year drought in California's recent history (Lund et al. 2018). The winter months, October-March, often deliver the majority of the total precipitation; however, the winter of 2014 was instead characterized by a reduction in the North Pacific jet wind speed and extent, anomalously high geopotential heights across the entire North Pacific Ocean basin and less than average integrated water vapor (IWV) near coastal California (Fig. 4. 4). This WY experienced below average AR events (16) and AR families (8), defined as successive AR events (Fish et al. 2019), likely due to the higher than average geopotential heights near the California coast. Conversely, WY 2017 was characterized by a dipole through the presence of anomalously low geopotential heights off the coast of British Columbia and anomalously high geopotential heights in the central Pacific (Fig. 4-5). The North Pacific jet shifted poleward and a secondary maximum occurred off the coast of California coinciding with additional IWV near the coast. WY 2017 had the second highest number of AR events impacting California when compared to all WYs from 1981-2019. This WY also experienced the second highest number of AR families, behind WY 1983 (Fish et al. 2020 *in review*), highlighting the connection between AR families and anomalously high precipitation.

This study will use these two WYs to compare persistent anomaly frequency and its relation to anomalous precipitation in California.

a. Sensitivities to detrending and magnitude selection

Before identifying persistent anomalies in the 500-hPa geopotential height field, the raw geopotential height data needed to be detrended. This study detrended the data using three methods, 1) daily detrending per point, 2) monthly detrending per point, and 3) a North Pacific monthly average detrending. The different methods produce different trends, some which vary in magnitude and/or sign from each other (Fig. 4-6). The NP detrending created only positive trends in time with the largest, in terms of magnitude, trend occurring during the month of August, and the smallest occurring during January (Fig. 4-6 A). At a randomly selected open ocean point of 50ºN -180ºE, the average monthly trend shows a range of positive and negative trends across the months, with magnitudes larger than the NP average (Fig. 4-6 B). August still has the largest magnitude, but December is quite similar. January also continues to show the smallest trend in time, but July shows a similar magnitude and trend; however both monthly trends are negative. The daily trend shown for both the 1st of each month (Fig. 4-6 C) and the 15th of each month (Fig. 4-6 D) vary greatly from the previously discussed trends. For different days in the month, there is no general consensus to which month has a positive, negative, largest or smallest trend as they dramatically change throughout the month. These trends ultimately impact the data and final results of the PA analysis.

Another sensitivity to this study is the choice of the magnitude the PA must maintain for the entire 5-day duration. Dole and Gordon (1983) used a fixed 150-m anomaly for detection of PAs. While that choice was ideal for identifying wintertime anomalies, it minimized summer PAs. Miller (2019) chose to use the daily averaged 2σ for each point for a seasonally varying threshold. We decided to use monthly percentiles, ranging from 75th to 90th, calculated both at each point and on average across the North Pacific. The monthly North Pacific average thresholds (Table 4-1) vary month to month with peaks in winter and minima in summer,

accounting for seasonal changes. It was hypothesized that the threshold based on the North Pacific average, would highlight PAs in regions of high variability, such as the region around the Aleutian Low. The monthly point-based thresholds (Fig. 4-7 and 4-8, A) show a spatially and seasonally varying 90th percentile. The (-)90th percentile and (+)90th percentile, show different regions of higher amplitude, and a higher threshold is located in the storm track region compared to near the Aleutian Islands, respectively. Comparing the two monthly threshold methods, North Pacific average versus point-based, shows how the identification and frequency of PAs will greatly change between the two methods (Fig. 4-7 and 4-8, B). This difference further validates our hypothesis that relatively lower frequencies would occur in the North Pacific for the point-based threshold, while relatively higher frequencies would occur in the tropics for the point-based thresholds. The opposite would be true for the North Pacific average-based thresholds.

Investigating the PA fraction of days during WY 2014, a WY with anomalously low precipitation and positive geopotential height anomalies, across the three different detrending methods, based on the North Pacific averaged 90th percentile and the point-based 90th percentile, show stark differences across the methods. While all six methods, show positive PAs in the Bering Sea, the frequency, determined by the number of days above the threshold, varies (Fig. 4-9). Additionally, only the North Pacific averaged threshold showed positive PAs in the Gulf of Alaska, a region the seasonal composites showed anomalously high geopotential heights (Fig. 4-4). In both percentile determining methods, the daily detrending identifies lower frequencies of positive PAs than the monthly or NP detrending, which could be a result of the different trends applied on a daily basis, limiting the consistency between days. The representation of negative PAs greatly differs between the North Pacific averaged percentiles and point-based percentiles. With higher thresholds in the storm track region for the point-based thresholds, there are

relatively few PAs identified. Comparatively the North Pacific averaged thresholds, show moderate frequency of negative PAs in the central Pacific and Gulf of Alaska.

Alternatively, investigating the PA frequency during WY 2017, characterized by anomalously high precipitation and negative geopotential heights close to the US West coast, all methods identify different regions of PAs and at different frequencies (Fig. 4-10). Similar to WY 2014, the negative PAs frequency is lower based on the point-based thresholds, but the region identified does overlap with the higher occurring PAs identified by the North Pacific averaged threshold. The frequencies identified from the daily detrending method for both positive and negative PAs is again lower compared to the two other detrending methods. The point-based threshold identified more positive PAs in the tropical region, south of 30N, whereas the North Pacific threshold, identified more in the Bering Sea, which was hypothesized.

The identified positive and negative PAs from 1981-2019 for both the North Pacific based thresholds (Fig. 4-11) and the point-based thresholds (Fig. 4-12) shows the discernable interannual variability between WYs, suggesting implications for a relationship to anomalous precipitation and/or AR events and AR families. The temporal length of this study also allows for an analysis applied to PA trends in time. Considering each detrending method and the North Pacific averaged thresholds, trends in the average frequency and maximum frequency across the North Pacific were assessed (Fig. 4-13). The strongest, largest in magnitude, trends occurred from the daily detrended dataset, which showed on average an increase in negative PAs and decrease in positive PAs (Fig. 4-13 A, B). In comparison, the NP detrending and monthly detrending showed more neutral trends across time. The maximum frequency of positive PAs is conflicting between trends as the daily detrending has a negative trend in time while the NP detrending shows a slight positive trend with time; monthly detrending is neutral (Fig. 4-13 C,

D). The maximum occurrence of negative PAs all exhibit neutral to slightly positive trends. However, in none of these instances were the trends significant. Evaluating trends using all detrending methods for the point-based percentiles, shows similar trends as previously discussed (Fig. 4-14). Average frequency for positive PAs is decreasing while increasing for negative PAs (Fig. 4-14 A, B). Maximum frequency of positive PAs across the North Pacific increase in time or are near neutral for each detrending method (Fig. 4-14 D). The maximum frequency of negative PAs is neutral (Fig. 4-14 C), as shown from the North Pacific percentiles too. Again, these trends are not significant but where the methods agree and disagree across time is worth investigating. Previous studies also note the lack in PA trends in various regions around the world, such as Central Europe (Horton et al. 2015, Huguenin et al. 2020) and the North Pacific (Miller 2019).

b. Persistent Anomalies, Precipitation & AR Families

The majority of California's precipitation occurs between October-March. Across the state average monthly accumulations vary from ~50 mm/month to > 400 mm/month (Fig. 4-15 A). The coastal mountains of Northern California and the Sierra Nevada mountains often receive the most precipitation. WY 2014 experienced on average below normal accumulation. A per month breakdown shows the lack of precipitation during December and January attributed to the WY's deficit (Fig. 4-15 B). In comparison, WY 2017, experienced above average precipitation accumulation. Average October-March accumulation showed exceptional precipitation accumulation for October, January and February (Fig. 4-15 C). Given that much of the precipitation falls in a condensed time period, the monthly accumulations highlight how one or two months of above or below average precipitation can affect the entire WY's accumulation.

Given that the lack of precipitation is often tied to positive geopotential heights via blocks and a surplus of precipitation can be due to negative geopotential heights via low-pressure systems, we wanted to investigate the relationship between interannual PA frequency and anomalous precipitation. Unfortunately, there is not a strong correlation of North Pacific PA frequency across all detrending methods for point-based percentiles and anomalous spatially averaged precipitation over California (Fig. 4-16 A, B) nor the West Coast (CA, OR, WA; Fig. 4-16 C, D). While there are some instances where low precipitation aligns with high-frequency, positive PAs, i.e., WY 1989, it is not a robust signal across the years. During the two WYs of interest for this chapter, the large anomalous precipitation in WY 2017, is not as reflected in the negative PA frequency. Similarly, for WY 2014 a moderate occurrence of positive PAs corresponds to negatively anomalous precipitation.

To further investigate the relationship of PAs and precipitation, we tested the correlation of PAs to AR events, AR families and single AR events. The majority of California's precipitation can be attributed to AR events (Dettinger et al. 2011, Ralph et al. 2013, Lamjiri et al. 2017). AR families are successive AR events that can lead to enhanced impacts with distinguishable large-scale environments (Fish et al. 2019, Fish et al. 2020 *in review*). AR families have semi-permanent features suggesting they could be identified via the persistent anomaly analysis. Alternatively, a lack of AR families or AR events in general may suggest persistent positive geopotential heights and could relate to low precipitation accumulation. The correlation between any detrending method, total AR events, AR families, or single AR events does not produce significant results (Fig. 4-17). This could be due to the large area in this analysis, the North Pacific, or because the traditional method for identifying PAs does not relate to meaningful assessment of impactful California events.

c. Influence of smoothing on persistent anomalies

Upon discovering that traditional methods of identifying PAs do not provide significant relationships to anomalous precipitation in California, we amended the method of identifying PAs to include a 5-day smoothing prior to PA identification and including lower thresholds, such as the 75th percentile. This change was partially motivated by the PAs inability to capture the 'Ridiculously Resilient Ridge' that occurred during the multi-year drought in California from 2012-2016 (Swain et al. 2014, Swain 2015) and to better capture successive storms that could lead to increased precipitation. Smoothing the detrended data then reduces the PA threshold that needs to be maintained at each location for at least 5-days; the averaged North Pacific thresholds are shown in Table 4-2. The smoothing was computed on the monthly detrended data and PAs were calculated for the 75th and 90th percentiles using both the North Pacific average and point-based thresholds.

Evaluating WY 2014 in comparison to the previously defined method, at the 90th percentile the smoothing increases the identification of PAs in the Gulf of Alaska and over Northern California (Fig. 4-18 B, D), regions which experienced positive anomalies during this WY (Fig. 4-4 B). While the ridge and drought conditions persisted for months to years, it does become clear that a 90th percentile PA is too strict to maintain for the entirety, or even part, of this phenomenon; thus the 75th percentile was assessed in addition. While the lower threshold would increase the frequency of PAs, the location and frequency shown with both the North Pacific averaged defined thresholds and the point-based thresholds are more consistent with what was observed, especially in the Gulf of Alaska and California (Fig. 4-18 A, C). Considering the wet year, WY 2017, the frequency and location of the negative 75th percentile PAs are consistent with the large number of AR events that occurred that year (Fig. 4-19 A, C), compared to the

stricter 90th percentile (Fig. 4-19 B, D). The increased frequency of PAs south of California using the point-based thresholds, is worth noting as the point-based thresholds allow for the identification of anomalous features compared to that location's innate variability (Fig. 4-19 C). This local perspective allows for events such as the Kona low, a low-pressure system that generally persists throughout the winter months north of Hawaii (Morrison and Businger 2001, Otkin and Martin 2004, Moore et al. 2008), to be identified as PAs. This connection can be important for California precipitation as the tropical moisture exports that can be tied to Kona Low conditions can lead to AR conditions in California (Steinschneider and Lall 2015). With WY 2017, following the extreme El Niño of 2015-2016, it is interesting to note the positive PAs identified in the western Pacific, suggesting the importance of the tropics for initiating the Rossby waves that led to the multiple extreme precipitation events and AR families experienced that year (Moore et al. 2020, Fish et al. 2019). For the study's focus on California precipitation, we conclude that maintaining a 75th percentile PA most accurately captures anomalies impactful to California.

However, to best compare to the previous methods, the frequency of negative and positive PAs after smoothing at the 90th percentile from 1981-2019 for both the North Pacific averaged threshold (Fig. 4-20) and the point-based threshold (Fig. 4-21) is examined. As seen with the previous methods, there is interannual variability of the frequency of PAs, both negative and positive, continuing to hint at the application of PAs to California's impacts.

For the dry and wet year examples, we wanted to further explore the monthly evolution of PA identification and anomalous geopotential heights. Over the winter months, October-March, of WY 2014, PAs were mainly identified in the Gulf of Alaska and off the coast of California (Fig. 4-22). Both methods for determining thresholds, NP averaged or point-based,

show no PAs in the eastern Pacific for November or March. Both methods do show February had the highest occurrence of PAs, up to ~15 days/month, extending over all of California and offshore. For context, the anomalous, compared to a DJF climatology, October-March geopotential heights are shown (Fig. 4-22, right). On average October-March of this WY experienced high geopotential heights across most of the North Pacific (Fig. 4-4), a monthly breakdown shows a more nuanced relationship. For example, December and January both average positively anomalous conditions over the Gulf of Alaska region, however only January identifies 5-10 days of PAs. Comparatively, February averaged neutral to negative anomalous heights near California's coast, yet showed up to 15 days of positive PAs. This further enforces the complex relationship between PAs and California's climate.

During the wet year, WY 2017, while a lower occurrence of PAs is shown, this result is expected due to the transient nature of low-pressure systems, yet there is more alignment between PAs identified during December-February and to regions of anomalously low geopotential heights (Fig. 4-23). The PAs during January last 5-15 days, depending on location, in the downstream region of the North Pacific jet. Similarly, the region of anomalously low geopotential heights can be found off the coast of California extending into the central Pacific Ocean. By February, the PAs have shifted further south, closer to the Kona low region, and the region of anomalously low geopotential heights do as well.

Since a main focus of current PA literature is assessing whether PA frequency is changing with time, we assessed the trend of average North Pacific PA frequency and found a stronger trend for declining positive PAs (not shown) compared to the previous method (Fig. 4-13 & 4-14). Negative PAs showed neutral to slightly declining conditions (not shown), which is similar to results in the previous method (Fig. 4-13 & 4-14). While the results of all methods

suggest a declining frequency of positive PAs across the North Pacific, recognizing the large size of the domain of interest was potentially removing local trends, such as near California, the spatial distribution of PA trends is assessed. The spatial map of PA trends shows an increase in negative PAs south of the Aleutian Islands and an increase in positive PAs near the western coastline of Alaska for both the North Pacific average and point based 75th percentile PAs (Fig. 4-24). However, while the two methods show similar trends in the central North Pacific, other regions of interest, such as the eastern Pacific and tropical western Pacific, differ between the methods. The point based 75th percentile negative PAs increase at ~0.6 days/WY compared to neutral trends based on the North Pacific average 75th percentile PAs. Off the coast of California, positive PAs are shown to be declining at a rate of ~0.6 days/WY, again compared to a neutral trend for PAs identified via the North Pacific average 75th percentile. Therefore, given the study's interest in California precipitation accumulation, it is determined that smoothed data and the PA identification based on point-based 75th percentile thresholds should be used to assess local and regional PAs across the North Pacific.

4.4 Discussion and Conclusion

This study aims to relate persistent 500-hPa geopotential height anomalies (PAs) to interannual variations in California's precipitation accumulation. PAs are calculated from water years (WY; October 1-September 30) 1981-2019 to align with anomalous precipitation. This study tested the sensitivity of PA identification and frequency using different types of detrending and methods for determining the PA threshold. WYs 2014 and 2017 were used as example dry and wet years, respectively, to compare methods and results.

It is clear that the detrending method chosen, such as daily, monthly or monthly averaged over the North Pacific (NP detrending), influences this analysis. The large variations among trends across the methods impacts the resulting PAs. This study also investigated how the method to determine an optimal PA threshold changes the distribution of identified PAs. For this part of the analysis, we used a monthly North Pacific average 75th or 90th percentile and a monthly point-based 75th or 90th percentile. The North Pacific average threshold would mainly represent PAs that occurred in regions of higher variability, such as the Aleutian Low, while the point-based threshold would allow for more local anomalies to be identified, in regions such as the tropics, offshore of California or the Kona low. As hypothesized, the two methods for determining the PA threshold have implications for the frequency and location of identified PAs. In general, the North Pacific average-based threshold identifies more PAs in the Bering Sea and Gulf of Alaska, while the point-based threshold more evenly identifies PAs across the domain. For the purposes of identifying impactful PAs to California, we believe the point-based threshold is more accurate, however this goes against traditional methodologies.

Despite the sensitivities to detrending and thresholds, we did not find significant trends in PA occurrence across this time period, which is consistent with previous studies (Horton et al. 2015, Miller 2019, Huguenin et al. 2020). We also did not find significant correlations to anomalous precipitation in California or the West Coast (CA, OR, WA) or to AR events, AR families or single AR events. These results highlight the need to further develop methodologies to identify PAs impactful to California. We have begun the process to alter the traditional PA methods, such as including 5-day smoothing to still retain some aspects of the synoptic variability. A monthly breakdown of PAs and anomalous geopotential heights for the wet and dry WYs, show that generally PAs identify the same region of anomalous geopotential heights

but add information on their length and magnitude. The spatial distribution of PA trends shows regional differences highlighting the importance of point-based thresholds and analyzing small regions for PA trends.

Further work to develop a comprehensive method for identifying PAs impactful to California should continue to advance. Given that California is downstream of the North Pacific jet, a region that often sheds low pressure systems, and regions of high blocking, it is important to understand the characteristics and persistence of these features in the present climate and how they relate to anomalous precipitation accumulation. Additionally, this analysis has the potential to inform our understanding of PAs in the future.

4.5 Acknowledgements

MAF and AM were supported by grant W912HZ-15-2-0019 from the US Army Corps of Engineers and grant 4600013361 from California Department of Water Resources. DLS was supported by a joint collaboration between the Institute of the Environment and Sustainability at the University of California, Los Angeles; the Center for Climate and Weather Extremes at the National Center for Atmospheric Research; and the Nature Conservancy of California. This research was additionally supported by NSF awards 1854940 (to JD) and 1854761 (to DLS). We gratefully acknowledge the availability of the MERRA-2 reanalysis dataset available through the National Aeronautics and Space Administration (NASA) Global modeling and Assimilation Office. These data are available at MDISC, which is managed by the NASA Goddard Earth Sciences Data and Information Services Center. We would also like to acknowledge high-performance computing support from Cheyenne provided by NCAR's Computational and

Information Systems Laboratory, sponsored by the National Science Foundation. The authors thank Andreas Prein for the preprocessed PRISM data.

Chapter 4, in part is currently being prepared for submission for publication of the material. Fish, M. A., Michaelis, A., D. L. Swain, J. M. Done, and F. M. Ralph. The dissertation author was the primary investigator and author of this paper.

Table 4-1: Monthly percentile thresholds based on average North Pacific box (30-60ºN, 120-240ºW). Hereafter referred to as North Pacific percentiles/thresholds.

Monthly	10	11	12	1	2	3	4	5	6	7	8	9
-90%tile	-155.4	-169.6	-160.6	-147.4	-157.6	-165.1	-169.7	-143.9	-117.4	-105.7	-108.7	-133.8
-80%tile	-117.5	-129.6	-126.7	-117.2	-124.4	-131.0	-130.6	-110.4	-86.86	-78.23	-80.36	-98.98
-75%tile	-103.6	-115.6	-114.4	-105.9	-112.2	-118.2	-116.7	-98.01	-76.59	-69.25	-70.59	-86.86
+90%tile	132.8	167.2	174.9	171.8	184.0	168.5	163.2	123.5	101.2	92.86	91.06	111.4
+80%tile	102.9	128.5	134.0	131.4	137.0	130.7	126.0	95.90	77.50	70.88	69.76	84.84
+75%tile	92.20	114.9	119.6	116.8	121.2	117.3	112.6	86.35	69.38	63.19	62.25	75.39

Table 4-2: 5-day smoothed monthly percentile thresholds based on average North Pacific box (30-60ºN, 120-240ºW).

Monthly	10	11	12	1	2	3	4	5	6	7	8	9
-90%tile	-82.29	-92.90	-83.67	-68.67	-75.80	-83.08	-90.24	-70.12	-59.98	-54.61	-47.75	-69.81
-80%tile	-61.94	-69.57	-65.43	-53.77	-59.12	-64.76	-69.80	-52.85	-45.52	-40.82	-35.30	-52.10
-75%tile	-54.73	-61.48	-58.77	-48.39	-53.26	-58.22	-62.44	-46.64	-40.47	-36.08	-31.03	-45.99
+90%tile	71.50	91.04	87.18	70.58	83.49	79.39	85.92	63.76	54.02	46.99	43.34	65.21
+80%tile	55.08	71.67	68.41	55.31	63.58	63.43	66.65	48.84	41.36	35.75	32.97	48.93
+75%tile	49.14	64.50	61.65	49.58	56.47	57.34	59.49	43.59	36.94	31.90	29.31	43.08

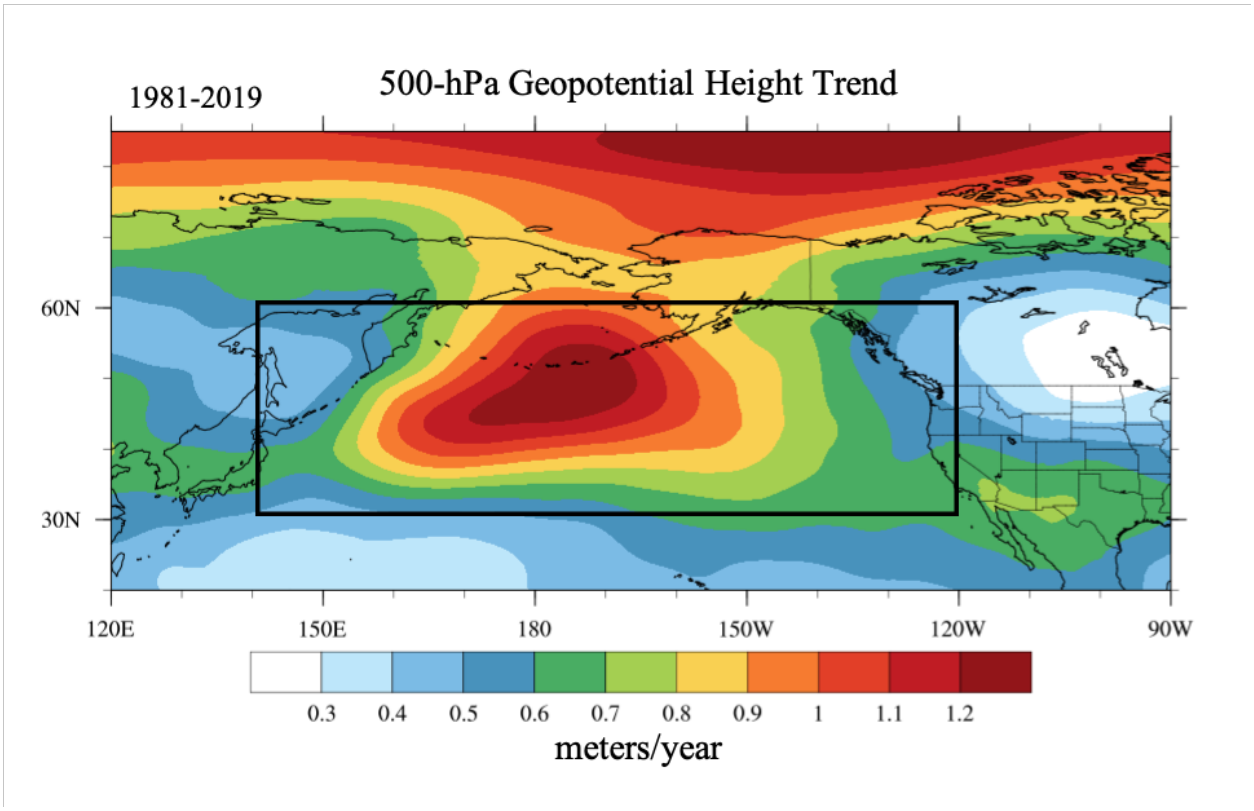

Figure 4-1: The average 500-hPa geopotential height trend per year in the MERRA-2 dataset observed from 1981-2019. The black box represents the defined North Pacific area, 30-60ºN, 120-240ºW.

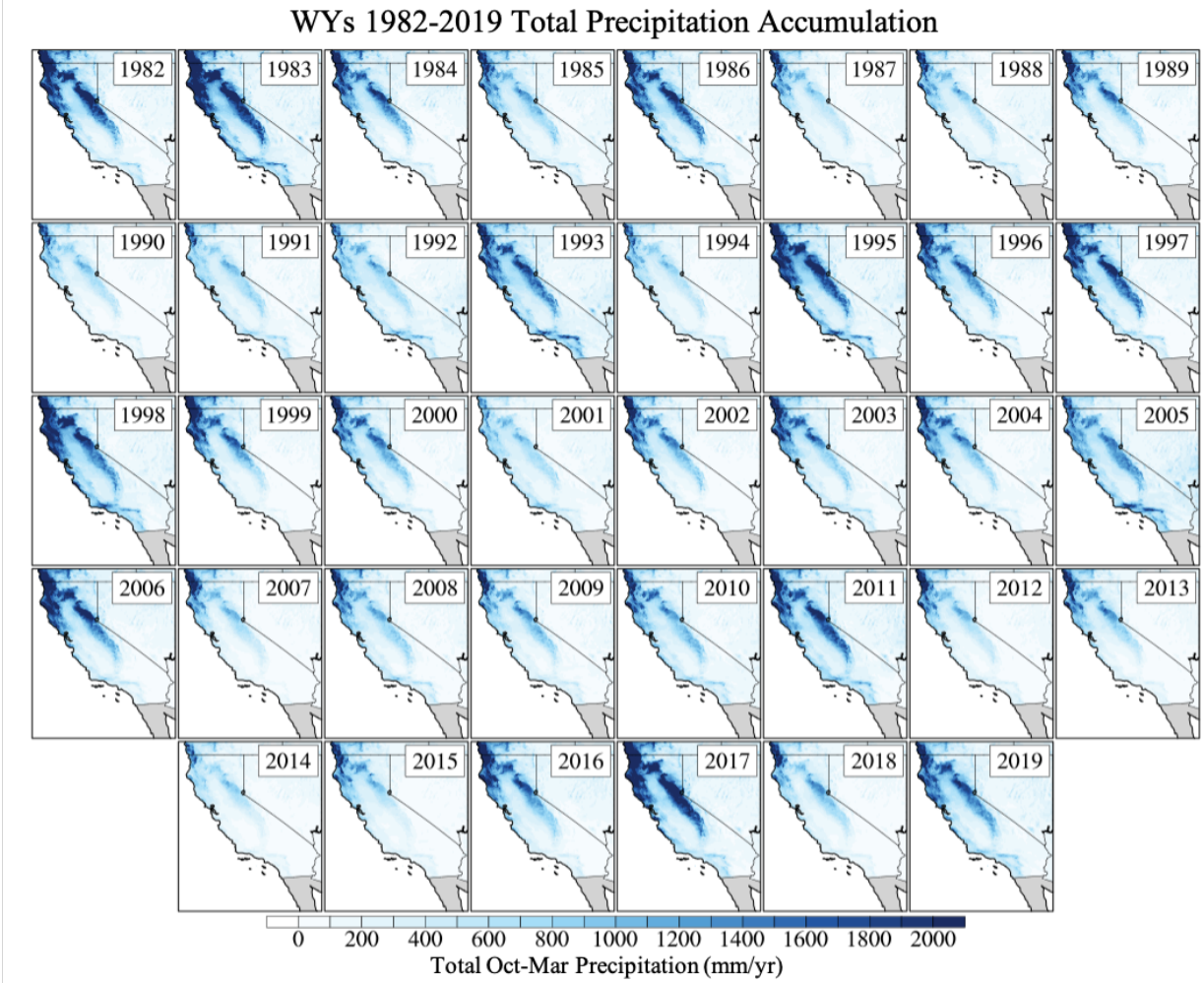

Figure 4-2: Total precipitation accumulation per WY (October 1-September 30, mm/yr) from 1981-2019.

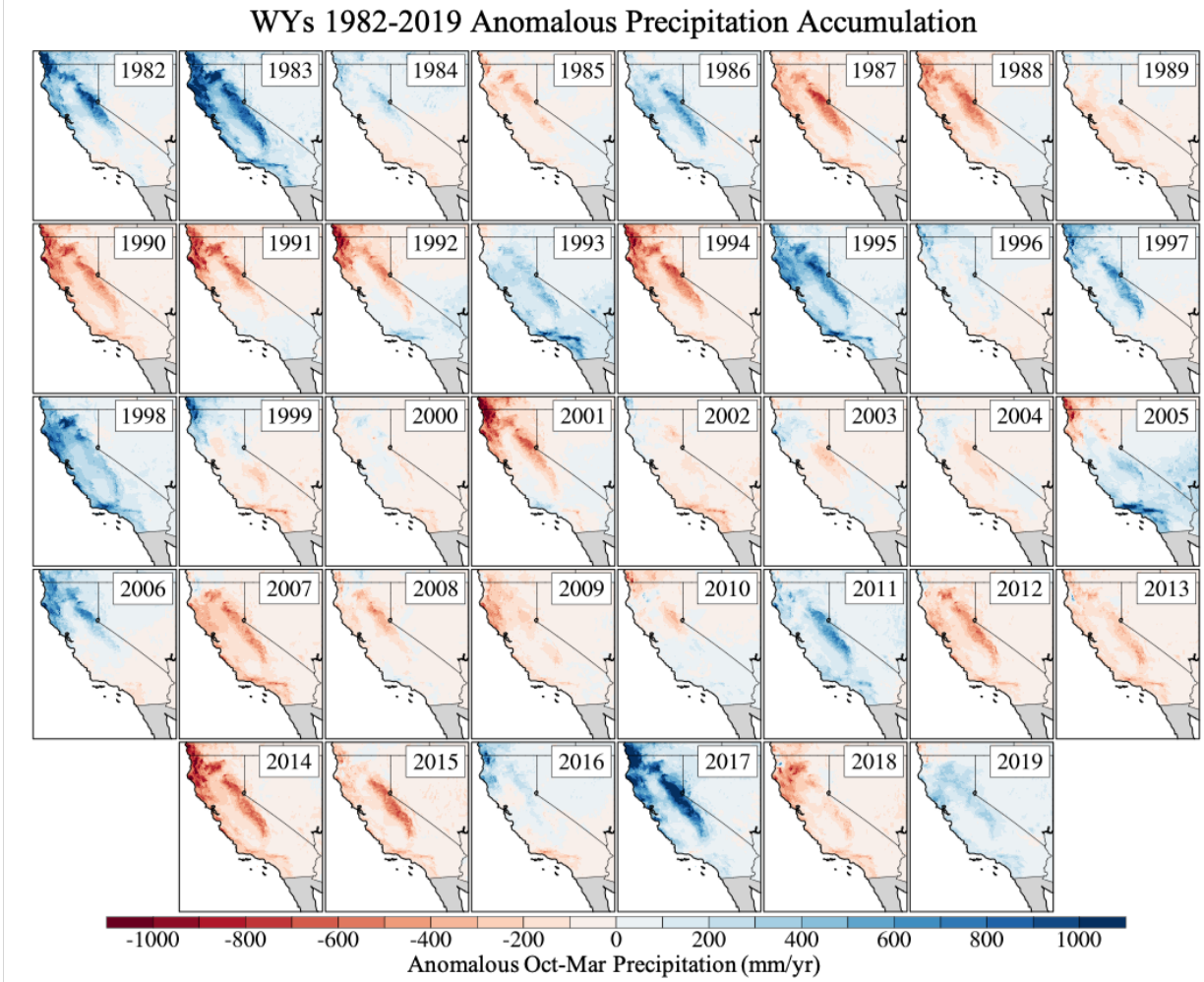

Figure 4-3: Anomalous precipitation accumulation per WY (mm/yr) calculated from the average total WY accumulation.

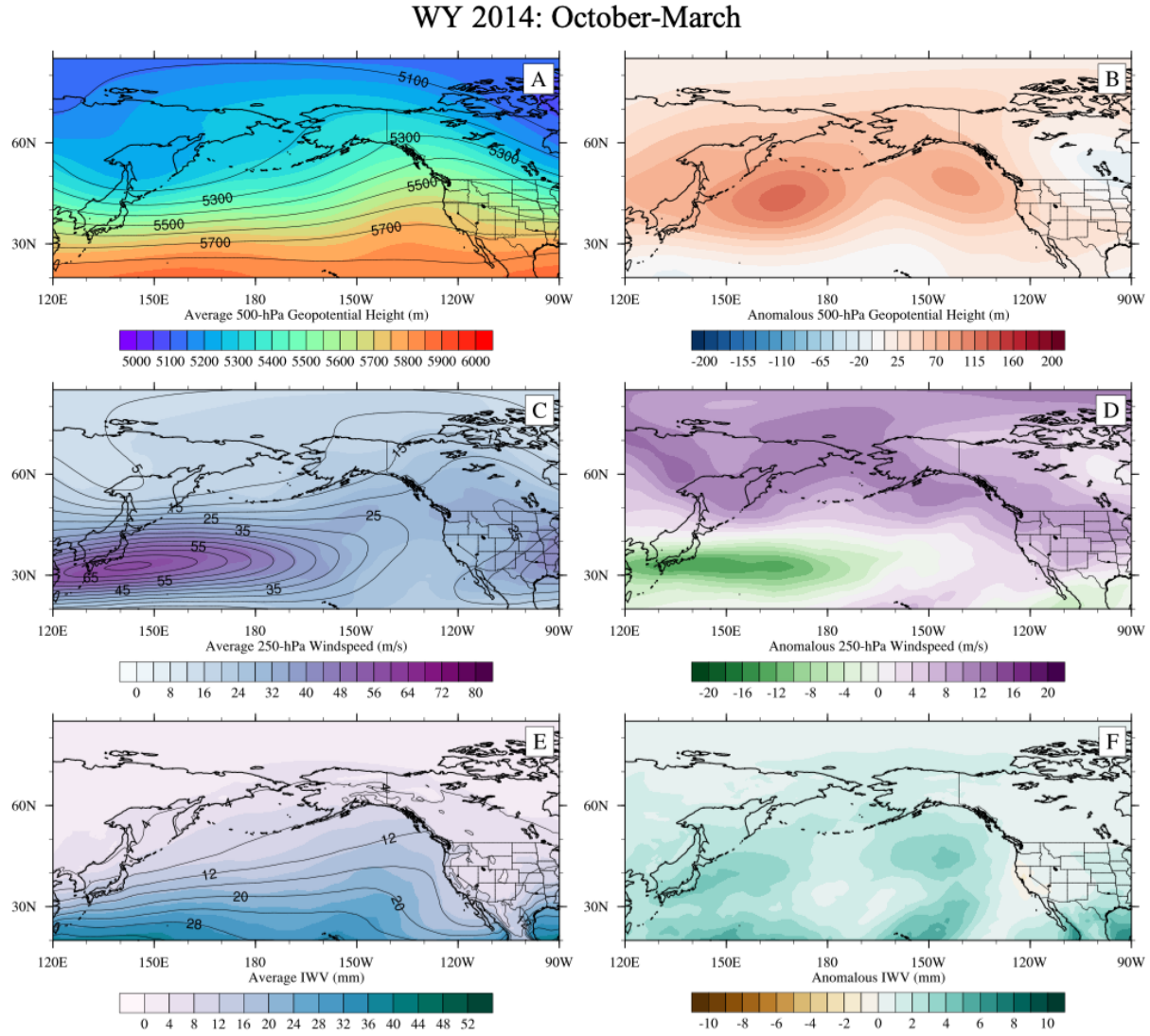

Figure 4-4: October-March of WY 2014 composite average (left, shaded) and DJF climatology (contours) of A) 500-hPa geopotential height (m), C) 250-hPa windspeed (m/s), and E) IWV (mm). Anomalous conditions from a DJF climatology of B) 500-hPa geopotential heights (m), D) 250-hPa windspeed (m/s) and F) IWV (mm).

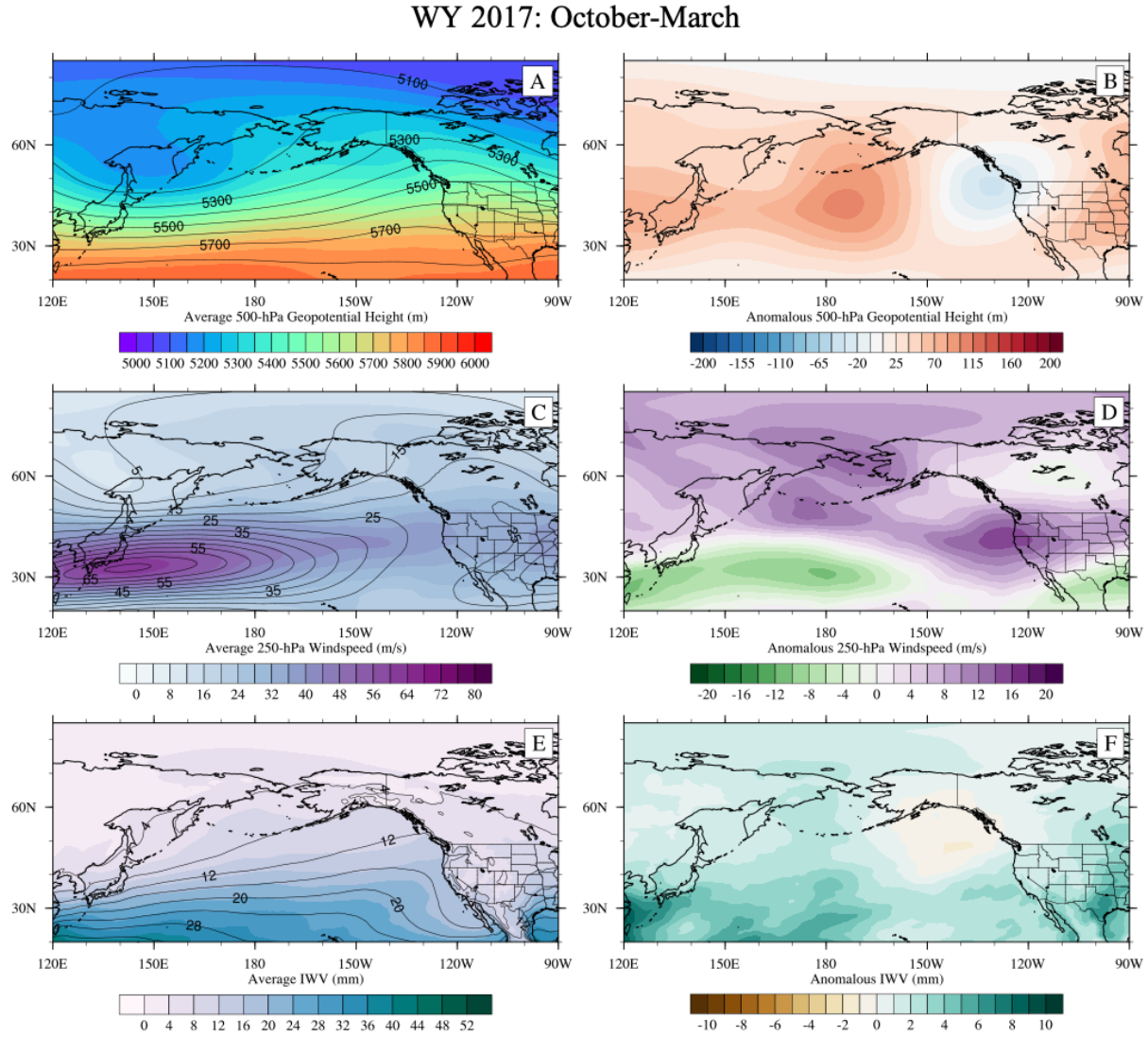

Figure 4-5: October-March of WY 2017 composite average (left, shaded) and DJF climatology (contours) of A) 500-hPa geopotential height (m), C) 250-hPa windspeed (m/s), and E) IWV (mm). Anomalous conditions from a DJF climatology of B) 500-hPa geopotential heights (m), D) 250-hPa windspeed (m/s) and F) IWV (mm).

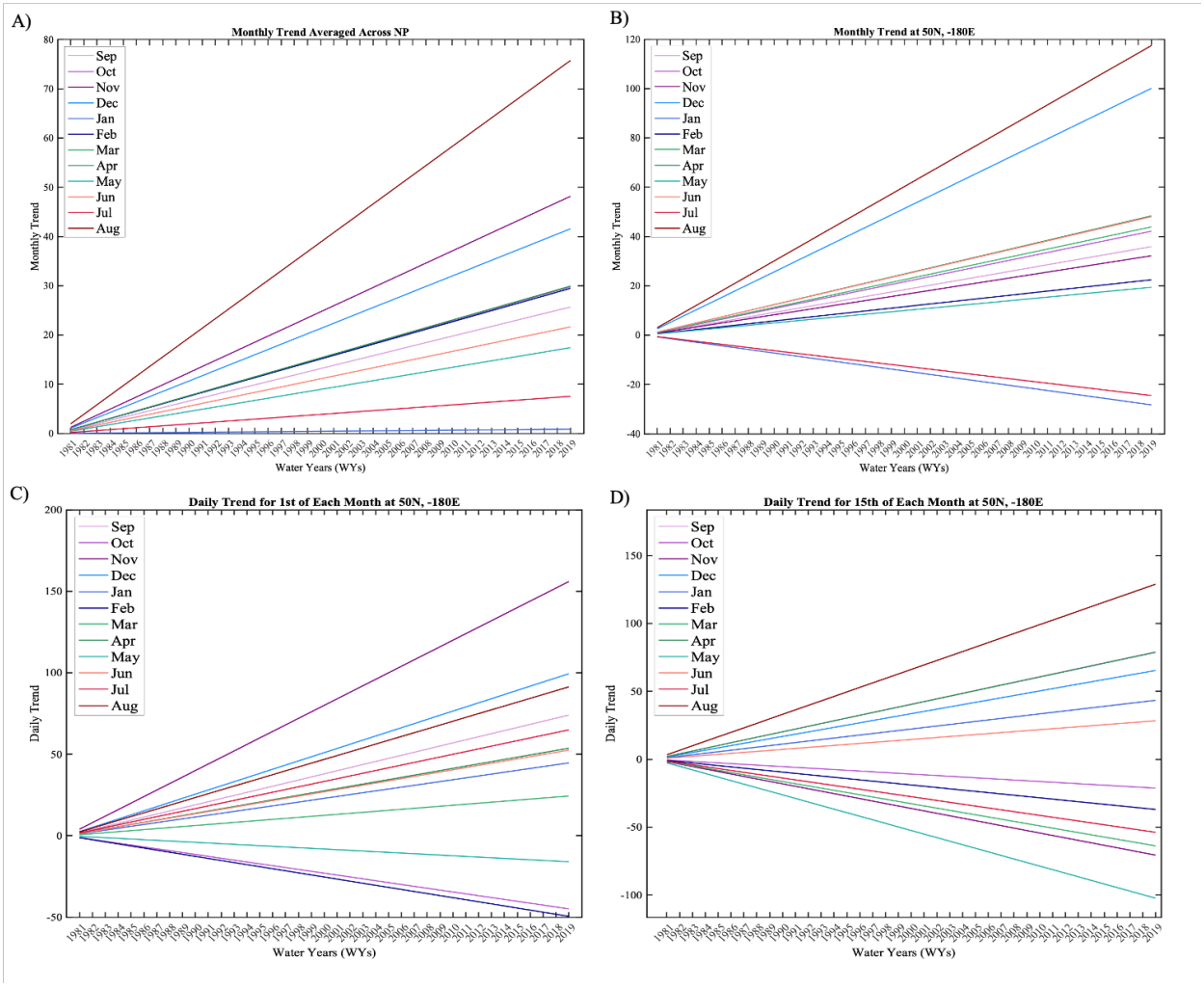

Figure 4-6: Trend lines applied to data for detrending. A) Monthly averaged trend averaged across the North Pacific, B) Monthly trend at 50ºN, -180ºE, C) Daily trend for the 1st of each month at 50ºN, -180ºE, and D) Daily trend for the 15th of each month at 50ºN, -180ºE.

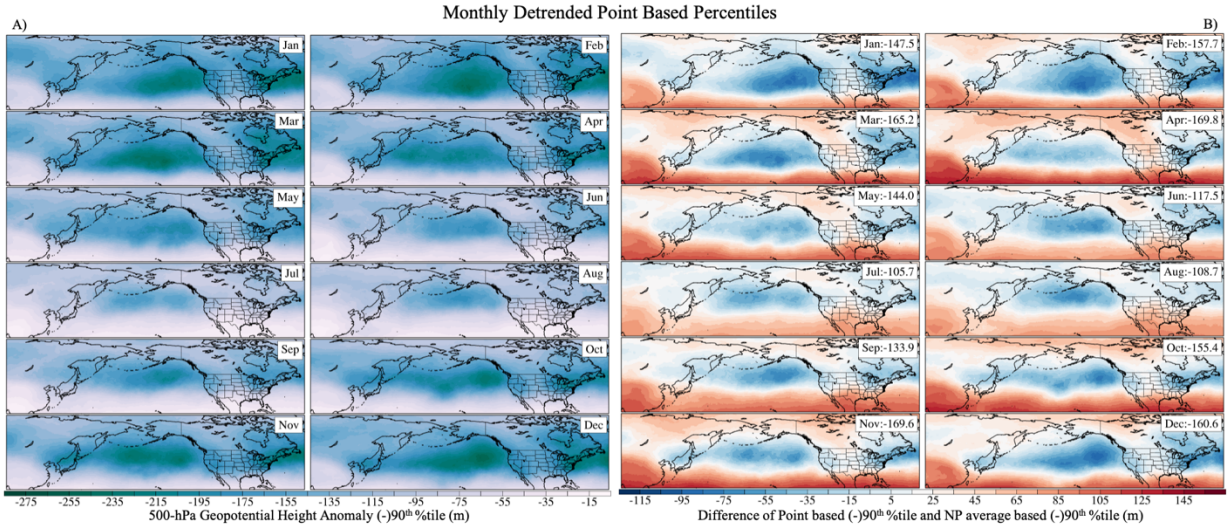

Figure 4-7: A) Monthly (-)90th percentile thresholds calculated at each point. B) The difference between the point based 90th percentile values and the North Pacific spatial average. The number in the caption refers to the monthly North Pacific value.

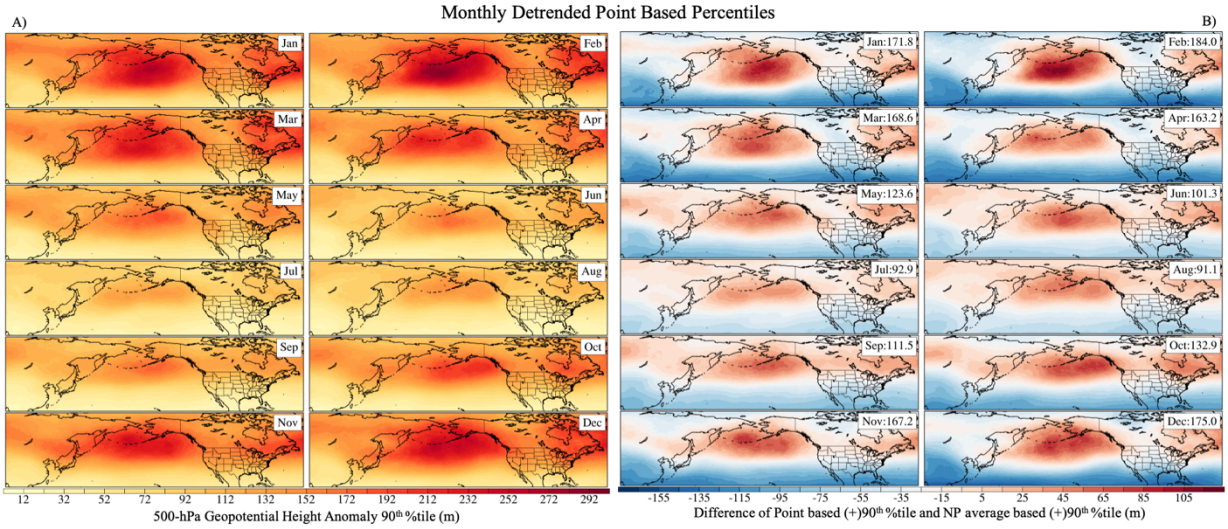

Figure 4-8: A) Monthly (+)90th percentile thresholds calculated at each point. B) The difference between the point based 90th percentile values and the North Pacific spatial average. The number in the caption refers to the monthly North Pacific value.

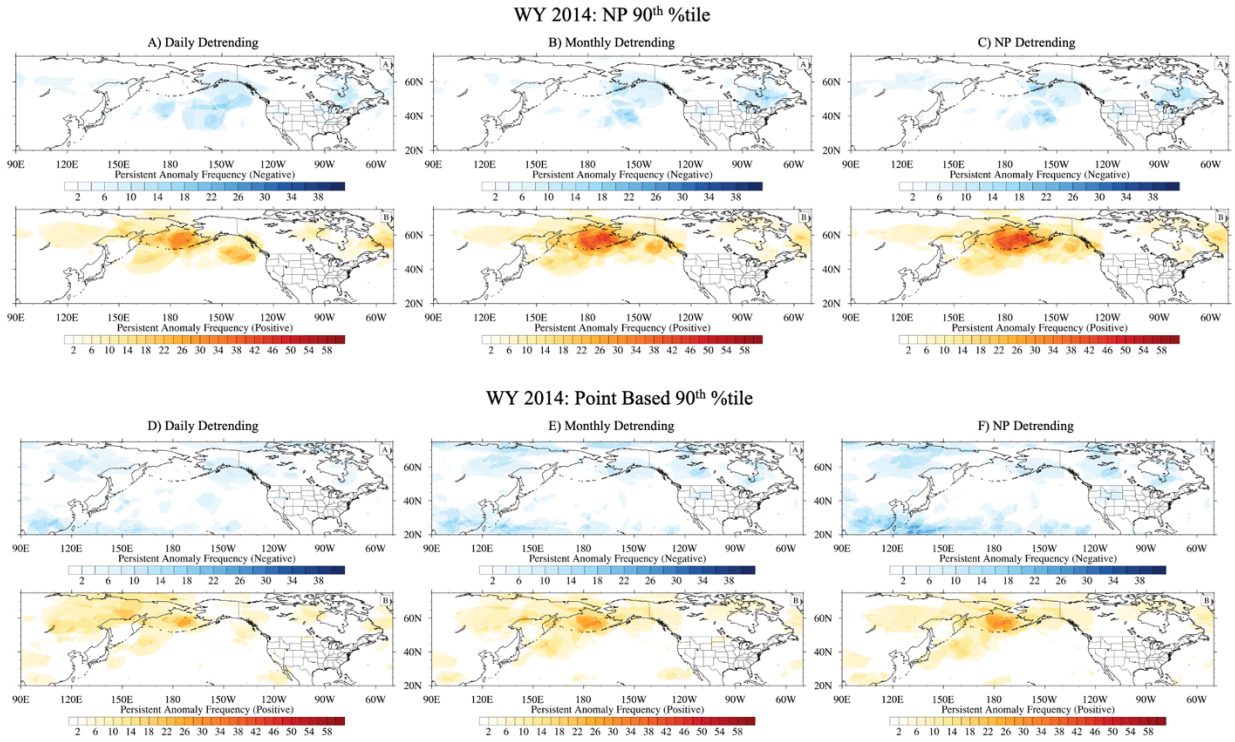

Figure 4-9: Frequency of persistent anomalies during WY 2014 (number of days) based on the North Pacific percentiles (A-C) and point-based percentiles (D-F) for each detrending method: daily (A, D), monthly (B, E), and NP (C, F). Blue refers to negative PAs, yellow/red refers to positive PAs.

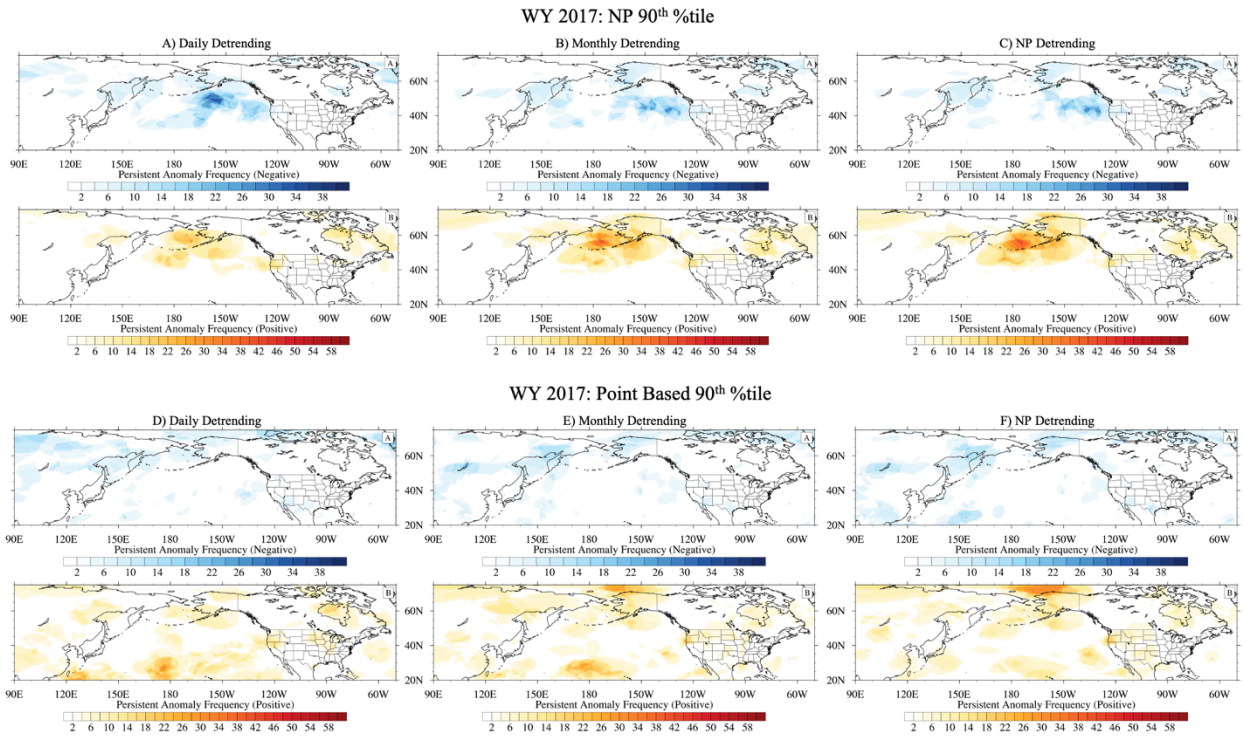

Figure 4-10: Frequency of persistent anomalies during WY 2017 (number of days) based on the North Pacific percentiles (A-C) and point-based percentiles (D-F) for each detrending method: daily (A, D), monthly (B, E), and NP (C, F). Blue refers to negative PAs, yellow/red refers to positive PAs.

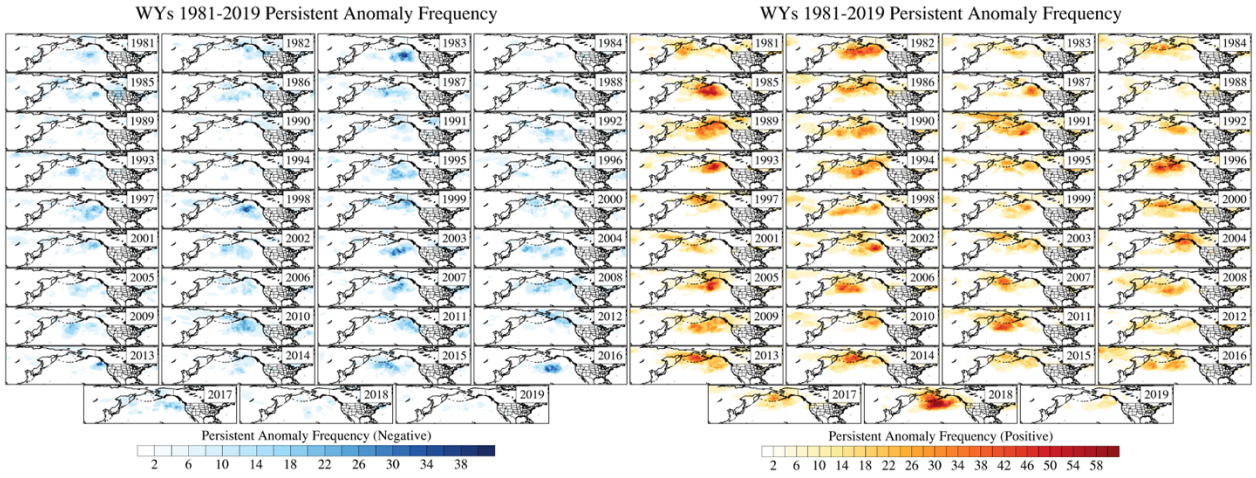

Figure 4-11: For WYs 1981-2019 the total frequency of the 90th percentile PAs, both negative (left) and positive (right) based on monthly detrending and the North Pacific percentiles.

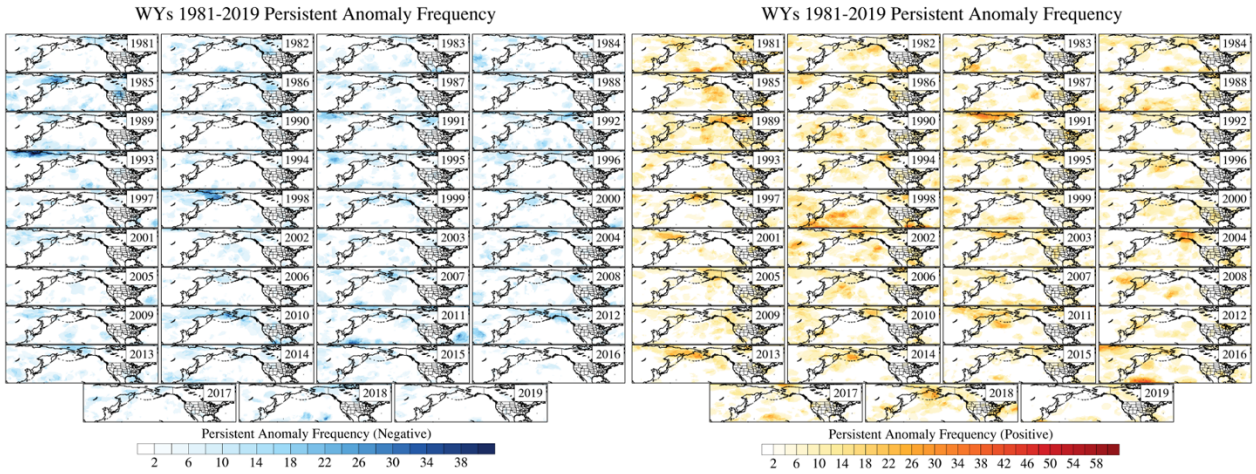

Figure 4-12: For WYs 1981-2019 the total frequency of the 90th percentile PAs, both negative (left) and positive (right) based on monthly detrending and the point-based percentiles.

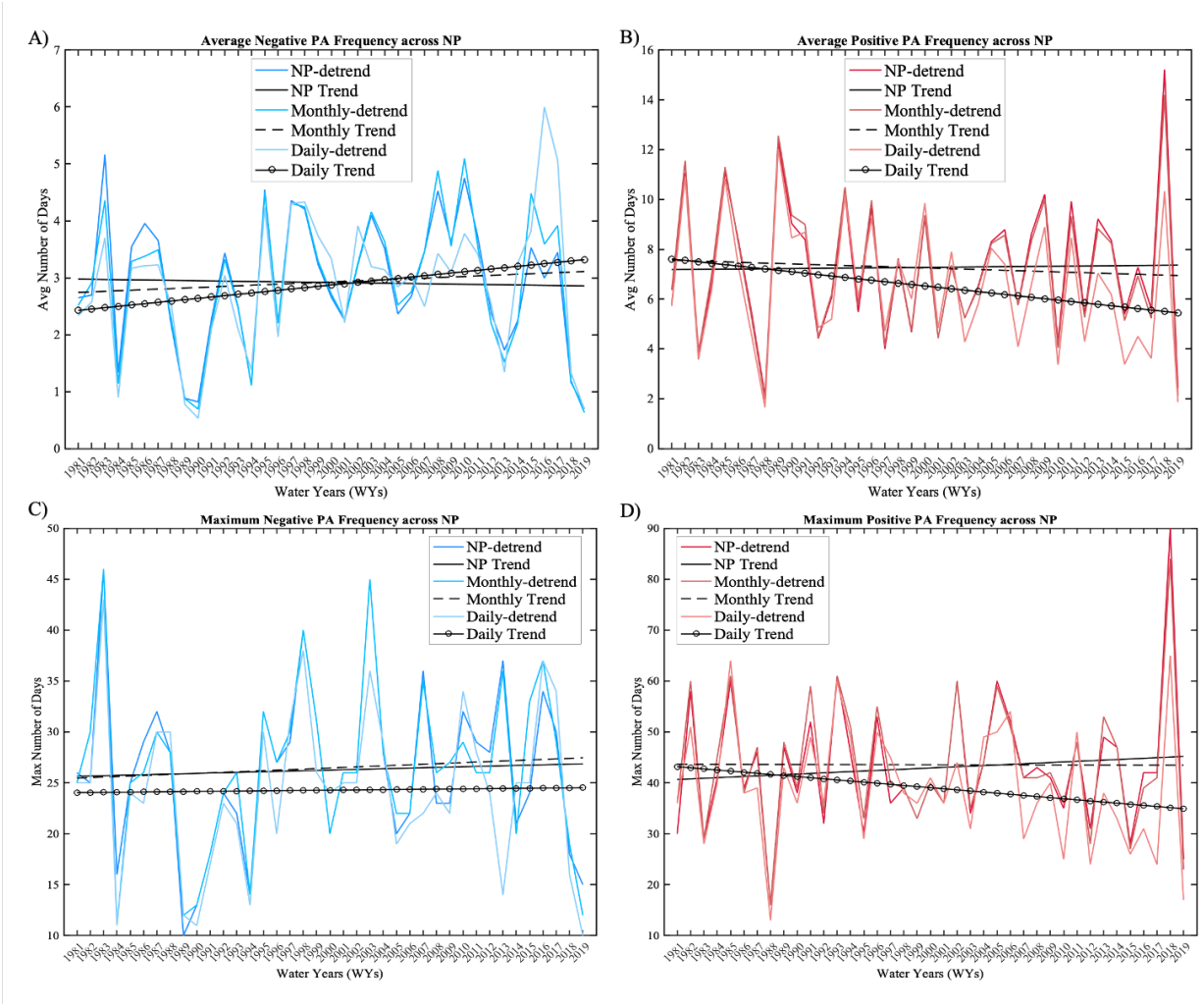

Figure 4-13: Persistent anomaly trends across the North Pacific in time based on North Pacific percentiles. A) the average frequency of -90th percentile PAs for all detrending methods (blue lines) and linear trends (black lines), B) the average frequency of +90th percentile PAs for all detrending methods (blue lines) and linear trends (black lines). C) the maximum frequency of -90th percentile PAs for all detrending methods (blue lines) and linear trends (black lines), B) the maximum frequency of +90th percentile PAs for all detrending methods (blue lines) and linear trends (black lines).

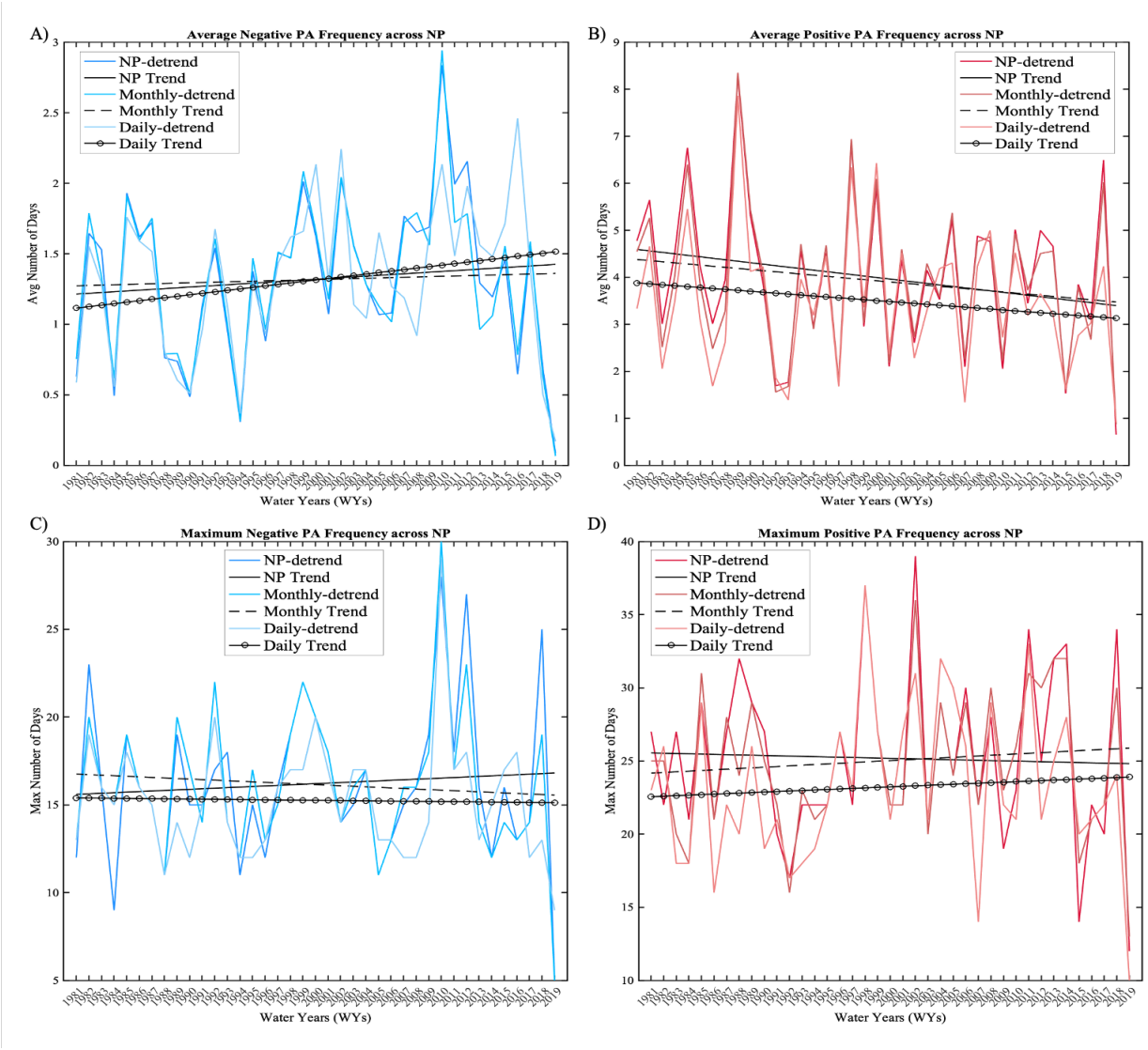

Figure 4-14: Persistent anomaly trends across the North Pacific in time based on point-based percentiles. A) the average frequency of -90th percentile PAs for all detrending methods (blue lines) and linear trends (black lines), B) the average frequency of +90th percentile PAs for all detrending methods (blue lines) and linear trends (black lines). C) the maximum frequency of -90th percentile PAs for all detrending methods (blue lines) and linear trends (black lines), B) the maximum frequency of +90th percentile PAs for all detrending methods (blue lines) and linear trends (black lines).

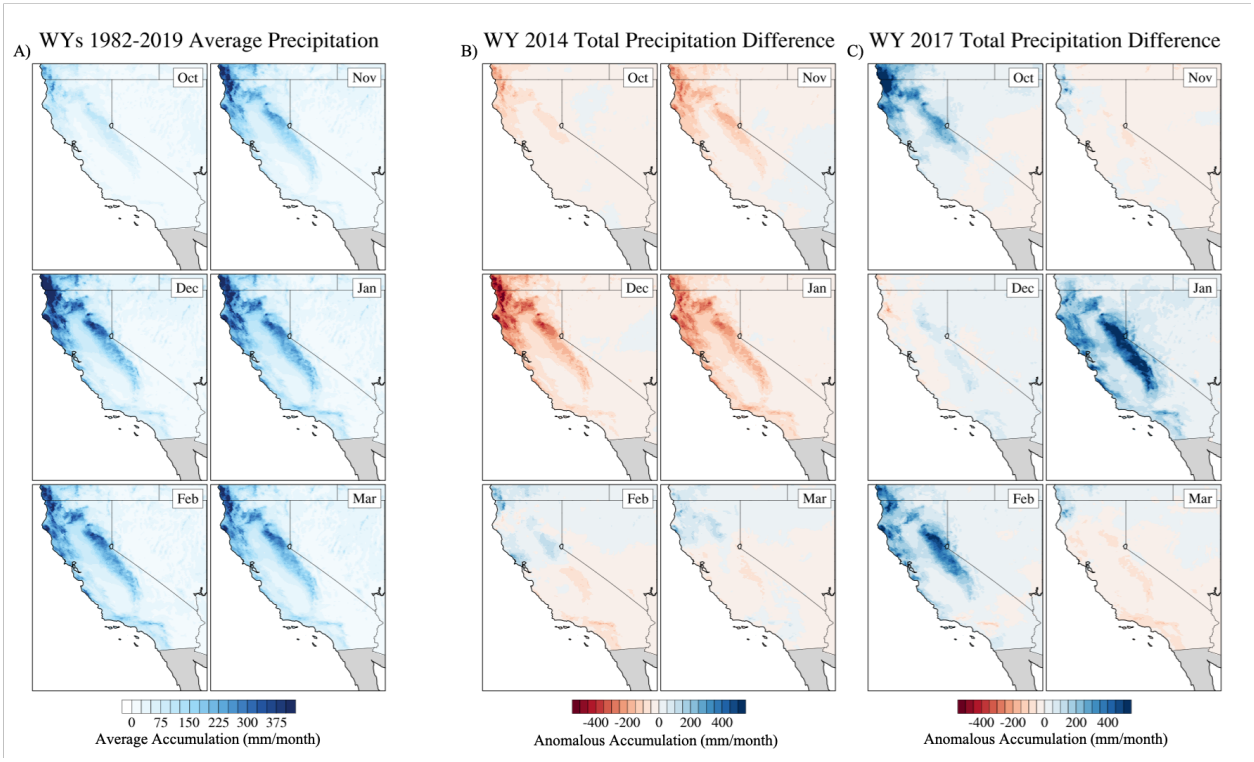

Figure 4-15: A) The average monthly precipitation accumulation from 1981-2019, for October-March. B) The anomalous monthly accumulation for October-March during WY 2014. C) The anomalous monthly accumulation for October-March during WY 2017.

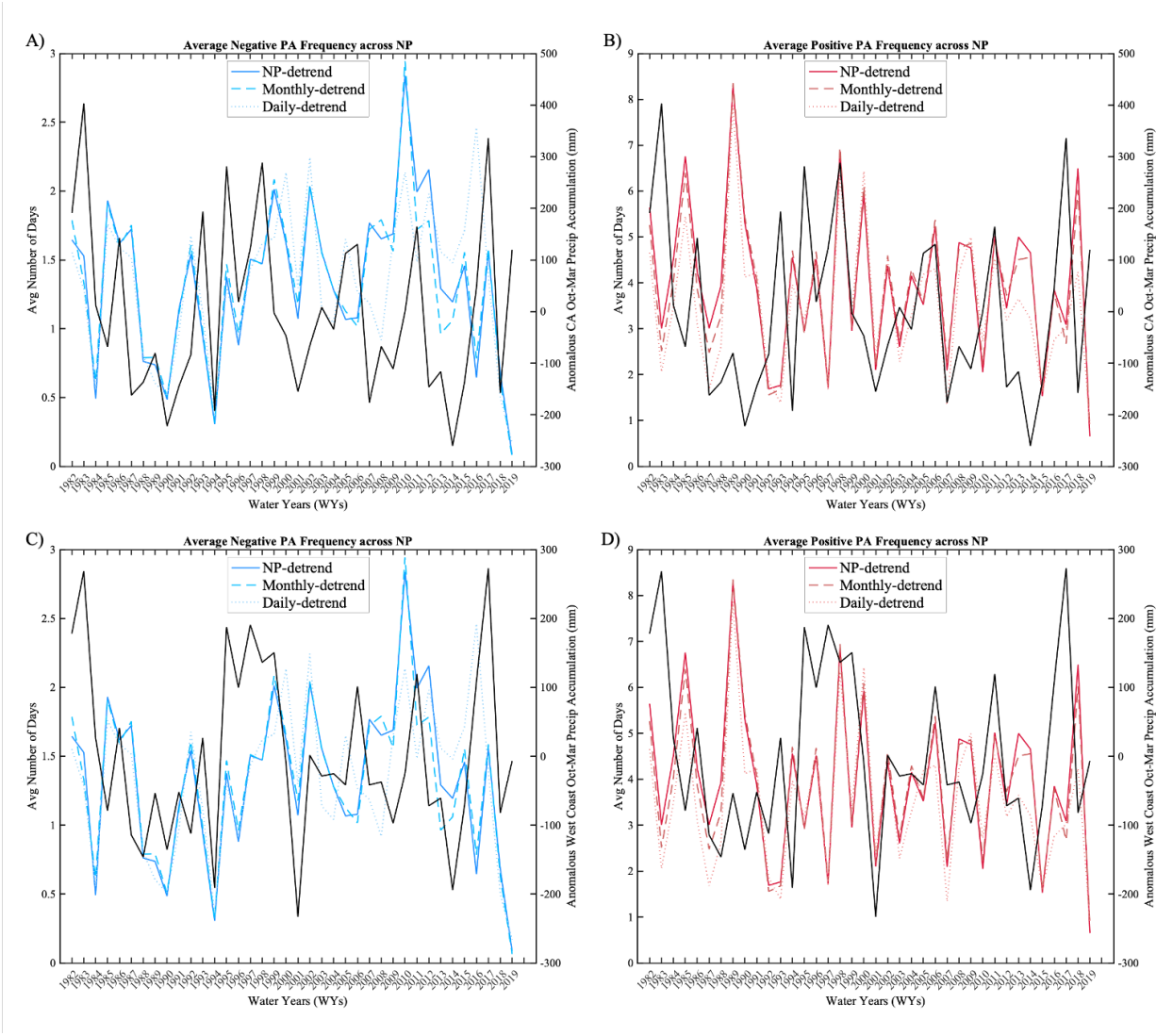

Figure 4-16: Correlations between PA frequency across the North Pacific and anomalous precipitation accumulation for California (top row) and the West Coast (CA, OR, WA; bottom row). Negative PA frequency (left column) correlated with anomalous October-March precipitation. Positive PA frequency (right column) correlated with anomalous October-March precipitation. Frequency in colored lines (blue=negative, red=positive) and anomalous precipitation shown on the black line.

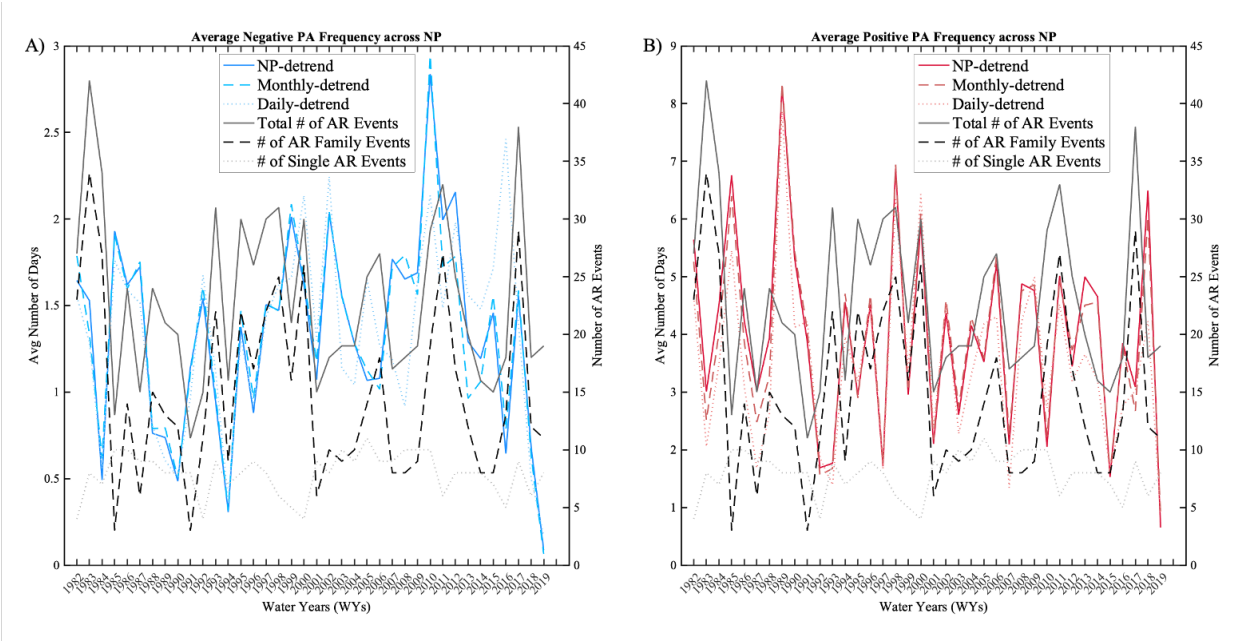

Figure 4-17: Correlations between negative (left) and positive (right) PA frequency across the North Pacific and AR events, AR families and single AR events. The different detrending methods are shown in colored lines and patterns with the timeseries of total AR events, number of AR family events and number of single AR events in gray solid, gray dashed and light gray dashed, respectively.

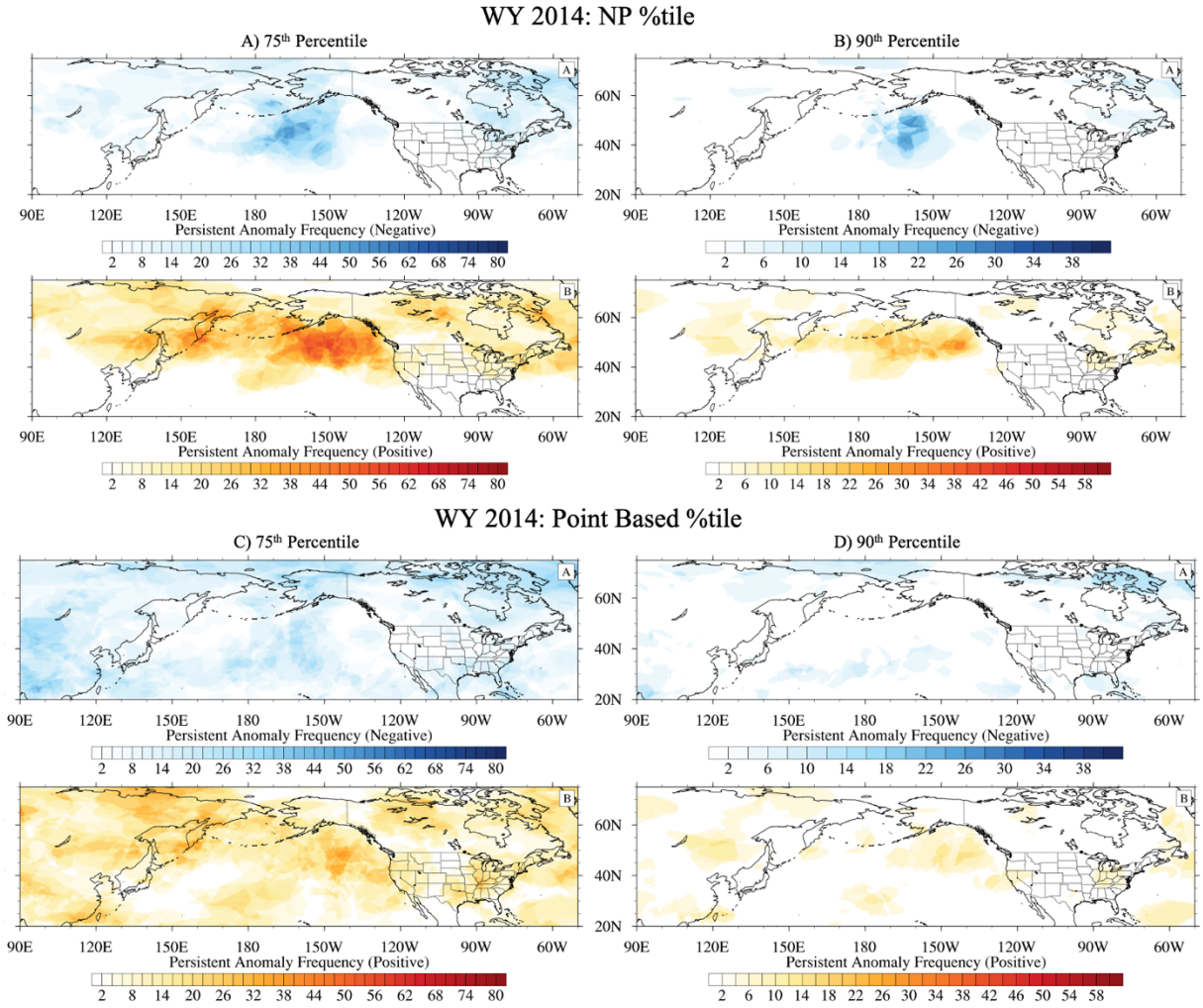

Figure 4-18: 5-day smoothing applied to the monthly detrended data over WY 2014 showing the persistent anomaly frequency (days/WY). Top row, percentiles are calculated based on a North Pacific average, bottom row, percentiles are calculated based on each point. A) and C) show the 75th percentiles and B) and D) show the 90th percentile.

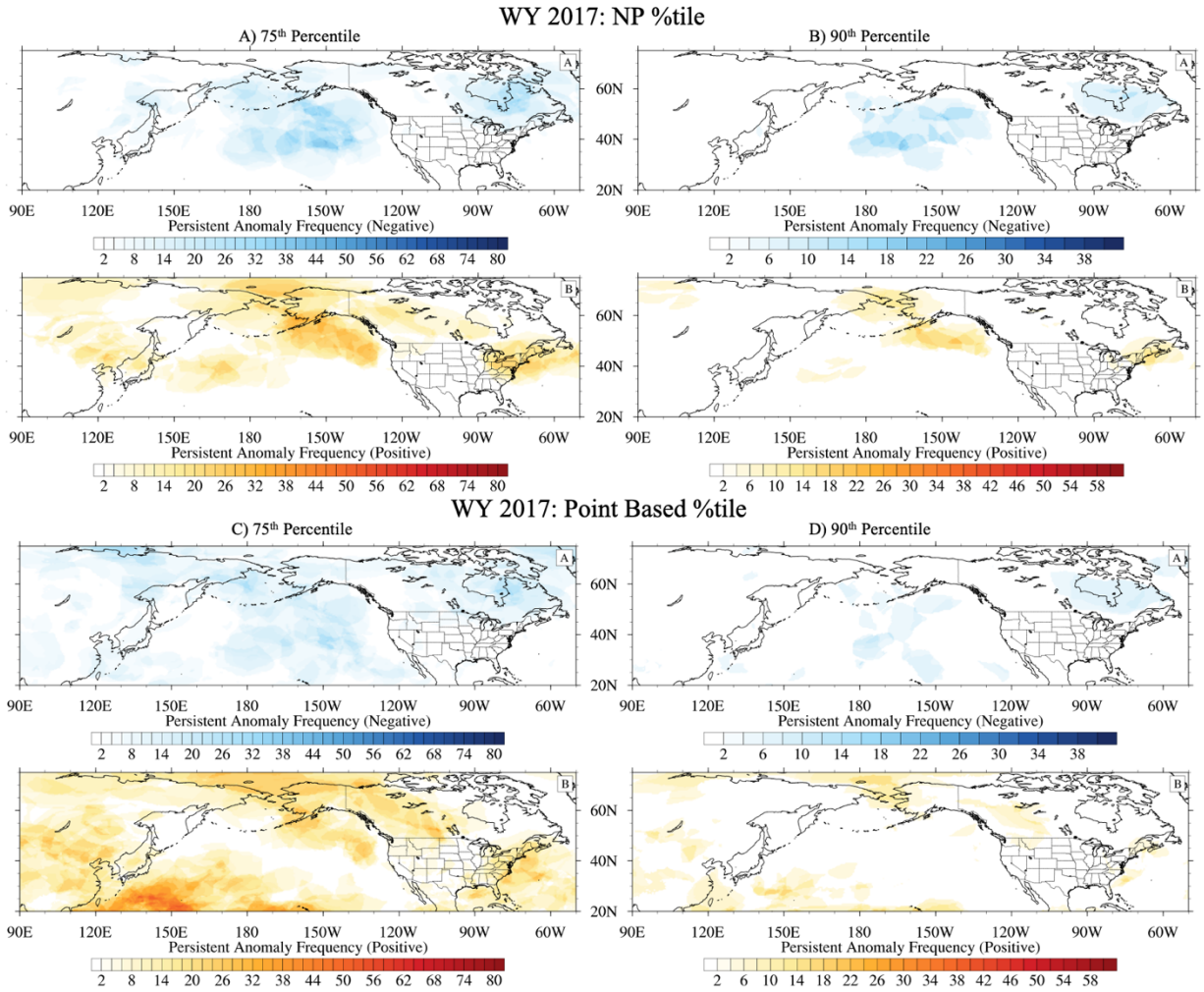

Figure 4-19: 5-day smoothing applied to the monthly detrended data over WY 2017 showing the persistent anomaly frequency (days/WY). Top row, percentiles are calculated based on a North Pacific average, bottom row, percentiles are calculated based on each point. A) and C) show the 75th percentiles and B) and D) show the 90th percentile.

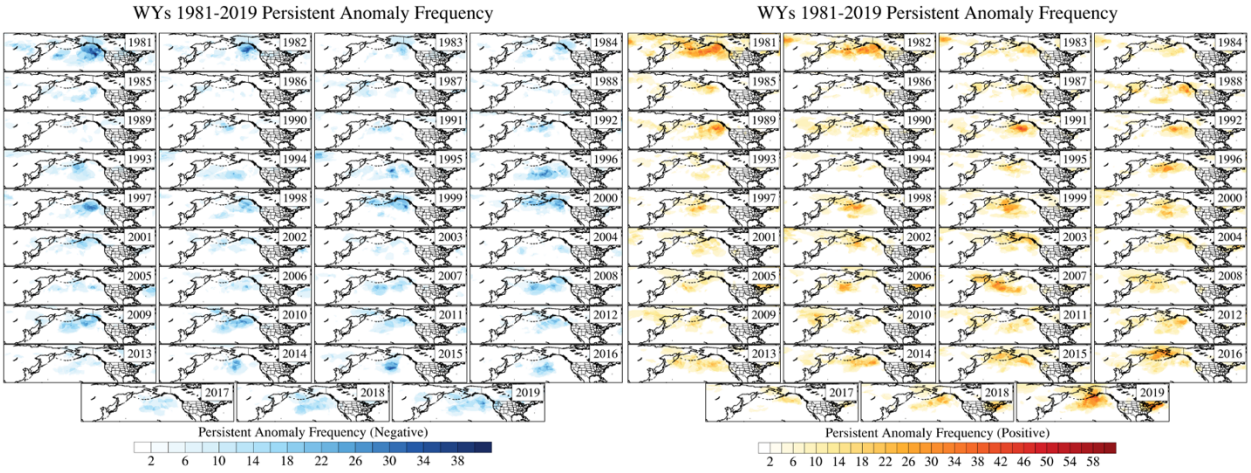

Figure 4-20: For WYs 1981-2019 the total frequency of the 90th percentile PAs, both negative (left) and positive (right) based on 5-day smoothed, monthly detrended, and North Pacific average-based percentiles.

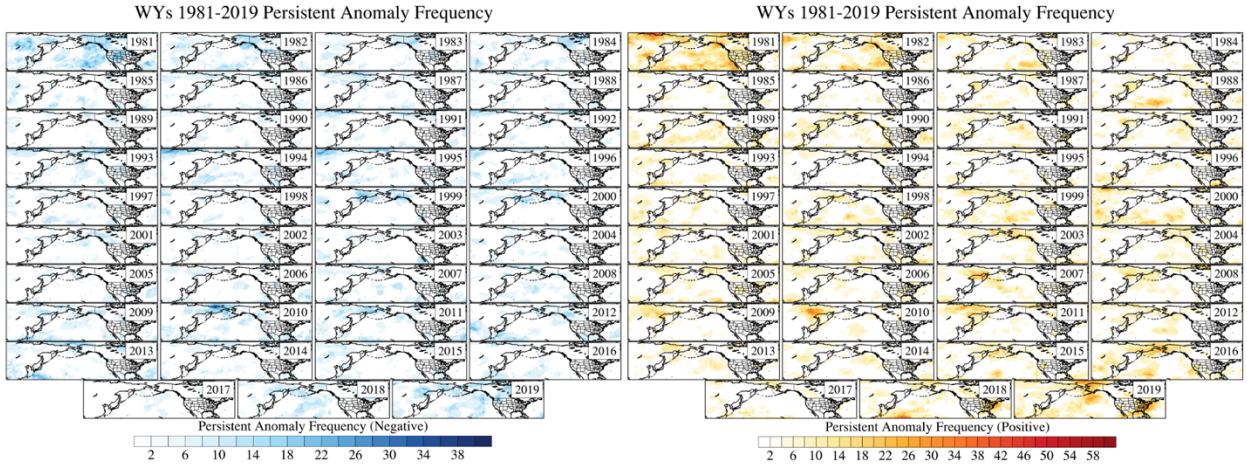

Figure 4-21: For WYs 1981-2019 the total frequency of the 90th percentile PAs, both negative (left) and positive (right) based on 5-day smoothed, monthly detrended, and point-based percentiles.

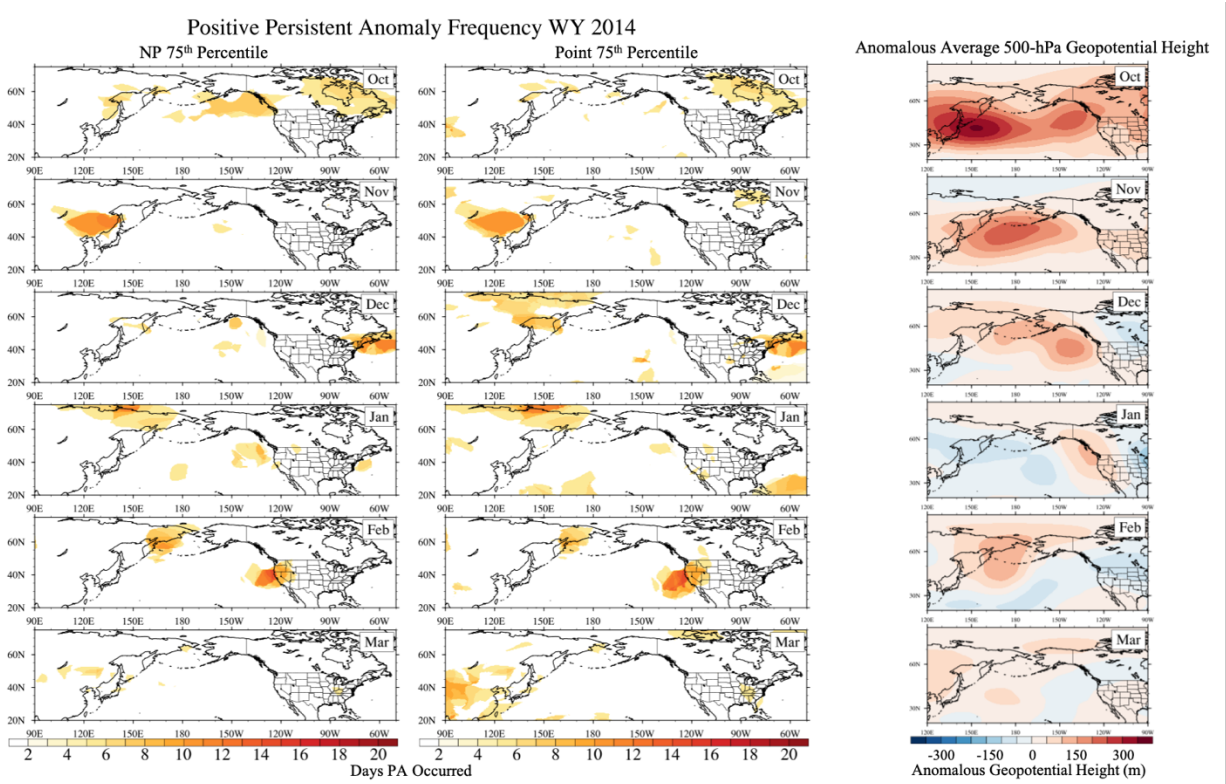

Figure 4-22: Smoothed, monthly detrended, 75th percentile persistent anomaly frequency (days/month) for October-March WY 2014 based on the North Pacific average-based percentiles (left) or point-based percentiles (center). Right: Anomalous 500-hPa geopotential heights compared to a DJF climatology for October-March WY 2014 (blue=anomalously low heights, red=anomalously high heights).

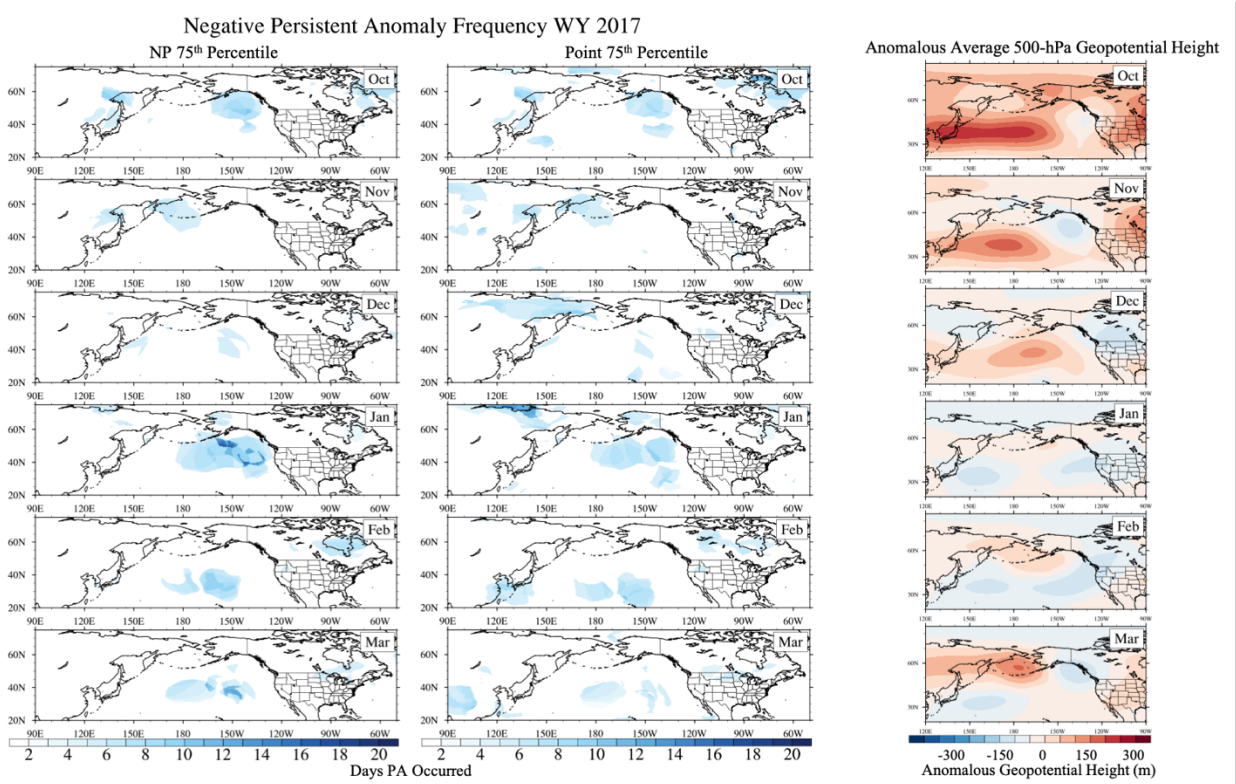

Figure 4-23: Smoothed, monthly detrended, 75th percentile persistent anomaly frequency (days/month) for October-March WY 2017 based on the North Pacific average-based percentiles (left) or point-based percentiles (center). Right: Anomalous 500-hPa geopotential heights compared to a DJF climatology for October-March WY 2014 (blue=anomalously low heights, red=anomalously high heights).

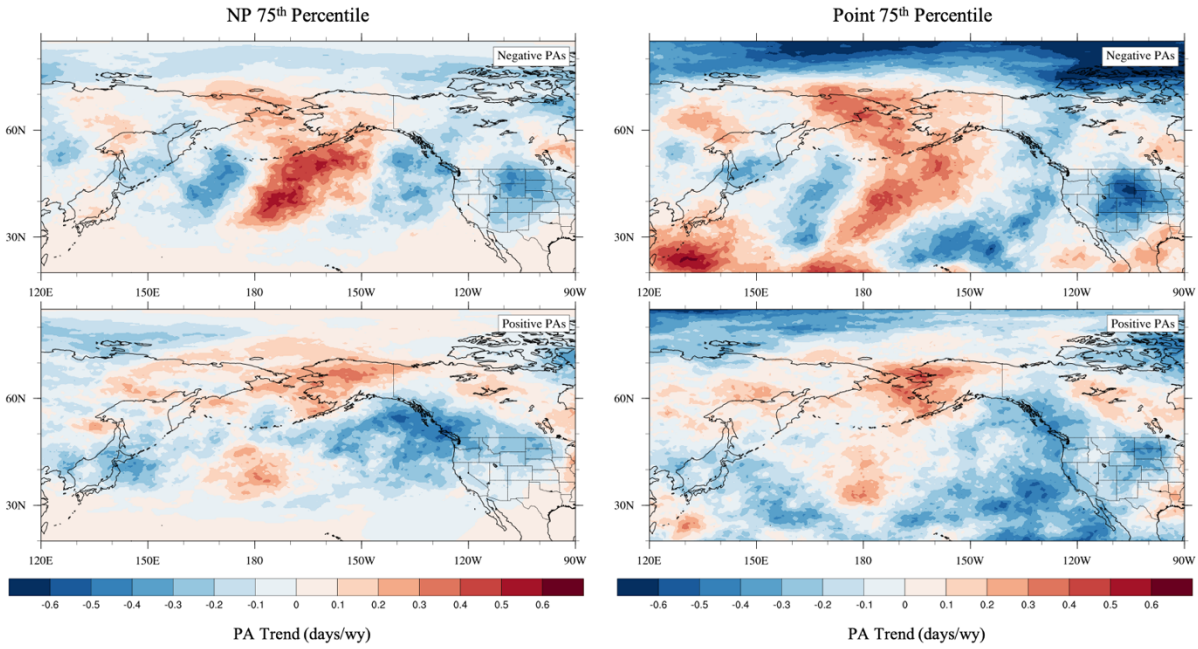

Figure 4-24: Smoothed, monthly detrended, 75th percentile persistent anomaly frequency trend (days/WY) based on the North Pacific average 75th percentile (left) and the point-based 75th percentile (right). Increasing (decreasing) persistent anomalies are shown in warm (cool) colors.

4.6 References

Breeden, M. L., B. T. Hoover, M. Newman, and D. J. Vimont, 2020: Optimal North pacific blocking precursors and their deterministic subseasonal evolution during boreal winter. *Mon. Weather Rev.*, **148**, 739–761, https://doi.org/10.1175/MWR-D-19-0273.1.

Carrera, M. L., R. W. Higgins, and V. E. Kousky, 2004: Downstream weather impacts associated with atmospheric blocking over the Northeast Pacific. *J. Clim.*, **17**, 4823–4839, https://doi.org/10.1175/JCLI-3237.1.

Daly, C., R. P. Neilson, and D. L. Phillips, 1994: A statistical-topographic model for mapping climatological precipitation over mountainous terrain. *J. Appl. Meteor.*, **33**, 140-158.

Daly, C., G. H. Taylor, W. P. Gibson, T. W. Parzybok, G. L. Johnson, and P. Pasteris, 2001: High-quality spatial climate data sets for the United States and beyond. *Trans. Amer. Soc. Agri. Eng.*, **43**, 1957-1962.

Daly, C., W. P. Gibson, G. H. Taylor, G. L. Johnson, and P. Pasteris, 2002: A knowledge-based approach to statistical mapping of climate. *Climate Res.*, 22, 99–113.

Dettinger, M. D., F. M. Ralph, T. Das, P. J. Neiman, and D. R. Cayan, 2011: Atmospheric Rivers, Floods and the Water Resources of California. *Water*, **3(2)**, 445-478, doi:10.3390/w3020445.

Dettinger, M. D., 2013: Atmospheric Rivers as Drought Busters on the U.S. West Coast. *J. Hydrometeor.*, **14**, 1721-1732, doi:10.1175/JHM-D-13-02.1.

Dole, R. M., 1989: Life cycles of persistent anomalies. Part I: evolution of 500 mb height fields. *Mon. Weather Rev.*, **117**, 177–211, https://doi.org/10.1175/1520-0493(1989)117<0177:LCOPAP>2.0.CO;2.

——, and N. D. Gordon, 1983: Persistent anomalies of the extratropical Northern Hemisphere wintertime circulation: Geographical Distribution and Regional Persistence Characteristics. *Mon. Weather Rev.*, **111**, 1567–1586, https://doi.org/10.1175/1520-0493(1986)114<0178:PAOTEN>2.0.CO;2.

——, and R. X. Black, 1990: Life cycles of persistent anomalies. Part II: the development of

persistent negative height anomalies over the north Pacific Ocean. *Mon. Weather Rev.*, **118**, 824–846, https://doi.org/10.1175/1520-0493(1990)118<0824:LCOPAP>2.0.CO;2.

Fish, M. A., A. M. Wilson, and F. M. Ralph, 2019: Atmospheric river families: Definition and associated synoptic conditions. *J. Hydrometeorol.*, **20**, 2091–2108, https://doi.org/10.1175/JHM-D-18-0217.1.

Fish, M. A., J. M. Done, A. M. Wilson, D. L. Swain, and F. M. Ralph, 2020: Large-scale drivers of successive atmospheric river events in California, *J. Climate (in review)*

Galarneau, T. J., T. M. Hamill, R. M. Dole, and J. Perlwitz, 2012: A multiscale analysis of the extreme weather events over Western Russia and Northern Pakistan during July 2010. *Mon. Weather Rev.*, **140**, 1639–1664, https://doi.org/10.1175/MWR-D-11-00191.1.

Gelaro, R., W. McCarty, M. J. Suarez, R. Todling, A. Molod, L. Takacs, C. A. Randles, A. Darmenov, M. G. Bosilovich, R. Reichle, K. Wargan, L. Coy, R. Cullather, C. Draper, S. Akella, V. Buchard, A. Conaty, A. M. da Silva, W. Gu, G.-K. Kim, R. Koster, R. Lucchesi, D. Merkova, J. E. Nielsen, G. Partyka, S. Pawson, W. Putman, M. Reinecker, S. D. Schubert, M. Sienkiewicz and B. Zhao, 2017: The Modern-Era Retrospective Analysis for Research and Applications, Version 2 (MERRA-2). *J. Climate*, **30**, 5419-5454, doi:10.1175/JCLI-D-16-0758.1.

Gershunov, A., T. Shulgina, F. M. Ralph, D. A. Lavers, and J. J. Rutz (2017), Assessing the climate-scale variability of atmospheric rivers affecting western North America, *Geophys. Res. Lett.*, 44, doi:10.1002/2017GL074175.

Griffin, K. S., and J. E. Martin, 2017: Synoptic features associated with temporally coherent modes of variability of the North Pacific jet stream. *J. Clim.*, **30**, 39–54, https://doi.org/10.1175/JCLI-D-15-0833.1.

Horton, D. E., N. C. Johnson, D. Singh, D. L. Swain, B. Rajaratnam, and N. S. Diffenbaugh, 2015: Contribution of changes in atmospheric circulation patterns to extreme temperature trends. *Nature*, **522**, 465–469, https://doi.org/10.1038/nature14550.

Hoskins, B., and T. Woollings, 2015: Persistent Extratropical Regimes and Climate Extremes. *Curr. Clim. Chang. Reports*, **1**, 115–124, https://doi.org/10.1007/s40641-015-0020-8.

Huguenin, M. F., E. M. Fischer, S. Kotlarski, S. C. Scherrer, C. Schwierz, and R. Knutti, 2020: Lack of Change in the Projected Frequency and Persistence of Atmospheric Circulation Types Over Central Europe. *Geophys. Res. Lett.*, **47**, https://doi.org/10.1029/2019GL086132.

Lamjiri, M. A., M. D. Dettinger, F. M. Ralph and B. Guan, 2017: Hourly storm characteristics along the U.S. West Coast: Role of atmospheric rivers in extreme precipitation. *Geophys. Res. Lett.*, 44, 7020-7028, doi:10.1002/2017GL074193.

Lamjiri, M. A., F. M. Ralph, and M. D. Dettinger, 2020: Recent Changes in United States Extreme 3-Day Precipitation Using the R-CAT Scale. *J. Hydrometeorol.*, 1207–1221, https://doi.org/10.1175/jhm-d-19-0171.1.

Lund, J., J. Medellin-Azuara, J. Durand, and K. Stone, 2018: Lessons from California's 2012-2016 drought. *J. Water Res. Planning Man.*, **144**(10), doi: 10.1061/(ASCE)WR.1943-5452.0000984.

Mann, M. E., S. Rahmstorf, K. Kornhuber, B. A. Steinman, S. K. Miller, S. Petri, and D. Coumou, 2018: Projected changes in persistent extreme summer weather events: The role of quasi-resonant amplification. *Sci. Adv.*, **4**, 1–10, https://doi.org/10.1126/sciadv.aat3272.

Marinaro, A., S. Hilberg, D. Changnon, and J. R. Angel, 2015: The North Pacific-driven severe Midwest winter of 2013/14. *J. Appl. Meteorol. Climatol.*, **54**, 2141–2151, https://doi.org/10.1175/JAMC-D-15-0084.1.

Moore, B. J., A. B. White, D. J. Gottas, and P. J. Neiman, 2020: Extreme Precipitation Events in Northern California during Winter 2016–17: Multiscale Analysis and Climatological Perspective. *Mon. Weather Rev.*, **148**, 1049–1074, https://doi.org/10.1175/mwr-d-19-0242.1.

Moore, R. W., O. Martius, and H. C. Davies, 2008: Downstream development and Kona low genesis. *Geophys. Res. Lett.*, **35**, 1–6, https://doi.org/10.1029/2008GL035502.

Morrison, I., and S. Businger, 2001: Synoptic structure and evolution of a Kona low. *Weather Forecast.*, **16**, 81–98, https://doi.org/10.1175/1520-0434(2001)016<0081:SSAEOA>2.0.CO;2.

Otkin, J. A., and J. E. Martin, 2004: A synoptic climatology of the subtropical kona storm. *Mon. Weather Rev.*, **132**, 1502–1517, https://doi.org/10.1175/1520-0493(2004)132<1502:ASCOTS>2.0.CO;2.

Pinheiro, M. C., P. A. Ullrich, and R. Grotjahn, 2019: Atmospheric blocking and intercomparison of objective detection methods: flow field characteristics. *Clim. Dyn.*, **53**, 4189–4216, https://doi.org/10.1007/s00382-019-04782-5.

Ralph, F. M., P. J. Neiman, and G. A. Wick, 2004: Satellite and CALJET Aircraft Observations of Atmospheric Rivers over the Eastern North Pacific during the Winter of 1997/1998. *Mon. Wea. Rev.*, **132**, 1721-1745, doi:10.1175/1520-0493(2004)132<1721:SACAOO>2.0.CO;2.

Ralph, F. M., P. J. Neiman, and R. Rotunno, 2005: Dropsonde observations in low-level jets over the northeastern Pacific Ocean from CALJET-1998 and PACJET-2001: Mean vertical-profile and atmospheric-river characteristics. *Mon. Wea. Rev.,* **133**, 889–910

Ralph, F. M., T. Coleman, P. J. Neiman, R. J. Zamora, and M. D. Dettinger, 2013: Observed impacts of duration and seasonality of atmospheric-river landfalls on soil moisture and runoff in coastal northern California. *J. Hydrometeorol.*, **14**, 121026084711009, https://doi.org/10.1175/JHM-D-12-076.1.

Steinschneider, S., and U. Lall, 2015: A hierarchical Bayesian regional model for nonstationary precipitation extremes in Northern California conditioned on tropical moisture exports. *Water Resour. Res.*, **51**, 1472–1492, https://doi.org/10.1002/2015WR017200.A.

Swain, D. L., 2015: A tale of two California droughts: Lessons amidst record warmth and dryness in a region of complex physical and human geography. *Geophys. Res. Lett.*, **42**, 9999–10003, https://doi.org/10.1002/2015GL066628.

——, M. Tsiang, M. Haugen, D. Singh, A. Charland, B. Rajaratnam, and N. S. Diffenbaugh, 2014: The Extraordinary California Drought of 2013/2014: Character, Context, and the Role of Climate Change. *Bull. Am. Meteorol. Soc.*, S3S96.

——, B. Langenbrunner, J. D. Neelin, and A. Hall, 2018: Increasing precipitation volatility in twenty-first-century California. *Nat. Clim. Chang.*, https://doi.org/10.1038/s41558-018-0140-y.

White, A. B., B. J. Moore, D. J. Gottas, and P. J. Neiman, 2019: Winter storm conditions leading to excessive runoff above California's Oroville dam during January and February 2017. *Bull. Am. Meteorol. Soc.*, **100**, 55–69, https://doi.org/10.1175/BAMS-D-18-0091.1.

Winters, A. C., L. F. Bosart, and D. Keyser, 2019: Antecedent north pacific jet regimes conducive to the development of continental U.S. extreme temperature events during the cool season. *Weather Forecast.*, **34**, 393–414, https://doi.org/10.1175/WAF-D-18-0168.1.

Zhang, Z. F. M. Ralph, and M. Zheng, 2018: The relationship between extratropical cyclone strength and atmospheric river intensity and position. *Geophys. Res. Lett.,* doi:10.1029/2018GL079071.

Chapter 5

Characterizing coastal air-sea surface temperature variability in Northern California during landfalling atmospheric rivers

Abstract

Wintertime sea surface temperature (SST) variability has received little attention in the California Current System (CCS). However, California receives the majority of its precipitation during the winter months, often from extra-tropical cyclones and atmospheric rivers (ARs). While the impact of SSTs on extra-tropical cyclones in western boundary currents is understood, little is known about the impact of SST variability on ARs. This study characterizes the average and standard deviation wintertime SST throughout the eastern North Pacific from two datasets: Optimal Interpolation (OI) v2 and Multi-scale Ultra-high Resolution (MUR). Consistent with seasonal changes, SST cools from October-March, with increased variability in the MUR SST, especially in regions of mesoscale eddy activity. An assessment of interannual variability of wintertime SST shows large differences year-to-year in both datasets. We find that some years of low variability are also years of low AR activity. Buoy stations in Northern California are used as an Eulerian perspective of SST, air temperature, and wind speed around AR conditions. ARs are identified using the Rutz et al. (2014) catalog at Bodega Bay, CA. The average air-sea temperature difference (ASTD) prior, during, and post AR passage, at the Point Reyes, CA station buoy shows increasing, positive, and decreasing values, consistent with an approaching warm front, AR conditions, and cold air advection, respectively. Due to the large variability within the general trends in ASTD, satellite and buoy observations of three recent case studies of

impactful precipitation events are evaluated providing further understanding into the relationship between AR activity, SST, and precipitation.

5.1 Introduction

The ocean plays a vital role in the Earth's climate. Its vast extent, ability to store and transport heat and its interactions with the atmosphere and land, shape weather and climate around the globe. As ocean currents meander and change they alter sea surface temperatures (SSTs) and surface wind patterns. On large scales, the atmosphere, primarily through surface winds, influences the ocean circulation. This feedback between ocean and atmosphere is important for the climate system, especially when modeling the climate past, present or future. High resolution SST is valuable for the accurate representation of atmospheric processes, and parameters such as storm track activity, extra-tropical cyclones, temperature, and precipitation (Kirtman et al. 2012, Ma et al. 2017, Parfitt et al. 2017). The air-sea interactions throughout the tropical Pacific, i.e. the El Niño/Southern Oscillation, are more heavily researched however, the importance of wintertime SSTs in the midlatitudes is less explored.

The development of SST and surface wind satellites was influential in the understanding of midlatitude air-sea interactions, particularly at the mesoscale (Chelton and Xie 2010). These advances led to the discovery of positive correlations between SST and surface wind speed at 10-1000 km, opposite of what is known about large scale processes (e.g., Liu et al. 1994). The positive correlation thus has a direct impact on the response of the atmospheric boundary layer. The coupling between the ocean and atmospheric boundary layer are related via two mechanisms: a) the dependence of the atmospheric boundary layer height on its stratification and b) the generation of horizontal pressure gradients (Small et al. 2008, Gemmrich and Monahan

2018). Mechanism a) occurs as positive SST anomalies create instability in the atmospheric boundary layer, increasing its height, while mechanism b) occurs because the SST anomaly forces an air temperature and moisture anomaly, increasing hydrostatic pressure and the resulting wind speed. In the eastern Pacific, where there is less variability in SST than in the Atlantic, SST anomalies are mainly driven by wind anomalies either through upward air-sea fluxes or through increased mixing of the oceans mixed layer (Gemmrich and Monahan 2018). The relationship between SST and the atmospheric boundary layer, particularly in the eastern Pacific, is of interest as ARs dominate the wind speed extremes in this region (Waliser and Guan 2017). ARs are long, narrow and transient corridors of atmospheric vapor transport that often occur ahead of the cold-front of an extra-tropical cyclone. ARs are responsible for extreme precipitation and flooding throughout the western US (Dettinger et al. 2011, Lamjiri et al. 2017, White et al. 2019, Moore et al. 2020). While the influence of extra-tropical cyclones and western boundary currents has been studied (Kelly et al. 2010, O'Reilly and Czaja 2015), little is known on the relationship between eastern Pacific SSTs and ARs.

During the CalWater-2015 campaign (Ralph et al. 2016), which included aircraft, land and ship-based observations, the NOAA *Ronald H. Brown* ship took unique observations in the data sparse Pacific Ocean during an AR (Neiman et al. 2017). The observations from January 20-26, 2015 included sea surface temperature, air temperature, sensible and latent heat fluxes and rawinsonde profiles. These observations were some of the first observed through a series of mesoscale frontal waves embedded in ARs (Martin et al. 2019). Timeseries throughout the seven-day event showed the variability of the air temperature due to the passage of multiple fronts, alternating greater or less than the SST, changing the heat fluxes and stability of the lower

atmosphere. However, this is just one case study investigating the relationship between SST, air temperature and heat fluxes.

This study aims to advance our understanding of air-sea interactions during AR events affecting Northern California. In the sections that follow, we introduce the two satellite SST datasets, buoy stations and locations for SST, air temperature and windspeed, AR catalog and precipitation dataset used. We then describe the results of the analysis as follows: a) climatological comparison of variability within two satellite SST datasets; b) variability of air-sea temperature difference during landfalling ARs; and c) case studies: event description and impact.

5.2 Methods

a. Satellite sea surface temperature

1. NOAA OI v2 SST

The National Oceanic and Atmospheric Administration (NOAA) high resolution optimal interpolation (OI) generated SST data (Reynolds et al. 2007) were used to evaluate North Pacific SST spatiotemporal variability. It is a blended analysis of daily global SST at 0.25º latitude x 0.25º longitude resolution, extending from 1981 to present.

This study used all full years of data, 1982-2019, to investigate the interannual variability and mean conditions of eastern North Pacific SST. While large improvements to increase SST variance and SST gradient occur when the Advanced Very High Resolution Radiometer (AVHRR) infrared satellite SST data and the Advanced Microwave Scanning Radiometer (ASMR) satellite SST data are combined (Reynolds et al. 2007), that dataset only extends from 2002-2011, thus the longer dataset, AVHRR-only, was chosen to better quantify long term trends

across the region of interest and evaluate recently occurred cases (Banzon et al. 2016). This AVHRR-only SST product integrates in situ ship and buoy data and includes large-scale adjustments from satellite biases due to those observations.

2. JPL MUR SST

The Group for High Resolution Sea Surface Temperature (GHRSST) Level 4 SST product produced at the Jet Propulsion Laboratory (JPL) Physical Oceanography Distributed Active Archive Center was used to analyze high resolution SST across the eastern North Pacific. This dataset is a blended SST product incorporating observations such as those from the AVHRR, the AMSR, the Moderate Resolution Imaging Spectroradiometers (MODIS) on both the Aqua and Terra NASA platforms as well as in situ SST observations. This SST product is a global daily, 0.01º latitude x 0.01º longitude resolution dataset, starting in late 2002 extending through present.

This study used the Multi-scale Ultra-high Resolution (MUR) SST (JPL MUR MEaSUREs Project, 2010) to evaluate SST and its evolution throughout various atmospheric river case studies. The MUR SST dataset was chosen due to the high spatial resolution, complementing the NOAA OI v2 SST, described further in section II.a.1. This study used full years of SST data from 2003-2019 to analyze the average wintertime SST characteristics and seasonal SST changes in the North Pacific. This dataset further complemented buoy data for the case studies investigated.

b. Surface buoy stations

The NOAA National Data Buoy Center (ndbc.noaa.gov) was used to select and obtain surface buoy data around Bodega Bay, CA. Three buoy stations were chosen for use due to their proximity to one another, relatively long duration of overlapping observations and availability of both atmosphere and sea surface temperature observations. The three stations selected were: Station PRYC1 Point Reyes, CA (PR; Lat: 37.996ºN, Lon: 122.977ºW), Station 46013 Bodega Bay, CA (BBY; Lat: 38.253ºN, Lon: 123.303ºW), and Station 46026 San Francisco, CA (SF; Lat: 37.754ºN, Lon: 122.839ºW) shown in Fig. 5-1. In addition to air (ºC) and sea surface temperature (ºC), wind speed (m/s) was also used in case study analyses from these buoys to identify frontal passage above the buoy. The BBY buoy records data every 10 minutes, the PR station every 6 minutes and the SF station every 60 minutes.

The PR station, due to its location and continuous air and sea surface temperature data from 2011-2017 was selected to evaluate the climatological air-sea temperature difference before, during and after atmospheric river activity.

c. Reanalysis data

The Modern-Era Retrospective analysis for Research and Applications, Version 2 (MERRA-2) dataset (Gelaro et al. 2017) is used to evaluate the case studies large-scale characteristics and available moisture. MERRA-2 is used for its high spatial resolution and numerous assimilated observations including satellite-derived atmospheric motion and surface wind vectors important for the accurate detection of ARs.

These reanalysis data are sampled to evaluate the 850-hPa geopotential heights and integrated water vapor (IWV) associated with each case study to provide an understanding of

low-level storm characteristics and water vapor content, respectively, across the North Pacific. These two variables combined allow for the inference of the amount water vapor transport, otherwise known as integrated water vapor transport (IVT), which is used to identify ARs, along with other criteria.

d. Atmospheric river catalog

The Rutz et al. (2014) atmospheric river (AR) catalog was used to identify landfalling ARs in Bodega Bay, CA in the MERRA-2 dataset described in II.c. This catalog defines an AR object based on grid box IVT values greater than 250 kg m^{-1} s^{-1} and an overall feature length greater than 2000 km. This catalog has no width requirement.

The grid box covering Bodega Bay, CA, located at 38.0ºN, 123.125ºW, was used to identify ARs advected over the buoys that made landfall east of their location. At this location and for the MERRA-2 AR catalog version, data are available from 1980-2017 at 3-hr intervals. Coinciding with the buoy data availability and the chosen case studies, this catalog was analyzed from 2011-2017.

e. Precipitation data

To investigate the precipitation magnitude and pattern of each case study, PRISM daily precipitation data are used. PRISM, available from 1981-2019, uses point data and a digital elevation model to generate gridded estimates of precipitation and other climate variables (Daly et al. 1994, 2001, 2002). The PRISM daily precipitation dataset is chosen for its strength in representing precipitation in mountainous regions such as the western US and its high spatial resolution of 4km.

5.3 Results

a. Climatological comparison of variability within satellite SST

ARs make landfall along the US West Coast seasonally, typically during winter months (DJF) and occasionally during shoulder season months (ON, MA) (Ralph et al. 2019, Rutz et al. 2019, Gershunov et al. 2017). A 38-year average of monthly (October-March) SST from 1982-2019 was computed to investigate the average sea surface ARs would encounter (Fig. 5-2). The well-documented coastal upwelling due to southerly winds along the California coast (e.g., Chelton et al. 2007) is still evident in October (Fig. 5-2, a). Domain wide cooling enhances every month with the largest extent of cool SSTs during March. The southward advection of cool waters in the California Current System (CCS) amplifies as the currents feeding the CCS, such as the North Pacific Current, and the Alaska Current seasonally cool. The coastal upwelling longitudinal extent varies monthly, as it decays over the winter months. In October, the cooler SSTs are constrained to the coast, and they extent 5ºW in November/December. The standard deviation of the monthly SST diminishes from October – March. In October/November, higher standard deviation values are found in the upper left quadrant of the eastern Pacific domain (Fig. 5-2, a), likely coinciding with the exit of the storm track region. By March, there is little variance across the eastern Pacific domain, consistent with previous studies (e.g. Gemmrich and Monahan 2018), indicating that early season AR events have a higher chance of experiencing a range of underlying SSTs and/or impacting the sea surface compared to late season AR events.

The same analysis was computed on the JPL MUR SST dataset, which has a shorter length of record but higher spatial resolution (Fig. 5-3). Similar average monthly conditions are found even with the shorter dataset, suggesting the representativeness of the last decade and a

half for the past 40 years. However, the increased resolution does contribute to more variance across the domain. To see the average SST conditions for each month, the contour interval was increased from 0.1 (Fig. 5-2) to 0.15 (Fig. 5-3). The increased variability was quite noticeable, albeit at small values, from January-March, where there is a lack of cohesive standard deviation. The MUR SST is able to capture the higher variability present in the CCS compared to the interior ocean (Fig. 5-3 a, b, c, f).

This study continues to use both the OI and MUR SST datasets because of the different benefits they add to the analysis, a longer-term record or higher resolution, and to highlight the implications resolution can have on understanding case study events.

The wintertime (October-March) monthly averaged standard deviation from the OI and MUR SST datasets are also examined (Figs. 5-4 and 5, respectively). Contrasting the figures above, which evaluated the average monthly conditions, we analyze the standard deviation of SST within a winter season (i.e., October 1982-Mar 1983). The OI SST, with the longer duration, shows the large variability of standard deviation across water years (WYs). For example, WYs 1986 and 2003, both have large standard deviations in the ocean interior of the eastern Pacific domain, while WYs 1985 and 2011 saw minimal variance in the same region. While not a focus of this study, the Gulf of California often has much larger standard deviations than the coastal regions. Comparing the two datasets, the magnitude and locations of variability is similar for the overlapping WYs.

The drought years in California, particularly 2011, 2012, 2014, and 2015 stand out as years with less SST change. However, that drought period, from 2011-2016, is only one event and other factors should be considered given that WY 2013 continued to experience normal SST variability. This raises the question whether the offshore variability in SST could be related to

increased storm activity. Using atmospheric reanalysis data, Fish et al. (2020, *in review*) analyzed atmospheric river (AR) activity impactful to California from 1981-2019, finding large year-to-year variability of AR and successive AR activity. For the eight years with less than 50% of all AR activity occurring in succession of one another, only four correspond to low variance (1985, 1991, 2008, 2009), with the others showing higher values of variability (1987, 2001, 2003, 2007). This suggests that AR activity alone does not support increased ocean surface variability despite the frequent association of ARs and extreme wind speed (Waliser and Guan 2017). Further analysis of storm track location, variability of the Kuroshio current and extra-tropical cyclone activity should be completed to add to the understanding of interannual offshore SST variability.

b. Variability of air-sea temperature difference during landfalling ARs

The air-sea temperature difference before, during, and after AR passage over the PR buoy station was evaluated from all ARs identified using Rutz et al. (2014) during 2011-2017 (Fig. 5-6). At 3-hr intervals, 24-hrs before and after the AR duration, the median air-sea temperature difference increased with time before the AR and decreased with time after the AR passage. This result agrees with our hypothesis that the pre-cold front area or warm sector would approach the station, followed by the passage of the cold front after the AR. During the AR, the median air-sea temperature is positive, 1ºC. While there is an increasing, constant positive and decreasing trend before, during and after an AR passage, respectively, the whiskers on the box plot show the large variability associated with each AR event. Prior to the AR passage, the air-sea temperature difference ranges from -4 to +4ºC; after the AR passage the range is similar. Even during AR hours, there is considerable spread in the air-sea temperature difference, which ranges from -2 to

+4ºC. These results, also replicated for Eureka, CA, Tanners Bank, CA and Santa Barbara, CA buoy stations with similar results (not shown), are further investigated by evaluating case studies to understand each event's background SST, strength of IVT, and wind speed changes, to better understand the potential feedback mechanism.

c. Case studies: Event description and impact

The case studies below were chosen for their impactful precipitation across California, the presence of multiple AR events, within a span of 5-days (referred to as AR families; Fish et al. 2019), and recent occurrence.

1. Case #1: February 5-10, 2015

The first case study analyzed occurred during February 5-10, 2015. This event was associated with multiple extra-tropical cyclones, two ARs, and a mesoscale frontal wave development (Neiman et al. 2016) (Fig. 5-7). During this case study, the multi-year CalWater field campaign was held, which included aircraft, ship, and ground observations (Ralph et al. 2016, Cordeira et al. 2017, Neiman et al. 2017). This AR family was mainly impactful, precipitation-wise, for Northern California (Fig. 5-7). The coastal mountains north of the Delta Region received the highest precipitation totals, greater than 300mm in some locations, while the Northern Sierra Nevada mountains were also impacted.

In the beginning of 2015, 'The Blob' was still impacting the North Pacific, which started in the fall of 2013 (Lee et al. 2015; Peterson et al. 2015; Hu et al. 2017). The warm SSTs in the region are evident on the Hovmöller diagram over the event's duration (Fig. 5-8). The Hovmöller diagram centered at 38ºN, extending from 140-123ºW for both the JPL MUR and NOAA OI SST show warm, greater than 14ºC temperatures over the nine-day period shown. Cooler

temperatures are located close to the coast, with warmer regions greater than 16ºC, around 134ºW and 130ºW. Comparing the MUR and OI SSTs shows general agreement between the two datasets, with higher resolution features, such as mesoscale eddies, more evident in the MUR SST. Noticeable differences include large magnitude differences between the two datasets near the end of the event (February 8-10, 2015) between 134-130ºW, with cooler SSTs in the MUR SST compared to the OI SST.

Over this six-day case study, there were two ARs to make landfall, the first event was much stronger, depicted by the thickness of the black arrows in Fig. 5-9 during February 5-6, 2015. The orientation of the IVT changes throughout the case study from southwest to northeast, parallel or perpendicular to the coast. Outside of the AR family duration, there is a third strong AR poised to impact California at the end of this case study. To determine if the strong water vapor transport, based on a combination of wind speed and low-level water vapor, impacts the SST, the daily values across a large region are shown (Fig. 5-9). While unable to visibly differentiate in the previous figure, the change of SST over the duration of the case study is plotted (Fig. 5-10). This figure highlights the cooling of SSTs offshore in central California and near the CA-OR boarder. Close to the coast and a large region south of 35ºN, experience warming SST instead. This divide in warming or cooling SST coincides with the strongest IVT from the first AR of this case.

The air temperature and SST were evaluated from the BBY, PR and SF buoy stations over the duration of this case study (Fig. 5-11). Generally, each buoy experiences the same air temperature increase during the first AR passage, shaded in gray, followed by a decrease as the cold front passes over the buoy. The second, shorter duration AR, brings a smaller but detectable air temperature increase. Strong cooling follows this AR event. Comparing start and end SST,

there is an increase in SST at each buoy over this five-day period. The BBY and SF buoys records a drop in SST during the first AR passage, while the PR buoy increases during the same event. Even though these buoys are within a latitude degree of one another, there are SST differences of up to 0.7ºC across the buoys at the same time. Changes between buoy observations at the same time, highlight the need for a multi-scale evaluation of SSTs during AR conditions. This is further highlighted when comparing the air-sea temperature difference, bottom panel, for each station. Each station experiences an increase in air-sea temperature difference as the first AR progresses, a drop between the events then a second period of positive air-sea temperature difference during the second event. However, the BBY and SF buoy both record periods of near neutral temperature differences, while the PR buoy is positive across the entire timeseries, seemingly from an increased SST recorded at that station. The PR station also experiences an increase in air-sea temperature difference near the end of the timeseries, not present at the other locations, likely due to the increase in air temperature only observed at that buoy.

Wind speed measurements across the three buoy stations were also analyzed (Fig. 5-12). The buoys recorded similar wind speed timeseries across this case. There is a steady increase in wind speed until February 7, a sharp decline until February 8th when wind speeds start to increase again, indicating the second approaching frontal passage. SF records the fastest wind speed, 18 m/s, during the first AR passage, while PR records 14 m/s at that same time.

This case from early February 2015, represents a standard AR and air-temperature, dominated event. While there were unusually warm SSTs throughout the duration of this event, the air-sea temperature response closely resembled average conditions before, during and after the AR passage. However, there were some noted differences across the event such as, SST agreement between the buoy stations and magnitudes in peak wind speed. This case further

highlights the importance of a complete and multi-scale analysis for the case studies to understand the relationship between SST, air temperature, wind speed, and AR characteristics and impacts.

2. Case #2: January 3-10, 2017

The second case study evaluated occurred from January 3-11, 2017. During this long event, there were multiple extra-tropical cyclones and associated ARs that propagated across the North Pacific (Fig. 5-13). This event was very impactful for California including the entire Sierra Nevada mountain range and the coastal mountains from the central coast to the CA-OR border. In many of these locations, precipitation was greater than 400mm. Compared to case #1, this case had more IWV north of 30ºN and each filament-like structure had greater than 50mm of IWV. The 0000 UTC snapshots of 850-hPa geopotential heights from January 3-10, highlight the numerous cyclones that were generated and propagating towards the US West Coast during this time period.

The Hovmöller diagram of this case study is quite different than case #1 (Fig. 5-14). The coastal SST are cool, 11-12ºC, and increase offshore to 14-15ºC in the MUR SST. The NOAA OI SST is characterized by cooler coastal SSTs, and lower SSTs offshore. Compared to the 2015 case study, the background warm SSTs have returned to more average January values. While there is general consensus between the two SST datasets, the magnitude, duration and extent of offshore warm SSTs differ as well as the magnitude and extent of cool coastal SSTs.

There were three ARs to make landfall during this event duration. The middle AR event occurring from January 7-9, 2017 was the strongest (Fig. 5-15). Out of the daily IVT average, three days displayed direct onshore IVT near the Delta Region, which has been shown to be a

direct corridor for moisture transport into the mountains (Lamjiri et al. 2018). The background SST during this event was cooler than case #1 with a more southerly extent of cold California Current SSTs. Over the course of the analyzed eight-day time period, SSTs warmed across the California Bight and offshore of central California (Fig. 5-16). There is strong cooling west of 140ºW and north of 39ºN. The pattern of cooling or warming does not follow IVT corridors as found during case #1 but instead appears more random.

The buoy timeseries during this event show similar trends found in the satellite SST data with some exceptions (Fig. 5-17). The PR and SF buoy both record SST cooling during the break between the first and second AR, while the BBY buoy records constant SST. All buoys from start to end time, increase SST. The air temperature variability associated with the passage of ARs follows an expected pattern of declining air temperature between the first two ARs, followed by an increase through the end of the second AR. The short break between the second and third AR records a decrease in air temperature, but it is short lived and small in magnitude. However, this event is interesting when considering the air-sea temperature difference. During all three AR events, this difference is markedly positive. Between the first and second AR, the air-sea temperature difference becomes negative, as the air temperature becomes much colder than the ocean surface, creating a stable layer near the sea surface. Between the second and third AR event, conditions are closer to near neutral. While it seems that the difference between these two types of post-AR air-sea temperature differences can be attributed to the ambient AR air temperature, further work should evaluate the impact of the near neutral conditions compared to a low-level stable layer on wind speed, IVT and other AR metrics.

The wind speed timeseries from the three buoys show the increase and decrease of wind speeds associated with the passage of extra-tropical cyclones and ARs (Fig. 5-18). The middle

AR has the highest observed wind speed during this time series at 16 m/s. The PR buoy captures weaker wind speeds than the BBY or SF buoy, potentially due to its proximity to the coast, but shows general agreement with the other two stations.

Case study #2 from January 2017, showed that while the background SST was cooler than the February 2015 case, the large presence of enhanced IWV and multiple cyclones routinely produce large amounts of precipitation. This case had a shorter duration of peak IVT than the February 2015 case but the event itself had a longer duration. The widespread warming of coastal SSTs south of 38ºN was different than seen in the February 2015 case, when warming was dominated by the lack of strong IVT. This January 2017 case provided the first example of negative air-sea temperature difference, potentially creating a stable layer near the surface due to the colder air temperature above the warm, unmixed ocean below. The February 2015 and January 2017 cases, while just two cases, show that overall warm SSTs do not necessarily drive higher precipitation but that this process if complex and storm/AR characteristics are also important.

3. Case #3: February 14-21, 2017

The third and final case evaluated in this study is from February 14-21, 2017. This event is characterized by three ARs, multiple associated cyclones and large precipitation across California (Fig. 5-19). The first AR in this series is short in duration while impacting BBY, yet is a long filament AR event, with moisture extending from the Pacific Northwest to the western Pacific. The entire North Pacific basin is dominated by the deep Aleutian low and its associated moisture transport for the first three days of this time period. Another disturbance off of China starts to develop by February 17, 2017 altering the large-scale pattern along with the

development of mid-Pacific mesoscale frontal waves, which ultimately develop into ARs that impact the US West Coast. Precipitation mainly falls in the coastal mountains of central and Northern California and in the northern Sierra Nevada mountains.

While just over a month after the January 2017 case, the Hovmöller SST diagram for the February 2017 is cooler, especially between 135-130ºW. Coastal, east of 125ºW, SSTs have warmed compared to the January 2017 case up to ~13.5ºC in both the MUR and OI SST datasets. The two different resolution datasets, while similar, differ the most on the two days prior to AR activity over February 12-13. The MUR SST is 1ºC or more warmer during those two days before AR activity.

Eastern North Pacific SSTs are visibly cooler compared to earlier case studies with offshore SSTs mostly between 11-15ºC (Fig. 5-21). The strength of the first AR event is depicted by daily averaged IVT from February 14-16. Inland penetrating IVT is visible throughout this event duration. Unlike the previous cases, this February 2017 case experiences widespread cooling throughout the event (Fig. 5-22). The only locations not experiencing cooling are two circular regions at 130ºW from 42-45ºN, which experience over 1ºC of warming.

The February 2017 case has two short duration AR events and one long duration AR event at Bodega Bay. Given the two, short duration ARs which start the timeseries buoy analysis, the expected warming during the AR is only recorded in the second and third AR event, but to a much greater extent and duration over the third AR (Fig. 5-23). This result is slightly unexpected as the first AR was the strongest according to IVT magnitude, compared to the other events, showing the importance in duration for the buoy to record warming air temperature. SST cooling is recorded at all three buoy stations decreasing from 14 to 12ºC but is less clear for BBY. Unlike the other two events, the air-sea temperature difference is not characterized by large magnitude

swings, long durations of positive difference, but instead exhibits near neutral conditions throughout most of the time series. The negative air-sea temperature differences occur during the AR breaks and into the beginning of the third AR, again due to a decrease in air temperature. As the SST decreases throughout the duration of the third AR, the air temperature rises quicker, resulting in the changed sign during this period.

The wind speed timeseries over this period, have stronger increases and declines than seen in the previous cases (Fig. 5-24). Minimum wind speeds occur during breaks in AR conditions as each buoy records similar magnitudes throughout the timeseries, differing from the January 2017 case study. Wind speeds peak at 15 m/s, similar to the other cases and is recorded at all stations.

Case study #3 from February 14-21, 2017 emphasizes that within season events, especially during active WYs, can influence the background SST even during less variable months such as February. This event occurred within a month of case study #2, yet the sea surface and event evolution were different for two impactful events. The change in SST over January-March 2017, which included multiple impactful precipitation events (White et al. 2019; Moore et al. 2020), further emphasizes the relatively large, ~3 K, seasonal change of SST across the eastern Pacific Ocean (Fig. 5-25). The analysis of these two events highlights the importance of studying case studies, within and across years, in addition to average trends to understand how the ocean responds to AR activity and the influences of the background state on AR characteristics.

5.4 Conclusion and Discussion

This study characterizes the average wintertime SST from two datasets: the NOAA OI v2 and JPL MUR. The two datasets, which vary in period covered and resolution, agree on average conditions throughout the eastern Pacific. Consistent with seasonal changes, SSTs cool during October-March. While previous studies often focus on summertime SSTs in the CCS, wintertime SSTs coincide with the peak of AR activity, usually in December-February. The two datasets differ on the amount of variability each month averages, with the MUR SST having higher variability then the OI SST, likely given its resolution. Specifically, the higher resolution from the MUR SST shows increased variability along coastal CA, consistent with mesoscale eddy activity often found in this region (Lynn and Simpson 1987, Simpson and Lynn 1990, Stegmann and Schwing 2007, Reynolds et al. 2007).

Interannual variability was also assessed, which showed large differences between year-to-year wintertime SST standard deviations. Some years of low variability correspond to low AR activity but further analysis into storm track location and extra-tropical cyclone activity should also be completed for a deeper understanding of year-to-year variability.

Average air-sea temperature differences from 2011-2017 at the PR buoy in Northern California corresponding to prior, during and post AR passage show an increase, positive and decreasing trend, respectively. This result agrees with our hypothesis that offshore buoys would experience a warming of the air temperature as the AR approaches, maintain positive air-sea differences throughout the duration of the often warm AR, then experience a decline in air temperature after the AR passage due to cold air advection into the region. However, this analysis also highlights the large variability in these characteristics. Both prior and post AR passage, the air-sea temperature difference ranges from -4 to +4ºC, and during the AR, the air-

sea temperature difference can be anywhere from -2 to +4ºC. This variability led to the analysis of case studies to further understanding the relationship between SST and AR associated air temperature.

Three case studies were analyzed: February 5-10, 2015, January 3-11, 2017 and February 14-21, 2017, each an impactful precipitation event in California, precipitating over 300mm in regions across the state. Two satellite SST products, the NOAA OI and JPL MUR, were analyzed in a temporal and spatial context. The Hovmöller diagrams highlight the differences in SST at 38ºN throughout each case study. During winter 2015, the eastern Pacific was still feeling the effects of 'The Blob', persistently warm, SSTs in the North Pacific. The two Hovmöllers in winter 2017, show the impact that active WYs can have on SSTs, greatly reducing SST from January to February. Daily IVT and domain SST changes were also calculated for each event, showing different patterns of cooling across the events. The February 2015 case showed cooling along the corridor of maximum IVT, the January 2017 case showed mixed warming and cooling across the basin, while the February 2017 case showed widespread cooling across the domain. Buoy observations of SST, air temperature, and wind speed at three locations (BBY, PR, SF) were analyzed for each event. Timeseries of these events at these locations allowed for comparisons of peak wind speeds, SST and air temperature changes throughout the multiple AR events within each case. The February 2015 case, with two ARs, was an exemplary case for expected air-sea interactions around AR conditions. During the first AR, air-sea temperature differences were positive and increasing, a sharp decline followed in post-AR conditions, then the pattern repeated for the second AR event. The January 2017 case, with three ARs, showed negative (~3ºC) air-sea temperature differences between the first and second AR, indicating heat and moisture fluxes were moving from the atmosphere to the ocean. Following the start of the

second AR, SST and air-temperatures steadily increased through the end of the timeseries. The February 2017 case, also with three ARs, experienced more neutral conditions throughout the timeseries. While there was an occurrence of negative air-sea temperature differences, the magnitude of this difference was much lower compared to the January 2017 case. Different SST cooling across cases was also identified in coupled regional model simulations (Sun et al., 2020 *submitted*), reinforcing an in-depth analysis into various case studies.

While more research needs to be completed to fully understand how SST variability impacts boundary layer conditions in ARs, this study is a first attempt to address various questions on the relationship between AR activity, sea surface temperature and precipitation. This work also highlights the importance of reanalysis, satellite and observational data for a complete understanding of this relationship. The use and comparison of two SST products, one with a longer-term record, the other, higher resolution, for climatological statistical assessment and case study analyses hints at the importance of SST resolution and the potential impact for modeling and event accuracy. The SST field is an important factor in extra-tropical (e.g., Persson et al. 2008) and tropical (e.g. Camargo et al. 2013) storm development, strength and decay, thus pointing to the potential effect on eastern Pacific ARs and associated extra-tropical cyclones. Additional case studies and further analysis on shoulder season events, including modeling with varying resolution of SSTs, to evaluate SST change and their impact on boundary layer characteristics and resulting precipitation should be completed next.

5.5 Acknowledgements

MAF, AMM, RW, LDM and FMR were supported by grant W912HZ-15-2-0019 from the US Army Corps of Engineers and grant 4600013361 from California Department of Water

Resources. The NOAA OI SST v2 data were provided by the NOAA/OAR/ESRL PSL at Boulder, CO, USA (psl.noaa.gov). The Group for High Resolution Sea Surface Temperature (GHRSST) Multi-scale Ultra-high Resolution (MUR) SST data were obtained from the NASA EOSDIS Physical Oceanography Distributed Active Archive Center (PO.DAAC) at the Jet Propulsion Laboratory, Pasadena, CA (http://dx.doi.org/10.5067/GHGMR-4FJ01). We gratefully acknowledge the availability of the MERRA-2 reanalysis dataset available through the National Aeronautics and Space Administration (NASA) Global modeling and Assimilation Office. These data are available at MDISC, which is managed by the NASA Goddard Earth Sciences Data and Information Services Center. The authors thank Andreas Prein for the preprocessed PRISM data and Jonathan Rutz for the publicly available AR catalogs.

Chapter 5, in part is currently being prepared for submission for publication of the material. Fish, M. A., R. Weihs, A. Michaelis, A. J. Miller, L. D. Monache, and F. M. Ralph. The dissertation author was the primary investigator and author of this paper.

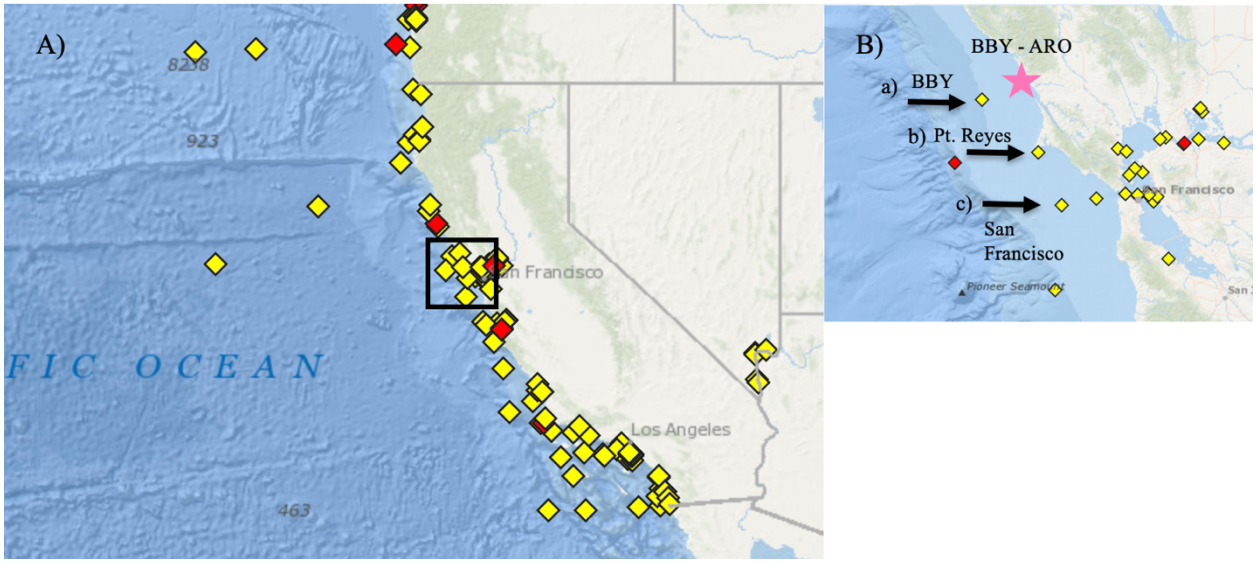

Figure 5-1. A) Buoy stations along the US West Coast (ndbc.noaa.gov). The black box represents the location of the inset. B) The San Francisco Bay area buoy station locations with the three buoys analyzed labeled: a) Bodega Bay, CA (BBY), b) Point Reyes, CA (PR), c) San Francisco, CA (SF).

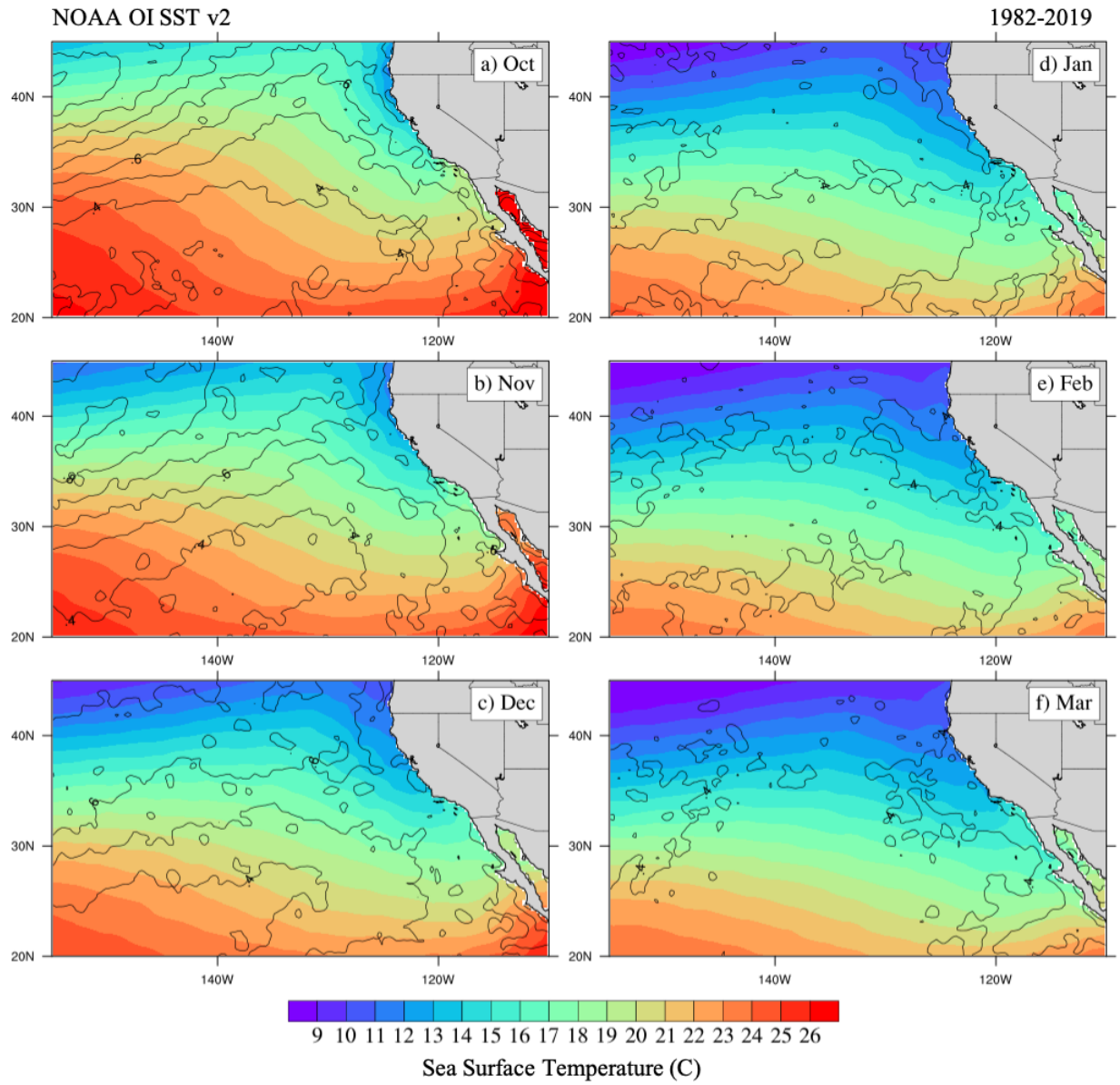

Figure 5-2. Average NOAA OI sea surface temperature v2 (C, shaded contour) and monthly mean standard deviation (C, contour line) for all a) October, b) November, c) December, d) January, e) February, f) March months from 1982-2019. Standard deviation contours 0-1.5, every 0.1.

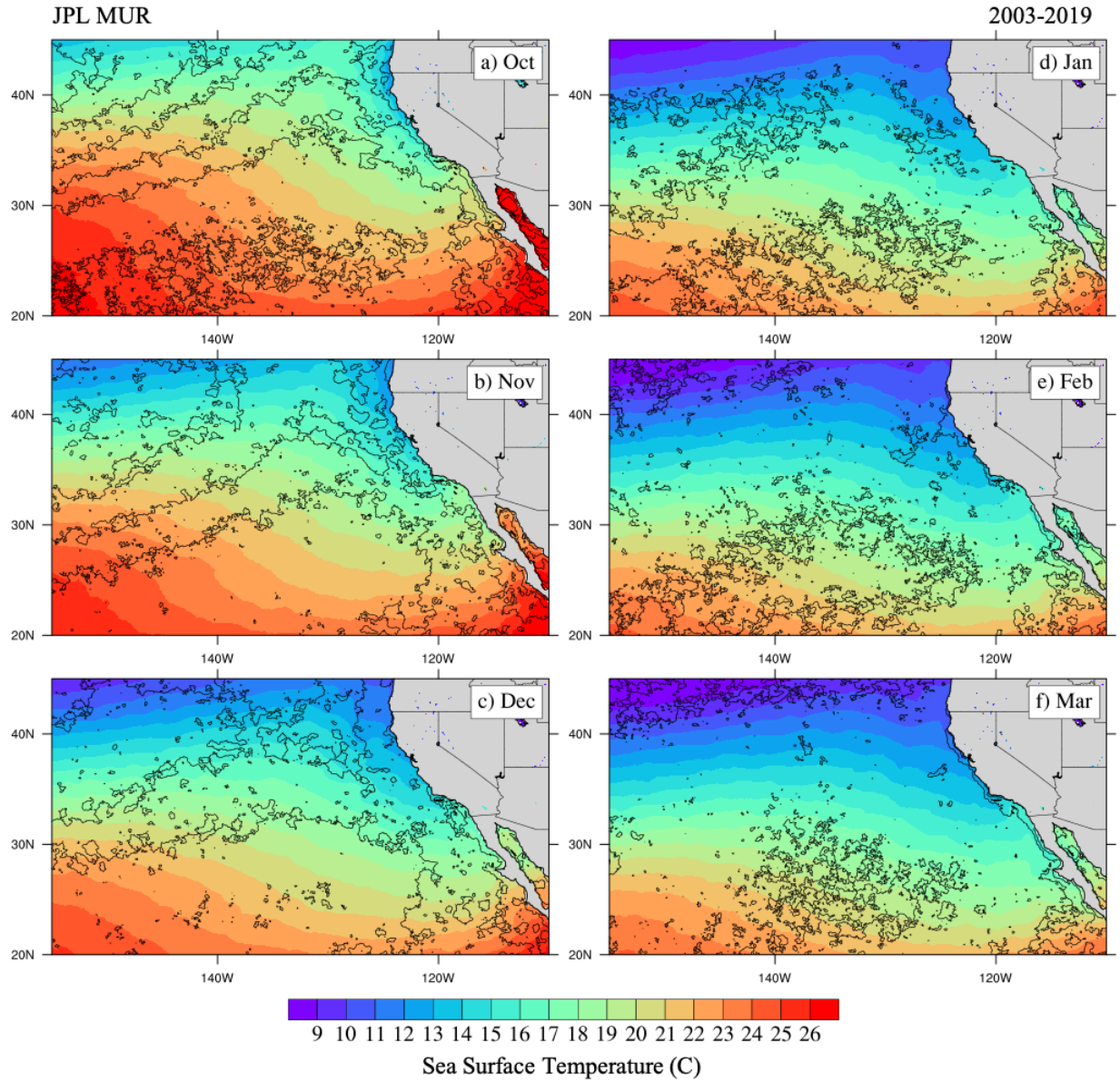

Figure 5-3. Average JPL MUR sea surface temperature (C, shaded contour) and monthly mean standard deviation (C, contour line) for all a) October, b) November, c) December, d) January, e) February, f) March months from 2003-2019. Standard deviation contours 0-1.5, every 0.15.

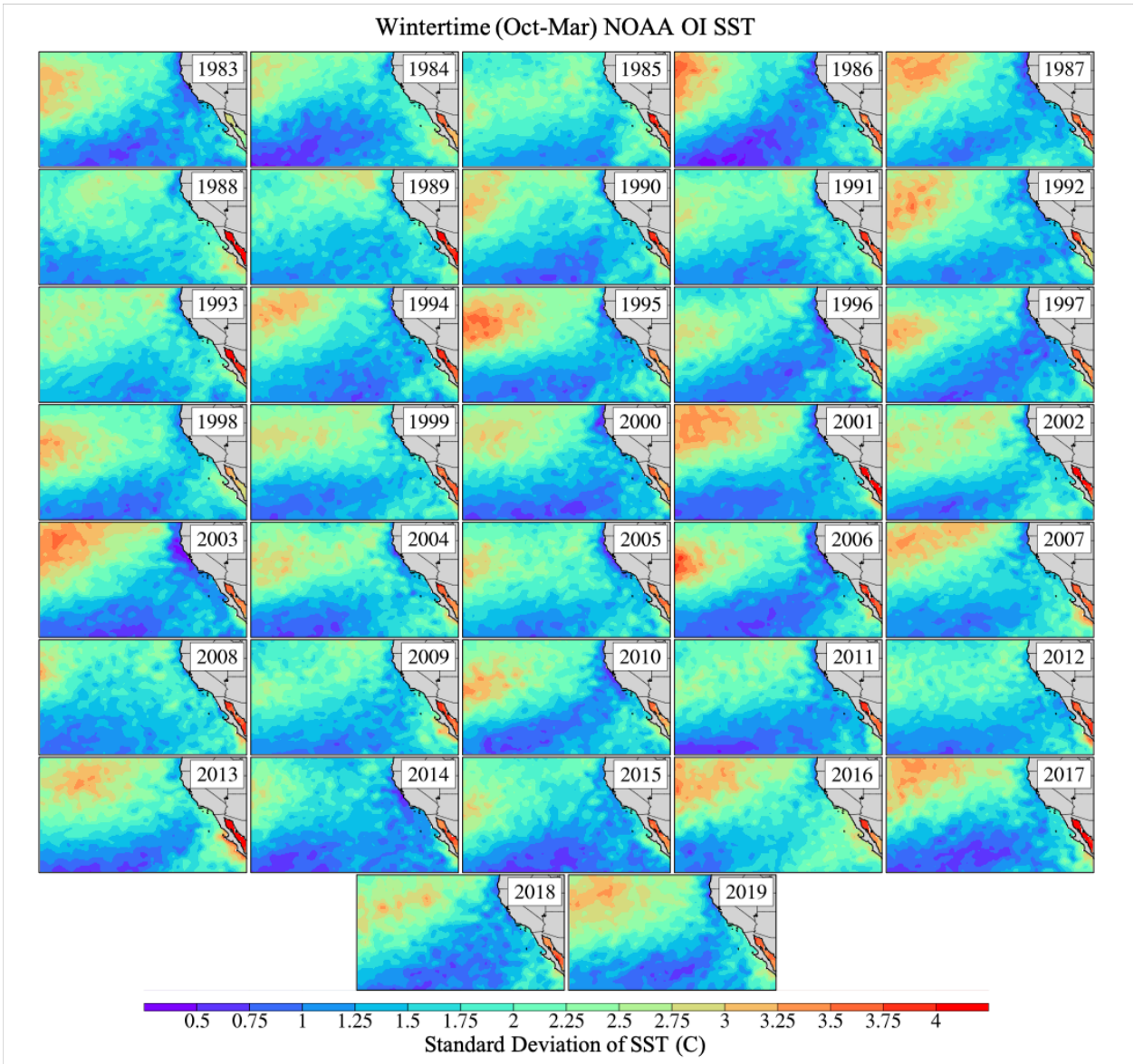

Figure 5-4. The standard deviation of wintertime, October-March, NOAA OI SST from 1982-2019 identifying variations in the seasonal cycle. Years displayed indicated water year (i.e., 1983: Oct-Dec 1982, Jan-Mar 1983).

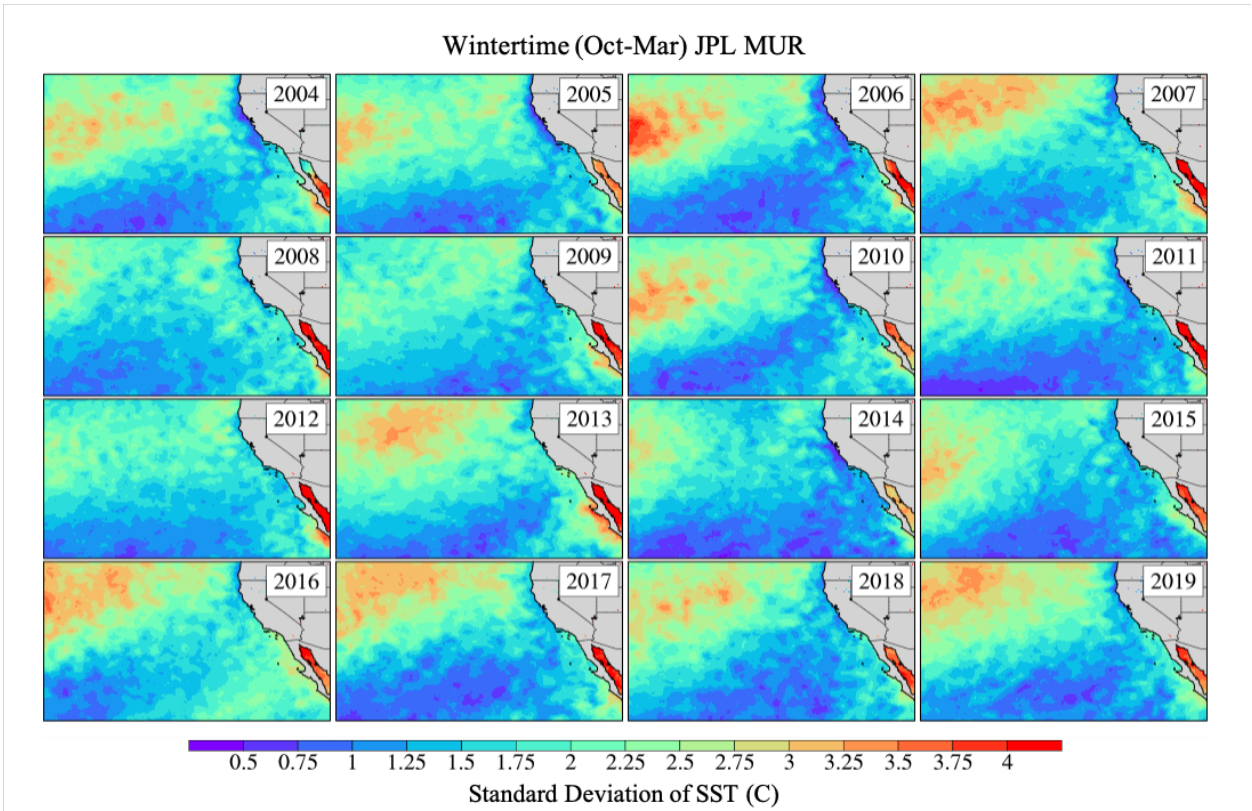

Figure 5-5. The standard deviation of wintertime, October-March, JPL MUR SST from 2003-2019 identifying variations in the seasonal cycle. Years displayed indicated water year (i.e., 1983: Oct-Dec 1982, Jan-Mar 1983).

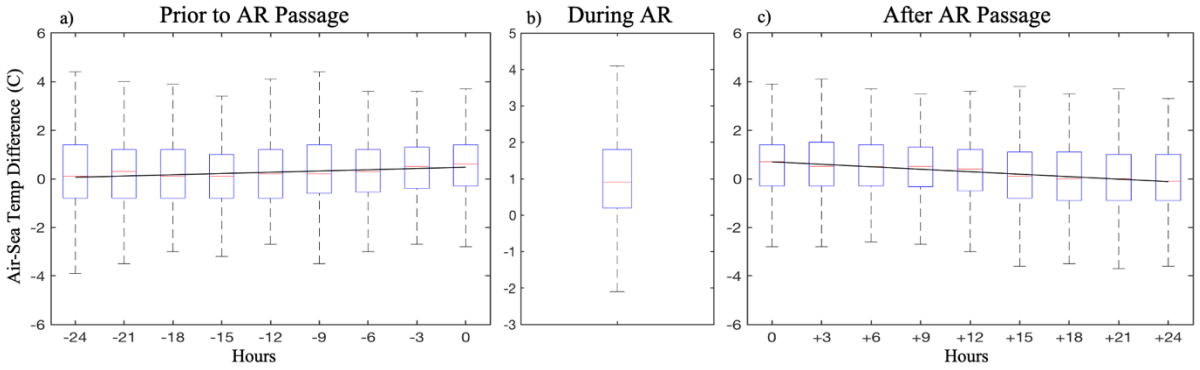

Figure 5-6. Air-sea temperature difference at the Point Reyes buoy a) before, b) during, and c) after the passage of all atmospheric river events from 2011-2017 according to the Rutz et al. (2014) AR catalog for 38ºN and 123.125ºW, the closest grid box for Bodega Bay.

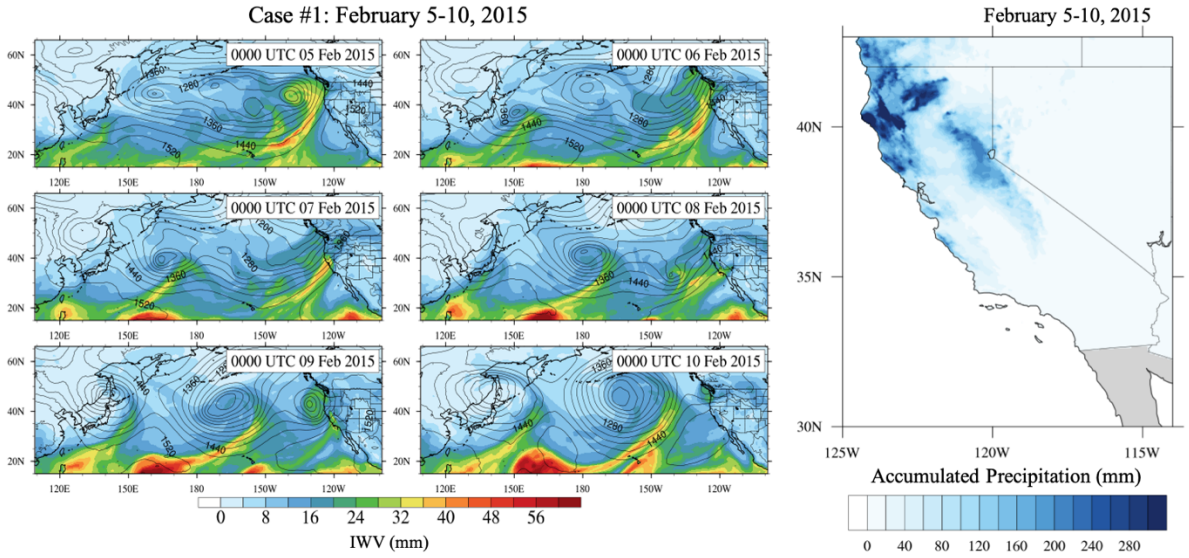

Figure 5-7. A) 850-hPa geopotential heights (m, contour) and IWV (mm, shaded contour) at 0000 UTC from February 5-10, 2015. B) Accumulated precipitation (mm) over the duration of case #1 from Feb. 5-10, 2015.

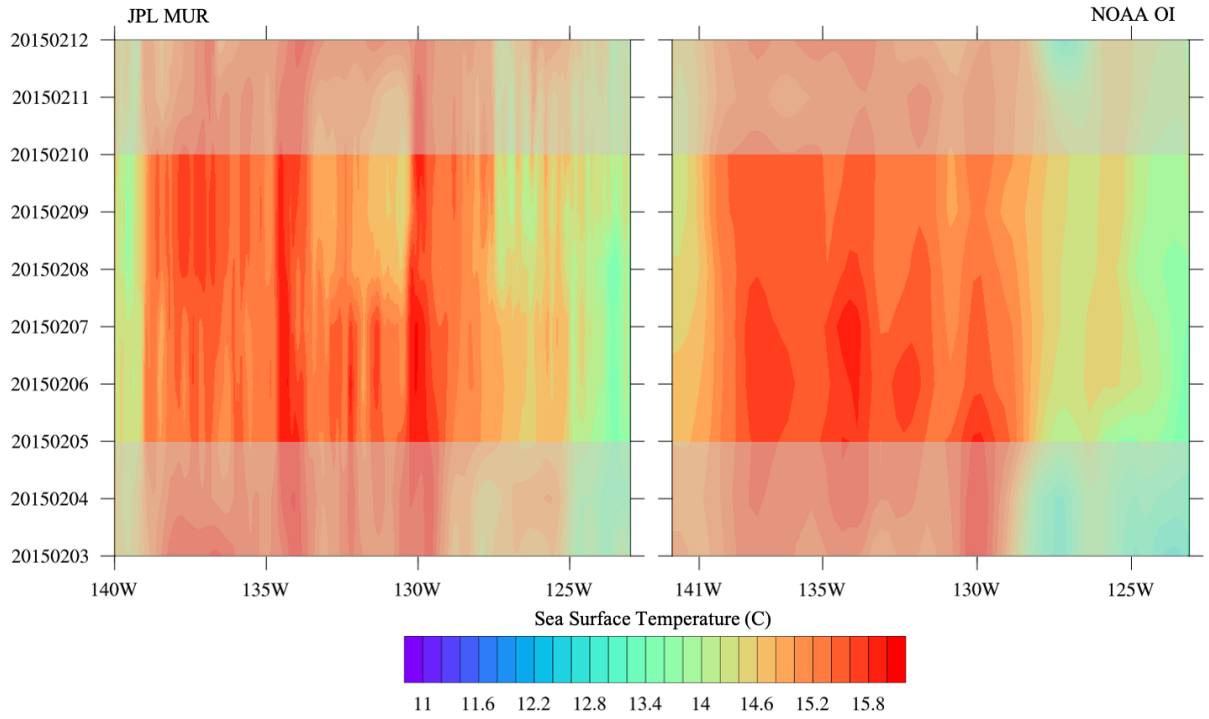

Figure 5-8. Hovmöller diagram of sea surface temperatures two days prior to the start of the case through two days after the event ends. Non-event days are shaded in transparent gray. A) JPL MUR SST, B) NOAA OI SST v2 both centered at 38ºN, extending from 140ºW to 123ºW.

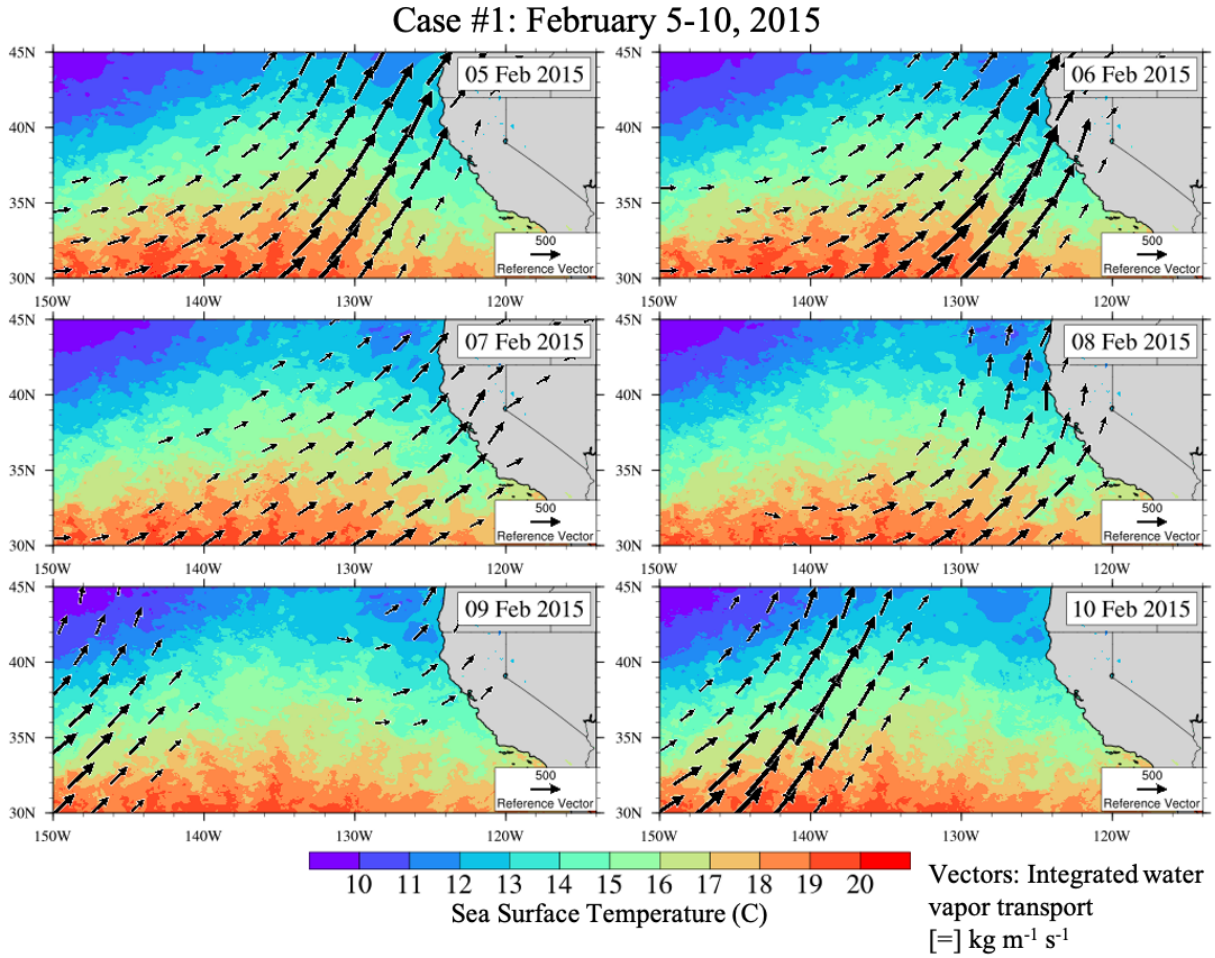

Figure 5-9. Daily MUR SST (C, shaded contour) and daily averaged IVT (kg m^{-1} s^{-1}, arrows) from Feb. 5-10, 2015.

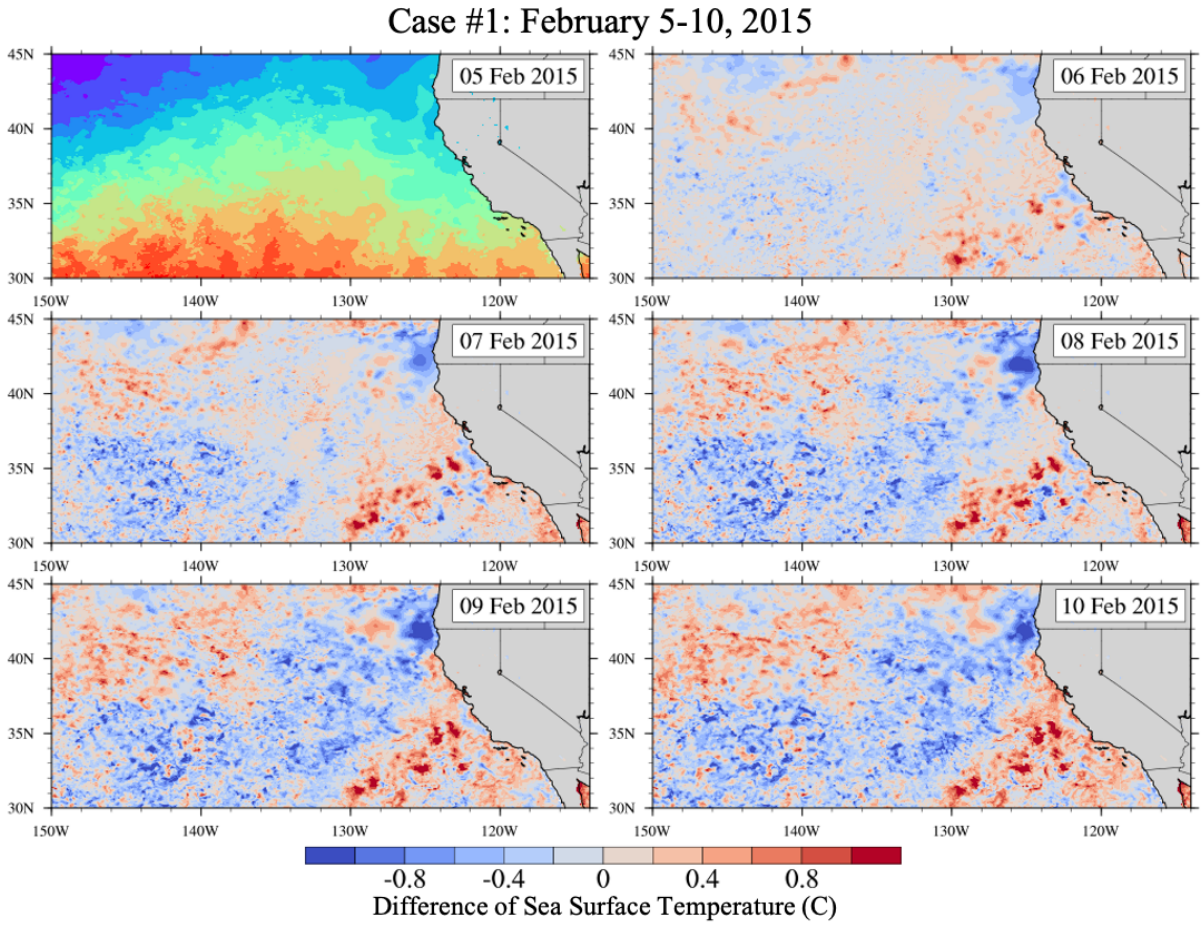

Figure 5-10. Cumulative difference in MUR SST (C, shaded contour) from the Feb. 5, 2015, the start of the case study time period, until the end of the event Feb. 10, 2015.

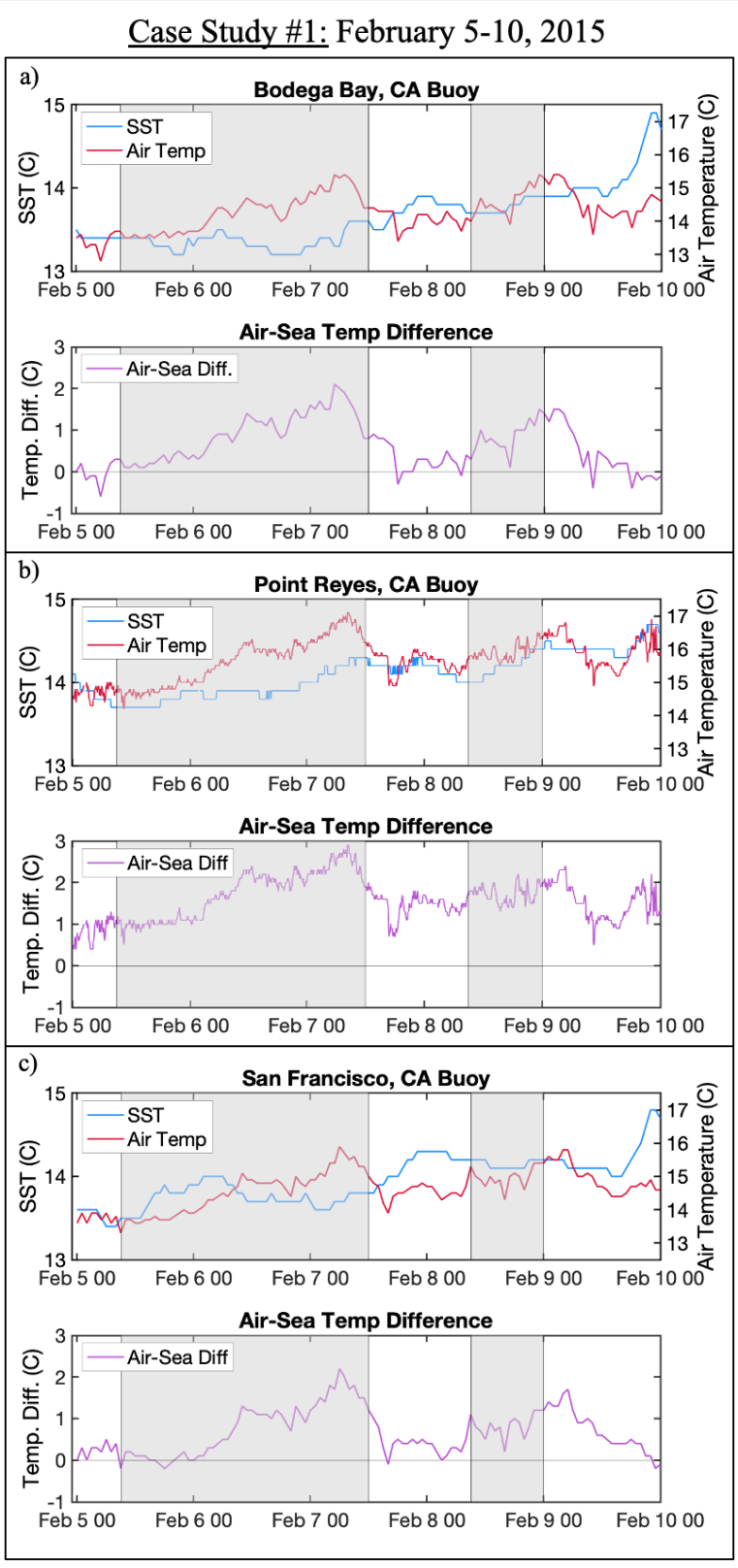

Figure 5-11. Buoy station timeseries of SST (C, top blue line), air temperature (C, top red line) and the air-sea temperature difference (C, bottom purple line) at A) BBY, B) PR, C) SF stations from Feb. 5-10, 2015.

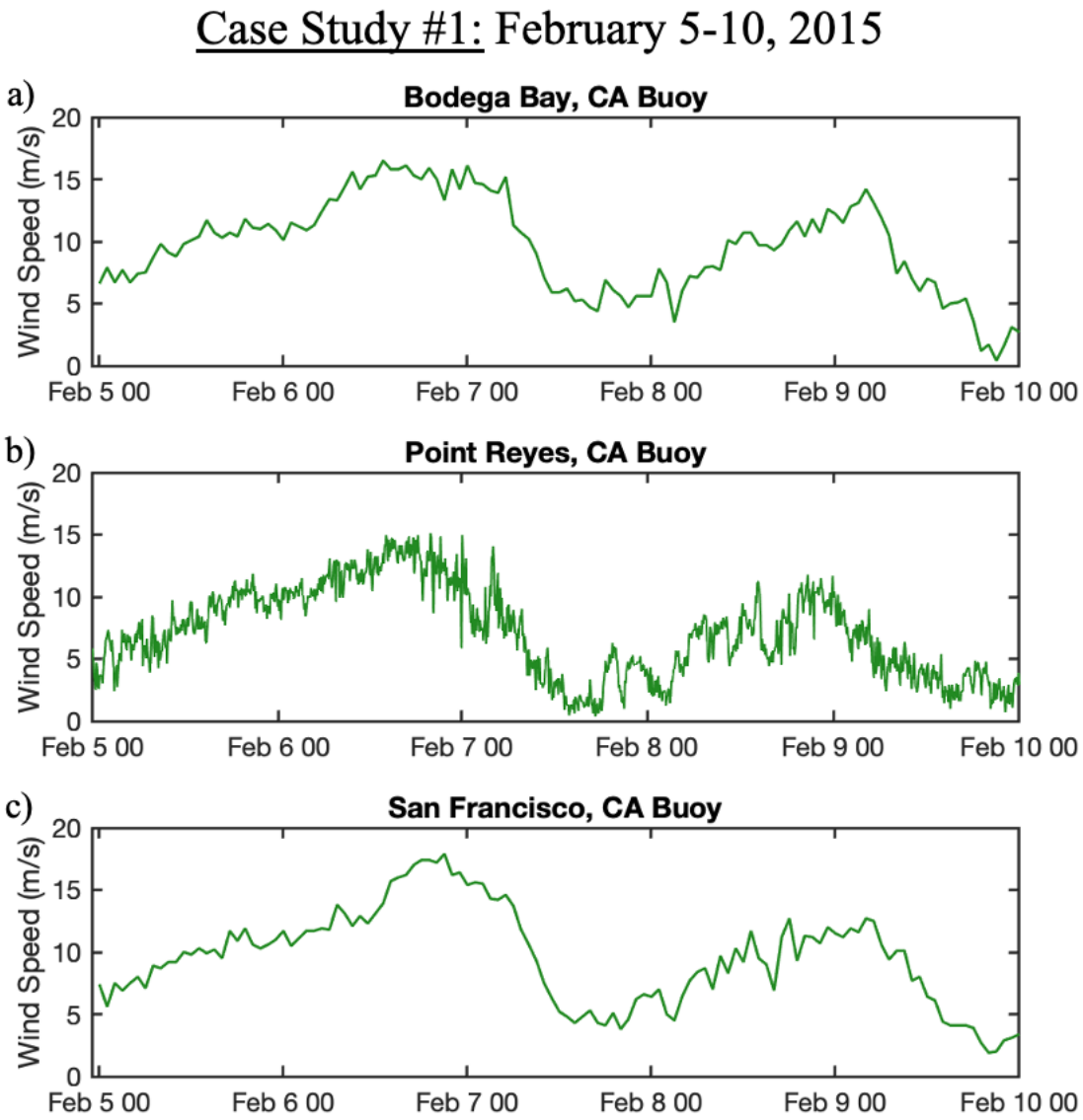

Figure 5-12. Wind speed timeseries from Feb. 5-10, 2015 at a) BBY, b) PR, and c) SF buoy stations.

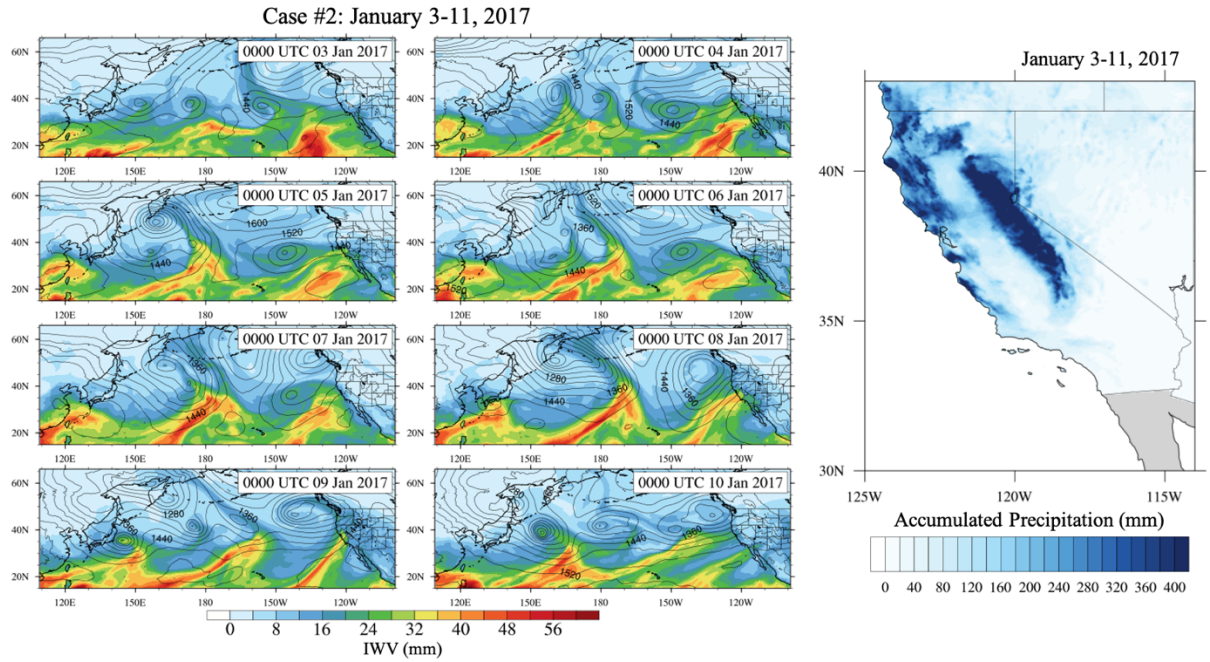

Figure 5-13. A) 850-hPa geopotential heights (m, contour) and IWV (mm, shaded contour) at 0000 UTC from January 3-10, 2017. B) Accumulated precipitation (mm) over the duration of case #2 from Jan. 3-11, 2017.

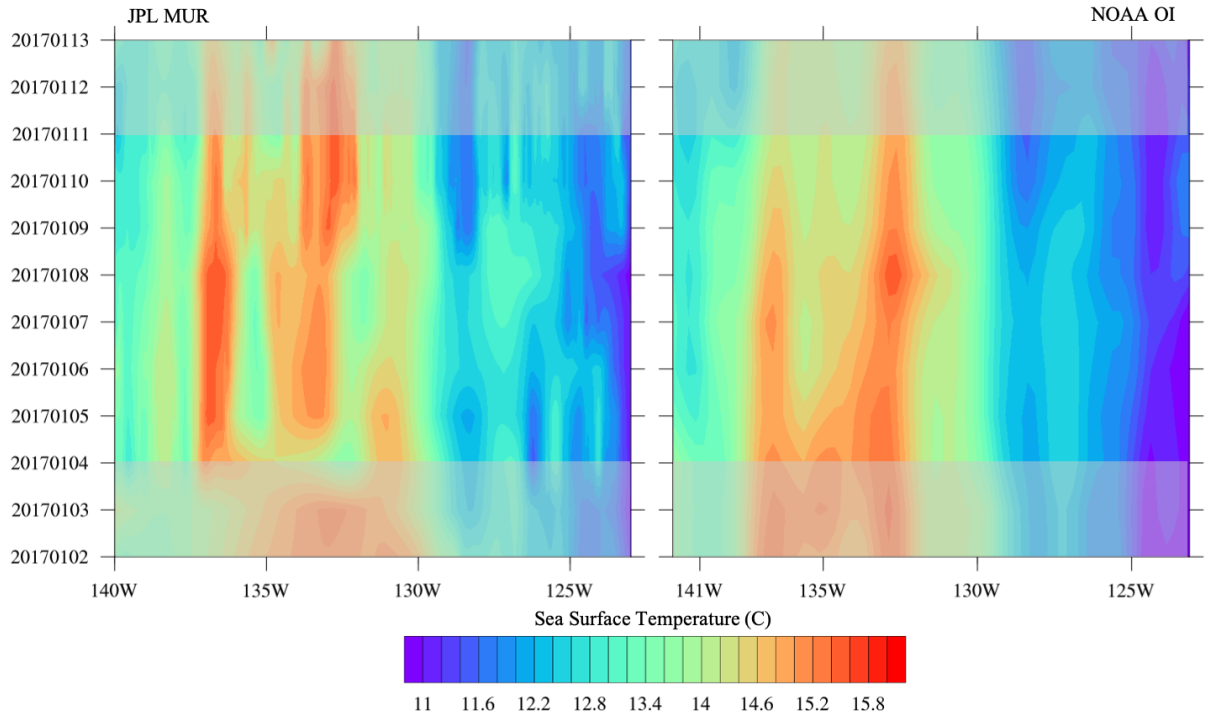

Figure 5-14. Hovmöller diagram of sea surface temperatures two days prior to the start of the case through two days after the event ends. Non-event days are shaded in transparent gray. A) JPL MUR SST, B) NOAA OI SST v2 both centered at 38ºN, extending from 140ºW to 123ºW.

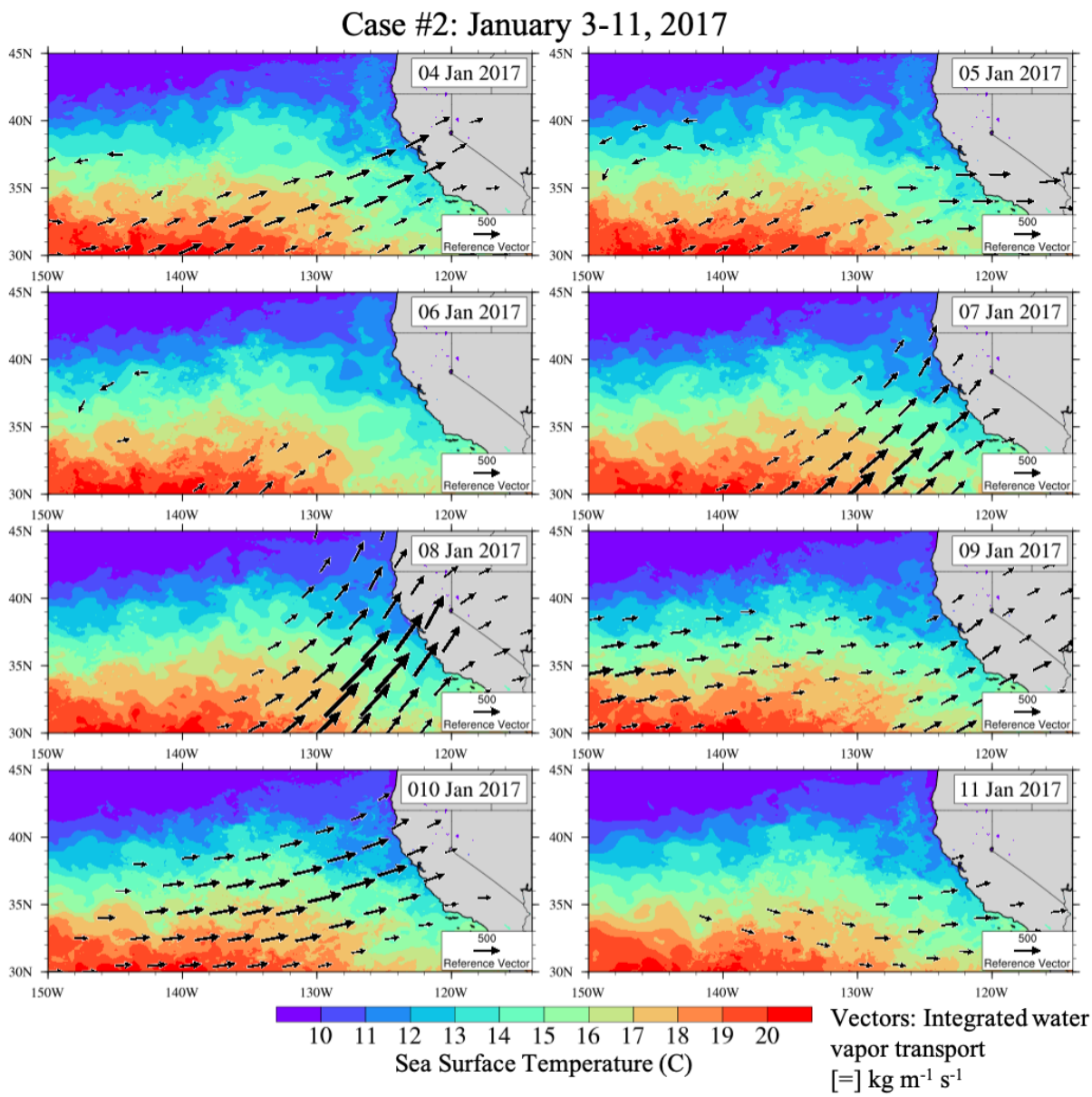

Figure 5-15. Daily MUR SST (C, shaded contour) and daily averaged IVT (kg m^{-1} s^{-1}, arrows) from Jan. 4-11, 2017.

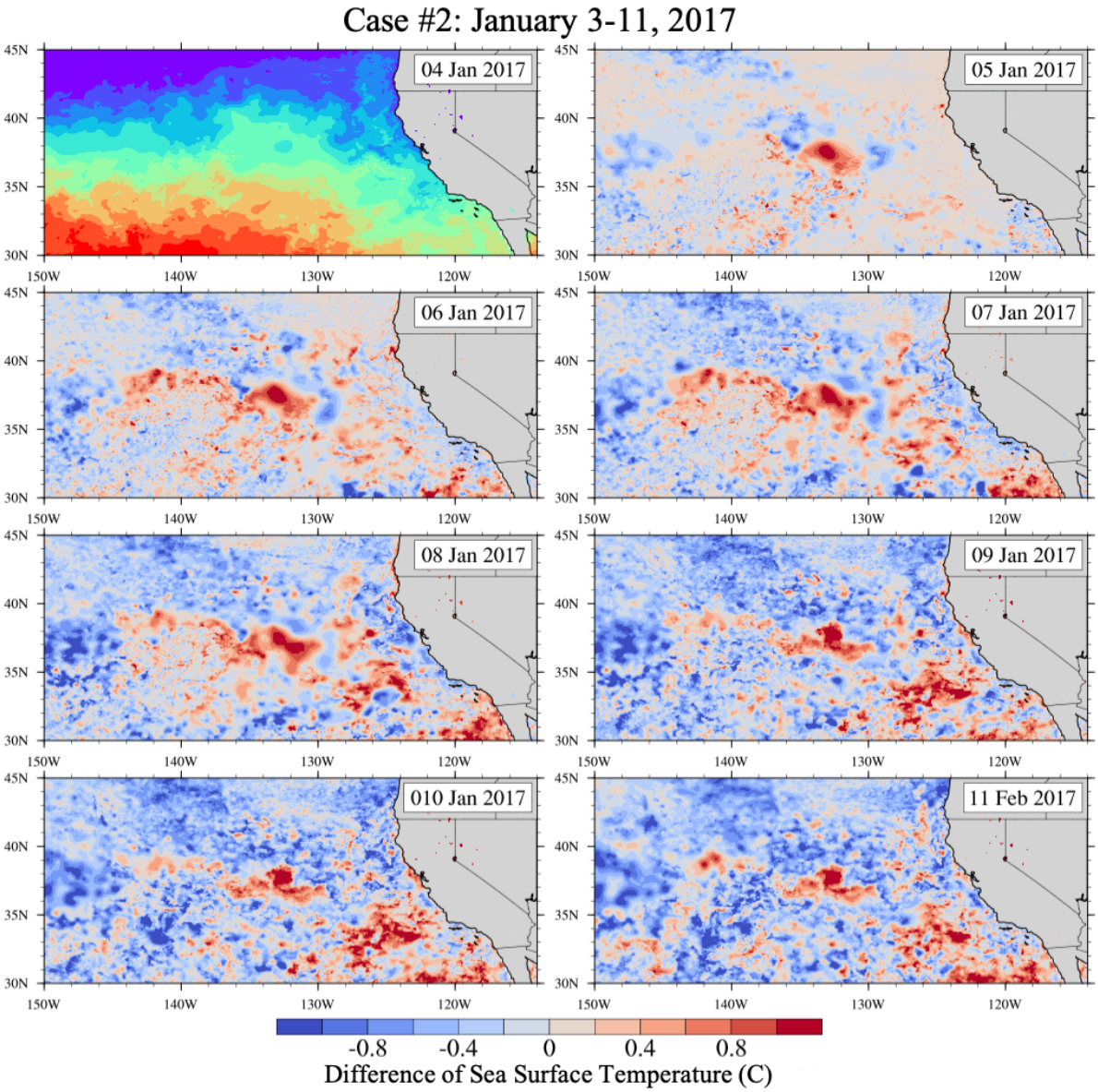

Figure 5-16. Cumulative difference in MUR SST (C, shaded contour) from the Jan. 4, 2017, the start of the case study time period, until the end of the event Jan. 11, 2017.

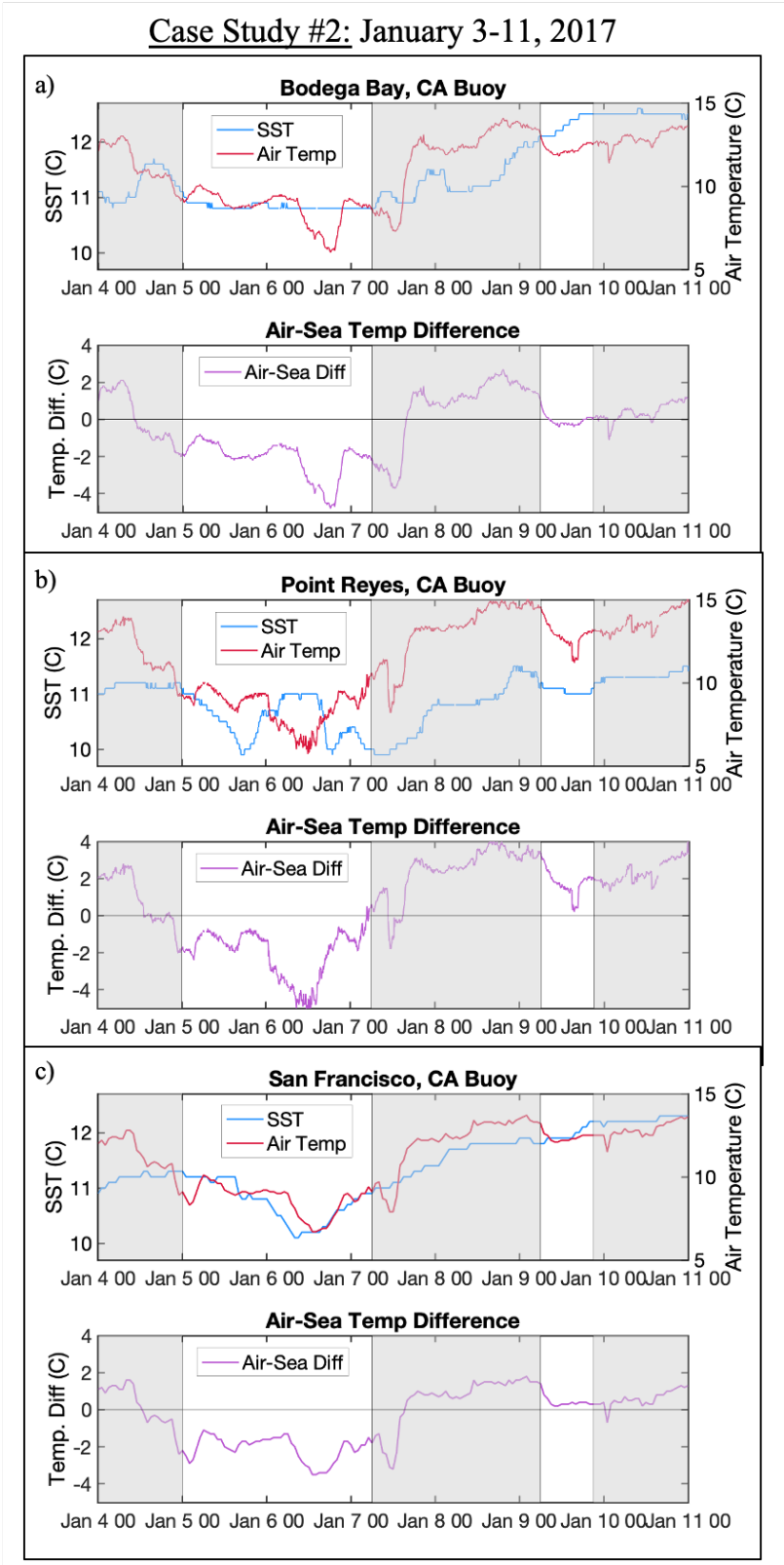

Figure 5-17. Buoy station timeseries of SST (C, top blue line), air temperature (C, top red line) and the air-sea temperature difference (C, bottom purple line) at A) BBY, B) PR, C) SF stations from Jan. 4-11, 2017.

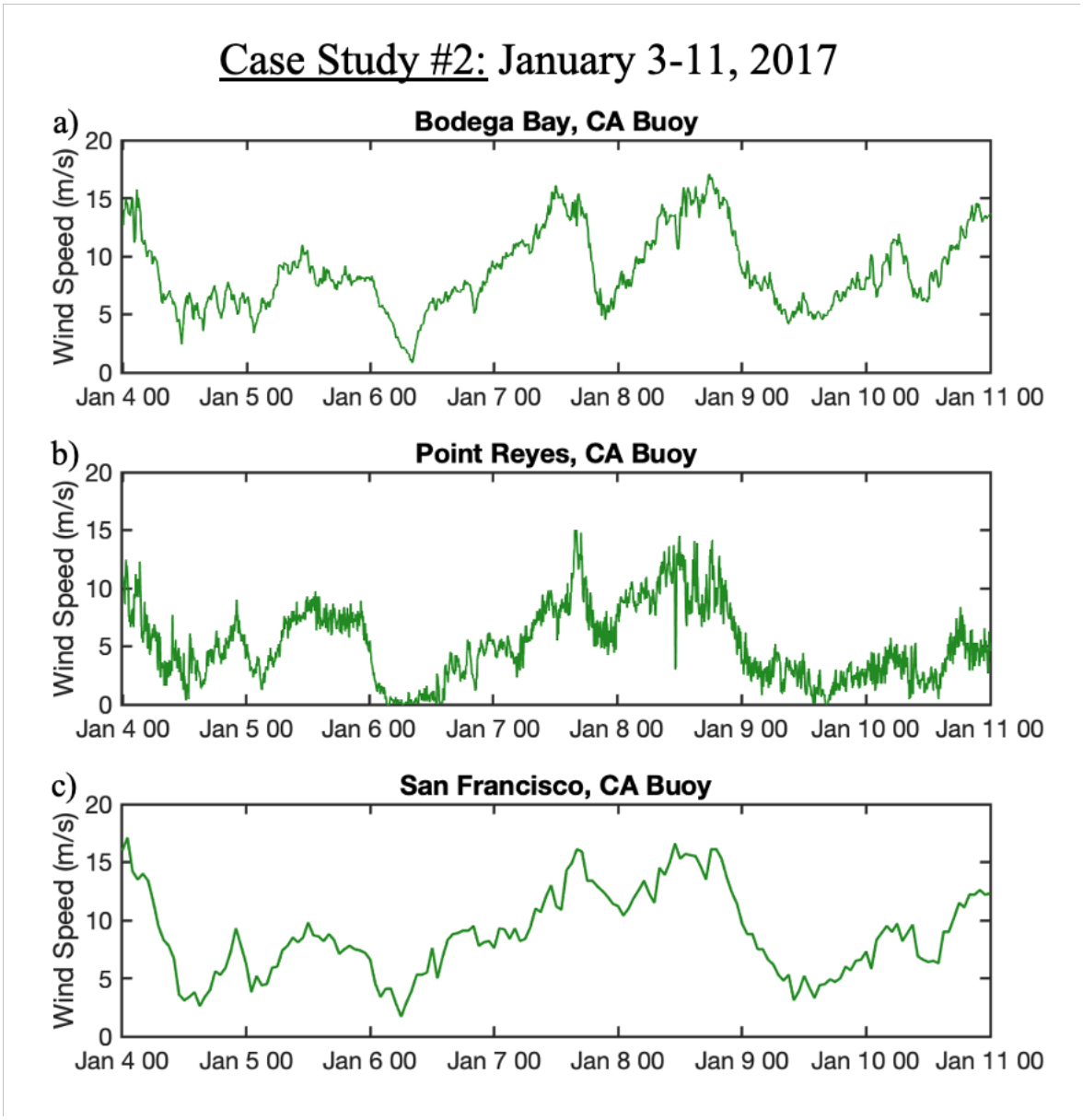

Figure 5-18. Wind speed timeseries from Jan. 4-11, 2017 at a) BBY, b) PR, and c) SF buoy stations.

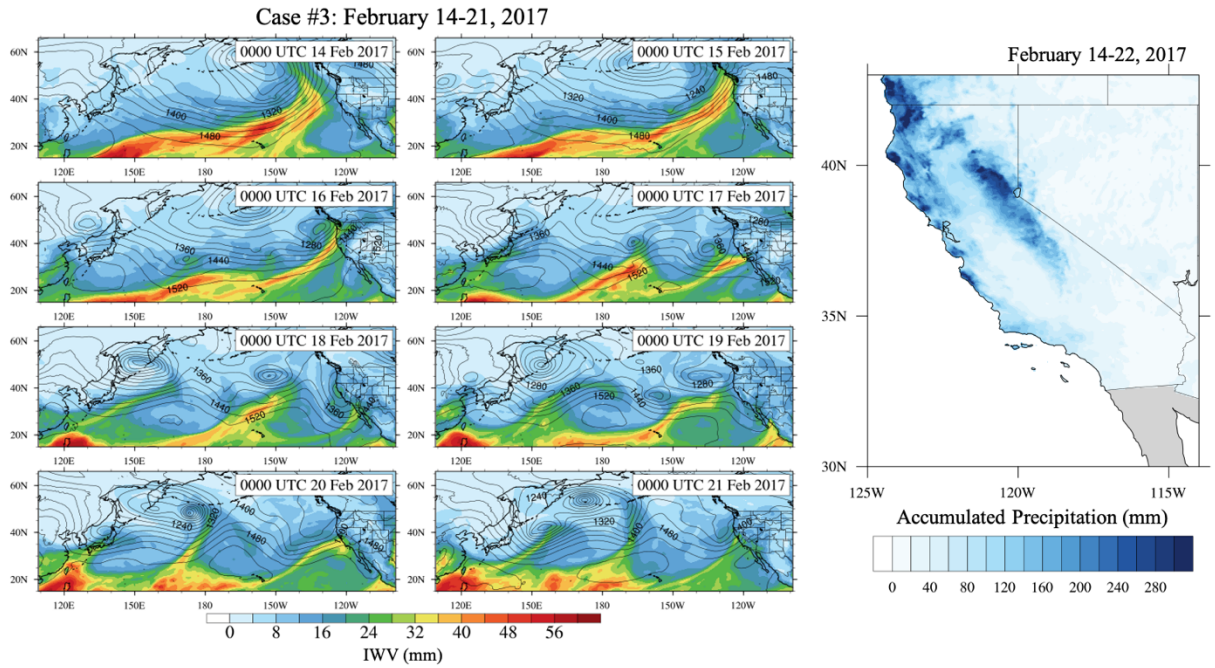

Figure 5-19. A) 850-hPa geopotential heights (m, contour) and IWV (mm, shaded contour) at 0000 UTC from February 14-21, 2017. B) Accumulated precipitation (mm) over the duration of case #3 from Feb. 14-22, 2017.

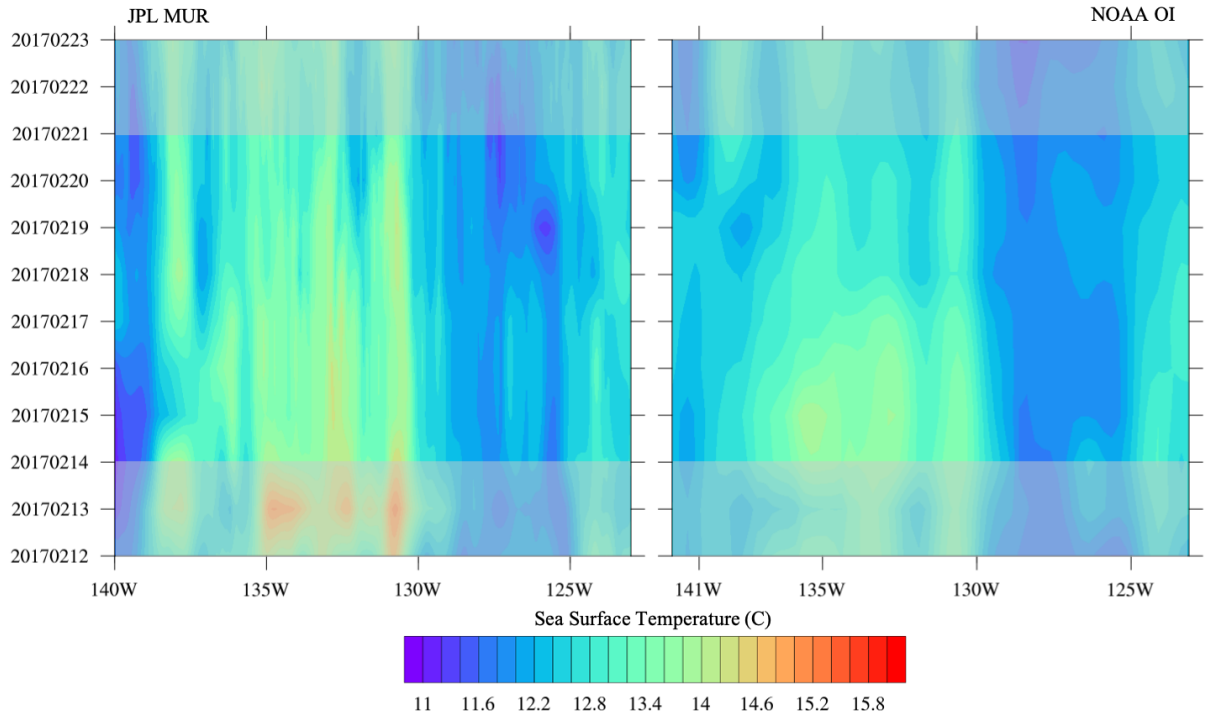

Figure 5-20. Hovmöller diagram of sea surface temperatures two days prior to the start of the case through two days after the event ends. Non-event days are shaded in transparent gray. A) JPL MUR SST, B) NOAA OI SST v2 both centered at 38ºN, extending from 140ºW to 123ºW.

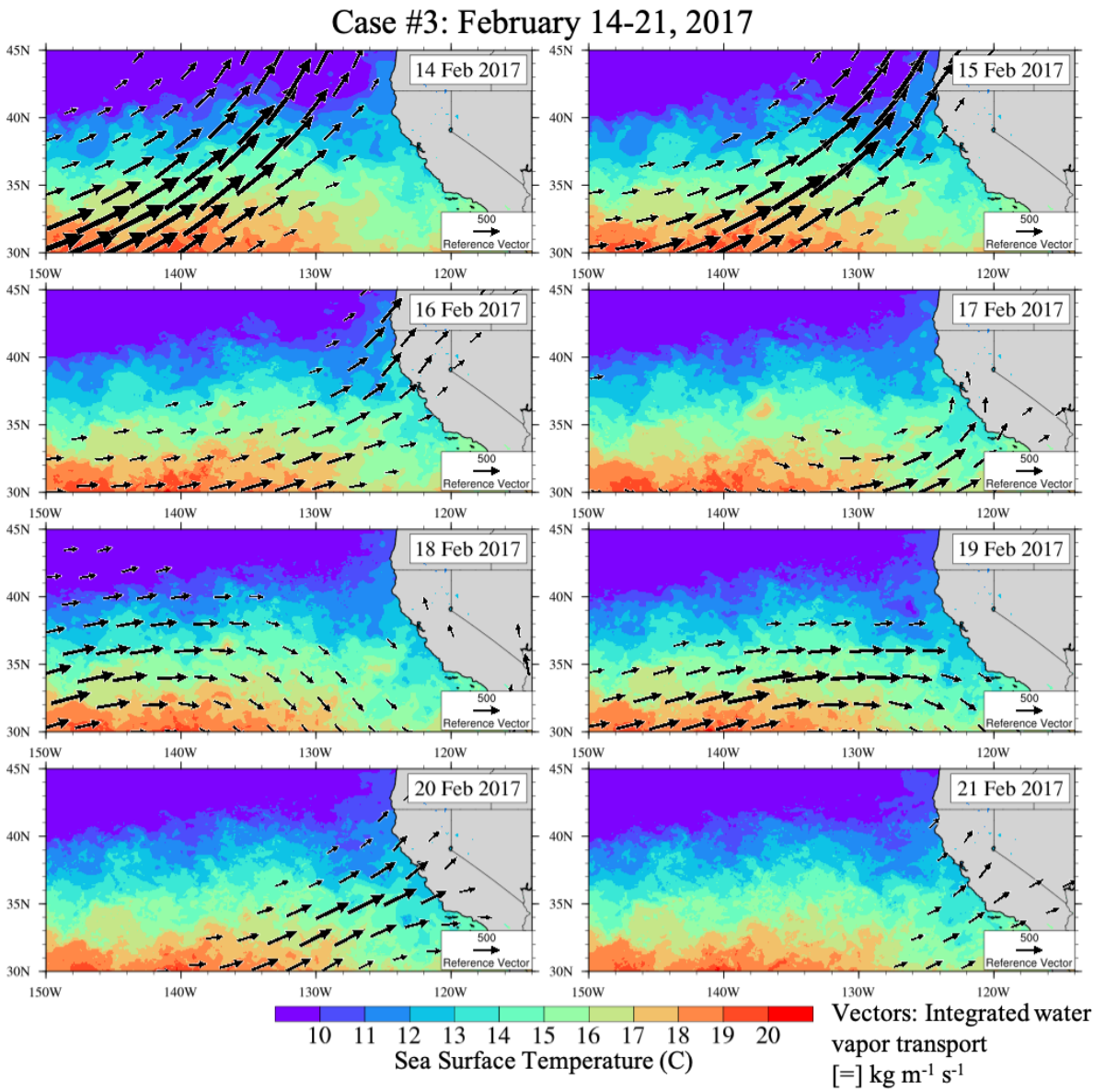

Figure 5-21. Daily MUR SST (C, shaded contour) and daily averaged IVT (kg m^{-1} s^{-1}, arrows) from Feb. 14-21, 2017.

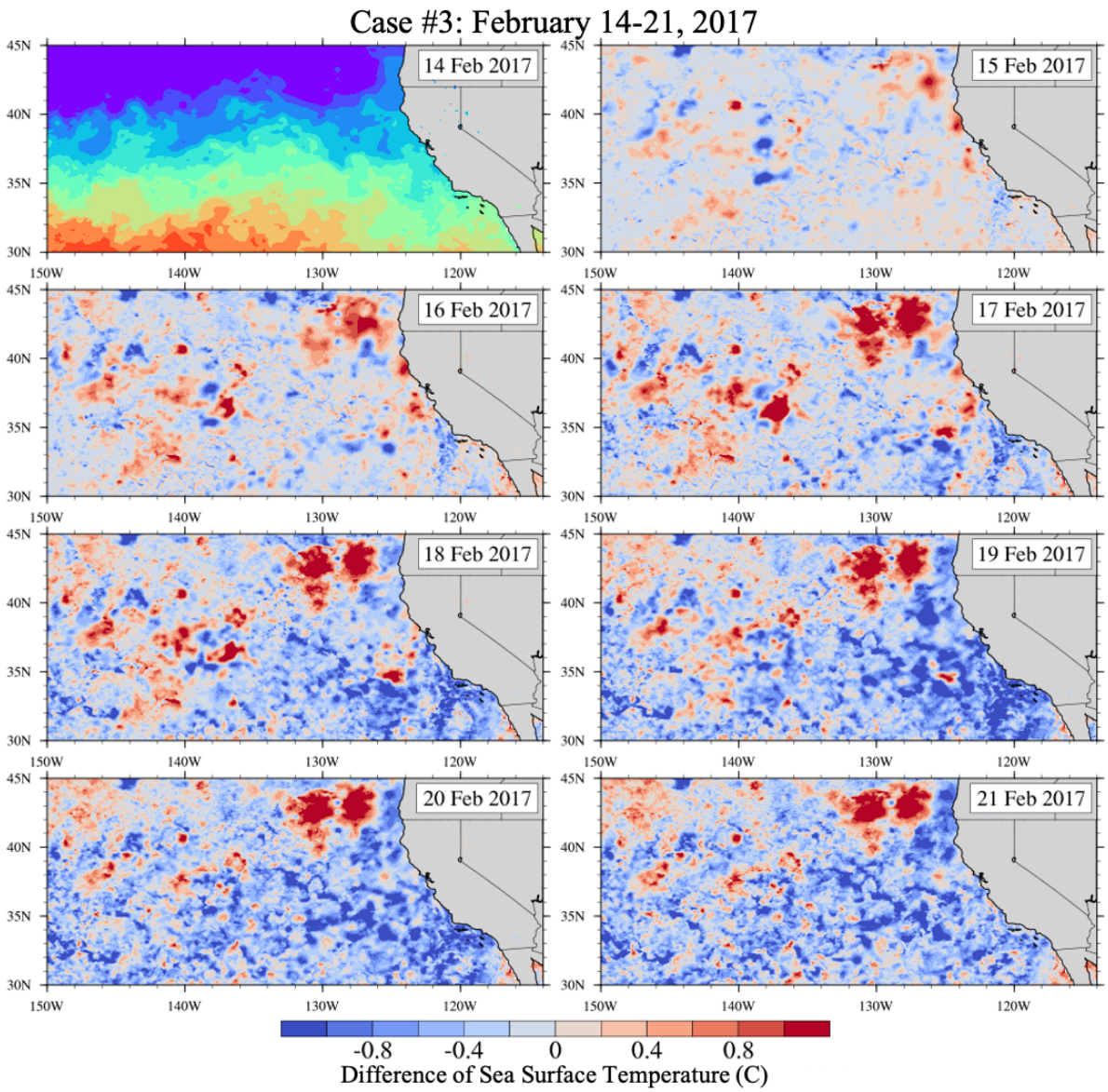

Figure 5-22. Cumulative difference in MUR SST (C, shaded contour) from the Feb. 14, 2017, the start of the case study time period, until the end of the event Feb. 21, 2017.

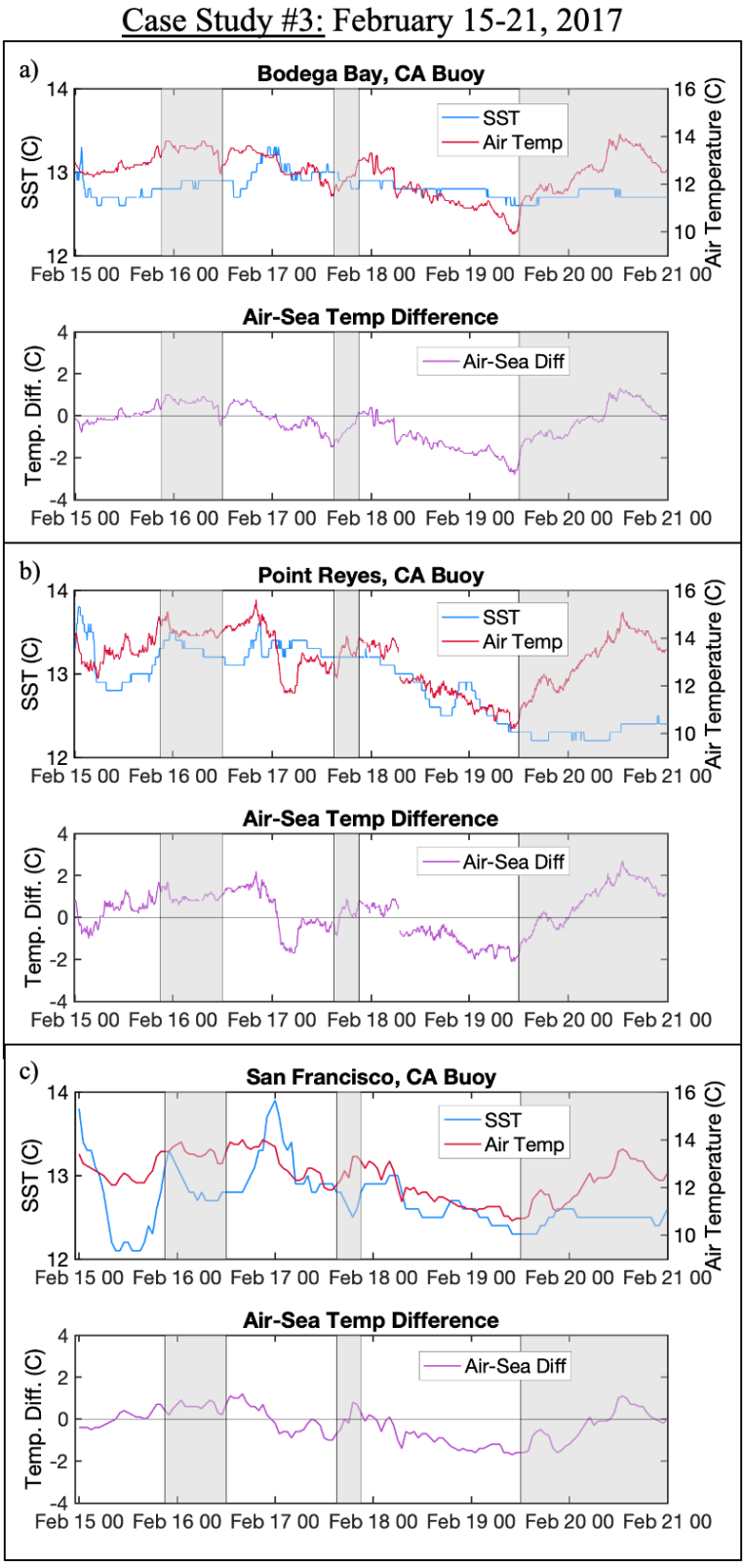

Figure 5-23. Buoy station timeseries of SST (C, top blue line), air temperature (C, top red line) and the air-sea temperature difference (C, bottom purple line) at A) BBY, B) PR, C) SF stations from Feb. 15-21, 2017.

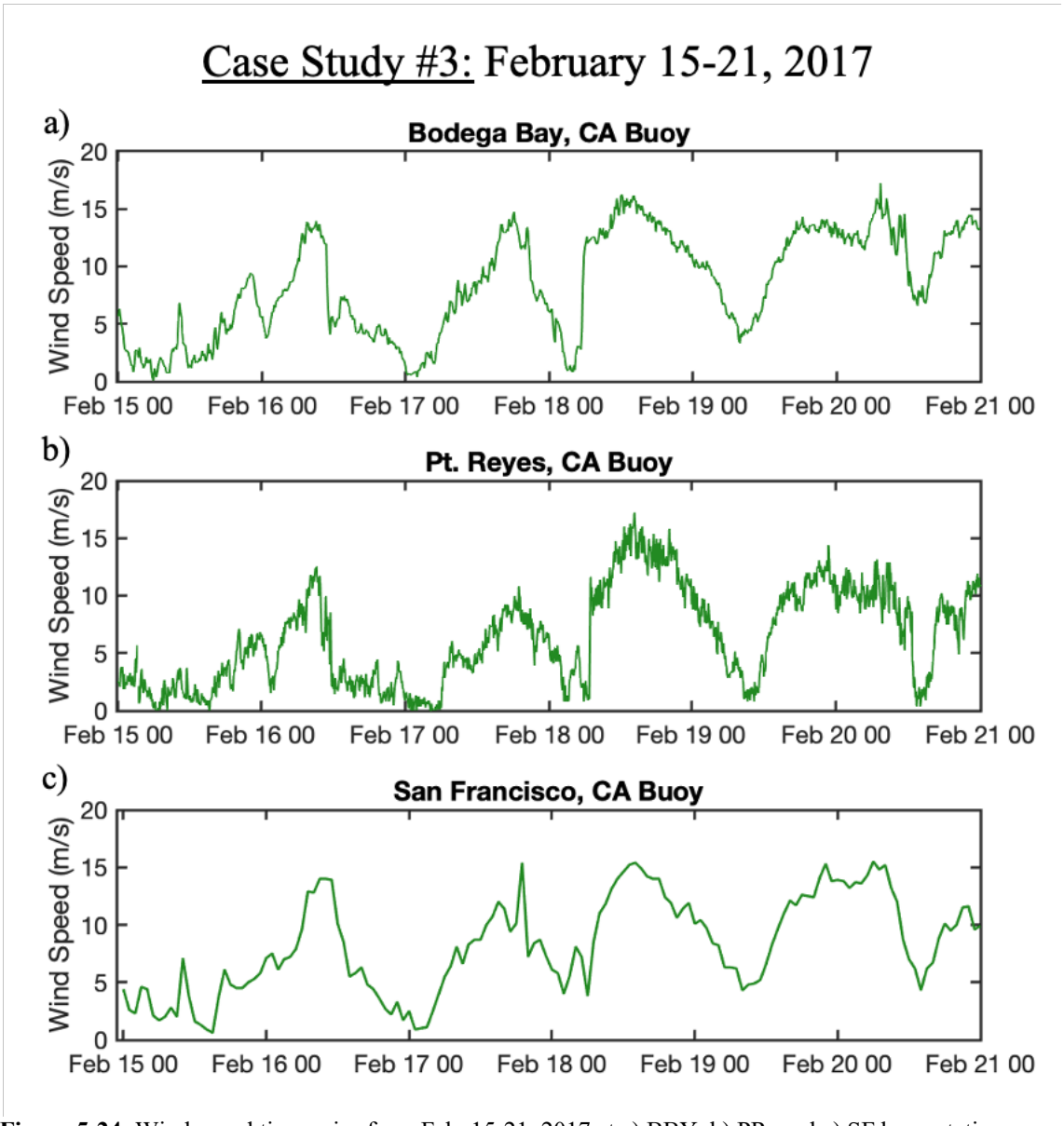

Figure 5-24. Wind speed timeseries from Feb. 15-21, 2017 at a) BBY, b) PR, and c) SF buoy stations.

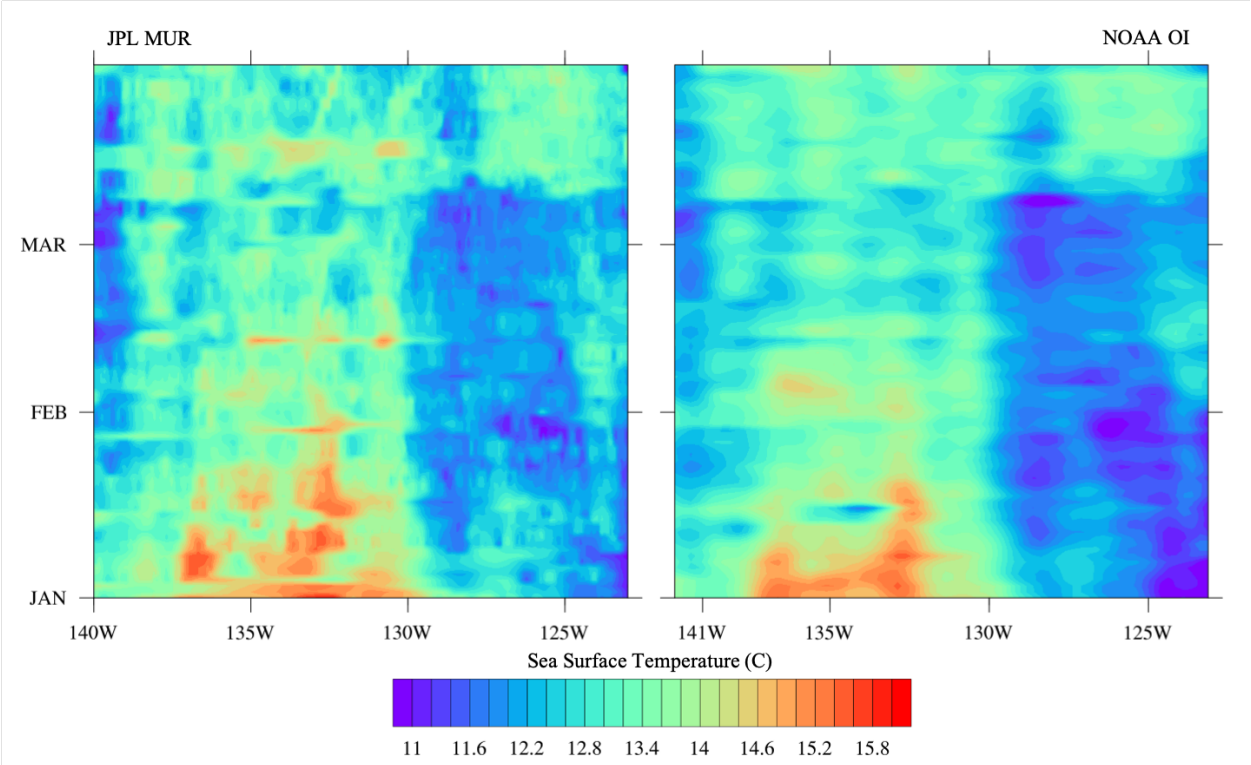

Figure 5-25. Hovmöller diagram of sea surface temperatures from Jan-Mar 2017. A) JPL MUR SST, B) NOAA OI SST v2 both centered at 38ºN, extending from 140ºW to 123ºW.

5.6 References

Banzon, V., T. M. Smith, C. Liu, and W. Hankins, 2016: A long-term record of blended satellite and in situ sea surface temperature for climate monitoring, modeling and environmental studies. *Earth Syst. Sci. Data Discuss.*, 1–13, https://doi.org/10.5194/essd-2015-44.

Camargo, S. J., M. Ting, and Y. Kushnir, 2013: Influence of local and remote SST on North Atlantic tropical cyclone potential intensity. *Clim. Dyn.*, **40**, 1515–1529, https://doi.org/10.1007/s00382-012-1536-4.

Chelton, D., and S.-P. Xie, 2010: Coupled Ocean-Atmosphere Interaction at Oceanic Mesoscales. *Oceanography*, https://doi.org/10.5670/oceanog.2010.05.

Chelton, D. B., M. G. Schlax, and R. M. Samelson, 2007: Summertime coupling between sea surface temperature and wind stress in the California current system. *J. Phys. Oceanogr.*, **37**, 495–517, https://doi.org/10.1175/JPO3025.1.

Cordeira, J. M., F. M. Ralph, A. Martin, N. Gaggini, J. R. Spackman, P. J. Neiman, J. J. Rutz, and R. Pierce, 2017: Forecasting atmospheric rivers during calwater 2015. *Bull. Am. Meteorol. Soc.*, **98**, 449–459, https://doi.org/10.1175/BAMS-D-15-00245.1.

Daly, C., R. P. Neilson, and D. L. Phillips, 1994: A statistical-topographic model for mapping climatological precipitation over mountainous terrain. *J. Appl. Meteor.*, **33**, 140-158.

Daly, C., G. H. Taylor, W. P. Gibson, T. W. Parzybok, G. L. Johnson, and P. Pasteris, 2001: High-quality spatial climate data sets for the United States and beyond. *Trans. Amer. Soc. Agri. Eng.*, **43**, 1957-1962.

Daly, C., W. P. Gibson, G. H. Taylor, G. L. Johnson, and P. Pasteris, 2002: A knowledge-based approach to statistical mapping of climate. *Climate Res.*, 22, 99–113.

Fish, M. A., A. M. Wilson, and F. M. Ralph, 2019: Atmospheric river families: Definition and associated synoptic conditions. *J. Hydrometeorol.*, **20**, 2091–2108, https://doi.org/10.1175/JHM-D-18-0217.1.

Gelaro, R., W. McCarty, M. J. Suarez, R. Todling, A. Molod, L. Takacs, C. A. Randles, A. Darmenov, M. G. Bosilovich, R. Reichle, K. Wargan, L. Coy, R. Cullather, C. Draper, S.

Akella, V. Buchard, A. Conaty, A. M. da Silva, W. Gu, G.-K. Kim, R. Koster, R. Lucchesi, D. Merkova, J. E. Nielsen, G. Partyka, S. Pawson, W. Putman, M. Reinecker, S. D. Schubert, M. Sienkiewicz and B. Zhao, 2017: The modern-era retrospective analysis for research and applications, version 2 (MERRA-2). *J. Clim.*, **30**, 5419–5454, https://doi.org/10.1175/JCLI-D-16-0758.1.

Gemmrich, J., and A. Monahan, 2018: Covariability of Near-Surface Wind Speed Statistics and Mesoscale Sea Surface Temperature Fluctuations. *J. Phys. Oceanogr.*, **48**, 465–478, https://doi.org/10.1175/JPO-D-17-0177.1.

Gershunov, A., T. Shulgina, F. M. Ralph, D. A. Lavers, and J. J. Rutz, 2017: Assessing the climate-scale variability of atmospheric rivers affecting western North America. *Geophys. Res. Lett.*, **44**, 7900–7908, https://doi.org/10.1002/2017GL074175.

Hu, Z. Z., A. Kumar, B. Jha, J. Zhu, and B. Huang, 2017: Persistence and predictions of the remarkable warm anomaly in the northeastern Pacific ocean during 2014-16. *J. Clim.*, **30**, 689–702, https://doi.org/10.1175/JCLI-D-16-0348.1.

JPL MUR MEaSUREs Project. 2010. GHRSST Level 4 MUR Global Foundation Sea Surface Temperature Analysis. Ver. 2. PO.DAAC, CA, USA. Dataset accessed [2017-11-05] at http://dx.doi.org/10.5067/GHGMR-4FJ01.

Kelly, K. A., R. J. Small, R. M. Samelson, B. Qiu, T. M. Joyce, Y. O. Kwon, and M. F. Cronin, 2010: Western boundary currents and frontal air-sea interaction: Gulf stream and Kuroshio Extension. *J. Clim.*, **23**, 5644–5667, https://doi.org/10.1175/2010JCLI3346.1.

Kirtman, B. P., C. Bitz, F. Bryan, W. Collins, J. Denns, N. Hearn, J. L. Kinter III, R. Loft, C. Rousset, L. Siqueria, C. Stan, R. Tomas and M. Vertenstein, 2012: Impact of ocean model resolution on CCSM climate simulations. *Clim. Dyn.*, **39**, 1303–1328, https://doi.org/10.1007/s00382-012-1500-3.

Lamjiri, M. A., M. D. Dettinger, F. M. Ralph, N. S. Oakley, and J. J. Rutz, 2018: Hourly analyses of the large storms and atmospheric rivers that provide most of California's precipitation in only 10 to 100 hours per year. *San Fr. Estuary Watershed Sci.*, **16**, https://doi.org/10.15447/sfews.2018v16iss4art1.

Lee, M. Y., C. C. Hong, and H. H. Hsu, 2015: Compounding effects of warm sea surface temperature and reduced sea ice on the extreme circulation over the extratropical North

Pacific and North America during the 2013-2014 boreal winter. *Geophys. Res. Lett.*, **42**, 1612–1618, https://doi.org/10.1002/2014GL062956.

Lynn, R. J., and J. J. Simpson, 1987: The California Current system: The seasonal variability of its physical characteristics. *J. Geophys. Res.*, **92**, 12947, https://doi.org/10.1029/jc092ic12p12947.

Ma, X., P. Chang, R. Saravanan, R. Montuoro, H. Nakamura, D. Wu, X. Lin, and L. Wu, 2017: Importance of resolving kuroshio front and eddy influence in simulating the north pacific storm track. *J. Clim.*, https://doi.org/10.1175/JCLI-D-16-0154.1.

Martin, A. C., F. M. Ralph, A. Wilson, L. Dehaan, and B. Kawzenuk, 2019: Rapid cyclogenesis from a mesoscale frontal wave on an atmospheric river: Impacts on forecast skill and predictability during atmospheric river landfall. *J. Hydrometeorol.*, **20**, 1779–1794, https://doi.org/10.1175/JHM-D-18-0239.1.

Moore, B. J., A. B. White, D. J. Gottas, and P. J. Neiman, 2020: Extreme Precipitation Events in Northern California during Winter 2016–17: Multiscale Analysis and Climatological Perspective. *Mon. Weather Rev.*, **148**, 1049–1074, https://doi.org/10.1175/mwr-d-19-0242.1.

Neiman, P. J., B. J. Moore, A. B. White, G. A. Wick, J. Aikins, D. L. Jackson, J. Ryan Spackman, and F. Martin Ralph, 2016: An airborne and ground-based study of a long-lived and intense atmospheric river with mesoscale frontal waves impacting California during CalWater-2014. *Mon. Weather Rev.*, **144**, 1115–1144, https://doi.org/10.1175/MWR-D-15-0319.1.

——, N. Gaggini, C. W. Fairall, J. Aikins, J. R. Spackman, L. R. Leung, J. Fan, J. Hardin, N. R. Nalli, and A. B. White, 2017: An Analysis of Coordinated Observations from NOAA's *Ronald H. Brown* Ship and G-IV Aircraft in a Landfalling Atmospheric River over the North Pacific during CalWater-2015. *Mon. Weather Rev.*, https://doi.org/10.1175/MWR-D-17-0055.1.

O'Reilly, C. H., and A. Czaja, 2015: The response of the pacific storm track and atmospheric circulation to kuroshio extension variability. *Q. J. R. Meteorol. Soc.*, **141**, 52–66, https://doi.org/10.1002/qj.2334.

Parfitt, R., A. Czaja, and Y. O. Kwon, 2017: The impact of SST resolution change in the ERA-

Interim reanalysis on wintertime Gulf Stream frontal air-sea interaction. *Geophys. Res. Lett.*, **44**, 3246–3254, https://doi.org/10.1002/2017GL073028.

Persson, P. O. G., J. E. Hare, L. B. Nance, and B. Walter, 2008: Impact of Air-Sea Interactions on Extra-Tropical Cyclones. *Proc. ECMWF Work. Ocean. Interact.*, 123–146.

Peterson, W., M. Robert, and N. Bond, 2015: The warm blob – Conditions in the northeastern Pacific Ocean. *PICES Press*, **23**, 36–38, https://doi.org/10.1177/0023830999042002090l.

Ralph, F. M., K. A. Prather, D. Cayan, J. R. Spackman, P. DeMott, M. Dettinger, C. Fairall, R. Leung, D. Rosenfeld, S. Rutledge, D. Waliser, A. B. White, J. Cordeira, A. Martin, J. Helly, and J. Intrieri, 2016: Calwater field studies designed to quantify the roles of atmospheric rivers and aerosols in modulating U.S. West Coast Precipitation in a changing climate. *Bull. Am. Meteorol. Soc.*, **97**, 1209–1228, https://doi.org/10.1175/BAMS-D-14-00043.1.

——, A. M. Wilson, T. Shulgina, B. Kawzenuk, S. Sellers, J. J. Rutz, M. A. Lamjiri, E. A. Barnes, A. Gershunov, B. Guan, K. M. Nardi, T. Osborne, and G. A. Wick, 2019: ARTMIP-early start comparison of atmospheric river detection tools: how many atmospheric rivers hit northern California's Russian River watershed? *Clim. Dyn.*, **52**, 4973–4994, https://doi.org/10.1007/s00382-018-4427-5.

Reynolds, R. W., T. M. Smith, C. Liu, D. B. Chelton, K. S. Casey, and M. G. Schlax, 2007: Daily high-resolution-blended analyses for sea surface temperature. *J. Clim.*, **20**, 5473–5496, https://doi.org/10.1175/2007JCLI1824.1.

Rutz, J. J., C. A Shields, J. M. Lora, A. E. Payne, B. Guan, P. Ullrich, T. O'Brien, L. R. Leung, F. M. Ralph, M. Wehner, S. Brands, A. Collow, N. Goldenson, I. Gorodetskya, H. Griffith, K. Kashinath, B. Kawzenuk, H. Krishnan, V. Kurlin, D. Lavers, G. Magnusdottir, K. Mahoney, E. McClenny, G. Muszynski, P. D. Nguyen, M. Prabhat, Y. Qian, A. M. Ramos, C. Sarangi, S. Sellers, T. Shulgina, R. Tome, D. Waliser, D. Walton, G. Wick, A. M. Wilson, and M. Viale, 2019: The Atmospheric River Tracking Method Intercomparison Project (ARTMIP): Quantifying Uncertainties in Atmospheric River Climatology. *J. Geophys. Res. Atmos.*, **124**, 13777–13802, https://doi.org/10.1029/2019JD030936.

Simpson, J. J., and R. J. Lynn, 1990: A Mesoscale Eddy Dipole in the Offshore California Current. *J. Geophys. Res.*, **95**, 13009–13022.

Small, R. J., S.P. deSzoeke, S.P. Xie, L. O'Neil, H. Seo, Q. Song, P. Cornillon, M. Spall and S.

Minobe, 2008: Air-sea interaction over ocean fronts and eddies. *Dyn. Atmos. Ocean.*, https://doi.org/10.1016/j.dynatmoce.2008.01.001.

Stegmann, P. M., and F. Schwing, 2007: Demographics of mesoscale eddies in the California Current. *Geophys. Res. Lett.*, **34**, 2–5, https://doi.org/10.1029/2007GL029504.

Sun, R., A. C. Subramanian, B. D. Cornuelle, I. Hoteit, M. R. Mazloff, A. J. Miller, H. Seo, 2020: The role of air-sea interactions in atmospheric river events: Case studies using the SKRIPS regional coupled model. *J. Geophys. Res.*

Waliser, D., and B. Guan, 2017: Extreme winds and precipitation during landfall of atmospheric rivers. *Nat. Geosci.*, **10**, 179–183, https://doi.org/10.1038/ngeo2894.

White, A. B., B. J. Moore, D. J. Gottas, and P. J. Neiman, 2019: Winter storm conditions leading to excessive runoff above California's Oroville dam during January and February 2017. *Bull. Am. Meteorol. Soc.*, **100**, 55–69, https://doi.org/10.1175/BAMS-D-18-0091.1.

Chapter 6

Conclusion

6.1 Summary of major contributions

This dissertation used atmospheric reanalysis and observational data to investigate the multi-scale processes that lead to successive atmospheric river (AR) events, herein termed AR families, in California. The main objective of this work was to identify the occurrence of successive AR events, further understand the synoptic and mesoscale environments of these events and begin to assess the potential for enhanced predictability of AR families and their impacts.

In Chapter 2, we use hourly measurements from an atmospheric river observatory at Bodega Bay, CA to identify periods when multiple AR events occur in rapid succession. Using the AR family identification method, a range of aggregation periods were tested. It was determined that in the North Pacific, AR events optimally cluster at 120-hours. AR families are defined as, "two or more AR events occurring within one aggregation period". The associated synoptic conditions of AR families and single AR events is explored. Compared to single AR events, the synoptic environment of AR families is characterized by lower geopotential heights throughout the mid-latitude North Pacific, an enhanced subtropical high, and a stronger zonal North Pacific jet. A case study on water year (WY; October 1-September 30) 2017, which had the highest number of AR families in the observational catalog, showed a persistent geopotential height dipole throughout the North Pacific and a positive anomaly of IWV extending toward

California. It was determined that AR families often developed and persisted when synoptic features were semi-stationary.

Chapter 3 was motivated by the results of Chapter 2, which identified AR families using an observational dataset from a single location in northern California over a period of 13 years. Therefore, Chapter 3 set out to expand the identification of AR families to all events impactful to California using atmospheric reanalysis data. This chapter in particular focuses on studying the large-scale meteorological drivers associated with these compound events. A new 39-year catalog of 248 AR family events impacting California between 1981 and 2019 is introduced. K-means clustering on the 500-hPa geopotential height field, allows for the classification of six distinct clusters that represent the large-scale patterns typically associated with AR families. These clusters broadly represent two types of predominant features: meridional and zonal patterns. Two clusters exhibit strong relationships with phases of the El Niño/Southern Oscillation, indicating a potential for increased predictability. This work advanced our understanding of the large-scale environment and underlying physical drivers associated with AR families.

While the two previous chapters identify the importance of large-scale patterns and AR families, Chapter 4 aims to connect interannual large-scale anomalies and anomalous impacts, such as the whiplash between extreme wet and extreme dry years in California. This objective is addressed by exploring the relationship between North Pacific persistent anomalies (PAs) and the interannual variability of West Coast precipitation. Before the above objective could be answered, it was found that PA analysis is sensitive to detrending methods and the method determining the appropriate magnitude of the PA. This chapter emphasizes that traditional PA methods do not meaningfully characterize PAs that are impactful for California or West Coast

states. Therefore, a new method for investigating PAs impactful to California is explored and additional analysis to develop a robust method for identifying PAs correlated to California's extreme weather is proposed.

The final chapter of the dissertation takes a different perspective on AR families. To complement the investigation of the large-scale environment in the North Pacific associated with AR families, the focus of this chapter is on coastal sea surface temperature (SST) variability and boundary layer properties. This chapter seeks to understand the coastal air-sea temperature variability in Northern California during landfalling ARs. Using two different spatial and temporal resolution SST datasets, this chapter characterizes the average and standard deviation wintertime SST throughout the North Pacific. An assessment of interannual variability of wintertime SST shows large differences between years, with low SST variability co-occurring during years of low AR activity. At near shore buoy stations, the average air-sea temperature difference prior, during, and post AR passage show increasing, positive, and decreasing values, consistent with an approaching warm front, AR conditions and cold air advection, respectively. Analysis into three case studies over impactful precipitation and AR family events is conducted to further understanding the variability of the relationship between AR activity, SST, and precipitation in Northern California.

6.2 Directions for future and related research

In WY 2017, periods of successive AR events led to an impactful WY, that culminated in the Oroville Dam crisis, prompting the evacuation of over 180,000 people. Motivated by that record setting WY, the research presented in this dissertation 1) advances our understanding of these compound events by creating a new classification termed "AR families" based on

successive AR events, 2) characterizes the large-scale environments in which these events occur, 3) explores the semi-stationary aspects of their occurrence and 4) investigates near shore air-sea temperature variability through event duration. This research also provides the foundation for integrating successive storms into water management and flood risk strategies for California.

While this dissertation strives to answer fundamental questions about AR families, there are still outstanding questions to be addressed. Foremost, quantification of the differences in impacts between AR families and single AR events, potentially determined through precipitation totals or streamflow amounts, needs to be completed to comprehensively understand how AR families can enhance impacts on watersheds. To further assess the probability of successive AR events, copulas, designed to model the dependence between multiple variables, should be applied to AR families to understand the correlated relationship between AR events. Additional joint distribution statistics, such as joint return periods should be considered to address the possible increased risk or return period of AR families compared to single AR events throughout California. To expand our understanding of the dynamics leading to successive AR events, potential planetary and synoptic scale modulators, such as the influence of Rossby wave breaking on the generation and termination of successive ARs, should be explored. Furthermore, the relationship between cyclone families and AR families should be investigated. This relationship is important to understand as ARs are often stronger when associated with extra-tropical cyclones and additional research indicating a more direct correlation could enrich our understanding of the physical processes and impacts of both phenomena (Zhang et al. 2018). Overall, expanding upon the results here, identifying and characterizing a significant subset of ARs will help to further improve our understanding of, and preparation for the impacts associated with these events.

6.3 References

Zhang, Z. F. M. Ralph, and M. Zheng, 2018: The relationship between extratropical cyclone strength and atmospheric river intensity and position. *Geophys. Res. Lett.,* doi:10.1029/2018GL079071.